

Universitat
de les Illes Balears

MASTER'S THESIS

PROBING THE BLACK HOLE RINGDOWN THROUGH NUMERICAL PERTURBATION THEORY

Alejandro Svyatkovskyy Kholyavka

Master's Degree in Advanced Physics and Applied Mathematics
(Specialisation in Astrophysics and Relativity)

Centre for Postgraduate Studies

Academic year 2025-26

PROBING THE BLACK HOLE RINGDOWN THROUGH NUMERICAL PERTURBATION THEORY

Alejandro Svyatkovskyy Kholyavka

Master's Thesis

Centre for Postgraduate Studies

University of the Balearic Islands

Academic year 2025-26

Keywords: Black holes, quasi-normal modes, ringdown, late-time tails, gravitational waves.

Supervisor: Dr. Xisco Jiménez Forteza

I hereby authorize the University to include this work in its institutional repository for open access consultation and to disseminate it online, exclusively for academic and research purposes.	Author		Supervisor	
	Yes	No	Yes	No
	☑	☐	☑	☐

The world is too loud to use words,
use equations instead.

This work has been carried out within the Relativity and Gravitation Group at the Institute of Applied Computing and Community Code (IAC3) of the University of the Balearic Islands. The author thankfully acknowledges the computer resources at MareNostrum and the technical support provided by Barcelona Supercomputing Center (RES-AECT-2025-1-0011, RES-AECT-2025-2-0038).



Acknowledgements

Before you, dear reader, immerse yourself in the following pages, allow me to take a moment to acknowledge those who have walked alongside me as this project took shape. To all of them, I owe deep admiration for having accompanied me—one way or another—through this journey.

First and foremost, to Xisco, because without him, this work would not exist (mainly because he is my supervisor :)). I want to thank him for his immense patience with me from the very first minute we began this adventure. I could not have wished for a better guide. I truly hope that, one day, we will have the chance to work together again. His unwavering energy and contagious motivation made even the toughest moments feel like an uphill climb, yes, but always a possible one.

To my parents, for continuing to fight so that I can reach my dreams. I have never told you enough: you are my greatest heroes. Thank you for supporting me even when you do not fully understand what I do, and for always believing in me. This work is yours as well. I hope it makes you proud.

To Iván, Óscar, and Diego, for always being there, even when you did not know you were. For giving me your strength unconditionally, for understanding without asking, and for showing up just when I needed it most. With you, flying has been easier, and the hard days, a little less hard. I admire not only your intelligence and your passion, but also the generosity with which you walk beside those around you. You are the best physicists I know, and I have no doubt you will go far—wherever you choose to go. And I will be there to celebrate it. Thank you for dressing up with me when needed, for never getting in the way, and for rescuing me so many times without ever asking for anything in return. You are, without a doubt, my *mujer de verde*.

To Jorge, Aníbal, Adri, Xabi, Thomas, and Borja, for making me feel welcome on this island from the very beginning, and for making space for me among you. Being with you all has made everything easier and lighter. Thank you for your simple—and precious—way of being present.

To Juan and Emilio, because even though you were far away, feeling you close helped me more than you can imagine. For every message, every call, and every gesture of affection from a distance. For always checking in, for making me laugh when I needed it most, and for reminding me that true friendship knows no distance. Thank you for accompanying me from afar, but with your hearts always close. And to Samu, who—without meaning to—has also been a source of momentum and joy along the way; I hope life brings us together again somewhere in the world, doing science together.

And I wish to give special thanks to Justin Lloyd Ripley, Jaime Redondo Yuste, Sayak Datta, and Enrique Pazos-Ávalos, for the conversations, shared ideas, and intellectual support throughout this project. Your willingness and generosity have been, without doubt, a source of inspiration. In particular, to Enrique, for providing me with his code, which was key to obtaining some of the results presented in this thesis.

Finally, to *you*: although our paths have diverged, you still orbit in a serene corner of my inner universe. You were once a star in my sky, and even if your light no longer brightens my days, its trace

remains within me. In my life I continue to carry the influence of what was once love, and for that reason you are, in some way, also present in these pages. This is how I choose to end it, quietly, in peace and surrounded by some equations you may have liked, bringing to an end with the same love what once began with love. Wherever you are, I truly wish that you achieve all your dreams, and see them shine with the same intensity with which you once shone in my life. Thank you, with love, always.

Two horizons touched,
then slipped from sight—
yet waves still carry
a glimpse of us.
Interlinked.

Abstract

The study of the ringdown phase of perturbed Black Hole (BH)s provides one of the most direct theoretical probes of the strong-field regime of General Relativity (GR). After a disturbance, the Gravitational Wave (GW) signal is well described at intermediate times by a superposition of Quasi–normal Modes (QNMs), exponentially damped oscillations whose frequencies and damping times depend solely on the mass and spin of the BH. At asymptotically late times, however, Black Hole Perturbation Theory (BHPT) predicts a qualitatively different regime: a polynomially decaying tail caused by the backscattering of waves off the spacetime curvature. Until very recently, these tails had remained elusive in Numerical Relativity (NR) simulations, despite being a robust prediction of GR. Remarkably, they have just been identified for the first time in February 2025, precisely during the development of this thesis.

This work investigates the onset and properties of late-time tails within the framework of BHPT, with the aim of clarifying the conditions under which they are excited and of providing guidance for NR studies. We perform time-domain evolutions of the Regge–Wheeler (RW) and Teukolsky master equations in Schwarzschild and Kerr spacetimes, imposing physically motivated boundary conditions and systematically varying the initial data. Two classes of perturbations are considered: head-on–type Gaussian profiles, where the width controls the relative excitation of high- and low-frequency modes, and quasi-circular–type Gaussians modulated by an orbital frequency, mimicking inspiraling binaries.

Our analysis reveals a clear dependence of tail excitation on the structure of the initial perturbation. Narrow, localized profiles predominantly excite high-frequency components and suppress tails, whereas extended perturbations enhance the low-frequency content and lead to more prominent power-law decays. The onset time of the tail regime is quantified, and the extracted decay exponents show excellent agreement with the predictions of Price's law. Furthermore, we investigate the interplay between fundamental and overtone QNMs and their transition to the tail regime, identifying signatures that could serve as diagnostics for NR simulations.

Although tails are far too weak to be observed with current or future detectors such as Laser Interferometer Space Antenna (LISA), they are theoretically fundamental. By clarifying their physical origin and identifying the conditions that govern their excitation, the analysis offers concrete guidelines for their treatment in NR simulations. The results highlight the importance of initial data choices in numerical simulations and provide timely insights into a phenomenon that has only just been observed numerically for the first time.

Summary (in English)

When two BHs collide, the violent encounter shakes the fabric of spacetime and produces a GW signal that can be roughly divided into three parts: the inspiral, the merger, and the ringdown. The first corresponds to the gradual dance of the two objects as they spiral closer together, the second to their final plunge into one another, and the third to the vibrations of the single BH that is left behind. This last stage, the ringdown, is often compared to the fading sound of a bell: the BH rings with characteristic tones until it eventually becomes silent.

The tones of this "cosmic bell" are known as QNMs. They are special because their frequencies and decay times depend only on the mass and spin of the BH, not on the details of the collision. This makes them invaluable: by measuring these tones, astronomers can perform "BH spectroscopy" and directly infer the properties of the remnant object. QNMs have now been identified both in observations and in NR simulations, confirming one of the most significant predictions of GR.

But GR also predicts that the story does not end there. After the main tones fade away, a new regime should appear: very small ripples called late-time tails. Unlike the exponential decay of QNMs, tails die away slowly, following a power law. They are caused by the scattering of waves off the curvature of spacetime far from the BH. These tails are far too weak to be observed with present or future detectors such as LISA, but they are an unavoidable mathematical feature of GR, and therefore of great theoretical importance.

For decades, however, late-time tails had never been seen in NR simulations. This mismatch between analytic predictions and computational results raised an open question: were tails simply too weak to appear, or were they being hidden by numerical noise and gauge effects? Remarkably, this long-standing puzzle was resolved only recently: in February 2025, while this thesis was being written, tails were reported for the first time in full NR simulations.

In this work we study tails from the complementary perspective of linear BHPT, which offers a simplified but rigorous framework to analyze perturbed BHs. By evolving the RW and Teukolsky equations with different types of perturbations, we explore which conditions make tails stronger or weaker. The results show that sharp, localized perturbations mainly produce QNMs, while broader or oscillatory disturbances enhance the low-frequency content of the signal and make tails more prominent. In this way, the thesis clarifies why tails are so difficult to capture in NR and provides criteria for when they should appear.

Even if we will never detect them directly, tails are an essential part of the full story of BH vibrations. They reveal how spacetime itself continues to respond long after the main ringing has died away, and they highlight the deep connection between perturbation theory and NR in the quest to understand the most extreme objects in the Universe.

Resum (en català)

Quan dos forats negres colisionen, la trobada sacseja fortament el teixit de l'espaitemps i produeix una ona gravitatòria que es pot dividir, a grans trets, en tres fases: l'inspiral, la fusió i el ringdown. La primera correspon a la dansa gradual dels dos objectes mentre s'acosten en espiral, la segona al seu xoc final, i la tercera son les vibracions del forat negre únic que en resulta. Aquesta darrera etapa, el ringdown, sovint s'ha comparat amb el so esmorteït d'una campana: el forat negre ressona amb tons característics fins que finalment es apagant.

Aquests tons de la "campana còsmica" s'anomenen modes quasi-normals. Són especials perque les seves freqüències i temps d'amortiment depenen només de la massa i la rotació del forat negre, i no dels detalls de la col · lisió. Això els fa molt valuosos: mesurant aquests tons els astrònoms poden fer espectroscopia de forats negres i inferir de forma directa les propietats de l'objecte restant. Els modes quasi-normals s'han identificat en observacions i també en simulacions numèriques, confirmant una de les prediccions més important de la relativitat general.

Tanmateix, la teoria diu que la història no acaba aquí. Un cop els tons principals s'han apagat, apareix un nou règim: petites oscilacions anomenades cues de temps tardà. A diferencia dels modes quasi-normals, que decauen exponencialment, les cues ho fan de manera molt més lenta, seguint una llei de potència. Estan causades per la dispersió de les ones amb la curvatura de l'espaitemps lluny del forat negre. Aquestes cues son massa dèbils per poder ser detectats amb detectors actuals o fins i tot futurs com LISA, però son una conseqüència matemàtica inevitable de la relativitat general i per tant tenen molta importància teòrica.

Durant dècades, però, les cues de temps tardà no es varen veure mai a les simulacions numèriques de forats negres. Aquesta contradicció entre les prediccions analítiques i els resultats computacionals obria una pregunta: les cues eren massa febles per aparèixer, o es quedaven amagades dins el soroll numèric i efectes de gauge? De manera sorprenent, aquest enigma s'ha resolt fa molt poc: al febrer de 2025, mentres aquesta tesi s'estava escrivint, es van trobar per primera vegada cues en simulacions completes de col · lisions de forats negres.

En aquest treball estudiem les cues utilitzant la teoria de pertorbacions lineals de forats negres, que dona un marc simplificat però rigorós per analitzar aquests processos. Fent evolucions de les equacions de Regge–Wheeler i Teukolsky amb diferents tipus de pertorbacions, es veu quines condicions fan les cues més visibles o més dèbils. Els resultats mostren que pertorbacions molt locals generen sobretot modes quasi-normals, mentre que pertorbacions més amples o oscil · lants creen més contingut de baixa freqüència i, per tant, cues més clares.

Encara que mai no es podran detectar directament, les cues son una part essencial de la història completa de les vibracions d'un forat negre. Ens mostren com l'espaitemps continua responent molt temps després de que el so principal s'hagi apagat, i ens recorda la connexió profunda entre la teoria i les simulacions numèriques en la recerca per entendre els objectes més extrems de l'Univers.

Resumen (en castellano)

Cuando dos agujeros negros colisionan, el violento encuentro sacude el tejido del espacio-tiempo y produce una onda gravitacional que puede dividirse en tres fases: la fase espiral, la fusión y el *ringdown*. La primera corresponde a la danza gradual de los dos objetos mientras se acercan en espiral, la segunda a su choque final, y la tercera a las vibraciones del agujero negro resultante. Esta última etapa, el *ringdown*, se compara con el sonido amortiguado de una campana: el agujero negro resuena con tonos característicos hasta que finalmente se apaga.

Estos tonos de la "campana cósmica" son los modos cuasinormales. Sus frecuencias y tiempos de decaimiento dependen solo de la masa y la rotación del agujero negro, y no de los detalles de la colisión. Esto los convierte en una herramienta valiosa: al medirlos, los astrónomos pueden realizar "espectroscopía de agujeros negros" e inferir las propiedades del objeto final. Los modos cuasinormales se han identificado tanto en observaciones como en simulaciones numéricas, confirmando una de las predicciones más significativas de la relatividad general.

La teoría también predice que, tras desvanecerse los tonos principales, aparece un nuevo régimen: pequeñas oscilaciones llamadas colas de tiempo tardío. A diferencia del decaimiento exponencial de los modos cuasinormales, estas colas decrecen lentamente, siguiendo una ley de potencias. Se originan en la dispersión de ondas en la curvatura del espacio-tiempo lejos del agujero negro. Aunque demasiado débiles para ser detectadas incluso con futuros proyectos espaciales como LISA, son una consecuencia inevitable de la relatividad general y tienen gran importancia teórica.

Durante décadas, las colas nunca se habían visto en simulaciones numéricas, lo que planteaba una cuestión: ¿eran demasiado débiles o quedaban ocultas por el ruido y los efectos de coordenadas? Este enigma se resolvió muy recientemente: en febrero de 2025, mientras se redactaba esta tesis, se informó por primera vez de su presencia en simulaciones completas de colisiones de agujeros negros.

En este trabajo estudiamos las colas desde la teoría lineal de perturbaciones de agujeros negros, que ofrece un marco simplificado pero riguroso para analizarlas. Al evolucionar las ecuaciones de Regge–Wheeler y Teukolsky con distintos tipos de perturbaciones, exploramos en qué condiciones las colas se hacen más intensas o más débiles. Los resultados muestran que perturbaciones localizadas generan sobre todo modos cuasinormales, mientras que perturbaciones más anchas u oscilatorias refuerzan el contenido de baja frecuencia y producen colas más visibles.

Aunque nunca se detecten directamente, las colas son una parte esencial de la historia completa de las vibraciones de un agujero negro. Revelan cómo el espacio-tiempo sigue respondiendo mucho después de que el sonido principal se ha extinguido y subrayan la profunda conexión entre la teoría y las simulaciones numéricas en el estudio de los objetos más extremos del Universo.

Contents

List of Figures **xix**

List of Tables **xxi**

Nomenclature **xxiii**

I Theoretical background **1**

1 Black holes and gravitational radiation **3**
1.1 General Relativity: a prelude to black holes . . . 3
1.1.1 Pseudo-Riemannian geometry . . . 3
1.1.2 Tetrad formalism . . . 5
1.2 Exact solutions: black holes in General Relativity . . . 6
1.2.1 Schwarzschild spacetime . . . 6
1.2.2 Kerr spacetime . . . 8
1.3 Linearized theory of gravity: a window to gravitational waves . . . 9
1.3.1 Linearization of Einstein's Field Equations . . . 9
1.3.2 Gravitational waves in the transverse-traceless gauge . . . 10
1.3.3 Geodesic deviation and physical effects of gravitational waves . . . 11
1.3.4 Quadrupole radiation . . . 13
1.3.5 Phases of a gravitational-wave signal . . . 13
1.3.6 Astrophysical significance of the ringdown . . . 15

2 Black Hole Perturbation Theory **17**
2.1 Perturbations on non-rotating backgrounds . . . 17
2.1.1 Massive scalar fields . . . 18
2.1.2 Gravitational perturbations . . . 22
2.1.3 General form of the effective potential . . . 29
2.1.4 Mapping to the gravitational wave signal . . . 29
2.2 Perturbation on rotating backgrounds . . . 30
2.2.1 The Newman-Penrose formalism and the Kinnersley null tetrad . . . 30
2.2.2 Extension to Petrov type D spacetimes . . . 31
2.2.3 Decoupling the equations . . . 32
2.2.4 Gravitational radiation at infinity . . . 33
2.2.4.1 Mapping to the RW/Zerilli–Moncrief (ZM) formalism . . . 34
2.3 Quasinormal modes of black holes . . . 34
2.3.1 Poles of the Green's function . . . 35

2.3.2 Beyond the toy model: the Pöschl–Teller potential . . . 38
2.4 Late–time tails . . . 39
2.4.1 Green's function origin . . . 39
2.4.2 Evaluation of the Green's function . . . 40
2.5 Overtones . . . 41

II Numerical framework **45**

3 Regge–Wheeler code **47**
3.1 1+1 wave equation . . . 48
3.2 Coordinate conversion and numerical grid . . . 48
3.3 Initial data . . . 49
3.4 Time evolution scheme . . . 50
3.5 Evaluation of the potential . . . 50
3.6 Sponge layers . . . 51
3.7 Boundary conditions . . . 52
3.8 Waveform extraction . . . 52
3.9 Radial convergence test . . . 54

4 Teukolsky code **57**
4.1 Rewriting the Teukolsky equation . . . 59
4.1.1 Separating ϕ dependence . . . 59
4.1.2 From second to first-order differential equations . . . 60
4.1.3 Decomposition into real and imaginary parts . . . 61
4.2 Derivation of the 4th order algorithm . . . 62
4.3 Stability analysis . . . 63
4.4 Boundary conditions . . . 64
4.4.1 Radial boundaries . . . 64
4.4.2 Angular boundary conditions . . . 65
4.5 Implementation . . . 66
4.6 Initial data . . . 67
4.7 Convergence tests . . . 68

IIIResults **71**

5 Numerical results in Schwarzschild spacetime **73**
5.1 Motivation . . . 73
5.2 Setup . . . 75
5.3 Tests for varying the Gaussian width . . . 76
5.3.1 Fundamental mode extraction . . . 76
5.3.2 Asymptotic regime: late-time tails . . . 81
5.3.3 Overtones analysis . . . 83
5.3.4 Tail starting time . . . 86
5.3.5 Recovery of the tail amplitude . . . 88
5.3.6 Prompt response . . . 90

5.4 Tests for changing the frequency . . . 91
5.4.1 QNM extraction . . . 92
5.4.2 Late–time tails . . . 94
5.4.3 Overtones . . . 94
5.4.4 Tail starting time . . . 97
5.4.5 Recovery of the tail amplitude . . . 97
5.4.6 Prompts . . . 98

6 Numerical results in Kerr spacetime 101
6.1 Motivation and Setup . . . 101
6.2 Head–on case varying the spin . . . 102
6.2.1 Local power index . . . 102
6.2.2 Amplitude ratios . . . 103
6.2.3 Tail starting time . . . 105
6.2.4 Amplitude and tail exponent recovery . . . 106
6.2.5 Prompt response . . . 107
6.3 Quasi-circular case varying ω_0 . . . 108
6.3.1 Amplitude ratios . . . 109
6.3.2 Tail starting time analysis . . . 111
6.3.3 Resonance amplitudes . . . 112
6.3.4 Amplitude and tail exponent recovery . . . 114
6.3.5 Prompts . . . 114

7 Discussion and conclusions 117

8 Future perspectives 119

Bibliography 121

A Geometrized unit system 127

B Spherical Harmonics 129
B.1 Scalar harmonics . . . 129
B.2 Vector harmonics . . . 130
B.3 Tensor harmonics . . . 130

C Perturbation on Schwarzschild spacetime 131
C.1 Perturbations of the Christoffel symbols . . . 131
C.2 Perturbations of the Riemann tensor . . . 132
C.3 Perturbations of the Ricci tensor . . . 132
C.4 Perturbations of the Ricci scalar . . . 132
C.5 Perturbations of the Einstein tensor . . . 133
C.6 Explicit calculations (2.41) and (2.49) . . . 134

D Newman–Penrose formalism 137
D.1 Directional derivatives and Ricci rotation coefficients . . . 137
D.2 Components of Weyl and Ricci tensors . . . 138

D.2.1 Weyl scalars 138
D.2.2 Ricci scalars 139
D.3 Commutation relations between directional derivatives 139
D.4 Ricci identities 139
D.5 Weyl scalars in terms of Ricci rotation coefficients 140
D.6 Components of the Bianchi identities 141

E Fourth–order finite difference formulas **143**
E.1 First derivative 143
E.2 Second derivative 143
E.3 Third derivative 144
E.4 Fourth derivative 144

List of Figures

1.1 Effective potential in Schwarzschild spacetime. 7
1.2 Polarizations of gravitational waves. 11
1.3 Circular polarization of gravitational waves. 12
1.4 Inspiral, merger and ringdown signal. 14
1.5 Fundamental QNM frequencies and quality factors. 16

2.1 Effective potentials for a scalar field in Schwarzschild spacetime. 20
2.2 Effective potentials in Schwarzschild spacetime 27
2.3 Effective potentials and derivatives for different field spins in Schwarzschild spacetime . . 29
2.4 Phases of black hole perturbations. 34
2.5 Inverse Fourier transform contour. 36
2.6 Quasinormal modes of a Schwarzschild black hole in the plane $(\mathrm{Re}(2M\omega), -\mathrm{Im}(2M\omega))$. . 39
2.7 Late–time tails of Schwarzschild perturbations. 42
2.8 Ringdown mismatch as function of fit time and number of overtones. 43

3.1 Initial data profiles at $t = 0$. 49
3.2 Waveform extracted at $r_*^{\mathrm{obs}} = 50$ for $\ell = 2$. 53
3.3 Radial convergence test for the Regge–Wheeler evolution 55

4.1 Amplification factor versus Courant number. 64
4.2 Staggered angular grid with ghost zones. 66
4.3 Two–dimensional computational grid. 68
4.4 Fourth–order convergence in the radial direction. 69
4.5 Fourth–order convergence in the radial direction. 69
4.6 Staggered angular grid points. 70
4.7 Fourth–order convergence in the angular direction. 70

5.1 Early expectations vs. numerical results for binary black hole waveforms. 74
5.2 Time-domain waveform for $\sigma = \sigma_1$ at $r^*_{\mathrm{obs}} = 50$. 76
5.3 Shifted waveform for $\sigma = 1$ 77
5.4 Quasi–normal mode fit of the waveform with $\sigma = 1$ 77
5.5 Fit including both quasi–normal mode and tail contributions for $\sigma = 1$. 78
5.6 Normalized quasi–normal mode frequency and damping time as functions of the Gaussian width 80
5.7 Waveforms extracted at $r^*_{\mathrm{obs}} = 50$ for three representative values of the Gaussian width. . 80
5.8 Late-time power-law decay for $\sigma = 1$ on a logarithmic scale. 81
5.9 Tail fits as a function of the Gaussian width. 82
5.10 Comparison of overtone QNM fits. 84

5.11 Comparison of overtone QNM + tail fits. 84
5.12 Amplitude ratios from ringdown fits for the first two overtones. 85
5.13 Amplitude ratios up to $|A_3/A_0|$. 86
5.14 Procedure to reveal the onset of the tail. 87
5.15 Determination of the tail starting time. 87
5.16 Smoothed waveform with zoom at the local minimum. 88
5.17 Tail onset vs. Gaussian width 88
5.18 Recovered tail amplitude for $\sigma = 1$. 89
5.19 Time evolution of the perturbed field for different Gaussian widths. 90
5.20 Dependence of the prompt response on the Gaussian width. 90
5.21 Three dynamical phases of the waveform for different Gaussian widths. 91
5.22 Normalised QNM frequency and damping time versus driving frequency. 92
5.23 Fitted amplitude as a function of the driving frequency. 93
5.24 Waveforms at selected driving frequencies. 93
5.25 Fitted tail parameters as functions of the driving frequency. 94
5.26 Amplitude ratios as a function of ω_0 95
5.27 Cosine–projected amplitude ratios 95
5.28 Amplitude ratios of overtones 96
5.29 Normalized overtone ratios versus ω_0 96
5.30 Tail starting time vs. injection frequency 97
5.31 Tail amplitude recovery 98
5.32 Prompt response vs. ω_0 98
5.33 Waveforms for different ω_0 99

6.1 Numerical waveforms for different spins 102
6.2 Local power index for different Kerr spins. 103
6.3 Amplitude ratios of overtones across spins 104
6.4 Tail onset versus spin 105
6.5 Tail onset versus horizon radius 105
6.6 Numerical waveform and reconstructed tail for $a = 0.998$ 106
6.7 Coefficient of determination versus tail exponent for $a = 0.998$ 107
6.8 Prompt response for different spins 107
6.9 Prompt peak timing and amplitude versus spin 108
6.10 Ringdown waveforms for different spins 109
6.11 Amplitude ratios $|A^R_{20n}|$ as a function of ω_0 110
6.12 Comparison of amplitude ratios for $\ell = 2$ and $\ell = 3$ 111
6.13 Amplitude ratios $|A^R_{201}|$ across spins 111
6.14 Tail starting times across spins and multipoles 112
6.15 Fitted amplitudes of the ringdown signal 113
6.16 Resonant amplitudes across spins 113
6.17 Amplitude recovery and R^2 for $a = 0.3$, $\omega_0 = 0.2$ 114
6.18 Prompt peak timing and amplitude for $\ell = 2$ 115
6.19 Prompt peak timing and amplitude for $\ell = 3$ 115

List of Tables

1.1 Stationary BHs in four-dimensional electrovacuum GR. 6

2.1 Spin–weight fields in the Newman–Penrose formalism. 33

4.1 Radial boundary conditions 65
4.2 Off-centered derivative operators 65

5.1 Fit results for $\sigma = 1$ 78
5.2 Fitted quasi–normal mode parameters for different σ 79
5.3 Fitted quasi–normal mode + tail parameters for different σ 79
5.4 Late-time tail fits in Schwarzschild 82
5.5 Onset of the tail as a function of ω_0 97

Nomenclature

BH Black Hole

BHPT Black Hole Perturbation Theory

BL Boyer–Lindquist

CFL Courant–Friedrichs–Levy

DT Darboux Transformation

EFE Einstein's Field Equations

EM Electromagnetic

EoM Equation of Motion

GR General Relativity

GW Gravitational Wave

ISCO Innermost Stable Circular Orbit

KG Klein–Gordon

NP Newman–Penrose

NR Numerical Relativity

QNM Quasi–normal Mode

RK Runge–Kutta

RW Regge–Wheeler

TT Transverse–Traceless

WKB Wentzel–Kramers–Brillouin

ZM Zerilli–Moncrief

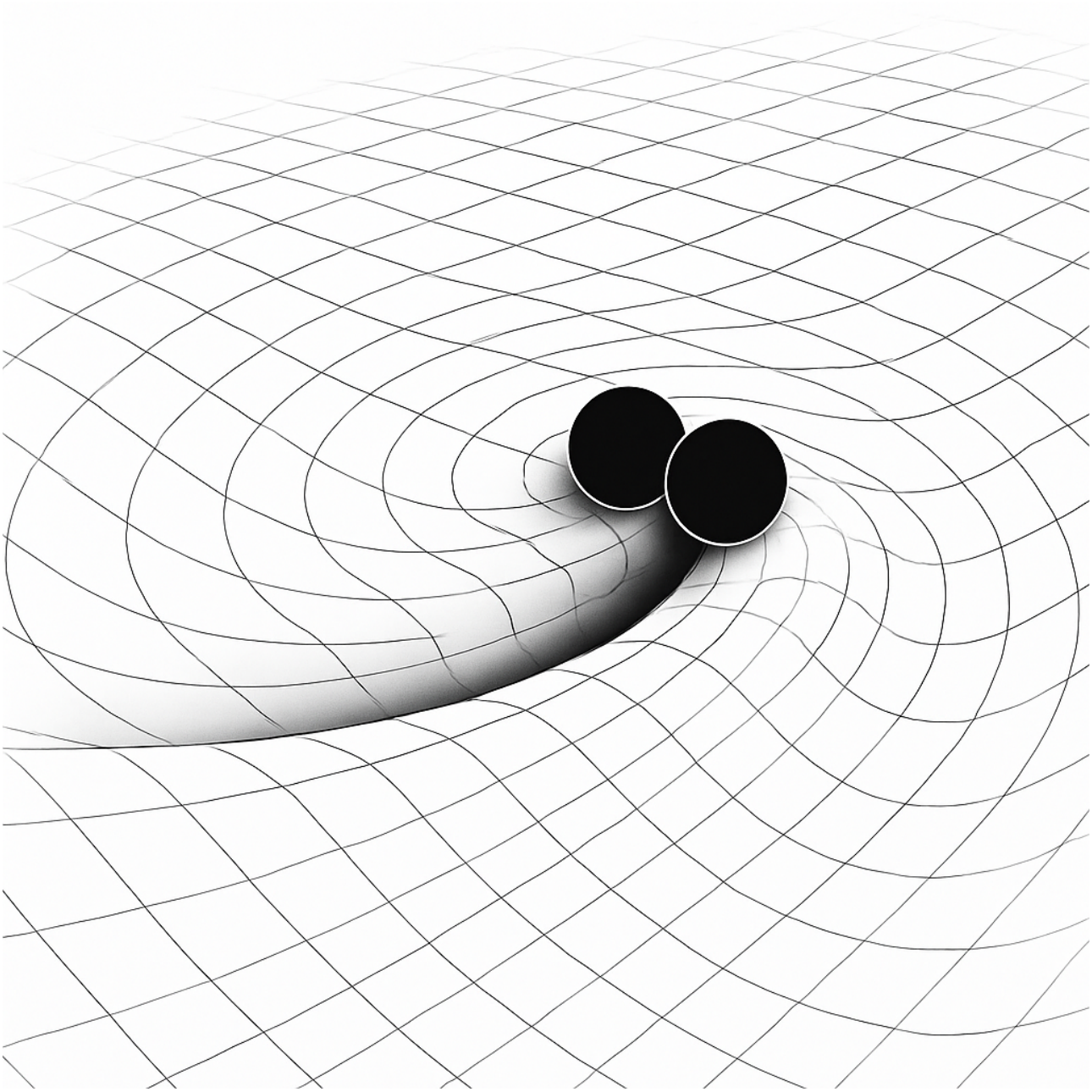
LPT Linear Perturbation Theory

NLPT Numerical Linear Perturbation Theory

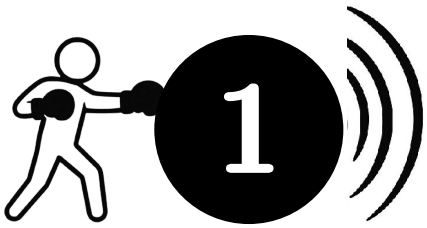
LISA Laser Interferometer Space Antenna

Part I

Theoretical background



CHAPTER



Black holes and gravitational radiation

Contents

1.1 General Relativity: a prelude to black holes **3**
1.2 Exact solutions: black holes in General Relativity **6**
1.3 Linearized theory of gravity: a window to gravitational waves **9**

1.1 General Relativity: a prelude to black holes

The development of GR by Einstein in 1915 [1] marked a profound departure from Newton's conception of gravity as a force, towards the modern understanding of gravity as the manifestation of spacetime curvature [2–5]. At the core of this framework lies the principle that freely falling test particles move along geodesics of the spacetime manifold, while matter and energy determine its geometry through the Einstein's Field Equations (EFE).

1.1.1 Pseudo-Riemannian geometry

In GR, spacetime is modeled as a differentiable manifold equipped with a *metric tensor* $(g_{\mu\nu})$, which is the fundamental object of (pseudo-)Riemannian geometry. The metric specifies how to measure lengths, angles, and causal relations through the line element

$$\mathrm{d}s^2 = g_{\mu\nu}\,\mathrm{d}x^\mu \mathrm{d}x^\nu, \tag{1.1}$$

and it is always symmetric $(g_{\mu\nu} = g_{\nu\mu})$ and non-degenerate. In the context of GR, it carries Lorentzian signature $(-,+,+,+)$. Thus, all geometric and causal properties of spacetime are contained in $g_{\mu\nu}$.

Once the metric is introduced, we need a consistent way of differentiating tensor fields on the manifold. This is achieved via the *covariant derivative*, defined in terms of the unique connection that is both torsion-free and metric-compatible: the *Levi-Civita connection*. Its components, the Christoffel

symbols, are given by

$$\Gamma^{\mu}_{\ \nu\rho} = \frac{1}{2}\, g^{\mu\sigma}\Big(\partial_\rho g_{\nu\sigma} + \partial_\nu g_{\rho\sigma} - \partial_\sigma g_{\nu\rho}\Big). \tag{1.2}$$

The presence of curvature is revealed when considering the commutator of two covariant derivatives acting on a vector field. This leads to the *Ricci identity*,

$$\Big[\nabla_\rho, \nabla_\sigma\Big] V^\mu = R^{\mu}_{\ \nu\rho\sigma}\, V^\nu, \tag{1.3}$$

where the assumption of vanishing torsion has been made, as is standard in GR. The tensor $R^{\mu}_{\ \nu\rho\sigma}$ defined here is the *Riemann tensor*, which measures the failure of parallel transport around closed loops and thus quantifies the intrinsic curvature of spacetime. In terms of the Christoffel symbols, it reads

$$R^{\mu}_{\ \nu\rho\sigma} = \partial_\rho \Gamma^{\mu}_{\ \nu\sigma} - \partial_\sigma \Gamma^{\mu}_{\ \nu\rho} + \Gamma^{\mu}_{\ \lambda\rho}\, \Gamma^{\lambda}_{\ \nu\sigma} - \Gamma^{\mu}_{\ \lambda\sigma}\, \Gamma^{\lambda}_{\ \nu\rho}. \tag{1.4}$$

By contraction of the Riemann tensor one obtains the *Ricci tensor* $(R_{\mu\nu})$ and the *Ricci scalar* (R),

$$R_{\mu\nu} = R^{\rho}_{\ \mu\rho\nu}, \qquad R = g^{\mu\nu} R_{\mu\nu}, \tag{1.5}$$

which condense the information on curvature and will play a central role in the dynamics of the gravitational field. While the Ricci tensor directly enters the EFE, it is often useful to separate out the traceless part of the curvature, known as the *Weyl tensor*. This object captures the "free" gravitational field, i.e. the part not locally determined by matter sources

$$C_{\mu\nu\rho\sigma} = R_{\mu\nu\rho\sigma} - \frac{1}{2}\Big(g_{\mu\rho}R_{\nu\sigma} - g_{\mu\sigma}R_{\nu\rho} - g_{\nu\rho}R_{\mu\sigma} + g_{\nu\sigma}R_{\mu\rho}\Big) + \frac{R}{6}\Big(g_{\mu\rho}g_{\nu\sigma} - g_{\mu\sigma}g_{\nu\rho}\Big). \tag{1.6}$$

The Riemann tensor also satisfies two fundamental relations: the algebraic *cyclic identity*,

$$R^{\mu}_{\ \nu\rho\sigma} + R^{\mu}_{\ \nu\sigma\rho} + R^{\mu}_{\ \nu\rho\sigma} = 0, \tag{1.7}$$

and the differential *Bianchi identity*,

$$\nabla_\lambda R^{\mu}_{\ \nu\rho\sigma} + \nabla_\rho R^{\mu}_{\ \nu\sigma\lambda} + \nabla_\sigma R^{\mu}_{\ \nu\lambda\rho} = 0. \tag{1.8}$$

The latter has direct physical significance: it guarantees that the Einstein tensor defined below is divergenceless, ensuring local conservation of energy and momentum.

Combining the Ricci tensor and scalar into the *Einstein tensor*,

$$G_{\mu\nu} \equiv R_{\mu\nu} - \frac{1}{2} g_{\mu\nu} R, \tag{1.9}$$

one arrives at the central equation of GR by equating geometry with matter content:

$$G_{\mu\nu} = 8\pi T_{\mu\nu}, \tag{1.10}$$

where geometrized units ($G = c = 1$, see Appendix A) are used, and $T_{\mu\nu}$ is the stress–energy tensor of matter and fields. In vacuum, where $T_{\mu\nu} = 0$, the system reduces to

$$R_{\mu\nu} = 0, \qquad \text{and} \qquad R = 0, \tag{1.11}$$

whose exact solutions include the Schwarzschild and Kerr BHs, which will be central to this work.

1.1.2 Tetrad formalism

In GR, the coordinate basis (∂_μ) provides a natural description of spacetime. However, it is often convenient to introduce at each point a local set of four linearly independent vectors $(e_{(a)})$ known as a *tetrad* (or vierbein) [6]. This construction defines a correspondence between the curved spacetime metric and a locally inertial Minkowskian frame $(\eta_{(a)(b)} = \mathrm{diag}(-1,1,1,1))$. For the present review, we follow the exposition in [7]. The tetrads satisfy the relations

$$e^{\mu}_{\ (a)}\, e^{(a)}_{\nu} = \delta^{\mu}_{\nu}, \qquad e^{\mu}_{\ (a)}\, e^{(b)}_{\mu} = \delta^{(b)}_{(a)}, \qquad e^{\mu}_{\ (a)}\, e_{\mu(b)} = \eta_{(a)(b)}, \qquad e^{(a)}_{\mu}\, e_{(a)\nu} = g_{\mu\nu}, \tag{1.12}$$

which guarantee that contractions in the tetrad frame reproduce the Minkowski structure. Here $(a),(b),\ldots$ are tetrad indices, while $\mu,\nu,\ldots$ denote spacetime coordinates.

Directional derivatives and Ricci rotation coefficients

Once a tetrad field is specified, one can introduce the associated directional derivatives,

$$e_{(a)} \equiv e^{\mu}_{\ (a)} \nabla_\mu, \tag{1.13}$$

which, when acting on scalar functions, reduce to

$$e_{(a)}\phi = e^{\mu}_{\ (a)}\, \partial_\mu \phi. \tag{1.14}$$

The connection in the tetrad basis is described by the *Ricci rotation coefficients*, defined as

$$\gamma_{(c)(a)(b)} \equiv e^{\nu}_{\ (c)}\, \nabla_\mu e^{\rho}_{\ (a)}\, e_{(b)\rho}, \tag{1.15}$$

which quantify how the tetrad vectors vary from point to point.

From the condition of metric compatibility, these coefficients obey the antisymmetry property

$$\gamma_{(c)(a)(b)} = -\,\gamma_{(a)(c)(b)}. \tag{1.16}$$

Structure constants

In general, the tetrad vectors do not commute, and their non-commutativity is characterized by the *structure constants*, defined through

$$\Big[e_{(a)}, e_{(b)}\Big] = C^{(c)}_{\ (a)(b)}\, e_{(c)}, \tag{1.17}$$

with

$$C^{(c)}_{\ (a)(b)} = \gamma^{(c)}_{\ (b)(a)} - \gamma^{(c)}_{\ (a)(b)}, \tag{1.18}$$

which play the role of the analogues of Lie algebra commutators in the tetrad frame.

Curvature in the tetrad basis

The Riemann tensor can be expressed directly in terms of the Ricci rotation coefficients, and in the tetrad basis its components read

$$R_{(a)(b)(c)(d)} = \nabla_{(c)}\gamma_{(a)(b)(d)} - \nabla_{(d)}\gamma_{(a)(b)(c)} + \gamma_{(b)(a)(i)}\, \gamma^{(i)}_{\ (c)(d)} - \gamma_{(i)(a)(c)}\, \gamma^{(i)}_{\ (b)(d)} + \gamma_{(i)(a)(d)}\, \gamma^{(i)}_{\ (b)(c)}, \tag{1.19}$$

which makes explicit that curvature arises from derivatives of, and quadratic combinations among, the Ricci rotation coefficients.

Bianchi identities

The Bianchi identities also admit a compact formulation in the tetrad framework, taking the form

$$R_{(a)(b)(c)(d)|(f)} = \frac{1}{6} \sum_{[(c)(d)(f)]} \Big[R_{(a)(b)(c)(d)|(f)} - \gamma^{(i)}_{(a)(f)} R_{(i)(b)(c)(d)} - \gamma^{(i)}_{(b)(f)} R_{(a)(i)(c)(d)} - \gamma^{(i)}_{(c)(f)} R_{(a)(b)(i)(d)} - \gamma^{(i)}_{(d)(f)} R_{(a)(b)(c)(i)} \Big], \quad (1.20)$$

where the cyclic summation is understood over permutations of the indices $(c)(d)(f)$, and can be represented with the totally antisymmetric symbol $\left(\epsilon_{(c)(d)(f)}\right)$.

1.2 Exact solutions: black holes in General Relativity

In vacuum, the EFE reduce to $R_{\mu\nu} = 0$, whose exact solutions describe self-consistent spacetimes without matter sources. Among them, the most remarkable are BHs, geometries containing an event horizon: a null hypersurface separating the region from which light and matter can escape to infinity from that which is inevitably drawn towards a singularity, where curvature invariants diverge and the classical description breaks down [8].

By imposing symmetry assumptions such as stationarity and asymptotic flatness, the problem of finding exact solutions to the EFE becomes tractable, yielding a remarkably small family of analytic spacetimes. According to the *no-hair theorem*, stationary, asymptotically flat, and regular solutions (possibly coupled to Electromagnetic (EM) fields) are completely characterized by only three parameters: the mass (M), the angular momentum (J), and the electric charge (Q) [8]. Consequently, in asymptotically flat electrovacuum, GR admits only four types of stationary BHs, summarized in Table 1.1.

Solution	**Mass (M)**	**Angular momentum (J)**	**Charge (Q)**	**Properties**
Schwarzschild	✓	✗	✗	Static, uncharged
Reissner–Nordström	✓	✗	✓	Static, charged
Kerr	✓	✓	✗	Rotating, uncharged
Kerr–Newman	✓	✓	✓	Rotating, charged

Table 1.1: Stationary BHs in four-dimensional electrovacuum GR.

1.2.1 Schwarzschild spacetime

Among the four stationary BH families summarized in Table 1.1, the simplest and historically first to be discovered is the Schwarzschild geometry [9]. It describes the spacetime outside a static, spherically symmetric, uncharged massive body, and constitutes the unique asymptotically flat, spherically symmetric vacuum solution of the EFE, with line element (in Schwarzschild coordinates)

$$\mathrm{d}s^2 = -\left(1 - \frac{2M}{r}\right)\mathrm{d}t^2 + \left(1 - \frac{2M}{r}\right)^{-1}\mathrm{d}r^2 + r^2\left(\mathrm{d}\theta^2 + \sin^2(\theta)\,\mathrm{d}\varphi^2\right). \quad (1.21)$$

The Schwarzschild geometry is defined by two characteristic radii: the event horizon at $r = 2M$, a null surface beyond which no signal can escape, and the curvature singularity at $r = 0$, where invariants such as the Kretschmann scalar diverge [10].

Geodesic motion illustrates the Schwarzschild geometry: time-translation and rotational symmetries ensure conservation of energy (E) and angular momentum (ℓ), associated with $(\partial_t$ and $\partial_\varphi)$. In the equatorial plane $(\theta = \pi/2)$, the radial Equation of Motion (EoM) is [11]

$$\left(\frac{\mathrm{d}r}{\mathrm{d}\tau}\right)^2 + V_{\mathrm{eff}}^2(r,\ell) = E^2, \qquad \text{with} \qquad V_{\mathrm{eff}}(r,\ell) = \sqrt{\left(1-\frac{2M}{r}\right)\left(1+\frac{\ell^2}{r^2}\right)}. \tag{1.22}$$

Circular orbits

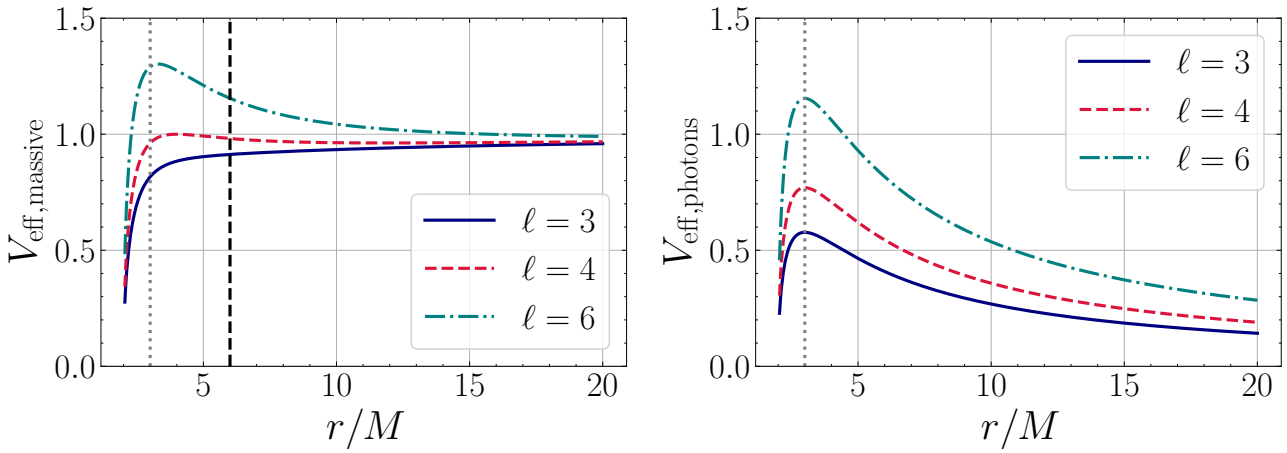
Circular geodesics occur at extrema of the effective potential. For massive particles, stable orbits exist only for $r > 6M$, with the Innermost Stable Circular Orbit (ISCO) located at $r_{\mathrm{ISCO}} = 6M$. Closer to the BH, no stable circular trajectories are possible, which has profound astrophysical consequences for accretion disks.

Photon sphere

For massless particles, the effective potential reduces to [11]

$$V_{\mathrm{eff}}^{(\gamma)}(r,\ell) = \sqrt{\left(1-\frac{2M}{r}\right)\frac{\ell^2}{r^2}}, \tag{1.23}$$

with an extremum at $r = 3M$. This defines the *photon sphere* or *lightring*: an unstable circular orbit for null geodesics. Any perturbation displaces the photon either out to infinity or into the BH.



(a) Massive particles.

(b) Photons.

Figure 1.1: **Effective potential in Schwarzschild spacetime.** (a) For massive particles, stable circular orbits exist for $r > 6M$, with the ISCO at $r = 6M$. (b) For photons, an unstable circular orbit appears at the photon sphere $r = 3M$, indicated by the vertical dotted grey line.

These geodesic structures also illuminate the behaviour of fields on a BH background. Linear perturbations of the Schwarzschild geometry satisfy wave equations of Schrödinger type, with an

effective potential peaking near the lightring. In the eikonal limit,[1] the dynamics of waves scattered in this region are governed by the unstable photon orbit at $r = 3M$: its orbital frequency fixes the oscillatory response of the BH, while its instability sets the damping timescale. This relation foreshadows the notion of QNMs, the characteristic vibrations of BHs to be discussed later, linking null geodesics with the ringdown signal observed in wave phenomena.

1.2.2 Kerr spacetime

The Kerr solution [13] describes the spacetime outside a rotating, uncharged mass with angular momentum. It is stationary and axisymmetric, and is fully determined by the mass and the spin parameter ($a = J/M$). In Boyer–Lindquist (BL) coordinates [14] (t, r, θ, ϕ) the line element reads

$$\mathrm{d}s^2 = -\frac{\Delta}{\Sigma}\left(\mathrm{d}t - a\sin^2(\theta)\,\mathrm{d}\phi\right)^2 + \frac{\sin^2(\theta)}{\Sigma}\left[\left(r^2+a^2\right)\mathrm{d}\phi - a\,\mathrm{d}t\right]^2 + \frac{\Sigma}{\Delta}\,\mathrm{d}r^2 + \Sigma\,\mathrm{d}\theta^2, \tag{1.24}$$

with

$$\Delta = r^2 - 2Mr + a^2, \qquad \Sigma = r^2 + a^2\cos^2(\theta). \tag{1.25}$$

The geometry presents two key structures:

- **Horizons:** roots of $\Delta = 0$,
$$r_\pm = M \pm \sqrt{M^2 - a^2}, \tag{1.26}$$
with r_+ the event horizon and r_- the inner (Cauchy) horizon.
- **Ergosphere:** the stationary limit surface, defined by the vanishing of the temporal component of the metric ($g_{tt} = 0$),
$$r_{\mathrm{ergo}}(\theta) = M + \sqrt{M^2 - a^2\cos^2(\theta)}, \tag{1.27}$$
which delimits a region outside the horizon where no observer can remain static with respect to infinity.

Rotation gives rise to the phenomenon of *frame dragging*, through which spacetime itself is carried along with the rotating BH [10]. This effect forces all worldlines inside the ergoregion to co-rotate with the horizon, thereby opening the possibility of extracting rotational energy, most notably through the Penrose process [15], and providing the basis for wave amplification mechanisms such as superradiance [16]. In addition, the central singularity is qualitatively altered: rather than being pointlike as in Schwarzschild, it takes the form of a ring, located at $\Sigma = 0$ on the equatorial plane..

Equatorial orbits

As in the Schwarzschild case, geodesic motion in Kerr spacetime can be described through an effective radial potential. In the equatorial plane, the location of the ISCO is strongly affected by the spin of the BH. For prograde orbits, which co-rotate with the horizon, the ISCO moves progressively inward as the spin increases, reaching $r_{\mathrm{ISCO}} = M$ in the extremal limit ($a = M$) [17]. In contrast, for retrograde (counter-rotating) orbits the ISCO shifts outward, up to $r_{\mathrm{ISCO}} = 9M$ in the extremal case [17].

[1] The Wentzel–Kramers–Brillouin (WKB) method provides a semiclassical expansion for wave equations with slowly varying potentials, allowing one to approximate quasi–bound states and resonances such as QNMs. See, e.g., [12].

Photon rings

Massless particles also admit unstable circular orbits whose radius depends on the spin. For prograde trajectories the light ring approaches $r = M$ as $a \to M$, whereas retrograde orbits are pushed outward beyond the Schwarzschild value $r = 3M$. These photon rings delineate the boundary of the BH shadow and, as in the non-rotating case, determine the location of the peak of the perturbation potential.

1.3 Linearized theory of gravity: a window to gravitational waves

GWs are one of the most remarkable predictions of GR [5, 18]. They arise because accelerated masses generate ripples in spacetime itself, propagating at the speed of light and carrying energy and angular momentum. In this sense, GWs resemble EM waves [19], but with a crucial distinction: they are not perturbations of a field on spacetime, but perturbations of the metric geometry.

From the mathematical point of view, the EFE are highly nonlinear [5, 11], making exact wave solutions difficult to obtain. In the weak–field and slow–motion limit, however, the theory can be consistently linearized [10, 18], yielding a framework in which GWs satisfy a wave equation closely analogous to Maxwell's theory.

The physical reality of GWs, debated for decades after Einstein's papers in 1916–18 [2, 20], was established through the linearized framework and the quadrupole formula. Observations of the Hulse–Taylor binary pulsar [21] and the first direct detection by LIGO in 2015 [22] provided compelling confirmation, opening a new era in astronomy.

1.3.1 Linearization of Einstein's Field Equations

The EFE are highly nonlinear in the metric, making them difficult to solve in general. However, the study of gravitational radiation requires only the weak–field limit, where spacetime can be viewed as a small perturbation of flat Minkowski space [23]

$$g^{p}_{\mu\nu} = g_{\mu\nu} + \gamma_{\mu\nu}, \qquad |\gamma_{\mu\nu}| \ll 1, \tag{1.28}$$

with $\eta_{\mu\nu} = \mathrm{diag}(-1, 1, 1, 1)$. In this approximation, indices are raised and lowered with $\eta_{\mu\nu}$, and we keep only terms linear in the perturbation $(\gamma_{\mu\nu})$.

The linearized expansion of the basic curvature tensors follows directly. The inverse metric is

$$(g^{p})^{\mu\nu} = g^{\mu\nu} - \gamma^{\mu\nu} + \mathcal{O}(\gamma^2), \tag{1.29}$$

with $\gamma^{\mu\nu} \equiv g^{\mu\alpha} g^{\nu\beta} \gamma_{\alpha\beta}$. From this, the Christoffel symbols reduce to

$$\Gamma^{\lambda}_{\mu\nu} = \frac{1}{2}\,\eta^{\lambda\rho}\Big(\partial_\mu \gamma_{\rho\nu} + \partial_\nu \gamma_{\rho\mu} - \partial_\rho \gamma_{\mu\nu}\Big). \tag{1.30}$$

Substituting into the definition of curvature (1.4), the Riemann tensor to first order becomes

$$R_{\lambda\mu\nu\rho} = \frac{1}{2}\Big(\partial_\nu\partial_\mu \gamma_{\lambda\rho} - \partial_\nu\partial_\lambda \gamma_{\mu\rho} - \partial_\rho\partial_\mu \gamma_{\lambda\nu} + \partial_\rho\partial_\lambda \gamma_{\mu\nu}\Big). \tag{1.31}$$

Contracting indices yields the Ricci tensor,

$$R_{\mu\nu} = \frac{1}{2}\Big(\partial^\lambda\partial_\mu \gamma_{\lambda\nu} + \partial^\lambda\partial_\nu \gamma_{\lambda\mu} - \Box\gamma_{\mu\nu} - \partial_\mu\partial_\nu\gamma\Big), \tag{1.32}$$

and the Ricci scalar,

$$R = \partial^\mu \partial^\nu \gamma_{\mu\nu} - \Box\gamma, \tag{1.33}$$

with $\gamma = \eta^{\alpha\beta}\gamma_{\alpha\beta}$ and $\Box = \eta^{\alpha\beta}\partial_\alpha\partial_\beta$. Combining them, the Einstein tensor linearized around Minkowski reads

$$G_{\mu\nu} = \frac{1}{2}\Big(\partial^\lambda\partial_\mu\gamma_{\lambda\nu} + \partial^\lambda\partial_\nu\gamma_{\lambda\mu} - \Box\gamma_{\mu\nu} - \partial_\mu\partial_\nu\gamma - \eta_{\mu\nu}\partial^\lambda\partial^\sigma\gamma_{\lambda\sigma} + \eta_{\mu\nu}\Box\gamma\Big). \tag{1.34}$$

Trace reversal and gauge choice

At this stage the equations still look cumbersome. A standard simplification is to introduce the *trace–reversed perturbation*,

$$\bar{\gamma}_{\mu\nu} \equiv \gamma_{\mu\nu} - \frac{1}{2}\,\eta_{\mu\nu}\,\gamma, \tag{1.35}$$

whose definition ensures $\bar{\gamma} = -\gamma$. Exploiting the coordinate freedom of GR, we can impose the *harmonic* (or de Donder) gauge [5],

$$\partial^\nu\bar{\gamma}_{\mu\nu} = 0, \tag{1.36}$$

which eliminates many redundant terms. In this gauge, the linearized EFE take the remarkably simple wave–like form

$$\Box\bar{\gamma}_{\mu\nu} = -16\pi\,T_{\mu\nu}. \tag{1.37}$$

This equation describes the dynamics of weak gravitational fields: in vacuum it reduces to the homogeneous wave equation $(\Box\bar{\gamma}_{\mu\nu} = 0)$, revealing the propagating nature of spacetime perturbations.

1.3.2 Gravitational waves in the transverse-traceless gauge

As we mentioned, in vacuum, the linearized field equations reduce to a homogeneous wave equation for the metric perturbation,

$$\Box\bar{\gamma}_{\mu\nu} = 0, \tag{1.38}$$

whose simplest solutions are plane waves of the form

$$\bar{\gamma}_{\mu\nu}(x) = \mathrm{Re}\left(C_{\mu\nu}\,e^{ik_\alpha x^\alpha}\right), \qquad \text{with} \qquad k^\alpha k_\alpha = 0, \tag{1.39}$$

where $C_{\mu\nu}$ is a constant symmetric tensor and k^α a null wavevector, ensuring propagation at the speed of light.

The harmonic gauge condition implies $k^\nu C_{\mu\nu} = 0$, which reduces the number of independent components of $C_{\mu\nu}$ from ten to six. Moreover, the residual coordinate freedom that preserves the harmonic condition allows us to eliminate four further components, leaving only two true degrees of freedom. These correspond to the physical radiative modes of the gravitational field.

It is convenient to make these explicit by adopting the so–called Transverse–Traceless (TT) gauge, in which the perturbation satisfies

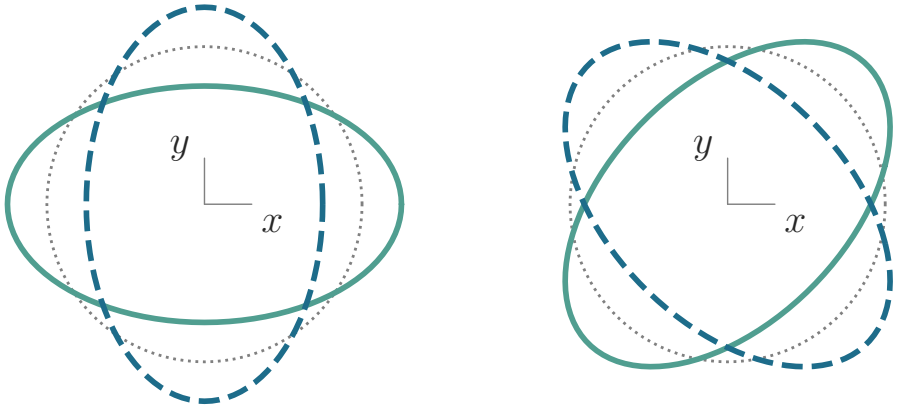
$$\gamma^{\mathrm{TT}}_{0\mu} = 0, \qquad \gamma^{\mathrm{TT}\,\mu}_{\ \ \mu} = 0, \qquad k^\nu\gamma^{\mathrm{TT}}_{\mu\nu} = 0. \tag{1.40}$$

Choosing, without loss of generality, a wave propagating in the z–direction $(k^\mu = (\omega, 0, 0, \omega))$, the metric perturbation can be expressed in matrix form as

$$\gamma^{\mathrm{TT}}_{\mu\nu}(t-z) = \begin{pmatrix} 0 & 0 & 0 & 0 \\ 0 & \gamma_+(t-z) & \gamma_\times(t-z) & 0 \\ 0 & \gamma_\times(t-z) & -\gamma_+(t-z) & 0 \\ 0 & 0 & 0 & 0 \end{pmatrix}, \tag{1.41}$$

where γ_+ and $\gamma_\times$ denote the two independent polarizations of the wave.

The physical meaning of these modes becomes clear if one imagines a ring of freely falling test particles lying in the x–y plane. For the γ_+ polarization, the ring is stretched along the x–axis while being compressed along the y–axis; half a period later, the effect is reversed. The $\gamma_\times$ polarization produces the same alternating stretching and squeezing, but along axes rotated by 45° [10, 18].



(a) h_+ polarization (b) $h_\times$ polarization

Figure 1.2: **Effect of the two GW polarizations on a ring of test particles.** The unperturbed ring is also shown for reference (dotted) [24].

1.3.3 Geodesic deviation and physical effects of gravitational waves

A powerful way to describe the observable effect of GWs is through the equation of geodesic deviation, which governs the relative acceleration of nearby free–falling particles under the influence of spacetime curvature. If U^μ denotes the four–velocity of a reference geodesic and S^μ the separation vector to a neighboring geodesic, the relative motion satisfies

$$\frac{D^2 S^\mu}{\mathrm{d}\tau^2} = R^\mu{}_{\nu\rho\sigma}\, U^\nu U^\rho S^\sigma, \tag{1.42}$$

where $R^\mu{}_{\nu\rho\sigma}$ is the Riemann tensor of the perturbed spacetime.

In the weak–field regime, the Riemann tensor is already of order $\mathcal{O}(\gamma)$, so one can consistently replace $U^\mu = (1,0,0,0) + \mathcal{O}(\gamma)$ for slowly moving test particles. The only nonvanishing components that contribute are then R_{i0j0}, which describe the tidal forces produced by the passing wave. In the TT gauge, these components reduce to

$$R_{i0j0} = -\frac{1}{2}\,\ddot{\gamma}^{\mathrm{TT}}_{ij}, \tag{1.43}$$

where overdots denote derivatives with respect to coordinate time. Substituting into (1.42), the deviation equation becomes

$$\frac{\mathrm{d}^2 S^i}{\mathrm{d}t^2} = -\frac{1}{2}\,\ddot{\gamma}^{\mathrm{TT}}_{ij}\, S^j. \tag{1.44}$$

This expression has a direct physical interpretation: a passing GW produces oscillations in the relative separation of freely falling particles, perpendicular to its direction of propagation [10, 11]. To visualize this, consider again a ring of particles in the x–y plane. If the wave travels along the z–axis, only the γ_+ and $\gamma_\times$ components act nontrivially. For instance, with $h_\times = 0$ and $\gamma_+(t) = \gamma_0 \cos(\omega t)$, the geodesic deviation equations read

$$\frac{\mathrm{d}^2 S^x}{\mathrm{d}t^2} = -\frac{1}{2}\,\ddot{\gamma}_+\, S^x, \qquad \frac{\mathrm{d}^2 S^y}{\mathrm{d}t^2} = +\frac{1}{2}\,\ddot{\gamma}_+\, S^y, \tag{1.45}$$

so the ring is periodically stretched along x while being compressed along y, and vice versa half a period later. If instead $\gamma_+ = 0$ and $\gamma_\times \neq 0$, the deformation occurs along axes rotated by 45°.

Therefore, the two polarization states γ_+ and $\gamma_\times$ represent distinct tidal patterns imprinted on matter, as shown in Fig. 1.2. More generally, arbitrary polarizations can be described as linear combinations of the two, or equivalently in terms of right– and left–circular modes,

$$\gamma_R = \frac{1}{\sqrt{2}}\big(\gamma_+ + i\gamma_\times\big), \qquad \gamma_L = \frac{1}{\sqrt{2}}\big(\gamma_+ - i\gamma_\times\big), \tag{1.46}$$

which are particularly useful in describing the helicity–2 nature of the graviton. The physical effect of a circularly polarized wave is illustrated in Fig. 1.3. This geometrical picture illustrates why

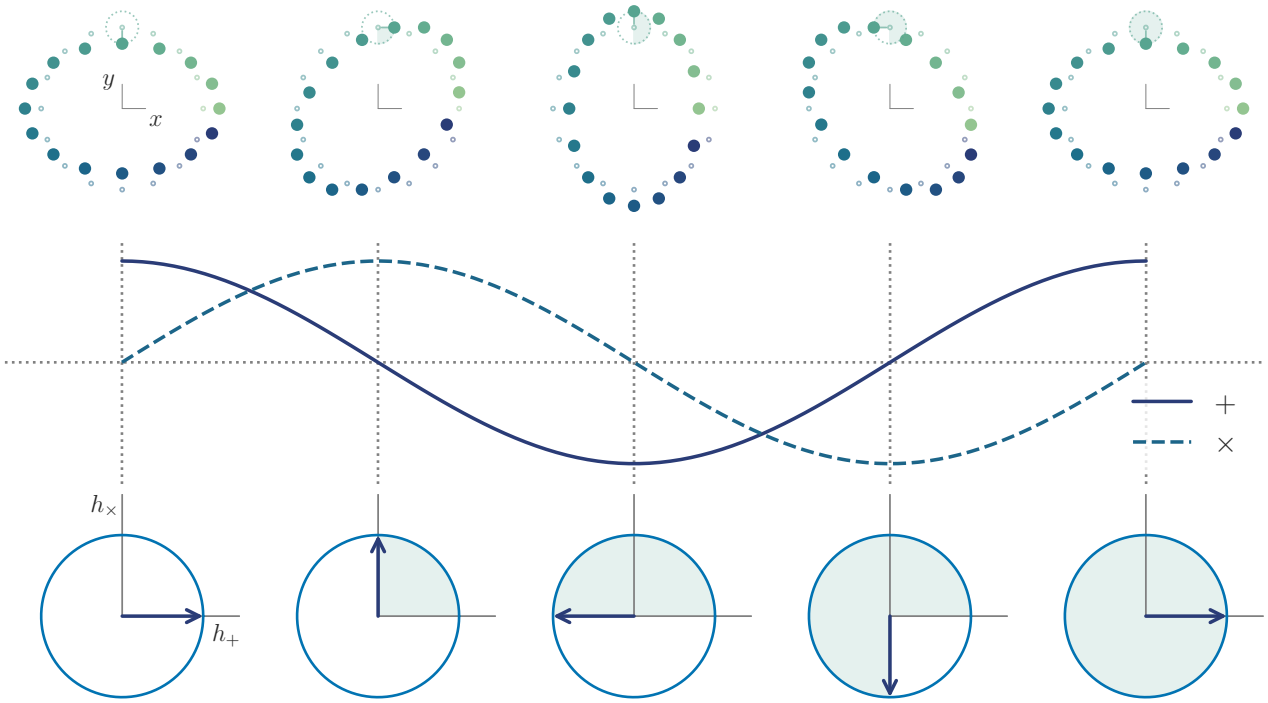


Figure 1.3: **Effect of a right–handed circularly polarized GW on a ring of test particles.** The ring is deformed into an ellipse whose axes rotate with time, so that each particle follows a circular trajectory around its unperturbed position [24].

interferometric detectors such as LIGO, Virgo or KAGRA are sensitive to GWs: the passage of a wave changes the relative distances between freely suspended test masses in a characteristic quadrupolar pattern.

1.3.4 Quadrupole radiation

A central prediction of linearized gravity is that accelerated masses emit gravitational radiation. By analogy with electromagnetism, where the leading radiation arises from the dipole moment, one might expect GWs to be sourced by mass dipole variations. Momentum conservation forbids this, however, since the mass dipole corresponds to the center of mass, which moves inertially in the absence of external forces. Monopole variations are likewise excluded by mass conservation, so the leading contribution is quadrupolar [20]. More precisely, the spatial components of the linearized metric perturbation in the TT gauge, at a distance r from a localized source, are given by [18]

$$\gamma_{ij}^{\mathrm{TT}}(t,\vec{x}) = \frac{2}{r}\,\ddot{Q}_{ij}(t-r)\,, \tag{1.47}$$

where Q_{ij} is the symmetric, trace–free mass quadrupole moment,

$$Q_{ij}(t) = \int d^3x'\,\rho(t,\vec{x}\,')\left(x_i'x_j' - \frac{1}{3}\,\delta_{ij}\,r'^2\right), \qquad r'^2 = \vec{x}\,'\cdot\vec{x}\,'. \tag{1.48}$$

Overdots denote derivatives with respect to the retarded time ($t_r = t - r$). Equation (1.47) shows that GWs are sourced by the second time derivative of the quadrupole; spherically symmetric configurations do not radiate. The total power radiated in GWs, from the Isaacson stress–energy tensor [25, 26], reduces to the quadrupole formula [5, 18]

$$P = -\frac{dE}{dt} = \frac{1}{5}\left\langle \dddot{Q}_{ij}(t)\,\dddot{Q}^{ij}(t)\right\rangle. \tag{1.49}$$

This expression highlights the weakness of gravitational radiation, suppressed by a 1/5 factor and governed by the third time derivative of the quadrupole moment, so that only astrophysical systems with large masses and relativistic accelerations (e.g. neutron star or BH binaries) can produce detectable waves.

1.3.5 Phases of a gravitational-wave signal

Astrophysical GWs from compact binaries exhibit a characteristic structure imprinted by the system's dynamics, with a typical divided into three main stages:

Inspiral

In the early stage, two compact objects orbit at large separations, gradually losing energy and angular momentum through gravitational radiation, which shrinks the orbit and increases its frequency. The waveform is well described by post-Newtonian theory and shows a characteristic "chirp," with both amplitude and frequency growing in time. At leading order, the frequency evolution is [18]

$$\dot{f} = \frac{96}{5}\,\pi^{8/3}\,\mathcal{M}^{5/3}\,f^{11/3}, \tag{1.50}$$

where $\mathcal{M} = (m_1 m_2)^{3/5}/(m_1+m_2)^{1/5}$ is the *chirp mass* of the binary, whose value determines the characteristic frequency increase observed during the inspiral phase.

Merger

As the separation decreases to a few Schwarzschild radii, relativistic effects become dominant and the system enters a highly nonlinear regime. The two horizons eventually merge into a single, distorted BH. This stage can only be accurately modeled using NR.

Ringdown

The newly formed BH relaxes to a stationary Kerr solution by emitting GWs in the form of damped oscillations. These are the so-called QNMs, which carry direct information about the remnant's mass and spin. At linear order, the perturbation can be written as a superposition of modes [27],

$$\gamma_{\ell m}(t) = \sum_{\ell m n} A_{\ell m n}\, e^{-t/\tau_{\ell m n}}\, \cos\!\left(\omega^{R}_{\ell m n}\, t + \phi_{\ell m n}\right), \tag{1.51}$$

where each mode is labeled by angular numbers (ℓ, m) and overtone index (n). The frequencies $(\omega^{R}_{\ell m n})$ and damping times $(\tau_{\ell m n})$ are determined uniquely by the final mass and spin of the remnant. The exponential decay of these oscillations is known as the *ringdown*. Verifying that the observed spectrum matches the Kerr prediction provides a stringent test of GR in the strong-field regime.

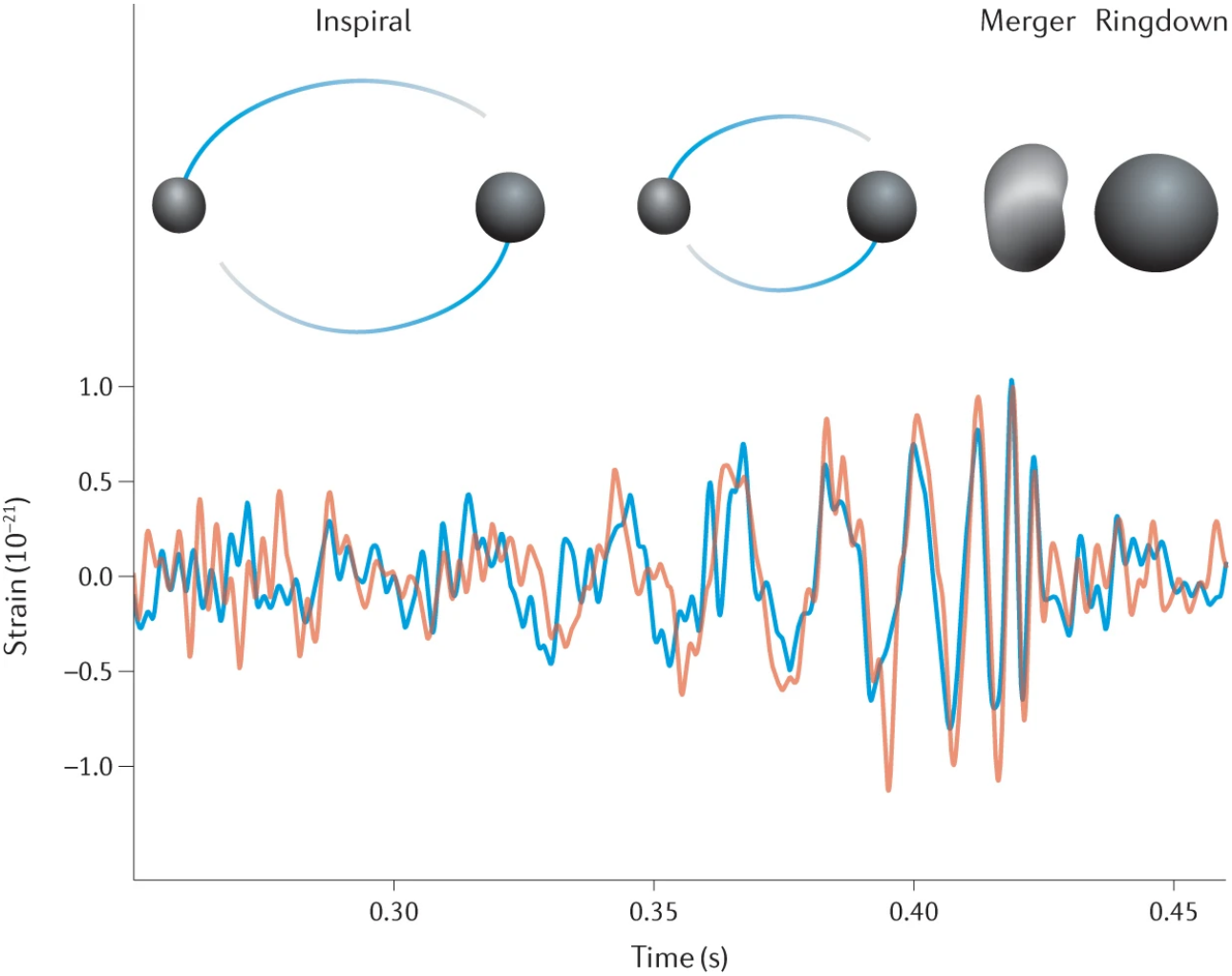


Figure 1.4: **Inspiral, merger and ringdown.** NR simulations of a binary BH coalescence (top) and the corresponding GW strain observed at Earth (bottom). The signal shows three phases: inspiral, driven by quadrupole radiation reaction; merger, when horizons merge into one; and ringdown, dominated by QNM of the remnant [28].

1.3.6 Astrophysical significance of the ringdown

According to the *no–hair theorem*, astrophysical BHs in equilibrium are fully determined by mass and spin, since electric charge is negligible in realistic environments. Thus, the Kerr metric describes astrophysical BHs, and the ringdown provides a direct observational test: after a binary merger, the remnant emits damped oscillations, the QNMs, each with a complex frequency encoding both oscillation and decay

$$\omega_{\ell mn}(M,a) = \omega^R_{\ell mn}(M,a) + i\,\omega^I_{\ell mn}(M,a), \tag{1.52}$$

where the real part ($\omega^R_{\ell mn} = 2\pi f_{\ell mn}$) determines the oscillation frequency and the imaginary part ($\omega^I_{\ell mn} = -1/\tau_{\ell mn}$) sets the damping time. Because the entire QNM spectrum depends solely on (M,a), the ringdown acts as a genuine "gravitational fingerprint" of the BH.

From an astrophysical perspective, this has several important consequences [29]:

- The frequencies scale inversely with mass ($\omega^R_{\ell mn} \propto 1/M$). More massive BHs ring at lower frequencies and decay on longer timescales.
- The spin shifts the spectrum: co–rotating modes ($m > 0$) increase in frequency as the spin grows, while the damping times are also modified.

These scalings can be illustrated by the fundamental quadrupolar mode ($\ell = 2, m = 0, n = 0$) of a Schwarzschild BH, whose frequency and damping time are [29]

$$f_{200} = 1.207 \times 10^{-2}\left(\frac{10^6 M_\odot}{M}\right)\text{Hz}, \qquad \tau_{200} = 55.37\left(\frac{M}{10^6 M_\odot}\right)\text{s}. \tag{1.53}$$

From these expressions it follows that stellar–mass BHs ring at frequencies of hundreds of Hz with millisecond damping times, whereas supermassive BHs oscillate at millihertz frequencies with damping times ranging from minutes to hours, well within the sensitivity band of LISA.

As a concrete astrophysical example, let us consider the remnant of the first detected GW event, GW150914. The final BH had a mass and spin measured as [22]

$$M_f = 62^{+4}_{-4}\,M_\odot, \qquad a_f = 0.67^{+0.05}_{-0.07}\,. \tag{1.54}$$

For these parameters, the fundamental quadrupolar mode ($\ell = 2, m = 2, n = 0$), i.e. the (220) mode, has a complex frequency

$$\omega_{220}\,M \simeq 0.524 + i\,0.0815, \tag{1.55}$$

so that

$$f_{220}\,M = \frac{\omega^R_{220}\,M}{2\pi} \simeq 0.0834, \qquad \frac{\tau_{220}}{M} = \frac{1}{\omega^I_{220}\,M} \simeq 12.3. \tag{1.56}$$

To convert these results to physical units we note that one solar mass corresponds to $1\,M_\odot = 4.9265 \times 10^{-6}\,\text{s}$ so that for $M_f = 62\,M_\odot$ the geometric mass is $M \simeq 3.05 \times 10^{-4}\,\text{s}$. Thus, the (220) ringdown mode has frequency and damping time

$$f_{220} = \frac{f_{220}\,M}{M} \simeq \frac{0.0834}{3.05 \times 10^{-4}} \simeq 273\,\text{Hz}, \qquad \tau_{220} = \left(\frac{\tau_{220}}{M}\right)M \simeq 12.3 \times 3.05 \times 10^{-4} \simeq 3.7\,\text{ms}. \tag{1.57}$$

As a second example, let us consider the supermassive BH at the center of our Galaxy, Sgr A*. Its mass and dimensionless spin parameter ($a_* \equiv J/M^2$) are estimated as [30, 31]

$$M_\bullet = \left(4.0^{+1.1}_{-0.6}\right) \times 10^6 M_\odot, \qquad a_* \simeq 0.90 \pm 0.06\,. \tag{1.58}$$

For these parameters, the fundamental (220) mode has

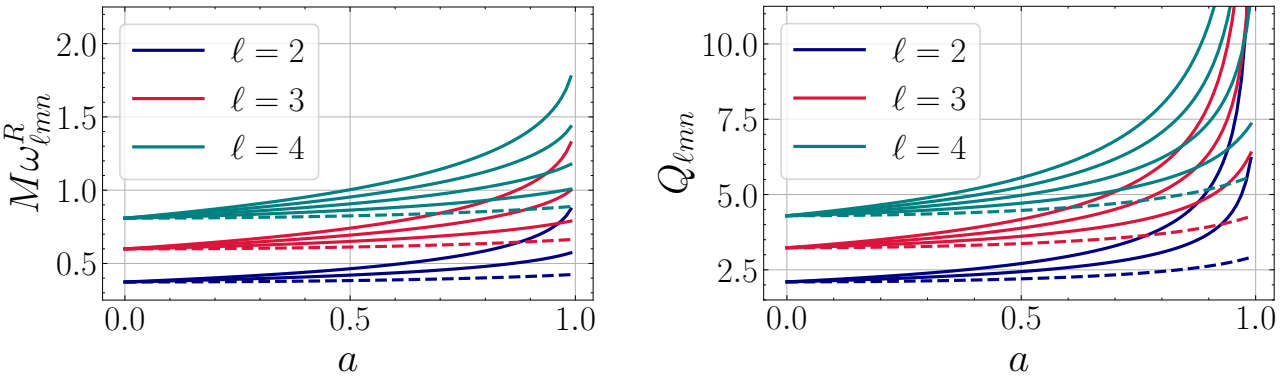
$$\omega_{220} M \simeq 0.672 + i\,0.0649, \qquad f_{220} \simeq 5.4 \times 10^{-3}\,\mathrm{Hz}, \qquad \tau_{220} \simeq 303\,\mathrm{s}. \tag{1.59}$$

Thus, Sgr A* rings at millihertz frequencies with damping times of several minutes, squarely in the sensitivity band of the LISA mission.

Another useful way to characterize these oscillations is through their quality factor [29],

$$Q_{\ell mn} \equiv \pi f_{\ell mn} \tau_{\ell mn} = \frac{\omega^R_{\ell mn} \tau_{\ell mn}}{2} = \frac{\omega^R_{\ell mn}}{2|\omega^I_{\ell mn}|}, \tag{1.60}$$

which quantifies the sharpness of the resonance. The value of $Q_{\ell mn}$ also depends on the spin of the BH: co–rotating modes in rapidly rotating holes typically exhibit larger quality factors, corresponding to longer–lived oscillations.



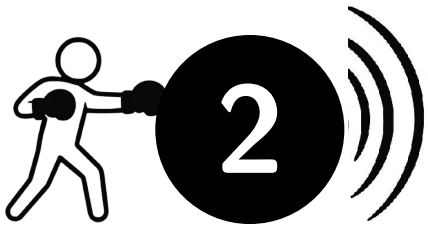
(a) QNM frequencies ($M\omega^R_{\ell mn}$). (b) Quality factors ($Q_{\ell mn}$).

Figure 1.5: **Frequencies and quality factors of fundamental QNMs.** The plots illustrate the dependence of the mode frequency (a) and the quality factor (b) on the azimuthal index m, for multipoles $\ell = 2, 3, 4$. Co–rotating modes ($m > 0$) are shown as solid lines, while the $m = 0$ case appears as dotted. Higher overtones are not displayed, since their quality factors are significantly smaller.

Measuring both the frequency and the damping time in GW data therefore enables a direct inference of the remnant's mass and spin, independently of the inspiral dynamics. This makes the ringdown an invaluable tool for BH astrophysics. Moreover, if multiple QNMs can be detected, one can perform *BH spectroscopy*: checking that all observed modes correspond to the same (M, a) pair. Any inconsistency would provide evidence against the no–hair theorem and hint at new physics beyond GR.

Current ground–based detectors (LIGO–Virgo–KAGRA) have already measured dominant ringdown frequencies, extracting masses and spins consistent with NR predictions. In the future, space–based detectors like LISA will observe ringdowns of supermassive BHs with high signal–to–noise ratios, enabling detailed spectroscopy and stringent tests of the *no–hair theorem* in the strong–field regime.

CHAPTER



Black Hole Perturbation Theory

Contents

2.1 Perturbations on non-rotating backgrounds **17**
2.2 Perturbation on rotating backgrounds **30**
2.3 Quasinormal modes of black holes **34**
2.4 Late–time tails **39**
2.5 Overtones **41**

The study of BHs as exact solutions of the EFE offers a powerful framework, but real astrophysical BHs are not isolated: they interact with matter, can be perturbed, and radiate GWs. To capture these phenomena one must go beyond static solutions and analyze how small disturbances evolve on a curved background spacetime, which is precisely the domain of BHPT.

The central idea is to treat a background BH (e.g. Schwarzschild or Kerr) as fixed and study the linear response of the geometry. In this way, the nonlinear EFE reduce to wave–like equations where curvature acts as an effective potential. The resulting dynamics describe how BHs emit GWs and relax back to equilibrium.

Historically, BHPT took shape through the pioneering works of Regge and Wheeler [32], who first formulated the dynamics of axial perturbations in Schwarzschild; Zerilli [33], who extended the analysis to polar modes; and Teukolsky [34], who generalized the framework to rotating spacetimes. These studies revealed that perturbed BHs behave as resonant systems, with characteristic oscillations that dominate the late–time ringdown and provide a direct observational window into the properties of the remnant.

2.1 Perturbations on non-rotating backgrounds

Before dealing with the full complexity of gravitational perturbations, it is instructive to analyse a simpler system: the propagation of a massive scalar field on a Schwarzschild background. This toy

model already encapsulates the essential ingredients of BHPT: the separation of variables in curved spacetime, the emergence of effective radial potentials, and the interplay between scattering, QNM oscillations, and late–time tails. Although the scalar field does not directly couple to the gravitational degrees of freedom, its dynamics provides a clear analogy and an ideal testing ground before moving to tensorial perturbations.

2.1.1 Massive scalar fields

The interaction between gravity and a scalar field (Φ) is described by the action [35]

$$S = \int \mathrm{d}^4x\,\sqrt{-g}\left[\frac{R}{\kappa} - \frac{1}{2}g^{\mu\nu}\nabla_\mu\Phi\,\nabla_\nu\Phi - \mu^2\Phi^2\right], \tag{2.1}$$

with $g = \det(g_{\mu\nu})$, μ the field mass, and $\kappa = 16\pi$ the *Einstein gravitational constant*. Variation with respect to the scalar field yields the covariant Klein–Gordon (KG) equation

$$\Big(\Box - \mu^2\Big)\Phi = 0, \tag{2.2}$$

with $\Box \equiv \nabla^\mu\nabla_\mu$, while variation with respect to the metric gives the EFE sourced by the scalar field

$$G_{\mu\nu} = \kappa\left[\frac{1}{2}\nabla^\mu\Phi\nabla^\nu\Phi - \frac{1}{4}g^{\mu\nu}\Big(\nabla_\alpha\Phi\nabla^\alpha\Phi + \mu^2\Phi^2\Big)\right]. \tag{2.3}$$

In the test–field approximation ($|\Phi| \ll 1$), the backreaction on the geometry can be neglected and the background is a vacuum solution, such as Kerr. In this case, one focuses solely on the KG equation (Eq. (2.2)), which can be equivalently written in coordinate form as

$$\frac{1}{\sqrt{-g}}\partial_\mu\Big(\sqrt{-g}\,g^{\mu\nu}\,\partial_\nu\Phi\Big) - \mu^2\Phi = 0. \tag{2.4}$$

The complexity of the KG equation suggests the use of separation of variables. In the Schwarzschild geometry, the underlying spherical symmetry naturally motivates an expansion in scalar spherical harmonics,

$$\Phi(t, r, \theta, \varphi) = \sum_{\ell=0}^{\infty}\sum_{m=-\ell}^{\ell}\Phi_{\ell m}(t, r)\,Y_{\ell m}(\theta, \phi), \tag{2.5}$$

with $Y_{\ell m}(\theta, \varphi) = P_{\ell m}(\cos(\theta))\,e^{im\varphi}$ the usual spherical harmonics.

The Schwarzschild background (Eq. (1.21)) is static and spherically symmetric, which permits further separation of the temporal and angular dependence. We adopt the ansatz

$$\Phi_{\ell m}(t, r, \theta, \varphi) = e^{-i\omega t}\,e^{im\varphi}\,R_\ell(r)\,S_{\ell m}(\cos(\theta)), \tag{2.6}$$

where we have introduced $\chi \equiv \cos(\theta) \in [-1, 1]$ as a compact angular coordinate [29]. This ansatz reduces the KG equation to a system of two ordinary differential equations, one for the radial part and one for the angular dependence

$$r\Big(r - 2M\Big)\frac{\mathrm{d}^2R}{\mathrm{d}r^2} + 2\Big(r - M\Big)\frac{\mathrm{d}R}{\mathrm{d}r} + \left[\frac{r^3\omega^2}{r - 2M} - r^2\mu^2 - \lambda\right]R(r) = 0, \tag{2.7a}$$

$$\Big(1 - \chi^2\Big)\frac{\mathrm{d}^2S}{\mathrm{d}\chi^2} - 2\chi\frac{\mathrm{d}S}{\mathrm{d}\chi} + \left(\lambda - \frac{m^2}{1 - \chi^2}\right)S(\chi) = 0. \tag{2.7b}$$

Equation (2.7b) is immediately recognized as the associated Legendre equation. Requiring regularity at the poles $(\chi = \pm 1)$ fixes the separation constant to the familiar form

$$\lambda = \ell(\ell+1), \qquad \ell \in \mathbb{N}. \tag{2.8}$$

The radial equation (2.7a) is still too cumbersome to solve in its present form. A common strategy is to perform a change of variables that recasts it into a wave equation resembling the Schrödinger form. This not only simplifies the analysis but also allows us to introduce coordinates better suited to the global structure of the Schwarzschild geometry, extending the radial domain so that the horizon and spatial infinity can be treated on equal footing. To this end, it is convenient to redefine the radial function by factoring out a power of r. Specifically, we set $R(r) \longrightarrow \Psi_\ell^{s=0}(t,r)/r$ so that the original mode decomposition of the scalar field becomes

$$\Phi(t,r,\theta,\varphi) = \sum_{\ell=0}^{\infty}\sum_{m=-\ell}^{\ell} \frac{\Psi_\ell^{s=0}(t,r)}{r}\, Y_{\ell m}(\theta,\varphi). \tag{2.9}$$

Note that we have dropped any m–dependence in $\Psi_\ell^{s=0}(t,r)$ since the Schwarzschild background is spherically symmetric [29]. Then, the left-hand side of radial equation (Eq. (2.7a)) will be

$$\left[\Big(r-2M\Big)\left(\lambda+\mu^2 r^2+\frac{2M}{r}\right)-r^3\omega^2\right]\Psi_\ell^{s=0}+\Big(2M-r\Big)\left(2M\,\frac{\mathrm{d}\Psi_\ell^{s=0}}{\mathrm{d}r}+r\Big(r-2M\Big)\,\frac{\mathrm{d}^2\Psi_\ell^{s=0}}{\mathrm{d}r^2}\right) \tag{2.10}$$

We now introduce the tortoise coordinate (r_*), defined by

$$\frac{\mathrm{d}r_*}{\mathrm{d}r} = \frac{r^2}{r^2-2Mr} \qquad \Longrightarrow \qquad r_* = r + 2M\ln\left(\frac{r}{2M}-1\right). \tag{2.11}$$

This change of variable implies

$$\frac{\mathrm{d}\Psi_\ell^{s=0}}{\mathrm{d}r} = \frac{\mathrm{d}\Psi_\ell^{s=0}}{\mathrm{d}r_*}\frac{\mathrm{d}r_*}{\mathrm{d}r}, \qquad \frac{\mathrm{d}^2\Psi_\ell^{s=0}}{\mathrm{d}r^2} = \frac{\mathrm{d}\Psi_\ell^{s=0}}{\mathrm{d}r_*}\frac{\mathrm{d}^2 r_*}{\mathrm{d}r^2} + \frac{\mathrm{d}^2\Psi_\ell^{s=0}}{\mathrm{d}r_*^2}\frac{\mathrm{d}^2 r_*}{\mathrm{d}r^2}. \tag{2.12}$$

and allows us to cast the radial equation into a Schrödinger–like form (known as the RW equation),

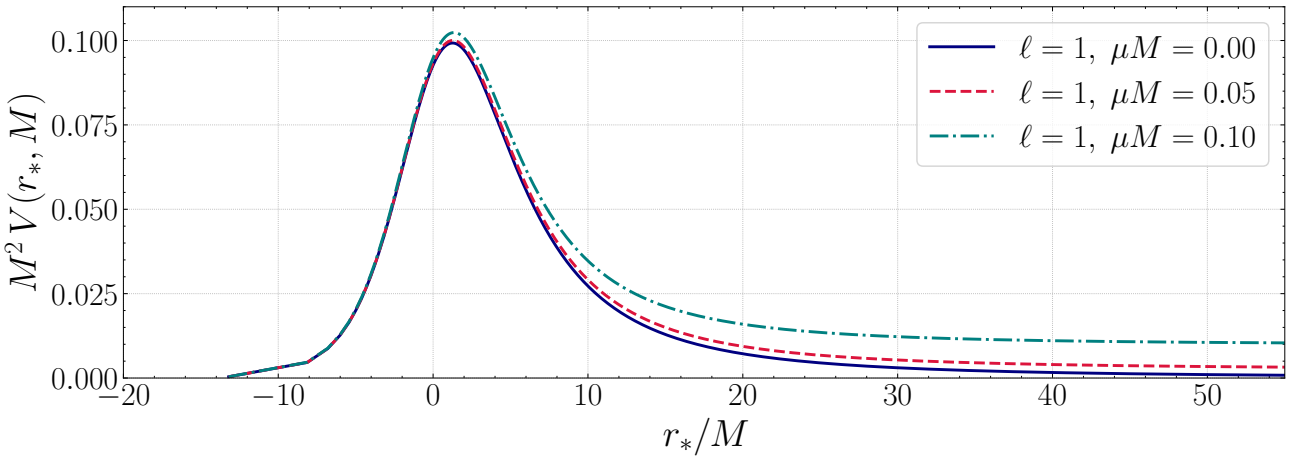
$$\frac{\mathrm{d}^2\Psi_\ell^{s=0}(t,r_*)}{\mathrm{d}r_*^2} + \Big[\omega^2 - V(r)\Big]\Psi_\ell^{s=0}(t,r_*) = 0, \tag{2.13}$$

with the effective potential (after substituting Eq. (2.8))

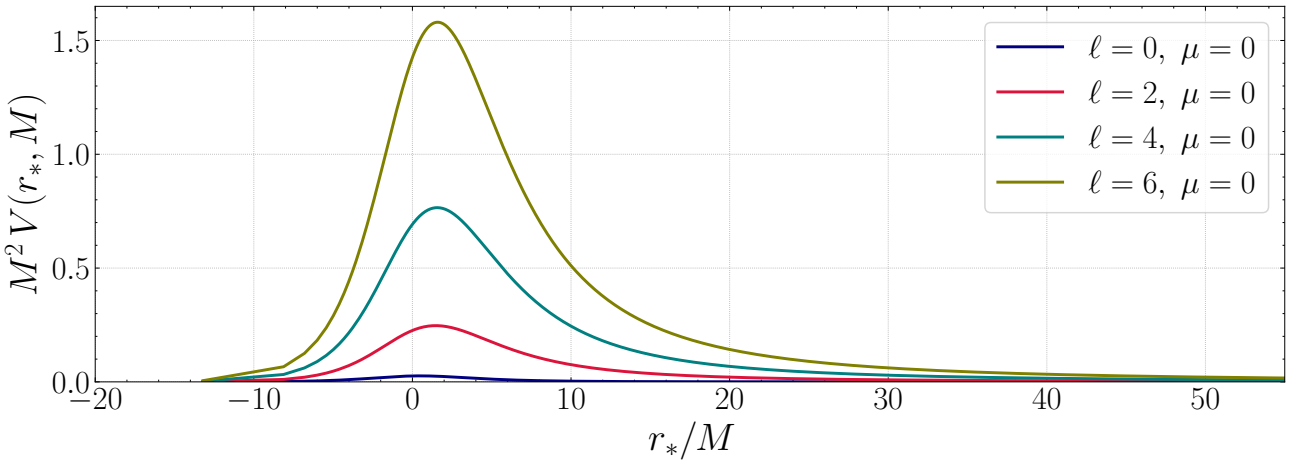
$$V(r) = \left(1-\frac{2M}{r}\right)\left(\mu^2+\frac{\ell(\ell+1)}{r^2}+\frac{2M}{r^3}\right). \tag{2.14}$$

We can now visualize the effective potential for different choices of the parameters ℓ and μ, since these determine the characteristic scattering properties of scalar perturbations. Figure 2.1 illustrates two representative cases.

Panel (a) shows the effect of the scalar field mass for a fixed angular number $\ell = 1$. In the massless limit $(\mu = 0)$, the potential vanishes asymptotically as $r_* \to \pm\infty$, allowing purely outgoing radiation at infinity. When $\mu \neq 0$, the potential tends to a constant value $V \to \mu^2$ as $r_* \to +\infty$, creating an effective mass gap.



(a) Dependence on μ at fixed $\ell = 1$.



(b) Dependence on ℓ at fixed $\mu = 0$.

Figure 2.1: **Effective potentials for a scalar field in Schwarzschild spacetime.** (a) Variation with the field mass parameter μM at fixed $\ell = 1$. (b) Variation with the angular momentum number ℓ for a massless field.

Panel (b) displays the dependence on angular momentum in the massless case ($\mu = 0$). For $\ell = 0$, the barrier is shallow and dominated by curvature scattering. As ℓ increases, the centrifugal term $(\ell(\ell+1)/r^2)$ raises the height of the barrier and shifts its maximum outward. For $\ell = 4$ and $\ell = 6$, the potential develops into the sharp peak familiar from the WKB analysis of QNMs. Thus, the parameters μ and ℓ jointly control the structure of the effective potential, shaping the spectrum of oscillations and decay at late times.

Asymptotic solutions

Now that the equation has been cast into a more familiar form, we can investigate its solutions near the BH horizon and far away at spatial infinity.

- **Solutions near the horizon:** close to the BH, we approach the region $r \to 2M$. In this limit, the tortoise coordinate behaves as $r_* \to -\infty$, and the effective potential vanishes $(V(r) \to 0)$.

Consequently, the radial equation reduces to

$$\frac{\mathrm{d}^2\Psi_\ell^{s=0}(t,r_*)}{\mathrm{d}r_*^2}+\omega^2\,\Psi_\ell^{s=0}(t,r_*)=0, \tag{2.15}$$

whose general solution is simply exponential

$$\Psi_\ell^{s=0}(t,r_*)\sim e^{\pm i\omega r_*}. \tag{2.16}$$

The positive exponent corresponds to an ingoing wave at the horizon, while the negative exponent corresponds to an outgoing wave.

- **Solutions at the infinity:** on the other hand, far from the BH $(r\to\infty)$, the tortoise coordinate approaches $r_*\to+\infty$. In this limit the potential acquires the asymptotic form $V(r)\sim\mu^2$, and the radial equation becomes

$$\frac{\mathrm{d}^2\Psi_\ell^{s=0}(t,r_*)}{\mathrm{d}r_*^2}+\left(\omega^2-\mu^2\right)\Psi_\ell^{s=0}(t,r_*)=0. \tag{2.17}$$

Its solutions are again exponential

$$\Psi_\ell^{s=0}(t,r_*)\sim e^{\pm ikr_*},\qquad k=\sqrt{\omega^2-\mu^2}. \tag{2.18}$$

Having obtained both asymptotic forms, we can combine them to describe the complete asymptotic behaviour of the system:

$$\Psi_\ell^{s=0}(t,r_*)\sim\begin{cases}A_{\mathrm{T}}e^{-i\omega r_*}+A_{\mathrm{R}}e^{+i\omega r_*}, & r_*\to-\infty,\\ A_{\mathrm{in}}e^{-ikr_*}+A_{\mathrm{out}}e^{+ikr_*}, & r_*\to+\infty.\end{cases} \tag{2.19}$$

The variables A_{T}, A_{R}, A_{in}, and A_{out} have the following interpretations:

- A_{T} denotes the amplitude of the wave transmitted into the BH.
- A_{R} denotes the amplitude of the wave reflected away from the BH. Since no outgoing modes are allowed at the event horizon in classical theory, one has $A_{\mathrm{R}}=0$.
- As $\omega>\mu$, A_{in} represents an incoming wave from spatial infinity, while A_{out} corresponds to an outgoing wave there.
- When $\omega<\mu$, A_{in} describes a mode that diverges exponentially at infinity, whereas A_{out} represents an exponentially damped mode.

So far, we have seen that the analysis of the scalar field reveals a structure that will reappear in more realistic scenarios: near the horizon, solutions behave as purely ingoing waves; at spatial infinity, they reduce to a superposition of outgoing and incoming modes; and in between, the dynamics is governed by an effective potential barrier. This configuration naturally gives rise to quasi–bound states and resonance phenomena, namely the QNMs, as well as to late–time power–law decays.

2.1.2 Gravitational perturbations

The high symmetry of the Schwarzschild geometry allows a systematic study of perturbations. Thanks to spherical symmetry, perturbations can be expanded in spherical harmonics, so the dynamics depend only on (t, r). They can then be classified by parity into odd (axial) and even (polar) modes, each described by its own master equation. After fixing the gauge (e.g. in the RW gauge), the problem reduces to two gauge–invariant functions, each satisfying a wave–like equation with an effective potential. We will follow [23, 36, 37] for this review.

In Schwarzschild coordinates (t, r, θ, φ) the line element takes the block–diagonal form

$$\mathrm{d}s^2 = g_{ab}\,\mathrm{d}x^a\mathrm{d}x^b + r^2\Omega_{AB}\,\mathrm{d}x^A\mathrm{d}x^B, \tag{2.20}$$

where g_{ab} denotes the metric on the (t, r) submanifold and Ω_{AB} the metric of the unit two–sphere $(\mathcal{S}^2)$. This decomposition makes explicit the product structure $\mathcal{M}^4 = \mathcal{M}^2 \times \mathcal{S}^2$ [36, 37]. With the conventions $\mu, \nu = 0, \ldots, 3$, $a, b = 0, 1$ for (t, r), and $A, B = 2, 3$ for (θ, φ), the metric and its inverse read

$$g_{\mu\nu} = \begin{pmatrix} g_{ab} & 0 \\ 0 & r^2\Omega_{AB} \end{pmatrix}, \qquad g^{\mu\nu} = \begin{pmatrix} g^{ab} & 0 \\ 0 & r^{-2}\Omega^{AB} \end{pmatrix}. \tag{2.21}$$

Since the Schwarzschild metric splits into a (t, r) part and a two–sphere, it is natural to introduce covariant derivatives adapted to each sector: ∇_μ on $\mathcal{M}^4$, $\mathcal{D}_a$ on $\mathcal{M}^2$, and D_A on $\mathcal{S}^2$. As g_{ab} depends only on (t, r) and Ω_{AB} only on (θ, φ), the two derivatives commute. In particular [36],

$$D_A r = 0, \qquad D_A g_{ab} = 0, \qquad \mathcal{D}_a \Omega_{AB} = 0. \tag{2.22}$$

We now introduce a perturbed metric by expanding the Schwarzschild background to first order in the perturbations, so that the metric and its inverse decompose as

$$g^p_{\mu\nu} = g_{\mu\nu} + \gamma_{\mu\nu}, \qquad (g^p)^{\mu\nu} = g^{\mu\nu} - \gamma^{\mu\nu}, \tag{2.23}$$

where $|\gamma_{\mu\nu}| \ll 1$. We allow the perturbation to mix temporal–radial with angular components, so that

$$\gamma_{\mu\nu} = \begin{pmatrix} \gamma_{ab} & \gamma_{aB} \\ \gamma_{Ab} & \gamma_{AB} \end{pmatrix}, \qquad \gamma^{\mu\nu} = \begin{pmatrix} \gamma^{ab} & (r^2)^{-1}\gamma^{aB} \\ (r^2)^{-1}\gamma^{Ab} & (r^4)^{-1}\gamma^{AB} \end{pmatrix}, \tag{2.24}$$

and, by raising and lowering indices with the background metric, we obtain to linear order

$$g^p_{ab} = g_{ab} + \gamma_{ab}, \qquad g^p_{aB} = \gamma_{aB}, \qquad g^p_{AB} = r^2\Omega_{AB} + \gamma_{AB}, \tag{2.25a}$$

$$(g^p)^{ab} = g^{ab} - \gamma^{ab}, \qquad (g^p)^{aB} = -\frac{1}{r^2}\gamma^{aB}, \qquad (g^p)^{AB} = \frac{1}{r^2}\Omega^{AB} - \frac{1}{r^4}\gamma^{AB}. \tag{2.25b}$$

Harmonic decomposition

To analyze metric perturbations of the Schwarzschild spacetime, it is natural to exploit its spherical symmetry and expand the perturbation tensor in scalar, vector, and tensor spherical harmonics (see Appendix B). This separates the angular dependence from the (t, r) dynamics, reducing the problem

to a set of radial–temporal equations. The perturbation takes the form [23]

$$\gamma_{ab} = \sum_{\ell m} f_{ab}^{\ell m}(t,r)\, Y^{\ell m}, \tag{2.26a}$$

$$\gamma_{aA} = \sum_{\ell m} \left(j_a^{\ell m}(t,r)\, Y_A^{\ell m} + h_a^{\ell m}(t,r)\, X_A^{\ell m} \right), \tag{2.26b}$$

$$\gamma_{AB} = \sum_{\ell m} \left(r^2 K^{\ell m}(t,r)\, Y^{\ell m}\, \Omega_{AB} + r^2 G^{\ell m}(t,r)\, Y_{AB}^{\ell m} + h_2^{\ell m}(t,r)\, X_{AB}^{\ell m} \right). \tag{2.26c}$$

where $Y^{\ell m}$ are scalar harmonics, $Y_A^{\ell m}$ and $X_A^{\ell m}$ the even- and odd-parity vector harmonics, and $Y_{AB}^{\ell m}$, $X_{AB}^{\ell m}$ the corresponding tensor harmonics. The amplitudes in the (t,r) sector are parametrized as

$$f_{ab}^{\ell m} = \begin{pmatrix} f(r) H_0^{\ell m}(t,r) & H_1^{\ell m}(t,r) \\ H_1^{\ell m}(t,r) & f(r)^{-1} H_2^{\ell m}(t,r) \end{pmatrix}, \qquad j_a^{\ell m} = \begin{pmatrix} j_0^{\ell m}(t,r) \\ j_1^{\ell m}(t,r) \end{pmatrix}, \qquad h_a^{\ell m} = \begin{pmatrix} h_0^{\ell m}(t,r) \\ h_1^{\ell m}(t,r) \end{pmatrix}. \tag{2.27}$$

Altogether, the decomposition singles out two independent families of perturbations: an *even-parity (polar)* sector with $\{H_0^{\ell m}, H_1^{\ell m}, H_2^{\ell m}, j_0^{\ell m}, j_1^{\ell m}, K^{\ell m}, G^{\ell m}\}$, and an *odd-parity (axial)* sector with $\{h_0^{\ell m}, h_1^{\ell m}, h_2^{\ell m}\}$.

Gauge transformations

Perturbations of the Schwarzschild metric are not unique, since they can be altered by infinitesimal coordinate transformations generated by a vector field (Ξ^μ), the *gauge vector*. Under such a transformation,

$$x^\mu \;\to\; x^\mu - \Xi^\mu. \tag{2.28}$$

The perturbation tensor then changes by the Lie derivative of the background metric with respect to the gauge vector,

$$\gamma_{\mu\nu} \;\to\; \gamma'_{\mu\nu} = \gamma_{\mu\nu} + \mathcal{L}_\Xi g_{\mu\nu} = \gamma_{\mu\nu} + g_{\lambda\nu}\nabla_\mu \Xi^\lambda + g_{\mu\lambda}\nabla_\nu \Xi^\lambda = \gamma_{\mu\nu} + 2\nabla_{(\mu}\Xi_{\nu)}. \tag{2.29}$$

The gauge vector itself admits a harmonic decomposition analogous to that of the perturbation tensor

$$\Xi_a = \sum_{\ell,m} \xi_a^{\ell m}(t,r)\, Y^{\ell m}, \qquad \Xi_A = \sum_{\ell,m} \left(\xi_2^{\ell m}(t,r)\, Y_A^{\ell m} + \xi_3^{\ell m}(t,r)\, X_A^{\ell m} \right). \tag{2.30}$$

Here, $\xi_a^{\ell m}$ and $\xi_2^{\ell m}$ generate even–parity transformations, while $\xi_3^{\ell m}$ corresponds to the odd–parity sector.

- **Odd–parity gauge transformations:** these are generated exclusively by the angular components of the gauge vector. In this case,

$$\Xi_\mu^{(\mathrm{odd})} = \left(0,\, \Xi_A^{(\mathrm{odd})}\right) = \left(0, \sum_{\ell,m} \xi_3^{\ell m}\, X_A^{\ell m}\right), \tag{2.31}$$

where $\xi_3^{\ell m}$ is the single odd–parity gauge function. The transformation laws for the metric perturbations then read [37]

$$\gamma_{aB} \;\to\; \gamma'_{aB} = h_a^{\ell m} X_B^{\ell m} - \mathcal{D}_a \xi_3^{\ell m} X_B^{\ell m} + \frac{2}{r} r_a \, \xi_3^{\ell m} X_B^{\ell m} := h_a'^{\ell m} X_B^{\ell m}, \tag{2.32a}$$

$$\gamma_{AB} \;\to\; \gamma'_{AB} = h_2^{\ell m} X_{AB}^{\ell m} - 2\xi_3^{\ell m} D_{(A} X_{B)}^{\ell m} := h_2'^{\ell m} X_{AB}^{\ell m}. \tag{2.32b}$$

Equivalently, the coefficients transform as

$$h_a^{\ell m} \;\to\; h_a'^{\ell m} = h_a^{\ell m} - \mathcal{D}_a \xi_3^{\ell m} + \frac{2}{r} r_a \xi_3^{\ell m}, \tag{2.33a}$$

$$h_2^{\ell m} \;\to\; h_2'^{\ell m} = h_2^{\ell m} - 2\xi_3^{\ell m}. \tag{2.33b}$$

From these relations, we can define gauge–invariant combinations. A useful odd–parity invariant quantity is

$$\tilde{h}_a^{\ell m} = h_a^{\ell m} - \frac{1}{2}\mathcal{D}_a h_2^{\ell m} + \frac{1}{r} r_a h_2^{\ell m}, \tag{2.34}$$

which is unaffected by gauge transformations. In particular, this implies

$$\tilde{h}_0^{\ell m} = h_0^{\ell m}, \qquad \tilde{h}_1^{\ell m} = h_1^{\ell m}. \tag{2.35}$$

Thus, within the RW gauge where $h_2^{\ell m} = 0$, the two independent odd–parity perturbations $h_0^{\ell m}$ and $h_1^{\ell m}$ are already gauge–invariant.

- **Even–parity gauge transformations:** these transformations involve both the (t, r) components and the polar vector harmonics. The gauge vector takes the form

$$\Xi_a^{(\text{even})} = \sum_{\ell,m} \xi_a^{\ell m} Y^{\ell m}, \qquad \Xi_A^{(\text{even})} = \sum_{\ell,m} \xi_2^{\ell m} Y_A^{\ell m}, \tag{2.36}$$

where $\xi_a^{\ell m}$ and $\xi_2^{\ell m}$ denote the even–parity gauge functions. Under such transformations, the metric perturbation amplitudes change according to [37]

$$f_{ab}^{\ell m} \;\to\; f_{ab}'^{\ell m} = f_{ab}^{\ell m} - 2\mathcal{D}_{(a}\xi_{b)}^{\ell m}, \tag{2.37a}$$

$$j_a^{\ell m} \;\to\; j_a'^{\ell m} = j_a^{\ell m} - \xi_a^{\ell m} - \mathcal{D}_a \xi_2^{\ell m} + \frac{2}{r} r_a \xi_2^{\ell m}, \tag{2.37b}$$

$$K^{\ell m} \;\to\; K'^{\ell m} = K^{\ell m} + \frac{\ell(\ell+1)}{r^2}\xi_2^{\ell m} - \frac{2}{r} r^a \xi_a^{\ell m}, \tag{2.37c}$$

$$G^{\ell m} \;\to\; G'^{\ell m} = G^{\ell m} - \frac{2}{r^2}\xi_2^{\ell m}. \tag{2.37d}$$

From these relations, one can construct gauge–invariant combinations that remain unchanged under even–parity transformations. A convenient choice is

$$\tilde{f}_{ab}^{\ell m} = f_{ab}^{\ell m} - \mathcal{D}_{(a} j_{b)}^{\ell m} - \frac{r^2}{2}\mathcal{D}_a \mathcal{D}_b G^{\ell m}, \tag{2.38a}$$

$$\tilde{K}^{\ell m} = K^{\ell m} + \frac{\ell(\ell+1)}{2} G^{\ell m} - \frac{2}{r} r^a j_a^{\ell m} - \frac{r^2}{2}\mathcal{D}^a \mathcal{D}_a G^{\ell m}. \tag{2.38b}$$

In the RW gauge, where $j_a^{\ell m} = G^{\ell m} = 0$, these invariants reduce to

$$\tilde{f}_{ab}^{\ell m} = f_{ab}^{\ell m}, \qquad \tilde{K}^{\ell m} = K^{\ell m}. \tag{2.39}$$

Thus, the remaining amplitudes $\{H_0^{\ell m}, H_1^{\ell m}, H_2^{\ell m}, K^{\ell m}\}$ provide a complete description of the even–parity sector in this gauge.

Regge-Wheeler equation

In the RW gauge, the odd–parity perturbations take the form

$$\gamma_{ab}^{(\mathrm{odd})} = 0, \qquad \gamma_{aB}^{(\mathrm{odd})} = h_a(t,r) X_B^{\ell m}, \qquad \gamma_{AB}^{(\mathrm{odd})} = 0. \tag{2.40}$$

To derive the corresponding field equations, one evaluates the perturbations of the Ricci tensor (see Appendix C) component by component. Explicit calculation yields to [37]

$$\delta R_{tA}^{(\mathrm{odd})} = \frac{1}{2}\left[f(r)\left(-\partial_t^2 h_0 + \left(\partial_r + \frac{2}{r}\right)\partial_t h_1 \right) + \left(\frac{\ell(\ell+1)}{r^2} - \frac{4M}{r^3} \right) h_0 \right] X_A, \tag{2.41a}$$

$$\delta R_{rA}^{(\mathrm{odd})} = \frac{1}{2}\left[\frac{1}{f(r)}\left(-\partial_t^2 h_1 + \left(\partial_r - \frac{2}{r}\right)\partial_t h_0 \right) + \left(\frac{(\ell-1)(\ell+2)}{r^2} + \frac{2M}{r^3} \right) h_1 \right] X_A, \tag{2.41b}$$

$$\delta R_{AB}^{(\mathrm{odd})} = \frac{1}{2}\left[-\frac{1}{f(r)}\,\partial_t h_0 + \partial_r\Big(f(r) h_1 \Big) \right] X_{AB}. \tag{2.41c}$$

It is possible to see that Eq. (2.41a) is not independent, being implied by Eqs. (2.41b) and (2.41c). The system is thus governed by the rA–component (2.41b) and the AB–component (2.41c). From the latter, one directly obtains a relation between h_0 and h_1

$$\partial_t h_0 = f(r)\,\partial_r\Big[f(r) h_1 \Big]. \tag{2.42}$$

Substituting this into the Eq. (2.41b) eliminates h_0 and produces a second–order equation for h_1,

$$-\frac{1}{f(r)}\partial_t^2 h_1 + \frac{1}{f(r)}\left(\partial_r - \frac{2}{r}\right)\left(f(r)\,\partial_r\Big[f(r) h_1 \Big] \right) - \frac{(\ell-1)(\ell+2)}{r^2} h_1 = 0. \tag{2.43}$$

The equation simplifies by introducing the RW function

$$\Psi_{\mathrm{RW}}(t,r) := \frac{f(r)}{r}\, h_1(t,r). \tag{2.44}$$

In terms of Ψ_{RW}, the dynamics reduces to a wave equation with an effective potential,

$$\Bigg[\underbrace{-\frac{1}{f(r)}\,\partial_t^2 + f(r)\,\partial_r^2 + \frac{2M}{r^2}\,\partial_r}_{\Box} \; \underbrace{- \left(\frac{\ell(\ell+1)}{r^2} - \frac{6M}{r^3} \right)}_{V_{\mathrm{RW}}(r)} \Bigg] \Psi_{\mathrm{RW}} = 0. \tag{2.45}$$

Introducing the tortoise coordinate defined by $dr/dr_* := f(r)$ so that

$$\partial_{r_*}^2 = f(r)^2 \partial_r^2 + f(r)\Big[\partial_r f(r)\Big]\,\partial_r, \tag{2.46}$$

and assuming harmonic time dependence $\Psi_{\mathrm{RW}}(t,r) = \Psi_{\mathrm{RW}}(r) e^{-i\omega t}$, the equation reduces to a Schrödinger–like form,

$$\frac{\mathrm{d}^2 \Psi_{\mathrm{RW}}}{\mathrm{d}r_*^2} + \Big[\omega^2 - V_{\mathrm{rw}}(r)\Big]\Psi_{\mathrm{RW}} = 0, \qquad V_{\mathrm{rw}}(r) := f(r)\, V_{\mathrm{RW}}(r). \tag{2.47}$$

Zerilli equation

While the RW equation governs the odd–parity sector, the even–parity perturbations are described by a different but related master equation, first derived by Zerilli [33] and later refined in a gauge–invariant form by Moncrief [38]. To set the stage, let us express the metric perturbations in terms of the even–parity harmonics in the RW gauge, where the angular–radial couplings vanish and only a reduced set of amplitudes survive

$$\gamma_{ab}^{(\mathrm{even})} = f_{ab}(t,r)Y, \qquad \gamma_{aA}^{(\mathrm{even})} = 0, \qquad \gamma_{AB}^{(\mathrm{even})} = r^2 K(t,r)\,\Omega_{AB}Y. \tag{2.48}$$

Substituting this ansatz into the linearized EFE leads, after some algebra, to a set of coupled conditions for the perturbation amplitudes [37]

$$\delta R_{ab}^{(\mathrm{even})} = 0 = \Bigg[\frac{1}{2}\mathcal{D}_b\mathcal{D}_m f_a^m + \frac{4M}{r^3}\Big(f_{ab} - g_{ba}f_m^m\Big) + \frac{1}{2}\mathcal{D}_a\mathcal{D}_m f_b^m - \frac{1}{2}\Box f_{ab} + \frac{1}{r}r_m\Big(\mathcal{D}_b f_a^m + \mathcal{D}_a f_b^m - \mathcal{D}^m f_{ab}\Big) - \frac{1}{2}\mathcal{D}_a\mathcal{D}_b f_m^m + \frac{\ell(\ell+1)}{2r^2}f_{ab} - \frac{1}{r}r_b\mathcal{D}_a K - \frac{1}{r}r_a\mathcal{D}_b K - \mathcal{D}_a\mathcal{D}_b K\Bigg]Y, \tag{2.49a}$$

$$\delta R_{aB}^{(\mathrm{even})} = 0 = \frac{1}{2}\Bigg[\mathcal{D}_b f_a^b - \mathcal{D}_a f_b^b + \frac{1}{r}r_a f_b^b - \mathcal{D}_a K\Bigg]Y_B, \tag{2.49b}$$

$$\delta R_{AB}^{(\mathrm{even})} = 0 = \Bigg[r r_a\mathcal{D}_b f^{ab} - \frac{1}{2}r r^b\mathcal{D}_b f_m^m + r_a r_b f^{ab} + r\mathcal{D}_a r_b f^{ab} - \frac{1}{2}\Box(r^2K) + \frac{1}{2}\ell(\ell+1)K + \frac{1}{4}\ell(\ell+1)f_a^a\Bigg]\Omega_{AB}Y - \frac{1}{2}f_a^a Y_{AB}. \tag{2.49c}$$

While the above expressions may seem rather intricate, their structure makes it possible to identify a single gauge–invariant quantity, the ZM function (Ψ_{ZM}), which fully characterizes the even–parity sector. Once redundant variables are removed and the RW gauge is imposed, the system reduces to a single wave–like equation of the form

$$\frac{\mathrm{d}^2\Psi_{\mathrm{ZM}}}{\mathrm{d}r_*^2} = \Big[V_{\mathrm{zm}}(r_*) + \partial_t^2\Big]\Psi_{\mathrm{ZM}}. \tag{2.50}$$

The ZM function can be written in terms of the original amplitudes as

$$\Psi_{\mathrm{ZM}} = \frac{r^2}{\lambda r + 3M}\left[K - \frac{2r}{\ell(\ell+1)}\left(\frac{r-3M}{r^2}K + f(r)\,\partial_r K - \frac{f(r)}{r}H_0\right)\right], \tag{2.51}$$

with $\lambda = 1/2(\ell-1)(\ell+2)$ and $H_0 = H_2$. The potential associated with the ZM function takes the explicit form

$$V_{\mathrm{zm}}(r_*) = 2f(r)\,\frac{\lambda^2(\lambda+1)r^3 + 3\lambda^2 M r^2 + 9\lambda M^2 r + 9M^3}{r^3(\lambda r + 3M)^2}, \tag{2.52}$$

so that the master equation can be cast into the compact gauge–invariant form

$$\Big[\Box - V_{\mathrm{ZM}}(r)\Big]\Psi_{\mathrm{ZM}} = 0, \tag{2.53}$$

with

$$V_{\rm ZM}(r) := \frac{1}{f(r)}\, V_{\rm zm}(r_*) = \frac{1}{\lambda^2}\left[\mu^2\left(\frac{\mu+2}{r^2}+\frac{6M}{r^3}\right)+\frac{36M^2}{r^4}\left(\mu+\frac{2M}{r}\right)\right]. \tag{2.54}$$

To illustrate the dynamical content of the master equations, Fig. 2.2 shows the effective Schwarzschild potentials in the tortoise coordinate r_* for multipoles $\ell = 2, 3, 4$. The axial RW potential (solid curves) and the polar ZM potential (dashed curves) share the same barrier–like structure and differ only by λ–dependent corrections. The insets zoom into the peak region for $\ell = 3$ and $\ell = 4$, where the small differences between the two sectors become most apparent.

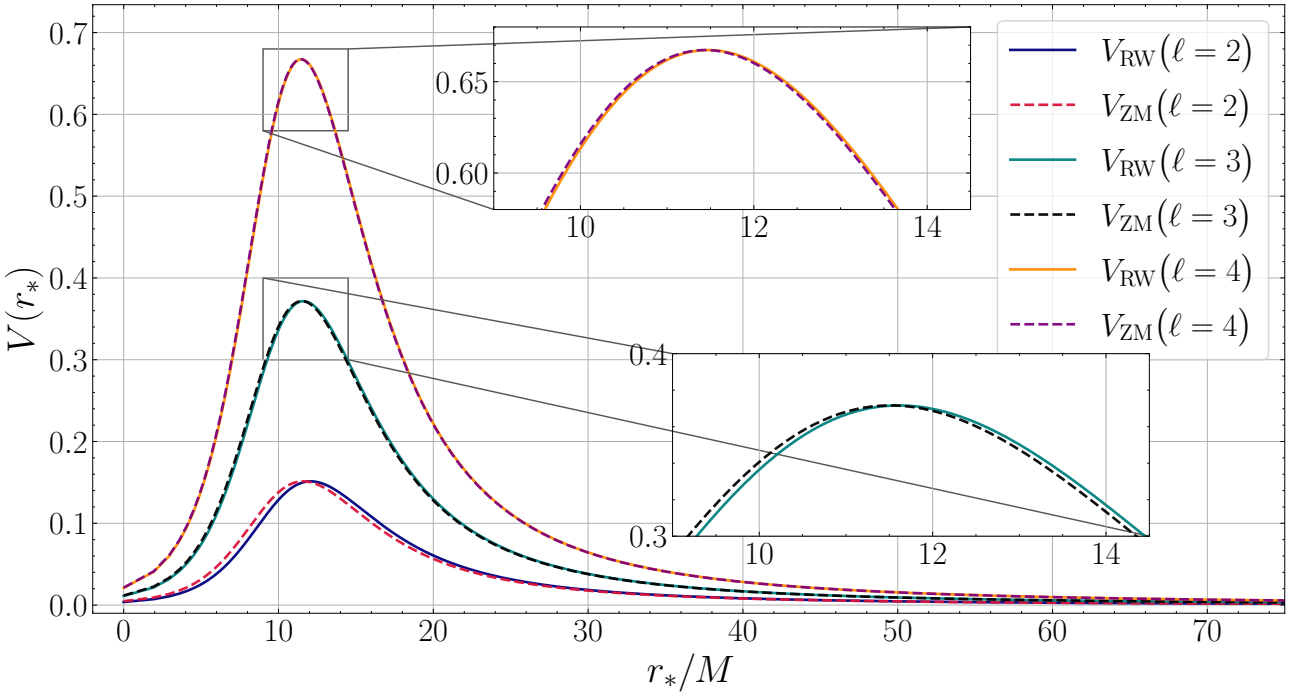


Figure 2.2: **Effective potentials in Schwarzschild spacetime.** Effective potentials for $\ell = 2, 3, 4$ as a function of the tortoise coordinate. Solid: axial RW potential $V_{\rm RW}(\ell)$; dashed: polar Zerilli potential $V_{\rm ZM}(\ell)$. Colors indicate the multipole order. Insets show the peak region for $\ell = 3, 4$, illustrating the near–isospectrality of both sectors.

Isospectrality of the solutions

A remarkable feature of Schwarzschild perturbations is the exact coincidence between the spectra of the RW and Zerilli equations. This correspondence can be established within the framework of a Darboux Transformation (DT). More generally, a DT provides a mapping between two second–order Schrödinger–type equations [39],

$$y''(x) + \Big[\alpha - V_1(x)\Big]\, y(x) = 0, \tag{2.55a}$$

$$Y''(x) + \Big[\alpha - V_2(x)\Big]\, Y(x) = 0. \tag{2.55b}$$

with a common eigenvalue (α). Their solutions are connected by

$$Y(x) = y'(x) + a(x)y(x), \tag{2.56}$$

where the auxiliary function $(a(x))$ is determined by consistency conditions that link V_1 and V_2. In particular, one finds that the potentials are related by

$$V_2(x) = V_1(x) + 2a'(x). \tag{2.57}$$

In the Schwarzschild case, the relevant equations are precisely the Schrödinger–like forms of the odd–parity and even–parity master functions,

$$\frac{\mathrm{d}^2\Psi_{\mathrm{RW}}}{\mathrm{d}r_*^2} + \left[\omega^2 - V_{\mathrm{rw}}(r)\right]\Psi_{\mathrm{RW}} = 0, \tag{2.58a}$$

$$\frac{\mathrm{d}^2\Psi_{\mathrm{ZM}}}{\mathrm{d}r_*^2} + \left[\omega^2 - V_{\mathrm{zm}}(r)\right]\Psi_{\mathrm{ZM}} = 0. \tag{2.58b}$$

Identifying $\alpha = \omega^2$, the DT takes the form

$$\Psi_{\mathrm{ZM}}(r) = \partial_{r_*}\Psi_{\mathrm{RW}}(r) + a(r)\Psi_{\mathrm{RW}}(r), \tag{2.59}$$

with the explicit coefficient

$$a(r) = \frac{\lambda(\lambda+1)}{3M} + \frac{3Mf(r)}{r(\lambda r + 3M)}. \tag{2.60}$$

From this relation it follows immediately that the potentials are Darboux partners,

$$V_{\mathrm{ZM}}(r) = V_{\mathrm{RW}}(r) + 2a'(r). \tag{2.61}$$

To understand why this implies identical QNM spectra, it is useful to recall the scattering picture. For a wave incident from spatial infinity, the RW solution behaves asymptotically as [37]

$$\Psi_{\mathrm{RW}}(r_* \to +\infty) = A_{\mathrm{in}}(\omega)\, e^{-i\omega r_*} + A_{\mathrm{out}}(\omega)\, e^{+i\omega r_*}, \tag{2.62}$$

$$\Psi_{\mathrm{RW}}(r_* \to -\infty) = B_{\mathrm{in}}(\omega)\, e^{-i\omega r_*}, \tag{2.63}$$

with reflection and transmission coefficients defined by

$$I_{\mathrm{ref}} = \frac{\left|A_{\mathrm{out}}\right|^2}{\left|A_{\mathrm{in}}\right|^2}, \qquad I_{\mathrm{trans}} = \frac{\left|B_{\mathrm{in}}\right|^2}{\left|A_{\mathrm{in}}\right|^2}. \tag{2.64}$$

As it will be shown later, the QNMs correspond to the special frequencies for which $A_{\mathrm{in}} = 0$, i.e. purely outgoing radiation at infinity and purely ingoing waves at the horizon. Applying the DT to these asymptotic solutions shows that the ZM function inherits the same boundary conditions, with the transformation coefficient $a(r)$ approaching a constant value at both asymptotic ends [37],

$$a(\pm\infty) = \frac{\lambda(\lambda+1)}{3M} + \mathcal{O}\left(\frac{1}{r_*}\right). \tag{2.65}$$

As a consequence, the reflection and transmission coefficients of the ZM function coincide with those of the RW function, and the QNM condition is identical in both cases. Therefore, the two equations —though associated with different parity sectors and distinct effective potentials— are strictly *isospectral*.

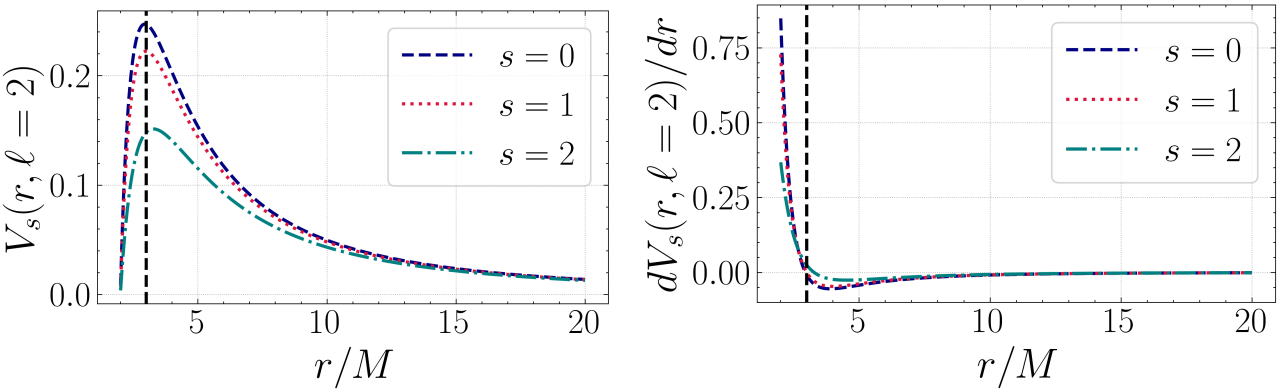
2.1.3 General form of the effective potential

So far we have derived the effective potential associated with scalar and gravitational perturbations of the Schwarzschild spacetime. A similar procedure can be carried out for EM fields, leading to a unified expression that depends explicitly on the spin (s) of the field. The result is

$$V_{s\ell}(r) = \left(1 - \frac{2M}{r}\right)\left[\frac{\ell(\ell+1)}{r^2} + \left(1 - s^2\right)\frac{2M}{r^3}\right], \tag{2.66}$$

where ℓ denotes the multipole number and s the spin weight of the perturbing field. In particular, $s = 0$ corresponds to scalar perturbations, $s = -1$ to vector (EM) perturbations, and $s = -2$ to tensor (gravitational) perturbations.

All spins share the same qualitative behaviour: the potential vanishes at the horizon, falls off as $1/r^2$ at infinity, and forms a barrier whose maximum lies close to the photon sphere at $r \approx 3M$. The correction term $((1 - s^2)2M/r^3)$ modifies the barrier differently for each spin: it increases the height for scalar fields, leaves it unchanged for electromagnetic waves, and lowers it for gravitational perturbations. These variations explain the distinct QNM spectra across different fields.



(a) **Effective potential.** $V_s(r)$ for $\ell = 2$.

(b) **Radial derivative.** dV_s/dr for $\ell = 2$.

Figure 2.3: Comparison of effective potentials in Schwarzschild spacetime for scalar ($s = 0$, dashed blue), vector ($s = -1$, dotted red), and tensor ($s = -2$, dash-dotted green) perturbations with $\ell = 2$. **Left:** potential profiles $V_s(r, \ell = 2)$. **Right:** derivatives $dV_s(r, \ell = 2)/dr$, whose zeros locate the barrier peak near the photon sphere.

The derivative plots (Fig. 2.3b) emphasize the position of the extremum, identifying the photon–sphere barrier. This region is central in BH spectroscopy: waves are temporarily trapped near the maximum, and their slow leakage to infinity or into the horizon produces the damped oscillations known as QNMs. Steeper barriers correspond to longer damping times, while shallower ones yield faster decay, thus encoding the spin–dependence of the spectrum.

2.1.4 Mapping to the gravitational wave signal

In the asymptotic region ($r \to \infty$), the master functions of even (polar) and odd (axial) parity can be directly combined to reconstruct the GW strain. Explicitly [40],

$$\gamma_+ - i\gamma_\times = \frac{1}{r}\sum_{\ell,m}\sqrt{\frac{(\ell+2)!}{(\ell-2)!}}\left(\Psi^{(\text{even})}_{\ell m} + i\Psi^{(\text{odd})}_{\ell m}\right){}_{-2}Y^{\ell m}(\theta,\phi) + \mathcal{O}\left(\frac{1}{r^2}\right). \tag{2.67}$$

Thus, the two real gauge–invariant fields combine into a single complex quantity that describes the observable GW. This clean mapping holds at future null infinity, while closer to the BH the relation between the master functions and the radiative strain becomes more involved. In what follows, when solving the problem numerically, we will restrict our analysis to the odd–parity sector.

2.2 Perturbation on rotating backgrounds

Having set up BH perturbation theory in Schwarzschild, we now move to the more realistic case of rotating BHs. In Kerr spacetime spherical symmetry is reduced to axial symmetry, and the equations for perturbations become coupled and more involved. The key advance came with Teukolsky's work in the 1970s [34]: within the Newman–Penrose (NP) formalism [41] he showed that perturbations of fields with spin $s = 0, \pm 1, \pm 2$ can be captured by a single master equation. Despite the lower symmetry, this Teukolsky equation still allows separation of variables, with spin–weighted spheroidal harmonics describing the angular sector and a radial equation governing wave propagation through the BH potential barrier.

2.2.1 The Newman-Penrose formalism and the Kinnersley null tetrad

The NP formalism reformulates GR using a null tetrad $(\{l^\mu, n^\mu, m^\mu, \bar{m}^\mu\})$, two real and two complex conjugate null vectors. Instead of working directly with the full Riemann tensor, curvature is projected along this tetrad and expressed in terms of a small set of complex scalars: the Weyl scalars (Ψ_i), the Ricci scalars (Φ_{ij}, Λ), and the so-called spin coefficients that encode the connection. This compact representation turns the EFE into first–order relations between scalars, a much more tractable system when dealing with perturbations. A detailed summary of the formalism, including definitions and identities, is provided in Appendix D.

We now apply this framework to the Kerr geometry, which describes a rotating, uncharged BH in vacuum. In BL coordinates, the line element reads[1]

$$\mathrm{d}s^2 = -\frac{\Delta_{BL}}{\Sigma_{BL}}\Big(\mathrm{d}t - a\sin^2(\theta)\,\mathrm{d}\phi\Big)^2 + \frac{\sin^2(\theta)}{\Sigma_{BL}}\Big[\Big(r^2+a^2\Big)\mathrm{d}\phi - a\,\mathrm{d}t\Big]^2 + \frac{\Sigma_{BL}}{\Delta_{BL}}\,\mathrm{d}r^2 + \Sigma_{BL}\,\mathrm{d}\theta^2, \quad (2.68)$$

with

$$\Delta_{BL} = r^2 - 2Mr + a^2, \qquad \Sigma_{BL} = r^2 + a^2\cos^2(\theta). \quad (2.69)$$

To apply the NP formalism to Kerr spacetime, one introduces a null tetrad adapted to its axial symmetry. A standard and particularly convenient choice is the *Kinnersley null tetrad*, written in BL coordinates as

$$l^\mu = \left(\frac{r^2+a^2}{\Delta_{BL}},\, 1,\, 0,\, \frac{a}{\Delta_{BL}}\right), \qquad m^\mu = \frac{1}{\sqrt{2}(r + ia\cos(\theta))}\left(ia\sin(\theta),\, 0,\, 1,\, \frac{i}{\sin(\theta)}\right),$$

$$n^\mu = \frac{1}{2\Sigma_{BL}}\Big(r^2+a^2,\, -\Delta_{BL},\, 0,\, a\Big), \quad \bar{m}^\mu = \frac{1}{\sqrt{2}(r - ia\cos(\theta))}\left(-ia\sin(\theta),\, 0,\, 1,\, -\frac{i}{\sin(\theta)}\right). \quad (2.70)$$

[1] Here we have added the subscript "BL" to emphasize that these functions are defined with respect to the Kerr metric in BL coordinates (see Eq. (1.24)), and to avoid confusion with symbols used later in the NP formalism.

This tetrad is aligned with the principal null directions of the Kerr geometry, a choice that drastically simplifies the curvature structure. Indeed, the only nonvanishing Weyl scalar is

$$\Psi_2 = M\rho^3, \qquad \text{with} \qquad \Psi_0 = \Psi_1 = \Psi_3 = \Psi_4 = 0, \tag{2.71}$$

so that the background curvature is encoded in a single quantity. The corresponding spin coefficients, obtained by contraction with the connection, reduce to a small set of nonvanishing terms

$$\rho = -\frac{1}{r - ia\cos(\theta)}, \qquad \beta = -\frac{\bar{\rho}\cot(\theta)}{2\sqrt{2}}, \qquad \pi = \frac{ia\rho^2\sin(\theta)}{\sqrt{2}}, \qquad \tau = -\frac{ia\rho\bar{\rho}\sin(\theta)}{\sqrt{2}},$$
$$\mu = \frac{1}{2}\rho^2\bar{\rho}\Delta_{BL}, \qquad \gamma = \mu + \frac{1}{2}\rho\bar{\rho}(r-M), \qquad \alpha = \pi - \bar{\beta}. \tag{2.72}$$

2.2.2 Extension to Petrov type D spacetimes

More generally, the same strategy applies to any vacuum Petrov type D geometry, i.e. spacetimes with two repeated principal null directions. Aligning the tetrad vectors with these directions again simplifies the curvature scalars and spin coefficients. In particular, one finds

$$\Psi_0^{(0)} = \Psi_1^{(0)} = \Psi_3^{(0)} = \Psi_4^{(0)} = 0, \qquad \Psi_2^{(0)} \neq 0, \tag{2.73}$$

and, by the Goldberg–Sachs theorem,

$$\kappa^{(0)} = \sigma^{(0)} = \nu^{(0)} = \lambda^{(0)} = 0. \tag{2.74}$$

If the outgoing principal null vector l^μ is chosen affine, then $\epsilon^{(0)} = 0$ as well.

To organize the perturbative expansion, we introduce a bookkeeping parameter ζ and expand any NP quantity as

$$\Psi = \Psi^{(0)} + \zeta\,\Psi^{(1)} + \zeta^2\Psi^{(2)} + \mathcal{O}(\zeta^3). \tag{2.75}$$

In vacuum the Ricci scalars vanish at zeroth order, though first–order sources can be included through the standard NP combinations.

First order system

Once the NP tetrad is aligned with the repeated principal null directions of a Petrov type D spacetime, the Bianchi identities together with the Ricci relations yield a set of transport equations for the perturbed Weyl scalars and spin coefficients. At first order, Ψ_0, Ψ_1 couple to the coefficients κ, σ, while Ψ_4, Ψ_3 couple to λ, ν. Introducing the standard directional derivatives (see Appendix D) the system reads [42]

$$\Big(\bar{\delta} - 4\alpha + \pi\Big)\Psi_0 - \Big(D - 2\epsilon - 4\bar{\rho}\Big)\Psi_1 - 3\kappa\,\Psi_2 = -\mathcal{R}_a, \tag{2.76a}$$

$$\Big(\Delta - 4\gamma + \mu\Big)\Psi_0 - \Big(\delta - 4\tau - 2\beta\Big)\Psi_1 - 3\sigma\,\Psi_2 = -\mathcal{R}_e, \tag{2.76b}$$

$$\Big(D - \rho - \bar{\rho} - 3\epsilon + \bar{\epsilon}\Big)\sigma - \Big(\delta - \tau + \bar{\pi} - \alpha - \bar{\alpha} - 3\beta\Big)\kappa = \Psi_0. \tag{2.76c}$$

and

$$\Big(D + 4\epsilon - \rho\Big)\Psi_4 - \Big(\delta + 2\alpha + 4\pi\Big)\Psi_3 + 3\lambda\,\Psi_2 = -\,\mathcal{R}_d, \tag{2.77a}$$

$$-\Big(\delta + 4\beta - \tau\Big)\Psi_4 + \Big(\Delta + 2\gamma + 4\mu\Big)\Psi_3 - 3\nu\,\Psi_2 = -\,\mathcal{R}_h, \tag{2.77b}$$

$$\Big(\Delta + \mu + \bar{\mu} + 3\gamma - \bar{\gamma}\Big)\lambda - \Big(\bar{\delta} + 3\alpha + \bar{\beta} - \bar{\pi}\Big)\nu = -\,\Psi_4. \tag{2.77c}$$

Here, $\mathcal{R}_d$ and $\mathcal{R}_h$ denote linear combinations of the first–order Ricci NP scalars; in vacuum they vanish identically. These relations are the starting point for deriving the decoupled Teukolsky equations once a specific type D background (e.g. Kerr) and a suitable null frame (e.g. Kinnersley) are specified.

2.2.3 Decoupling the equations

To simplify the coupled system, it is convenient to introduce the shorthand [42, 43]

$$\mathfrak{D}_1 \equiv \delta + 3\alpha + \bar{\beta} + 4\pi - \bar{\tau}, \tag{2.78}$$

$$\mathfrak{D}_2 \equiv \Delta + 4\mu + \bar{\mu} + 3\gamma - \bar{\gamma}. \tag{2.79}$$

Acting with $\mathfrak{D}_2^{(0)}$ on Eq. (2.77a) and $\mathfrak{D}_1^{(0)}$ on Eq. (2.77b), and combining the results, one obtains

$$\Big[\mathfrak{D}_2^{(0)}\Big(D + 4\epsilon - \rho\Big) - \mathfrak{D}_1^{(0)}\Big(\delta + 4\beta - \tau\Big)\Big]\Psi_4 + \Big[-\mathfrak{D}_2^{(0)}\Big(\delta + 2\alpha + 4\pi\Big) + \mathfrak{D}_1^{(0)}\Big(\Delta + 2\gamma + 4\mu\Big)\Big]\Psi_3$$
$$+ 3\Big[\mathfrak{D}_2^{(0)}\lambda - \mathfrak{D}_1^{(0)}\nu\Big]\Psi_2 = -\mathfrak{D}_2^{(0)}\mathcal{R}_d - \mathfrak{D}_1^{(0)}\mathcal{R}_h. \tag{2.80}$$

Substituting the perturbative expansion and using standard NP identities, only the leading term in Eq. (2.80) survives, yielding the Teukolsky master equation [42]

$$\mathcal{T}\,\Psi_4^{(1)} = \mathcal{R}_4^{(1)}, \tag{2.81}$$

where the *Teukolsky operator* is

$$\mathcal{T} \equiv \Big[\mathfrak{D}_2^{(0)}\Big(D + 4\epsilon - \rho\Big) - \mathfrak{D}_1^{(0)}\Big(\delta + 4\beta - \tau\Big)\Big]^{(0)}, \tag{2.82}$$

and the source term reads

$$\mathcal{R}_4^{(1)} \equiv -\,\mathfrak{D}_2^{(0)}\mathcal{R}_d^{(1)} - \mathfrak{D}_1^{(0)}\mathcal{R}_h^{(1)}. \tag{2.83}$$

Equation (2.81) is the master equation describing gravitational perturbations in any Petrov type D spacetime satisfying the vacuum Einstein equations. Teukolsky showed that, by introducing a suitably rescaled field ψ, the equation admits separation of variables. Depending on the spin of the perturbing field, the relevant variable (ψ_s) is defined as summarized in Table 2.1.

Spin s	0	$+\frac{1}{2}$	$-\frac{1}{2}$	$+1$	-1	$+2$	-2
Field ψ_s	Φ	χ_0	$\rho^{-1}\chi_1$	Φ_0	$\rho^{-2}\Phi_2$	Ψ_0	$\rho^{-4}\Psi_4$

Table 2.1: Spin–weight field (ψ_s) for different values of the spin s. The spin coefficient (ρ) allows one to redefine the NP quantities (χ_1, Φ_2 and Ψ_4), so that the Teukolsky master equation takes the compact form (2.81).

In terms of the spin–weight field ψ_{-2}, which describes the outgoing component of the gravitational radiation, the Teukolsky master equation reads [34]

$$\left\{\left[\frac{r^2+a^2}{\Delta_{BL}}-a^2\sin^2\theta\right]\frac{\partial^2}{\partial t^2}+\frac{4Mar}{\Delta_{BL}}\frac{\partial^2}{\partial t\partial\phi}-4\left[r+ia\cos\theta-\frac{M(r^2+a^2)}{\Delta_{BL}}\right]\frac{\partial}{\partial t}-\Delta_{BL}^2\frac{\partial}{\partial r}\left(\Delta_{BL}^{-1}\frac{\partial}{\partial r}\right)\right.$$
$$\left.-\frac{1}{\sin\theta}\frac{\partial}{\partial\theta}\left(\sin\theta\frac{\partial}{\partial\theta}\right)-\left(\frac{1}{\sin^2\theta}-\frac{a^2}{\Delta_{BL}}\right)\frac{\partial^2}{\partial\phi^2}+4\left[\frac{a(r-M)}{\Delta}+\frac{i\cos\theta}{\sin^2\theta}\right]\frac{\partial}{\partial\phi}+(4\cot^2\theta+2)\right\}\psi_{-2}=0. \tag{2.84}$$

Also, with the ansatz [44]

$$\psi_{-2}=e^{-i\omega t}e^{im\phi}R(r)S(\theta), \tag{2.85}$$

the equation separates into a radial and an angular part

$$\Delta_{BL}^2\frac{\mathrm{d}}{\mathrm{d}r}\left(\Delta_{BL}^{-1}\frac{\mathrm{d}R}{\mathrm{d}r}\right)+\left(\frac{K^2+4i(r-M)K}{\Delta_{BL}}-8i\omega r-B\right)R=0, \tag{2.86a}$$

$$\frac{1}{\sin\theta}\frac{\mathrm{d}}{\mathrm{d}\theta}\left(\sin\theta\frac{\mathrm{d}S}{\mathrm{d}\theta}\right)+\left(a^2\omega^2\cos^2\theta-\frac{m^2}{\sin^2\theta}+4a\omega\cos\theta+\frac{4m\cos\theta-4\cos^2\theta}{\sin^2\theta}-2+A\right)S=0, \tag{2.86b}$$

where $K=(r^2+a^2)\omega-am$, $B=A+a^2\omega^2-2am\omega$, and $A=A_{\ell m}(a\omega)$.

2.2.4 Gravitational radiation at infinity

The radial Teukolsky equation can be cast into a Schrödinger–like form by redefining the field [42]

$$Y=\frac{(r^2+a^2)^{1/2}}{\Delta}R \tag{2.87}$$

and introducing the tortoise coordinate. In terms of Y, the equation simplifies asymptotically ($r\to\infty$, $r_*\to\infty$) to

$$Y''+\left(\omega^2-\frac{4i\omega}{r}\right)Y=0, \tag{2.88}$$

whose solution is a superposition of ingoing and outgoing waves. Transforming back to the Teukolsky variable one finds

$$\Psi_4^{(1)}\sim\left(\frac{a_0}{r^5}e^{-i\omega r_*}+\frac{b_0}{r}e^{i\omega r_*}\right)e^{-i\omega t+im\phi}\,{}_{-2}S_{\ell m}(\theta), \tag{2.89}$$

where ${}_{-2}S_{\ell m}(\theta)$ denotes the spin–weighted spheroidal harmonic of spin weight $s=-2$, which generalizes the spherical harmonics to the Kerr background and represents the angular dependence of the wave. Imposing no incoming radiation from infinity ($a_0=0$) and $b_0={}_{-2}\mathcal{A}_{\ell m}$ gives the asymptotic waveform

$$\Psi_4^{(1)} = \frac{{}_{-2}\mathcal{A}_{\ell m}}{r}\, e^{i\left(m\phi-\omega(t-r_*)\right)}\, {}_{-2}S_{\ell m}(\theta), \tag{2.90}$$

with $\mathcal{A}_{\ell m}$ the excitation amplitude of each mode. In the outgoing radiation gauge one finds [42, 45]

$$\Psi_4^{(1,2)} = -\frac{1}{2}\left(\partial_t^2\gamma_+^{(1,2)} - i\,\partial_t^2\gamma_\times^{(1,2)}\right), \tag{2.91}$$

which follows directly from the Riemann tensor projection (Eq. (1.43)). This establishes the link between the Weyl scalar Ψ_4 and the metric polarizations observed at infinity. The late–time behaviour of Ψ_4 is governed by a discrete set of damped oscillations, the QNMs, whose frequencies and decay times depend only on the mass and spin of the remnant. This remarkable property makes the asymptotic analysis of the Teukolsky equation a cornerstone for waveform modelling and for the observational programme of GW astronomy, from LIGO/Virgo detections to the future space–based LISA mission.

2.2.4.1 Mapping to the RW/ZM formalism

The correspondence with gauge–invariant master functions such as RW and ZM is not a direct identification, but involves explicit transformation formulas. At future null infinity, the strain can be reconstructed from Ψ_4 via a double time integration,

$$\gamma \equiv \gamma_+ - i\gamma_\times = -2\int^t dt' \int^{t'} dt''\, \Psi_4(t'', r\to\infty, \theta, \phi)\,. \tag{2.92}$$

At the multipolar level this mapping reduces to

$$\int dt\, dt'\, \Psi_{4,\ell m} \;\propto\; \Psi_{\ell m}^{(\mathrm{odd})} + i\Psi_{\ell m}^{(\mathrm{even})}. \tag{2.93}$$

Thus, at future null infinity the two real gauge–invariant fields (RW and ZM) naturally combine into the single complex waveform that describes the observable GW. Closer to the BH, however, additional gauge, tetrad and coupling effects complicate the mapping.

2.3 Quasinormal modes of black holes

From the theoretical point of view, the damped oscillations observed in the ringdown are understood as QNMs. These are the characteristic excitations of the BH geometry itself: when perturbed, the spacetime responds at a discrete set of complex frequencies. Unlike the normal modes of conservative systems, QNMs arise because the exterior of a BH is an open system. The effective potential surrounding the horizon behaves as a scattering barrier: part of the radiation is absorbed by the horizon, while the rest escapes

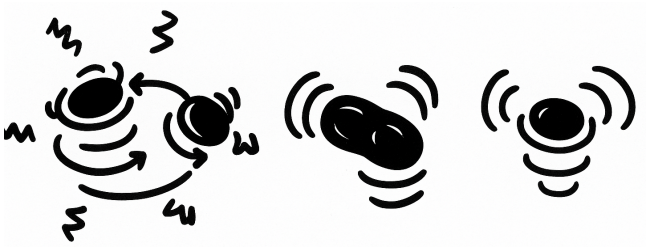


Figure 2.4: **Phases of BH perturbations.** Qualitative stages of BH perturbations, ending in the QNM ringdown. Reproduced from [46].

to infinity. Imposing purely ingoing boundary conditions at the horizon and purely outgoing ones at infinity leads to a non–Hermitian eigenvalue problem with a discrete spectrum of complex frequencies.

These modes provide the natural language to describe the relaxation of a perturbed BH. Their spectrum $\{\omega_{\ell mn}\}$ depends only on the mass and spin of the remnant, consistent with the no–hair theorem discussed in Sec. 1.3.6. From the observational side, the ringdown detected in GW data corresponds precisely to the excitation of these quasinormal oscillations. From the theoretical side, they represent the intrinsic response of the Kerr spacetime to perturbations and therefore play a central role in BHPT.

2.3.1 Poles of the Green's function

In GR, the two polarizations of a GW, γ_+ and $\gamma_\times$, are often grouped into a single complex quantity [47],

$$\gamma_+ - i\,\gamma_\times = \sum_{\ell m} \gamma_{\ell m}(t)\, {}_{-2}Y_{\ell m}(\iota,\phi), \tag{2.94}$$

where the spin–weighted spherical harmonics ${}_{-2}Y_{\ell m}$ represent the angular structure of the radiation as seen by an observer located at angles (ι,ϕ).

In the framework of BHPT, each multipole mode $\big(h_{\ell m}(t)\big)$ exhibits a distinctive temporal behaviour. After the prompt response of the system and before the onset of the late–time power–law tails, the signal is well approximated by a sum of QNMs. These modes are characterized by complex frequencies whose real part controls the oscillation rate and whose imaginary part dictates the damping. A practical representation of this intermediate regime is [47]

$$\gamma_{\ell m}(t) \simeq \sum_n \mathcal{A}_{\ell mn}\, e^{-i\omega_{\ell mn}t}\, e^{-t/\tau_{\ell mn}}, \tag{2.95}$$

with $\mathcal{A}_{\ell mn} = A_{\ell mn}e^{i\phi_{\ell mn}}$ denoting excitation amplitudes and phase, $\omega_{\ell mn}$ the real frequencies, and $\tau_{\ell mn}$ damping times as we mentioned previously. Expression (2.95) therefore represents the *ringdown waveform*, namely a linear combination of exponentially damped oscillations. In what follows, and in order to make the emergence of this structure explicit, we shall study a toy scattering problem with a δ–function potential.

Consider the simplified one–dimensional wave equation [47]

$$\frac{\partial^2\psi}{\partial x^2} - \frac{\partial^2\psi}{\partial t^2} - 2V_0\delta(x)\,\psi = 0, \tag{2.96}$$

which describes wave propagation in the presence of a δ–like scattering potential of strength V_0.

To analyze its solutions, it is convenient to apply a Laplace transform in time, converting the partial differential equation into an ordinary differential equation in the spatial variable (x). We define

$$\Psi(s,x) = \int_0^\infty e^{-st}\,\psi(t,x)\,dt, \tag{2.97}$$

where s denotes the Laplace parameter. The transform rules for the time derivatives are

$$\mathcal{L}\left[\frac{\partial\psi(t,x)}{\partial t}\right] = s\Psi(s,x) - \psi(0,x), \qquad \mathcal{L}\left[\frac{\partial^2\psi(t,x)}{\partial t^2}\right] = s^2\Psi(s,x) - s\,\psi(0,x) - \left.\frac{\partial\psi}{\partial t}\right|_{t=0}. \tag{2.98}$$

Substituting into Eq. (2.96) and setting $\omega = is$ (so that $s^2 = -\omega^2$), the Laplace–transformed wave equation reduces to

$$\frac{\partial^2 \Psi}{\partial x^2} + \Big[\omega^2 - 2V_0\delta(x)\Big]\Psi = -\left.\frac{\partial \psi}{\partial t}\right|_{t=0} + i\omega\psi(0,x) \;\equiv\; S, \tag{2.99}$$

where the right-hand side has the source terms given by the initial data.

Next, we define the homogeneous solution as the one that satisfies the physical boundary conditions. At $x \to -\infty$ we require that the solution contains only outgoing waves, i.e. waves propagating away from the origin towards negative infinity. This means that any incoming wave component from $x \to -\infty$ must be eliminated. The full solution can be written as

$$\psi_L(x) = \begin{cases} e^{-i\omega x}, & x \to -\infty, \\ A_{\rm in}\, e^{-i\omega x} + A_{\rm out}\, e^{+i\omega x}, & x \to +\infty, \end{cases} \qquad \psi_R(x) = \Big\{ e^{+i\omega x}, \quad x \to +\infty. \tag{2.100}$$

The Wronskian of two functions measures their linear dependence. For (2.100) it is defined as

$$\mathcal{W} = \psi_L \frac{\mathrm{d}\psi_R}{\mathrm{d}x} - \frac{\mathrm{d}\psi_L}{\mathrm{d}x}\,\psi_R = \psi_L\, i\omega e^{+i\omega x} - \Big(- i\omega A_{\rm in}\, e^{-i\omega x} + i\omega A_{\rm out}\, e^{+i\omega x}\Big)\psi_R = 2i\omega A_{\rm in}. \tag{2.101}$$

Now, we impose the matching conditions at $x = 0$. The field (ψ) is continuous, while its derivative (ψ') acquires a jump from the δ–potential

$$\psi_L(0) = \psi_R(0) \;\;\Rightarrow\;\; A_{\rm in} + A_{\rm out} = 1, \qquad \psi_R'(0) - \psi_L'(0) = 2V_0\psi(0). \tag{2.102}$$

Using $\psi_L'(0) = -i\omega A_{\rm in} + i\omega A_{\rm out}$, $\psi_R'(0) = i\omega$, and $\psi(0) = 1$, we obtain

$$-A_{\rm in} + A_{\rm out} + 1 = \frac{2V_0}{i\omega}. \tag{2.103}$$

Together with $A_{\rm in} + A_{\rm out} = 1$, this yields

$$A_{\rm in} = \frac{V_0}{i\omega}, \qquad A_{\rm out} = 1 + \frac{V_0}{i\omega}. \tag{2.104}$$

The Wronskian then reads

$$\mathcal{W} = 2i\omega A_{\rm in} = 2i\omega\left(1 + \frac{V_0}{i\omega}\right), \tag{2.105}$$

and the condition $A_{\rm in} = 0$ gives a single quasi–normal frequency $\omega = -iV_0$ for which $\mathcal{W} = 0$. For $x > 1$, the scattering solution reads

$$\Psi(x) = e^{i\omega x}\int dx\, \frac{\psi_L S}{\mathcal{W}}, \tag{2.106}$$

with the initial source $S = \delta(x - x_0)$ $(x_0 > 0)$. This gives

$$\begin{aligned}\Psi(x) &= e^{i\omega x}\frac{i\omega}{\mathcal{W}}\Big(A_{\rm in}e^{-i\omega x_0} + A_{\rm out}e^{+i\omega x_0}\Big) \\ &= \frac{e^{i\omega(x-x_0)}}{2} + e^{i\omega(x+x_0)}\frac{A_{\rm out}}{2A_{\rm in}},\end{aligned} \tag{2.107}$$

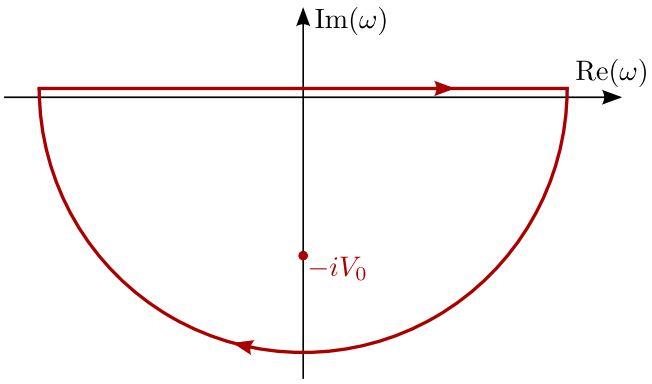


Figure 2.5: **Inverse Fourier transform contour.** Contour in the complex ω–plane, where the only contribution arises from the pole at $\omega = -iV_0$ [47].

which is the full Fourier–space solution. To recover the time dependence, we invert the transform

$$\Psi(t) = \frac{1}{2\pi}\int d\omega\, e^{-i\omega t}\psi = \frac{1}{2}\delta(x - x_0 - t) + \frac{1}{4\pi}\int d\omega\, \frac{-iV_0}{\omega + iV_0}\, e^{i\omega\left(x+x_0-t\right)}. \tag{2.108}$$

The remaining integral is evaluated in the complex ω–plane by contour integration. Since no branch cuts appear, only the simple pole at $\omega = -iV_0$ contributes, as illustrated in Fig. 2.5. The solution can be written as

$$\Psi = \frac{1}{2}\delta(x - x_0 - t) + \frac{1}{2\pi i}\int d\omega\, \frac{-V_0}{\omega + iV_0}\, e^{-i\omega\left(x+x_0-t\right)}. \tag{2.109}$$

The integrand has a simple pole at $\omega = -iV_0$ and we will evaluate it using contour integration in the complex ω–plane.

Case 1: $t < x + x_0$ $\left(x + x_0 - t > 0\right)$

Here $e^{-i\omega\left(x+x_0-t\right)} = e^{-i\omega(+)}$. Closing the contour in the upper half–plane excludes the pole, so the integral vanishes

$$\mathcal{I} = 0 \quad \Rightarrow \quad \Psi = \frac{1}{2}\delta(x - x_0 - t). \tag{2.110}$$

Case 2: $t > x + x_0$ $\left(x + x_0 - t < 0\right)$

Now $e^{-i\omega\left(x+x_0-t\right)} = e^{-i\omega(-)}$. Closing the contour in the lower half–plane encloses the pole at $\omega = -iV_0$, yielding

$$\mathcal{I} = 2\pi i\,\mathrm{Res}\left(\frac{-V_0}{\omega + iV_0}, -iV_0\right) = -2\pi i V_0 e^{-V_0\left(x+x_0-t\right)}. \tag{2.111}$$

Thus,

$$\Psi = \frac{1}{2}\delta(x - x_0 - t) + \frac{1}{2}V_0\, e^{-V_0\left(x+x_0-t\right)}. \tag{2.112}$$

So, depending on $(t - x + x_0)$,

$$\Psi(x,t) = \begin{cases} \dfrac{1}{2}\,\delta(x - x_0 - t), & t < x + x_0, \\ \dfrac{1}{2}\,\delta(x - x_0 - t) + \dfrac{1}{2}V_0 e^{-V_0\left(t-x-x_0\right)}, & t > x + x_0. \end{cases} \tag{2.113}$$

Then, we see that for $t < x + x_0$, only the prompt Dirac delta response is present. And for $t > x + x_0$, a delayed exponentially–decaying contribution appears, mimicking a QNM–like signal.

Finally, for an extended source composed of two deltas

$$S = \delta(x - x_0) + \delta(x - x_1), \qquad x_1 > x_0, \tag{2.114}$$

the initial data excite two stages of ringdown with different amplitudes. The solution is

$$\Psi(x,t) = \begin{cases} \dfrac{1}{2}\delta(x - x_0 - t) + \dfrac{1}{2}\delta(x - x_1 - t), & t < x + x_0, \\ \dfrac{1}{2}\delta(x - x_0 - t) + \dfrac{1}{2}\delta(x - x_1 - t) + \dfrac{V_0}{2}e^{-V_0\left(t-(x+x_0)\right)}, & x + x_0 < t < x + x_1, \\ \dfrac{1}{2}\delta(x - x_0 - t) + \dfrac{1}{2}\delta(x - x_1 - t) + \dfrac{V_0}{2}e^{-V_0(t-x)}\left(e^{V_0 x_0} + e^{V_0 x_1}\right), & t > x + x_1. \end{cases} \tag{2.115}$$

Summarizing, this toy model illustrates that ringdown cannot be universally described as a purely damped sinusoid with fixed frequency and constant amplitude. Instead, the waveform always combines a prompt response with a backscattered contribution produced by the potential. Moreover, the onset of the ringdown phase is not sharply defined: it depends sensitively on the field under consideration, on the nature of the source, and on how the initial data project onto the QNM spectrum.

2.3.2 Beyond the toy model: the Pöschl–Teller potential

A useful analytical model for studying QNMs is the Pöschl–Teller potential, defined by [48]

$$\frac{\mathrm{d}^2\Psi}{\mathrm{d}r_*^2} + \left[\omega^2 - \frac{V_0}{\cosh^2\big(\alpha(r_* - \bar{r}_*)\big)}\right]\Psi = 0, \tag{2.116}$$

where $\bar{r}_*$ denotes the location of the potential maximum, $V_0 = V(\bar{r}_*)$, and

$$\alpha^2 = -\frac{1}{2V_0}\left.\frac{\mathrm{d}^2V}{\mathrm{d}r_*^2}\right|_{r_*=\bar{r}_*} \tag{2.117}$$

controls the curvature of the barrier.

Introducing the new variable

$$\xi = \left[1 + e^{-2\alpha\left(r_* - \bar{r}_*\right)}\right]^{-1}, \tag{2.118}$$

Eq. (2.116) becomes a hypergeometric equation,

$$\xi(1-\xi)\frac{\mathrm{d}^2\Psi}{\mathrm{d}\xi^2} + (1-2\xi)\frac{\mathrm{d}\Psi}{\mathrm{d}\xi} + \left[\frac{\omega^2}{4\alpha^2} - \frac{V_0}{\alpha^2}\,\xi(1-\xi)\right]\Psi = 0, \tag{2.119}$$

whose general solution can be written as

$$\Psi(\xi) = A\,\xi^{i\omega/(2\alpha)}(1-\xi)^{-i\omega/(2\alpha)}F(a,b;c;\xi) + B\,\xi^{-i\omega/(2\alpha)}(1-\xi)^{i\omega/(2\alpha)}F(a-c+1,b-c+1;2-c;\xi), \tag{2.120}$$

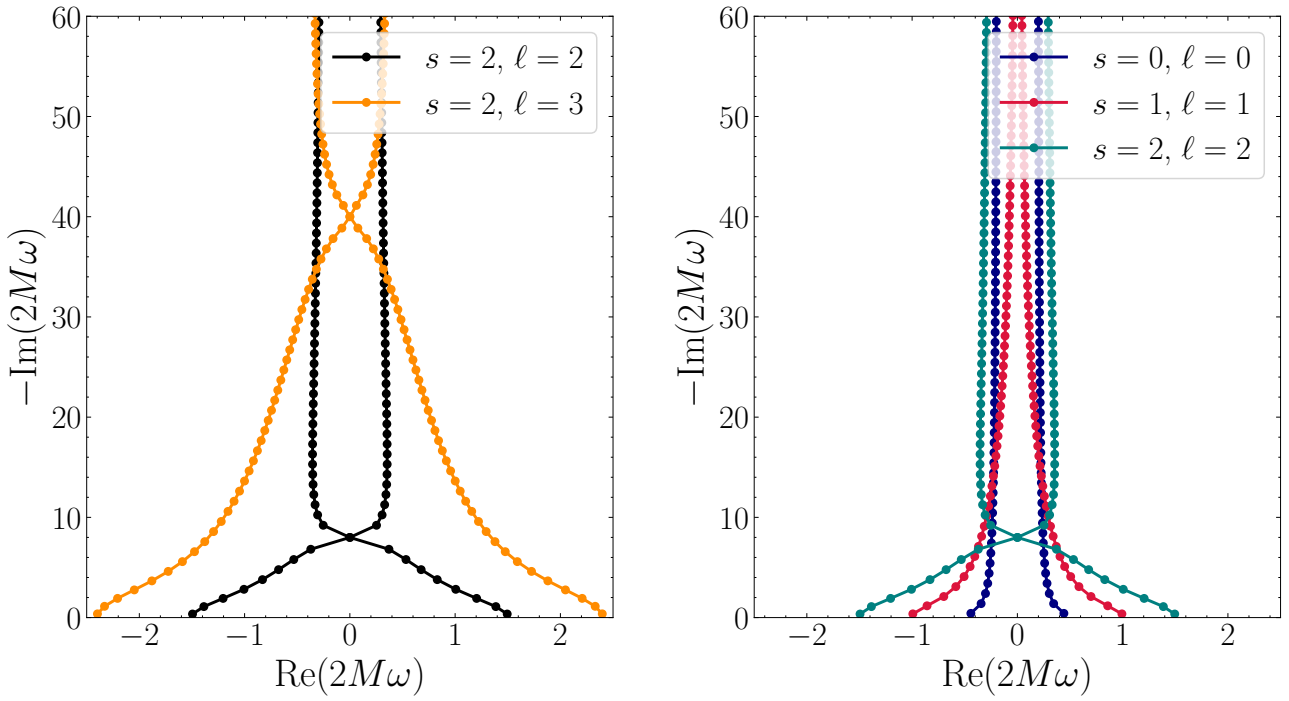
with F the hypergeometric function and (a,b,c) determined by ω, V_0, α.

Applying the boundary conditions for QNMs (purely ingoing at the horizon, purely outgoing at infinity) eliminates one of the terms. The remaining solution exists only for discrete complex frequencies,

$$\omega = \pm\sqrt{V_0 - \frac{\alpha^2}{4}} - i\alpha\left(n + \frac{1}{2}\right), \quad n = 0, 1, 2, \ldots \tag{2.121}$$

Then, we see that the Pöschl–Teller potential serves as an accurate approximation to the effective potentials of BH spacetimes. For instance, for low multipoles in Schwarzschild geometry the prediction agrees closely with numerical results, and in the eikonal limit ($\ell \to \infty$) it reproduces the known asymptotic scaling,

$$\omega \sim \ell - i\alpha\left(n + \frac{1}{2}\right). \tag{2.122}$$



(a) Gravitational modes ($s = 2$) for $\ell = 2$ (black) and $\ell = 3$ (dark orange).

(b) Comparison of different spin fields: scalar ($s = 0$, blue), EM ($s = 1$, red), and gravitational ($s = 2$, teal).

Figure 2.6: **QNMs of a Schwarzschild BH.** Distribution of QNM frequencies in the plane $(\mathrm{Re}(2M\omega), -\mathrm{Im}(2M\omega))$. **Left:** gravitational perturbations with multipoles $\ell = 2, 3$. **Right:** comparison across spin fields: scalar ($s = 0$), electromagnetic ($s = 1$), and gravitational ($s = 2$). Data taken from [49].

2.4 Late–time tails

After the prompt response and the exponentially damped ringdown dominated by QNMs, BH perturbations decay through a slower, universal power law known as the *late–time tail* [50]. This effect, first identified by Price [51], originates from the backscattering of waves off the asymptotic curvature of spacetime.

2.4.1 Green's function origin

Following the approach given in [50], consider, again, the master wave equation for a perturbation field $(\Psi_{\ell m}(t, r_*))$

$$\left(\frac{\partial^2}{\partial r_*^2} - \frac{\partial^2}{\partial t^2} - V_{\ell m}(r_*)\right) \Psi_{\ell m}(r_*, t) = S_{\ell m}(r_*, t)\,. \tag{2.123}$$

The late–time behavior of the Green function $(G(r_*, t|r'_*, t'))$ associated with Eq. (2.123) can be studied through its Fourier representation. The time–domain Green function is obtained from the inverse Fourier transform

$$G(r_*, t|r'_*, t') = \lim_{\epsilon\to 0} \frac{1}{2\pi} \int_{-\infty+i\epsilon}^{+\infty+i\epsilon} d\omega\, e^{i\omega(t'-t)}\, g(r_*, r'_*, \omega), \tag{2.124}$$

where the contour shift ($i\epsilon$) ensures that the $\omega = 0$ mode does not contribute. The frequency–domain Green function is in turn defined through

$$g(r_*, r'_*, \omega) = \int_{t'}^{\infty} dt\, e^{-i\omega(t'-t)}\, G(r_*, t | r'_*, t'). \tag{2.125}$$

It can be shown that for a BH, Eq. (2.124) takes the form [50]

$$G_B^{\rm BH}(r_*, t\,|\,r'_*, t') = \frac{1}{2\pi}\int_0^{-i\infty} d\omega\, e^{-i\omega(t-t')}\, K(\omega)\, \left[\frac{\psi_{r_-}(r_<,\omega)\,\psi_{r_-}(r_>,\omega)}{2i\omega A_{\rm in}(\omega)\left(A_{\rm in}(\omega) + K(\omega)A_{\rm out}(\omega)\right)}\right], \tag{2.126}$$

where $r_< = \min(r_*, r'_*)$ and $r_> = \max(r_*, r'_*)$. On the other hand, the function $K(\omega)$ is given by $K(\omega) = -4\pi M\,\omega\,(-1)^\ell$. Starting from the homogeneous sector of Eq. (2.123), one can recast it in terms of the radial coordinate (r) for a static, spherically symmetric vacuum background described by the line element

$$\mathrm{d}s^2 = -f(r)\,\mathrm{d}t^2 + \frac{\mathrm{d}r^2}{f(r)} + r^2\mathrm{d}\Omega^2, \tag{2.127}$$

to obtain

$$\left(f^2\frac{\mathrm{d}^2}{\mathrm{d}r^2} + ff'\frac{\mathrm{d}}{\mathrm{d}r} + \omega^2 - V_{\ell m}(r)\right)\Psi_{\ell m} = 0, \tag{2.128}$$

where the effective potential is parametrized as

$$V_{\ell m}(r) = f(r)\left(\frac{\ell(\ell+1)}{r^2} + \frac{AM^{\alpha-2}}{r^\alpha} + \frac{BM^{\beta-2}}{r^\beta}\right), \tag{2.129}$$

with A, α, B, β dimensionless constants. This parametrization is flexible enough to reproduce several physically relevant cases. For instance, in the Schwarzschild geometry,

$$f(r) = 1 - \frac{2M}{r}, \qquad A = 2\Big(1 - s^2\Big), \qquad B = 0, \qquad \alpha = 3, \tag{2.130}$$

which for a spin-s perturbation reduces to the standard form of the RW potential (for $s = 2$ this corresponds to the odd-parity sector).

2.4.2 Evaluation of the Green's function

In order to evaluate the Green function (2.126) in the low–frequency regime, one needs the behavior of the coefficients $A_{\rm in}(\omega)$ and $A_{\rm out}(\omega)$. These are determined by solving the matching relations between the independent solutions at the horizon and at spatial infinity,

$$\begin{cases} \psi_{r_-} = A_{\rm in}\psi_{\infty-} + A_{\rm out}\psi_{\infty+}, \\ \partial_r\psi_{r_-} = A_{\rm in}\partial_r\psi_{\infty-} + A_{\rm out}\partial_r\psi_{\infty+}, \end{cases} \tag{2.131}$$

which is valid for any value of r. Taking the limit $\omega \to 0$, one finds that the coefficients scale as

$$\lim_{\omega\to0} A_{\rm out}(\omega) \sim -(-1)^\ell \lim_{\omega\to0} A_{\rm in}(\omega), \tag{2.132}$$

$$\lim_{\omega\to0} 2i\omega A_{\rm in}(\omega) \sim -(2\ell+1)!!\,(i)^\ell\,\omega^{-\ell}. \tag{2.133}$$

Substituting these relations into the Green function (2.126) and considering the case $r_* > r'_*$, the expression reduces in the small–frequency limit to

$$G_B^{\rm BH}(r_*, t\,|\,r'_*, t') \sim 2iM \int_0^{-i\infty} d\omega\, \frac{f(r)}{f(r')}\, \frac{e^{-2iM\omega}}{F_\ell(0,\omega r) F_\ell(0,\omega r')}\, e^{-i\omega(t-t')}. \tag{2.134}$$

Introducing the retarded times

$$t_r = t + 2M \log f(r), \qquad t'_r = t' - 2M \log f(r'), \tag{2.135}$$

Eq. (2.134) can be cast as

$$G_B^{\rm BH}(r_*, t\,|\,r'_*, t') \sim 2iM \int_0^{-i\infty} d\omega\, F_\ell(0,\omega r) F_\ell(0,\omega r')\, e^{-i\omega(t_r - t'_r)}. \tag{2.136}$$

Depending on the asymptotic regime, two distinct behaviors emerge:

- **Spatial infinity** ($\mathscr{I}^+$): The Coulomb functions scale as

$$F_\ell(0,\omega r') \sim \frac{(\omega r')^{\ell+1}}{(2\ell+1)!}, \qquad F_\ell(0,\omega r) \sim \sin\!\left(\omega r - \frac{\ell\pi}{2}\right), \tag{2.137}$$

  so that integrating by parts one obtains the power–law behavior

$$G_{\mathscr{I}^+}^{\rm BH}(r_*, t\,|\,r'_*, t') \sim M A_\ell\, \frac{(r')^{\ell+1}}{(t_r - t'_r - r_*)^{\ell+2}}, \qquad \text{with} \qquad A_\ell = (-1)^{\ell+1}\, \frac{(2\ell+1)!}{(2\ell+1)!!}. \tag{2.138}$$

- **Timelike infinity** (i^+): In this regime one finds

$$F_\ell(0,\omega r) \sim \frac{(\omega r)^{\ell+1}}{(2\ell+1)!}, \tag{2.139}$$

  which leads to

$$G_{i^+}^{\rm BH}(r_*, t\,|\,r'_*, t') \sim M B_\ell\, \frac{(r r')^{\ell+1}}{(t_r - t'_r)^{2\ell+3}}, \qquad \text{with} \qquad B_\ell = (-1)^{\ell+1}\, \frac{(2\ell+2)!}{(2\ell+1)!!}. \tag{2.140}$$

Equations (2.138) and (2.140) show that, at late times, the Green function decays as a power law $\sim t^{-(2\ell+3)}$. This reproduces the classical result originally obtained by Price [51] for massless perturbations around Schwarzschild BHs.

2.5 Overtones

After the merger, the GW signal can be expressed as a superposition of QNMs. Traditionally, it was assumed that the *fundamental mode* ($n = 0$) dominates the dynamics shortly after the peak of the waveform. However, recent studies have shown that the *overtones* ($n \geq 1$), although more heavily damped, play a crucial role in accurately describing the ringdown at earlier times. Despite their short lifetime, overtones play a crucial role in the early stages of the ringdown. NR simulations have demonstrated that the signal immediately after the peak of the strain can be modeled with high accuracy if several overtones are included in Eq. (2.95). For the dominant $(\ell, m) = (2, 2)$ mode,

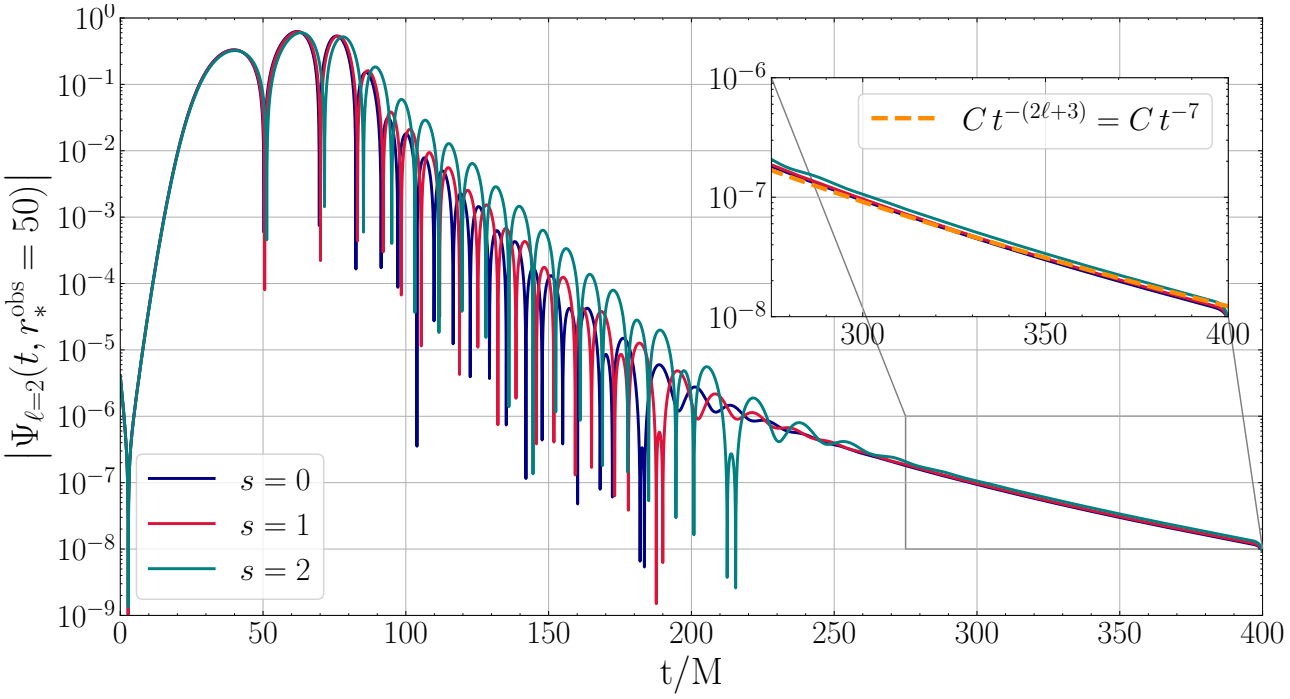


Figure 2.7: **Late–time decay of Schwarzschild perturbations.** Evolution of scalar ($s = 0$), vector ($s = 1$), and tensor ($s = 2$) fields with $\ell = 2$ in Schwarzschild spacetime. The numerical results (solid lines) follow the predicted power–law decay $\sim t^{-(2\ell+3)}$ at late times (dashed orange line).

fits with up to $n_{\rm max} = 7$ overtones reproduce the waveform from $t = 0$ onwards, providing unbiased estimates of the final BH's mass and spin [52]. Subsequent works extended this approach to larger values of $n_{\rm max}$ and to different binary configurations, confirming the robustness of the result [53].

A quantitative measure of the agreement between analytical models and NR waveforms is the mismatch, defined as

$$\mathcal{M} = 1 - \frac{\left\langle \gamma_{22} \,\middle|\, \bar{\gamma}_{22}\left(\vec{\lambda}^{\rm bf}\right)\right\rangle}{\sqrt{\left\langle \gamma_{22} \,\middle|\, \gamma_{22}\right\rangle \left\langle \bar{\gamma}_{22}\left(\vec{\lambda}^{\rm bf}\right) \,\middle|\, \bar{\gamma}_{22}\left(\vec{\lambda}^{\rm bf}\right)\right\rangle}}\,, \tag{2.141}$$

with the inner product defined by

$$\langle f|g\rangle = \int_{t_0}^{t_f} f(t)\, g(t)^*\, dt\,. \tag{2.142}$$

Here γ_{22} denotes the NR waveform and $\bar{\gamma}_{22}\left(\vec{\lambda}^{\rm bf}\right)$ the best–fit model with parameters $\vec{\lambda}^{\rm bf}$. By construction, $\mathcal{M} = 0$ indicates a perfect match. Figure 2.8 illustrates this behavior for GW150914. Increasing the number of overtones systematically reduces the mismatch and pushes the onset of the ringdown description closer to the peak of the waveform.

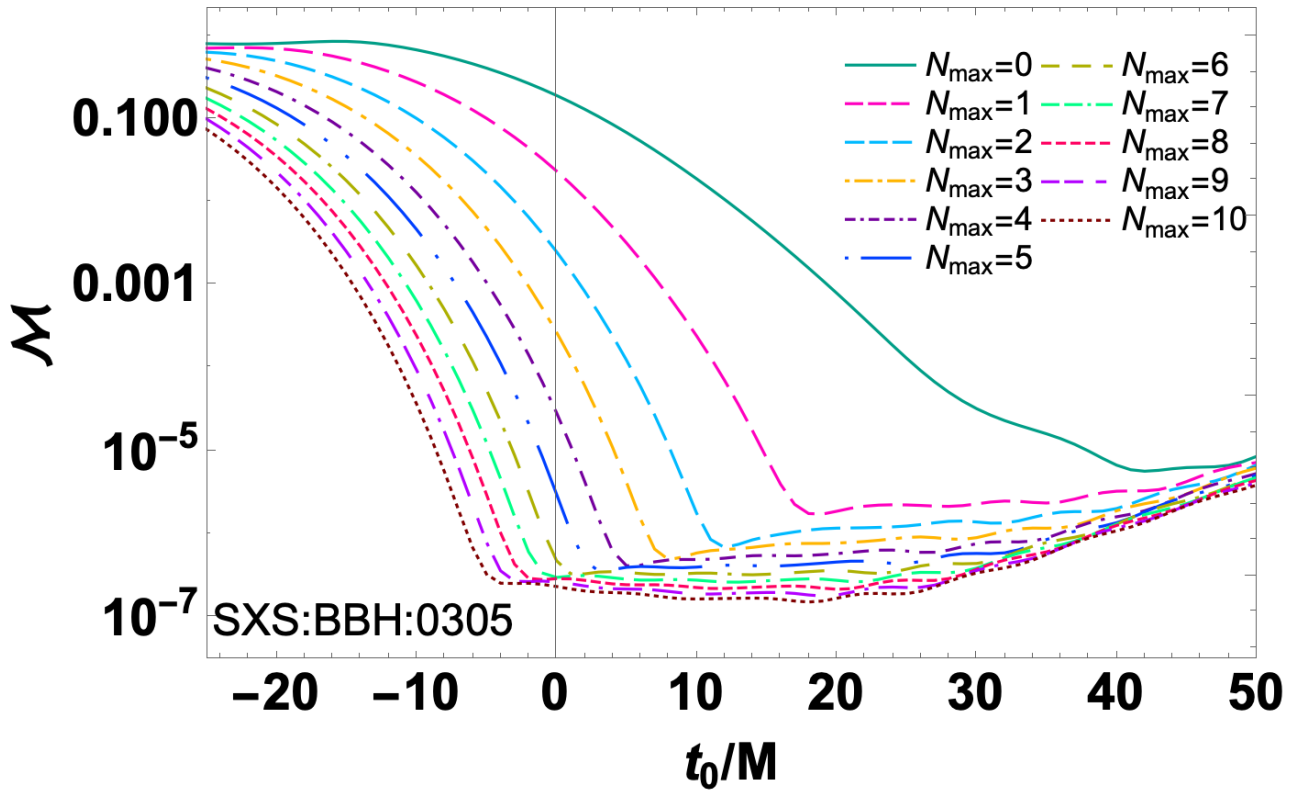
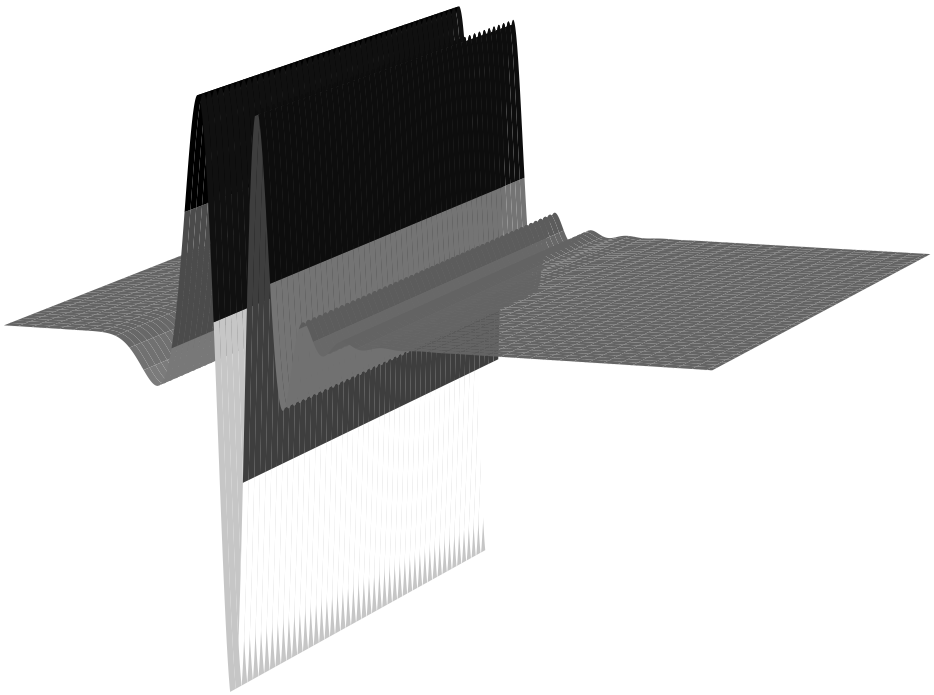


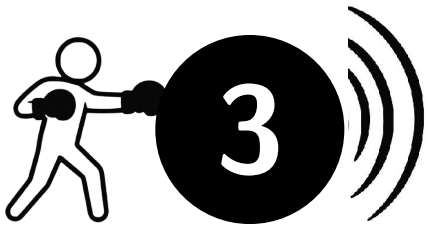
Figure 2.8: **Mismatch of ringdown models.** Best–fit mismatch $\mathcal{M}$ from Eq. (2.141) as a function of the fit starting time t_0/M, for models with up to $n_{\max} \in \{0, \ldots, 10\}$ overtones. Increasing the number of tones progressively reduces the mismatch. For each $n_{\max}$ a local minimum of $\mathcal{M}$ shifts to earlier t_0/M as $n_{\max}$ grows [53].

Part II

Numerical framework



Chapter



Regge–Wheeler code

Contents

3.1 1+1 wave equation **48**

3.2 Coordinate conversion and numerical grid **48**

3.3 Initial data **49**

3.4 Time evolution scheme **50**

3.5 Evaluation of the potential **50**

3.6 Sponge layers **51**

3.7 Boundary conditions **52**

3.8 Waveform extraction **52**

3.9 Radial convergence test **54**

In this chapter we present the numerical framework employed to evolve linear perturbations of the Schwarzschild geometry within the context of BHPT. Our implementation, written in Python, is based on the 1+1 wave equation in tortoise coordinates and combines finite–difference operators in space with a Runge–Kutta (RK) integrator in time. The main objective is to reproduce the characteristic response of a BH when perturbed: an intermediate regime dominated by damped oscillations, followed by the late–time decay known as the power–law tail.

The structure of the chapter is as follows. We begin by introducing the wave equation in tortoise coordinates and the associated effective potential. We then describe the numerical grid, the prescription of initial data, and the regularization of the potential near the boundaries. The time evolution algorithm, absorbing layers, and boundary conditions are discussed next. Finally, we collect the simulation parameters, explain the procedure for waveform extraction, and illustrate typical outputs of the code.

3.1 1+1 wave equation

The numerical evolution is carried out in terms of the tortoise coordinate r_*, which was already introduced in the previous chapters. In these variables, the perturbation field $\Psi_\ell(t, r_*)$ satisfies once again the 1+1 dimensional wave equation

$$\left(\frac{\partial^2}{\partial r_*^2} - \frac{\partial^2}{\partial t^2} - V_{\rm RW}(r)\right)\Psi_\ell(r_*, t) = 0\,, \tag{3.1}$$

where $V_{\rm RW}(r)$ denotes the effective potential. In the case of axial (odd–parity) gravitational perturbations, governed by the RW equation, the potential takes the explicit form

$$V_{\rm RW}(r) = \left(1 - \frac{2M}{r}\right)\left[\frac{\ell(\ell+1)}{r^2} - \frac{6M}{r^3}\right]. \tag{3.2}$$

3.2 Coordinate conversion and numerical grid

The time evolution is performed in the tortoise coordinate r_*, whereas the Regge–Wheeler potential $V_{\rm RW}(r)$ is naturally expressed in terms of the areal radius r. Since the relation $r_*(r)$ has no closed analytic inverse, we compute $r(r_*)$ numerically at each grid point using standard root–finding methods (e.g. Brent's algorithm [54]). Close to the horizon ($r \to 2M$), where numerical inversion becomes ill–conditioned, we replace the procedure with a local series expansion to preserve accuracy.

The computational domain is discretized uniformly in r_* as

$$r_* \in \left[r_*^{\rm min},\, r_*^{\rm max}\right], \qquad r_{*,j} = r_*^{\rm min} + j\,\Delta r_*, \quad j = 0, \ldots, N-1, \tag{3.3}$$

with spacing

$$\Delta r_* = \frac{r_*^{\rm max} - r_*^{\rm min}}{N-1}. \tag{3.4}$$

In all simulations we adopt the parameters

$$M = 1, \qquad r_*^{\rm min} = -200, \qquad r_*^{\rm max} = 1000, \qquad N = 5000. \tag{3.5}$$

Spatial derivatives are approximated with second–order finite differences, in particular the standard three–point stencil for the Laplacian,

$$\left(\Delta_2\Psi\right)_j = \frac{\Psi_{j+1} - 2\Psi_j + \Psi_{j-1}}{\left(\Delta r_*\right)^2}, \tag{3.6}$$

and the potential $V(r_*)$ is tabulated at the same grid nodes.

The time step is constrained by the Courant–Friedrichs–Levy (CFL) condition,

$$\Delta t \le C\,\Delta r_*. \tag{3.7}$$

Throughout, we set

$$\Delta t = 0.1\,\Delta r_*, \qquad t_{\rm final} = 400, \qquad N_{\rm steps} = t_{\rm final}/\Delta t, \tag{3.8}$$

which ensures stability with a comfortable safety margin.

3.3 Initial data

To trigger the BH ringdown we prescribe localized Gaussian pulses as initial data on the $t = 0$ slice. The simplest choice is a pure Gaussian pulse,

$$\Psi(0, r_*) = A \exp\left[- \frac{(r_* - r_*^0)^2}{2\sigma^2} \right], \qquad \partial_t \Psi(0, r_*) \simeq \partial_{r_*} \Psi(0, r_*), \tag{3.9}$$

where A is the amplitude, r_*^0 its central location, and σ the width of the packet. The condition on $\partial_t \Psi$ enforces an ingoing character, ensuring that the pulse efficiently excites the BH ringing. In the numerical implementation, this derivative is obtained through a smoothed finite–difference operator, which suppresses grid–scale noise.

In addition, we employ a modulated Gaussian of the form

$$\Psi(0, r_*) = A \exp\left[- \frac{(r_* - r_*^0)^2}{2\sigma^2} \right] \cos\left[\omega_0 (r_* - r_*^0)\right], \tag{3.10}$$

with carrier frequency ω_0. This initial data is more selective, allowing us to probe the response of the system around specific frequencies, and is therefore particularly useful to highlight the excitation of certain QNMs. As before, the time derivative at $t = 0$ is obtained with the same smoothed differentiation procedure.

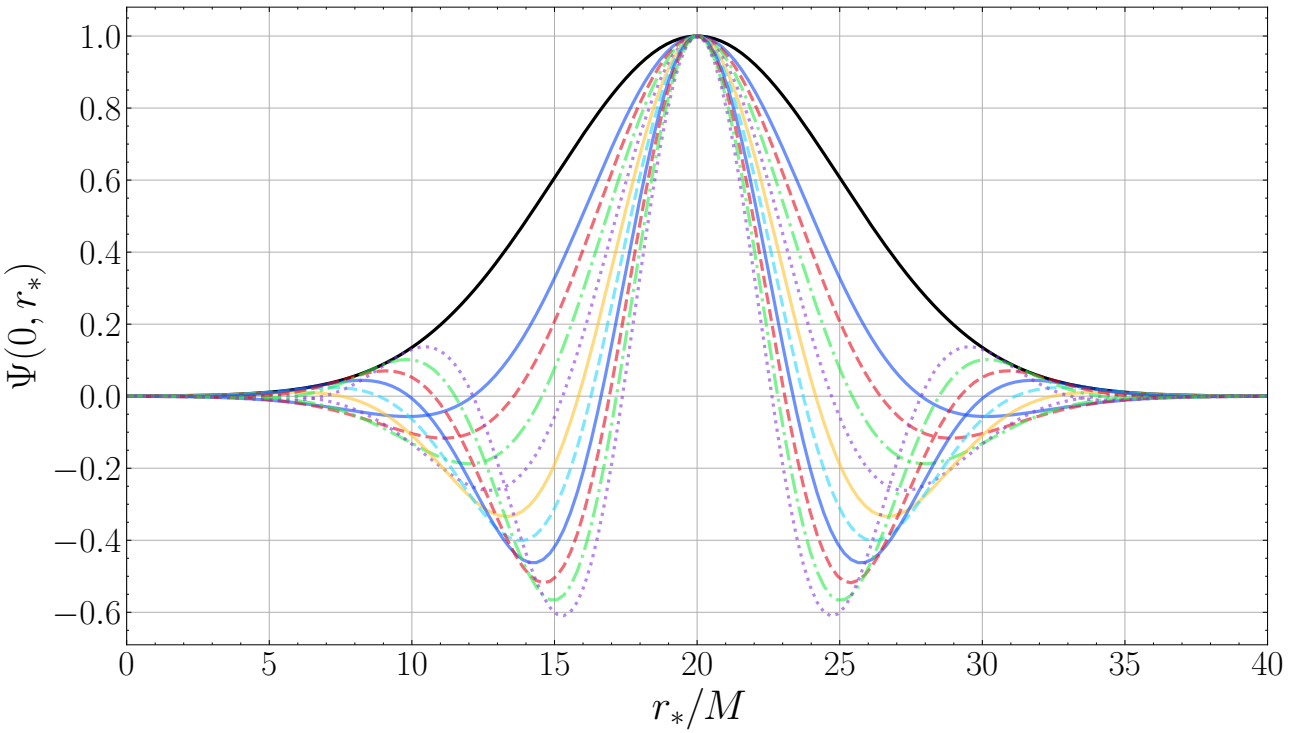


Figure 3.1: **Initial data profiles at $t = 0$.** The black curve shows a pure Gaussian pulse centered at $r_*^0 = 20$ with width $\sigma = 5$, while the colored curves correspond to Gaussian pulses modulated with different values of the carrier frequency ω_0. The pure Gaussian excites a broad frequency spectrum, whereas the modulated pulses localize the excitation around ω_0, providing a more selective probing of the QNMs.

3.4 Time evolution scheme

The perturbation field is evolved directly in tortoise coordinates r_*. Starting from the wave equation (3.1), it is convenient to introduce the auxiliary variables

$$\Psi(t, r_*), \qquad \Pi(t, r_*) := \frac{\partial \Psi(t, r_*)}{\partial t}, \tag{3.11}$$

so that the system becomes first order in time,

$$\frac{\partial \Psi}{\partial t} = \Pi, \qquad \frac{\partial \Pi}{\partial t} = \frac{\partial^2 \Psi}{\partial r_*^2} - V(r_*)\,\Psi. \tag{3.12}$$

The evolution of system (3.12) is carried out with the classical fourth–order Runge–Kutta (RK4) method. Defining $\mathbf{U} = [\Psi, \Pi]^T$, the right–hand side can be written compactly as

$$\mathbf{F}(\Psi, \Pi) = \begin{bmatrix} \Pi \\ \Delta_2 \Psi - V \odot \Psi \end{bmatrix}, \tag{3.13}$$

where Δ_2 is the discrete Laplacian operator, implemented by the standard second–order finite difference stencil

$$\left(\Delta_2 \Psi\right)_j = \frac{\Psi_{j+1} - 2\Psi_j + \Psi_{j-1}}{\left(\Delta r_*\right)^2}, \tag{3.14}$$

as in Eq. (3.6).

The intermediate RK4 stages are

$$\mathbf{k}_1 = \mathbf{F}\left(\Psi^n, \Pi^n\right), \tag{3.15a}$$

$$\mathbf{k}_2 = \mathbf{F}\left(\Psi^n + \frac{\Delta t}{2} k_{1,\Psi},\ \Pi^n + \frac{\Delta t}{2} k_{1,\Pi}\right), \tag{3.15b}$$

$$\mathbf{k}_3 = \mathbf{F}\left(\Psi^n + \frac{\Delta t}{2} k_{2,\Psi},\ \Pi^n + \frac{\Delta t}{2} k_{2,\Pi}\right), \tag{3.15c}$$

$$\mathbf{k}_4 = \mathbf{F}\left(\Psi^n + \Delta t\, k_{3,\Psi},\ \Pi^n + \Delta t\, k_{3,\Pi}\right), \tag{3.15d}$$

and the update reads

$$\begin{bmatrix} \Psi^{n+1} \\ \Pi^{n+1} \end{bmatrix} = \begin{bmatrix} \Psi^n \\ \Pi^n \end{bmatrix} + \frac{\Delta t}{6}\left(\mathbf{k}_1 + 2\mathbf{k}_2 + 2\mathbf{k}_3 + \mathbf{k}_4\right). \tag{3.16}$$

This algorithm provides fourth–order accuracy in time and second–order accuracy in space.

3.5 Evaluation of the potential

To evaluate the effective potential on the tortoise grid, we first invert numerically the relation $r_*(r)$ using Brent's root–finding method, which provides the mapping $r(r_*)$. The Regge–Wheeler potential $V_{\mathrm{RW}}(r)$ can then be tabulated at the grid points r_*. In order to regularize the edges of the computational domain, we introduce smooth window functions that suppress spurious boundary effects,

$$W(r) = w_L(r)\, w_R(r), \tag{3.17}$$

with

$$w_L(r) = \begin{cases} 0, & r \le r_{\min}, \\ \sin^2\!\left(\dfrac{\pi}{2}\,\dfrac{r - r_{\min}}{r_{\mathrm{ramp}} - r_{\min}}\right), & r_{\min} < r < r_{\mathrm{ramp}}, \\ 1, & r \ge r_{\mathrm{ramp}}, \end{cases} \tag{3.18a}$$

$$w_R(r) = \begin{cases} 1, & r \le r_{\mathrm{start}}, \\ \cos^2\!\left(\dfrac{\pi}{2}\,\dfrac{r - r_{\mathrm{start}}}{r_{\mathrm{cut}} - r_{\mathrm{start}}}\right), & r_{\mathrm{start}} < r < r_{\mathrm{cut}}, \\ 0, & r \ge r_{\mathrm{cut}}. \end{cases} \tag{3.18b}$$

The left window $(w_L(r))$ suppresses numerical artefacts in the near–horizon region, while the right window $(w_R(r))$ smoothly truncates the potential at large radii, thus preventing spurious reflections at the numerical boundaries. In the simulations we adopt the parameters

$$r_{\min} = 2.01M, \quad r_{\mathrm{ramp}} = 2.2M, \quad r_{\mathrm{start}} = 500M, \quad r_{\mathrm{cut}} = 1000M. \tag{3.19}$$

The numerical potential is therefore defined as

$$V_{\mathrm{num}}(r_*) = W\big(r(r_*)\big)\, V_{\mathrm{RW}}\big(r(r_*)\big), \tag{3.20}$$

which coincides with the physical potential in the bulk of the domain and vanishes smoothly at the boundaries.

3.6 Sponge layers

In addition to the boundary conditions, we implement sponge layers to suppress residual reflections at the edges of the grid. These layers act over $N_{\mathrm{damp}} = 100$ points on each side of the domain, with a quadratic profile that increases smoothly from zero to a maximum damping coefficient $\gamma_{\max} = 0.02$. The damping strength is prescribed as

$$\gamma_j = \begin{cases} \gamma_{\max}\left(\dfrac{j}{N_{\mathrm{damp}}}\right)^2, & j = 0, \dots, N_{\mathrm{damp}} - 1, \\ 0, & j = N_{\mathrm{damp}}, \dots, N{-}1{-}N_{\mathrm{damp}}, \\ \gamma_{\max}\left(\dfrac{N{-}1{-}j}{N_{\mathrm{damp}}}\right)^2, & j = N{-}N_{\mathrm{damp}}, \dots, N{-}1. \end{cases} \tag{3.21}$$

After each RK step, the fields are multiplied by a damping factor that gradually attenuates outgoing waves as they cross the sponge region,

$$\Psi_j^{n+1} \;\to\; e^{-\gamma_j \Delta t}\, \Psi_j^{n+1}, \qquad \Pi_j^{n+1} \;\to\; e^{-\gamma_j \Delta t}\, \Pi_j^{n+1}. \tag{3.22}$$

This mechanism absorbs the wave before it reaches the boundary, preventing spurious reflections from reentering the computational domain.

3.7 Boundary conditions

To complement the sponge layers, we impose simple radiative boundary conditions that enforce the correct physical behavior at the edges of the domain. On the horizon side ($r_* \to -\infty$), only ingoing waves should be present. This condition is imposed in discrete form as

$$\frac{\partial \Psi}{\partial t} + \frac{\partial \Psi}{\partial r_*} = 0 \quad \Rightarrow \quad \Psi_0^{n+1} \approx \left(1 - \frac{\Delta t}{\Delta r_*}\right) \Psi_1^{n+1}. \tag{3.23}$$

At the opposite edge ($r_* \to +\infty$), the physically relevant solution corresponds to purely outgoing waves, implemented as

$$\frac{\partial \Psi}{\partial t} - \frac{\partial \Psi}{\partial r_*} = 0 \quad \Rightarrow \quad \Psi_{N-1}^{n+1} \approx \left(1 + \frac{\Delta t}{\Delta r_*}\right) \Psi_{N-2}^{n+1}. \tag{3.24}$$

These conditions are only first–order accurate, but in practice they work effectively when combined with the sponge layers, preventing spurious reflections from contaminating the waveform inside the computational domain.

3.8 Waveform extraction

The waveform is monitored at a fixed observer position $r_*^{\rm obs}$, by selecting the nearest grid index $j_{\rm obs}$ and recording

$$\Psi_{\rm obs}(t^n) = \Psi^n_{j_{\rm obs}}, \qquad n = 0, 1, \ldots, N_{\rm steps}. \tag{3.25}$$

Plots of $|\Psi_{\rm obs}(t)|$ in both linear and logarithmic scales provide complementary views of the dynamics: the linear representation highlights the early oscillatory behavior, while the logarithmic one reveals more clearly the three stages of the evolution—initial transient, QNM ringdown, and the late–time power–law tail.

In practice, these three phases can be distinguished as follows. The *prompt response* corresponds to the early–time burst generated directly by the initial data and by the scattering of the wave packet on the potential barrier, dominating the signal until its maximum amplitude is reached. The subsequent *QNM ringing* is characterized by exponentially damped oscillations with well–defined frequency and decay rate, representing the intrinsic oscillatory response of the BH spacetime. Finally, at sufficiently late times, the waveform enters the *power–law tail*, a slow algebraic decay arising from the backscattering of radiation off the asymptotic curvature of spacetime. These stages appear sequentially and can be cleanly separated in the logarithmic plot, where the exponential decay of the QNMs and the eventual power–law regime become particularly evident.

Beyond this general phenomenology, the detailed evolution of the waveform can be interpreted in terms of the propagation of the initial Gaussian pulse across the Schwarzschild geometry. The chosen initial data correspond to an ingoing Gaussian wave packet centered at $r_*^0 = 25$, which travels leftward (decreasing r_*) towards the BH. The effective potential for the $\ell = 2$ RW perturbation peaks near the photon sphere, located at $r = 3M$, corresponding to $r_* \approx 1.6$. This barrier plays a central role in shaping the signal observed at large distances.

As the ingoing pulse reaches the potential peak, part of its energy is transmitted through the barrier and falls irreversibly into the horizon, while another fraction is reflected back and propagates outward

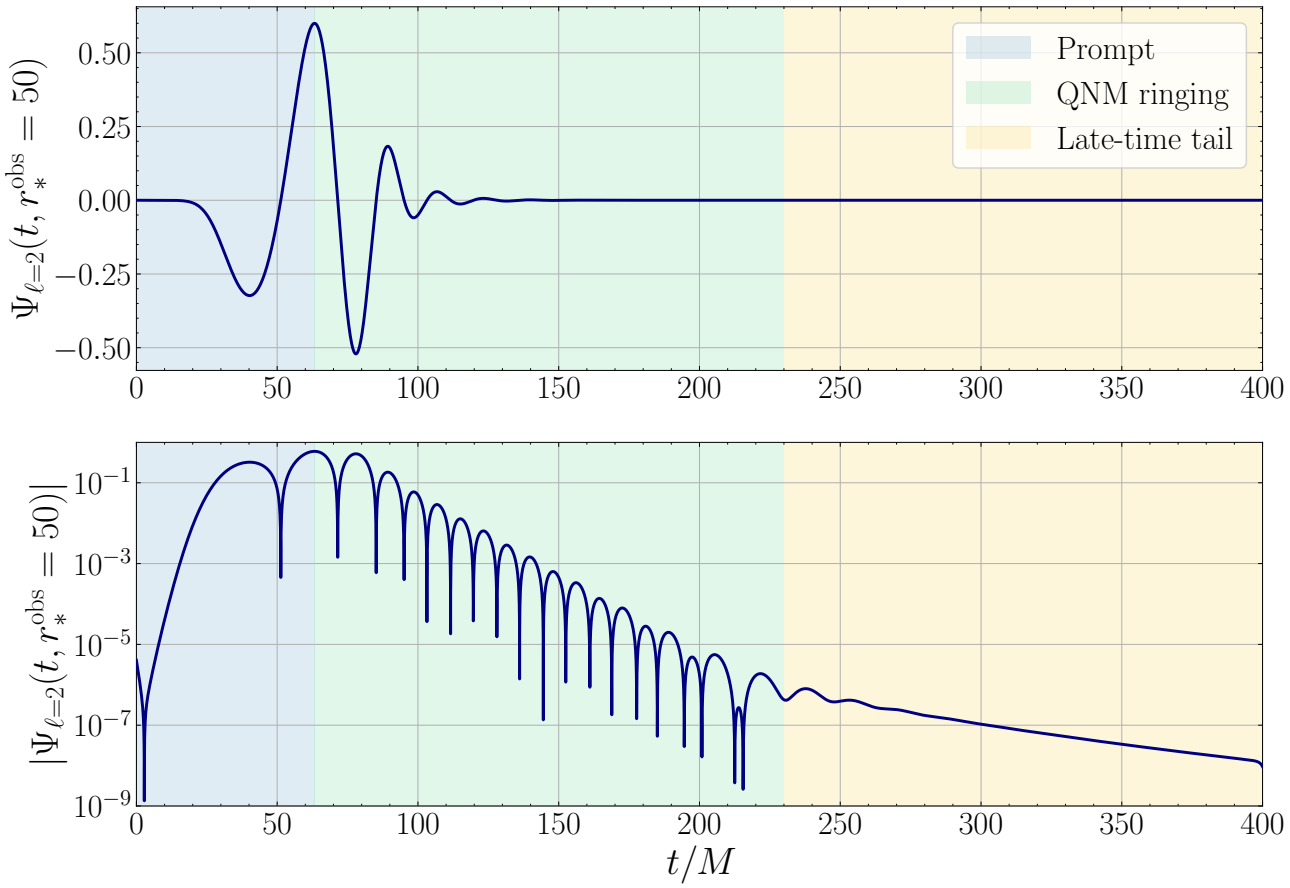


Figure 3.2: **Waveform extracted at $r_*^{\rm obs} = 50$ for $\ell = 2$.** The upper panel shows $\Psi(t, r_*^{\rm obs})$ on a linear scale, emphasizing the oscillatory character of the signal, while the lower panel displays the same data on a logarithmic scale, making evident the three characteristic phases: initial transient, QNM ringdown, and late–time power–law tail. The simulation uses the tensorial RW potential with domain $r_* \in [-200, 1000]$, $N = 5000$, $\Delta t = 0.1\,\Delta r_*$, $t_{\rm final} = 400$, Gaussian initial data $(A, r_*^0, \sigma) = (1, 25, 5)$, and sponge layers at both boundaries.

to the wave zone ($r_* \gg 1$). The prompt response observed at $r_*^{\rm obs} = 50$ corresponds precisely to this reflected component: it arrives after a delay consistent with the two–way travel time between the initial packet position, the potential barrier, and the observer. In the present setup, the dominant prompt burst reaches $r_*^{\rm obs}$ around $t \sim 70M$, in good agreement with the geometrical propagation estimate

$$t_{\rm arrival} \;\approx\; \left(r_*^0 - r_*^{\rm peak}\right) + \left(r_*^{\rm obs} - r_*^{\rm peak}\right) = \left(25 - 1.6\right) + \left(50 - 1.6\right) \;\approx\; 71.8M. \tag{3.26}$$

Once the prompt burst has passed, the waveform is dominated by the intrinsic oscillatory response of the barrier region. The cavity around the photon sphere acts as a resonant system that temporarily traps perturbations. The ensuing radiation is characterized by exponentially damped oscillations at the discrete complex frequencies of the QNMs. For the fundamental quadrupolar mode of a Schwarzschild BH, we saw earlier that the frequency and damping time are

$$M\omega_{200} \approx 0.37367 - 0.08896\,i, \qquad T \approx \frac{2\pi}{\omega_R} \simeq 16.81M, \qquad \tau \approx \frac{1}{|\omega_I|} \simeq 11.24M, \tag{3.27}$$

which are clearly visible in the oscillatory segment of the signal. The logarithmic representation in Fig. 3.2 highlights this stage as a straight segment, reflecting the exponential decay ($\sim e^{-t/\tau}$).

At much later times, the exponential ringing is superseded by a slower algebraic decay. This regime corresponds to the so–called Price tail, arising from the backscattering of radiation off the weak curvature at large radii. For gravitational perturbations with $\ell = 2$, the expected asymptotic behavior is $|\Psi(t, r_*^{\rm obs})| \propto t^{-7}$. This tail manifests in the logarithmic plot as a gradual departure from exponential decay, transitioning into a power–law falloff. The emergence of such tails reflects the fact that, unlike in flat space, perturbations in curved spacetimes never disperse completely but leave a long–lived imprint.

Altogether, the waveform extracted at a fixed observer position provides a faithful picture of the threefold dynamics of BH perturbations: (i) the prompt response due to direct scattering of the initial data, (ii) the QNM ringing representing the characteristic "voice" of the BH, and (iii) the power–law tail imprinted by the asymptotic curvature. These features are universal and appear in any sufficiently generic perturbation, establishing the ringdown as one of the most robust observational signatures of BH spacetimes.

3.9 Radial convergence test

In order to assess the reliability of the numerical scheme employed in the evolution of the RW equation, we performed a systematic convergence test focused on the radial discretization of the problem. The strategy consists in evolving the same initial data on a sequence of grids of increasing resolution and comparing the resulting waveforms at a fixed extraction radius. If the numerical method is consistent, the differences between successive resolutions should follow a predictable scaling law that reflects the formal order of convergence of the scheme.

The initial data is chosen to be a Gaussian wave packet centered at $r_0^* = 25M$ with a characteristic width of $\sigma = 5M$, and it is evolved on three grids covering the interval $r^* \in [-200M, 1000M]$. The three resolutions considered are: a coarse grid with $N = 2500$ points, a medium grid with $N = 5000$ points, and a fine grid with $N = 10000$ points. In each case the waveform is extracted at the observation point $r^* = 50M$, and the time series obtained from the different runs are interpolated to a common temporal grid to allow for a direct comparison.

The analysis is based on the differences between successive resolutions,

$$\Delta_{mc}(t) = \Psi_{\rm medium}(t) - \Psi_{\rm coarse}(t), \qquad \Delta_{fm}(t) = \Psi_{\rm fine}(t) - \Psi_{\rm medium}(t), \tag{3.28}$$

which represent the truncation errors at medium and fine resolution respectively. If the scheme is convergent with order p, then these differences should satisfy the approximate relation

$$\Delta_{mc}(t) \;\approx\; \left(\frac{h_c}{h_m}\right)^p \Delta_{fm}(t), \tag{3.29}$$

where h_c and h_m are the grid spacings of the coarse and medium runs. Since in our setup each refinement step doubles the number of points, the ratio of grid spacings is $h_c/h_m = 2$, and thus the theoretical rescaling factor is 2^p. When applying this procedure to the data, we observe that the best overlap between the curves is not obtained by multiplying the difference $\Psi_{\rm fine} - \Psi_{\rm medium}$ by the factor 2^4, which would correspond to perfect fourth–order convergence, but rather by rescaling it with 1.3^4.

This adjustment suggests that the effective order of convergence of the scheme is closer to $p \simeq 1.5$. An independent estimate obtained from the L_2 norms of the differences,

$$p \approx \frac{\ln\Big(\|\Psi_{\rm medium} - \Psi_{\rm coarse}\| \,/\, \|\Psi_{\rm fine} - \Psi_{\rm medium}\|\Big)}{\ln(2)}, \tag{3.30}$$

yields values fluctuating around the same number. The reduction with respect to the ideal fourth–order behavior is not unexpected, since boundary treatments, smoothing near the horizon, or details in the implementation of the potential can all affect the effective convergence.

Figure 3.3 illustrates this analysis where the rescaled difference $1.3^4(\Psi_{\rm fine} - \Psi_{\rm medium})$ lies almost on top of $(\Psi_{\rm medium} - \Psi_{\rm coarse})$, both in linear and logarithmic scale, confirming that the effective order of convergence of the implementation is close to $p \approx 1.5$. Although lower than the nominal fourth–order accuracy of the scheme, this behavior provides strong evidence of the robustness and internal consistency of the code.

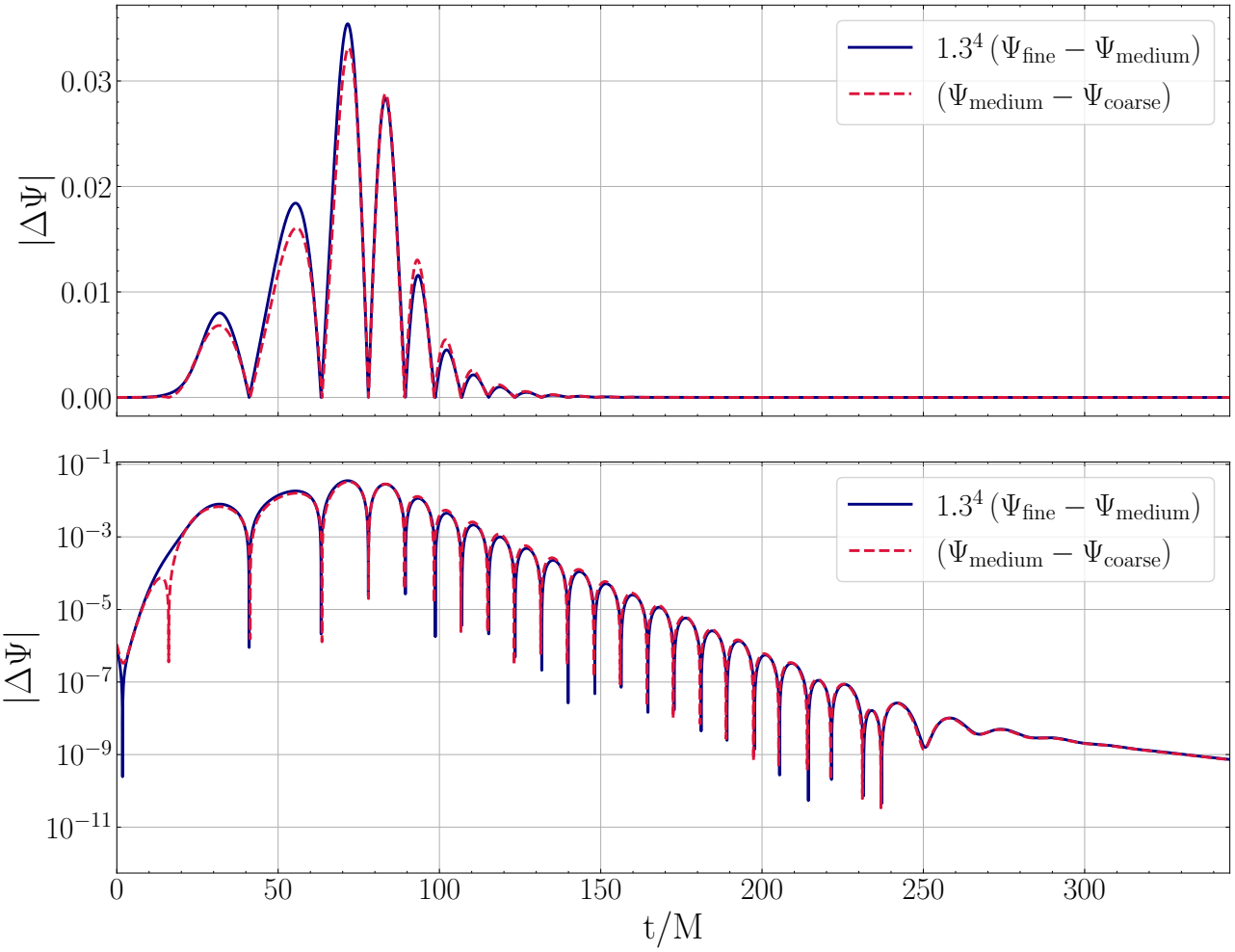
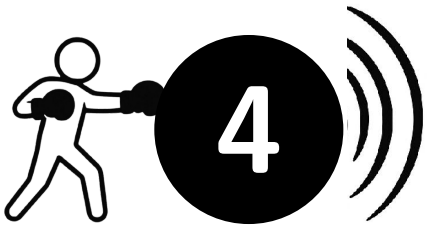


Figure 3.3: **Radial convergence test for the RW evolution at $r^* = 50M$. Top panel:** differences plotted in linear scale. **Bottom panel:** same data represented in logarithmic scale. The fact that the rescaled curve $1.3^4(\Psi_{\rm fine} - \Psi_{\rm medium})$ almost coincides with $(\Psi_{\rm medium} - \Psi_{\rm coarse})$ indicates an effective convergence order of about $p \approx 1.5$.

Chapter



Teukolsky code

Contents

4.1 Rewriting the Teukolsky equation **59**
4.2 Derivation of the 4th order algorithm **62**
4.3 Stability analysis **63**
4.4 Boundary conditions **64**
4.5 Implementation **66**
4.6 Initial data **67**
4.7 Convergence tests **68**

The starting point of our analysis is the Teukolsky master equation, derived in the previous chapters, which governs the evolution of fields of arbitrary spin on a Kerr background. In this chapter we revisit the numerical implementation of this equation, following the scheme presented in [55], which provides a systematic formulation in first–order form suitable for time evolutions. In BL coordinates it takes the form

$$\left\{\left[\frac{r^2+a^2}{\Delta_{BL}}-a^2\sin^2\theta\right]\frac{\partial^2}{\partial t^2}+\frac{4Mar}{\Delta_{BL}}\frac{\partial^2}{\partial t\partial\phi}-4\left[r+ia\cos\theta-\frac{M(r^2+a^2)}{\Delta_{BL}}\right]\frac{\partial}{\partial t}-\Delta_{BL}^{-s}\frac{\partial}{\partial r}\left(\Delta_{BL}^{s+1}\frac{\partial}{\partial r}\right)\right.$$
$$\left.-\frac{1}{\sin\theta}\frac{\partial}{\partial\theta}\left(\sin\theta\frac{\partial}{\partial\theta}\right)-\left(\frac{1}{\sin^2\theta}-\frac{a^2}{\Delta_{BL}}\right)\frac{\partial^2}{\partial\phi^2}+4\left[\frac{a(r-M)}{\Delta}+\frac{i\cos\theta}{\sin^2\theta}\right]\frac{\partial}{\partial\phi}+(4\cot^2\theta+2)\right\}\Psi_s=0 \tag{4.1}$$

For the study of gravitational perturbations one usually focuses on spin weight $s=-2$. This choice has a practical advantage: it ensures that solutions are regular both at the horizon ($r_*\to-\infty$) and at infinity ($r_*\to+\infty$), for ingoing and outgoing wave components. Their asymptotic behaviour can be summarised as

$$\lim_{r_*\to+\infty}|\Psi_s| \sim \begin{cases} 1/r^{2s+1}, & \text{outgoing}, \\ 1/r, & \text{ingoing}, \end{cases} \tag{4.2a}$$

$$\lim_{r_*\to-\infty}|\Psi_s| \sim \begin{cases} 1, & \text{outgoing}, \\ \Delta^{-s}, & \text{ingoing}. \end{cases} \tag{4.2b}$$

In order to simplify the time–domain formulation, it is advantageous to factor out the explicit azimuthal dependence together with a suitable radial weight. We therefore adopt the ansatz [34, 55, 56]

$$\Psi(t, r_*, \theta, \widetilde{\phi}) = \sum_m r^3\, e^{im\widetilde{\phi}}\, \Phi(t, r_*, \theta), \tag{4.3}$$

which removes the growth of the solution at infinity and isolates the dependence on the azimuthal number (m). Here, r_* is the Kerr tortoise coordinate, defined by

$$\frac{\mathrm{d}r_*}{\mathrm{d}r} = \frac{r^2+a^2}{\Delta_{BL}} \quad \Rightarrow \quad r_* = r + \frac{r_+^2+a^2}{r_+-r_-}\ln\left|\frac{r-r_+}{2M}\right| - \frac{r_-^2+a^2}{r_+-r_-}\ln\left|\frac{r-r_-}{2M}\right|, \tag{4.4}$$

with $r_\pm = M \pm \sqrt{M^2-a^2}$. Additionally, the use of a modified azimuthal coordinate ($\widetilde{\phi}$) improves the behaviour near the horizon by absorbing the frame dragging contribution:

$$\mathrm{d}\widetilde{\phi} = \mathrm{d}\phi + \frac{a}{\Delta_{BL}}\,\mathrm{d}r \quad \Rightarrow \quad \widetilde{\phi} = \phi + \frac{a}{r_+-r_-}\ln\left|\frac{r-r_+}{r-r_-}\right|. \tag{4.5}$$

To cast the Teukolsky equation into a first-order-in-time form, it is convenient to define an auxiliary field

$$\Pi \;\equiv\; \frac{\partial\Phi}{\partial t} \;+\; b\,\frac{\partial\Phi}{\partial r_*}, \tag{4.6}$$

with $b \equiv (r^2+a^2)/\Sigma_{BL}$ and $\Sigma_{BL}^2 \equiv (r^2+a^2)^2 - a^2\Delta_{BL}\sin^2(\theta)$. This construction allows one to rewrite the original second-order partial derivative equations as a first-order system coupling the fields Φ and Π. Introducing the real and imaginary parts, $\mathbf{u} \equiv (\Phi_R, \Phi_I, \Pi_R, \Pi_I)^T$, the evolution takes the generic form [55]

$$\frac{\partial\mathbf{u}}{\partial t} \;+\; \mathbf{M}\,\frac{\partial\mathbf{u}}{\partial r_*} \;+\; \mathbf{L}\,\mathbf{u} \;+\; \mathbf{A}\,\mathbf{u} \;=\; 0, \tag{4.7}$$

where the matrices $\mathbf{M}$, $\mathbf{L}$ and $\mathbf{A}$ represent the radial and angular couplings as well as source-like terms. Their explicit entries follow directly from the coefficients of the Teukolsky equation

$$\mathbf{M} \;=\; \begin{bmatrix} b & 0 & 0 & 0 \\ 0 & b & 0 & 0 \\ m_{31} & m_{32} & -b & 0 \\ -m_{32} & m_{31} & 0 & -b \end{bmatrix}, \quad \mathbf{A} \;=\; \begin{bmatrix} 0 & 0 & -1 & 0 \\ 0 & 0 & 0 & -1 \\ a_{31} & a_{32} & a_{33} & a_{34} \\ -a_{32} & a_{31} & -a_{34} & a_{33} \end{bmatrix}, \quad \mathbf{L} \;=\; \begin{bmatrix} 0 & 0 & 0 & 0 \\ 0 & 0 & 0 & 0 \\ l_{31} & 0 & 0 & 0 \\ 0 & l_{31} & 0 & 0 \end{bmatrix}. \tag{4.8}$$

For the purpose of time integration, the first–order system can be recast in an "advection + source" form, where the principal radial part is separated from the remaining terms [55]

$$\frac{\partial\mathbf{u}}{\partial t} \;+\; \mathbf{D}\,\frac{\partial\mathbf{u}}{\partial r_*} \;=\; \mathbf{S}, \tag{4.9}$$

where

$$\mathbf{D} = \mathrm{diag}(b,\, b,\, -b,\, -b), \qquad \mathbf{S} = -(\mathbf{M}-\mathbf{D})\,\frac{\partial\mathbf{u}}{\partial r_*} - \mathbf{L}\,\mathbf{u} - \mathbf{A}\,\mathbf{u}. \tag{4.10}$$

This decomposition isolates the leading-order transport along the radial direction, encoded in $\mathbf{D}$, while $\mathbf{S}$ collects angular couplings, source-like contributions and the residual radial terms. In this form the system can be advanced with finite-difference schemes designed for hyperbolic equations.

4.1 Rewriting the Teukolsky equation

4.1.1 Separating ϕ dependence

For fields with nonzero spin in the Kerr background ($s \neq 0$, $a \neq 0$), the Teukolsky equation remains separable in the azimuthal coordinate. It is convenient to work in the modified BL coordinates $(t, r_*, \theta, \widetilde{\phi})$. This choice improves the regularity of the fields near the horizon: as $r_* \to -\infty$, the inner boundary of the computational domain approaches the horizon from the outside, while the frame–dragging contribution is absorbed into the redefined angle $(\widetilde{\phi})$.

Substituting the ansatz (4.3) into the Teukolsky equation (4.1) and factoring out the global prefactor $r^3 e^{im\widetilde{\phi}}$, one obtains a reduced evolution equation for $\Phi(t, r_*, \theta)$ of the form [55]

$$
\begin{aligned}
&-\left[\frac{(r^2+a^2)^2}{\Delta_{BL}} - a^2\sin^2(\theta)\right]\frac{\partial^2\Phi}{\partial t^2} + \frac{2}{\Delta}\Big[Ms(r^2-a^2) - rs\Delta_{BL}\Big]\frac{\partial\Phi}{\partial t} - ia\Big(s\Delta_{BL}\cos(\theta) + 2Mmr\Big)\frac{\partial\Phi}{\partial t} \\
&+ \frac{(r^2+a^2)^2}{\Delta_{BL}}\frac{\partial^2\Phi}{\partial r_*^2} + \frac{1}{r\Delta}\Big[(8r^2+6a^2)\Delta_{BL} - 2rs(r^2+a^2)(M-r) + 2iamr(r^2+a^2)\Big]\frac{\partial\Phi}{\partial r_*} + \frac{\partial^2\Phi}{\partial\theta^2} \\
&+ \cot(\theta)\frac{\partial\Phi}{\partial\theta} + \frac{1}{r^2\Delta_{BL}}\Big\{6\Delta_{BL}^2 - r\Delta_{BL}\Big[6M(s+1) - r(7s+6)\Big] + r\Big(s\cot(\theta) + m\csc(\theta)\Big)^2 \\
&- 2iamr\Big[2rs(M-r) - 3\Delta_{BL}\Big]\Big\}\Phi = 0,
\end{aligned}
\tag{4.11}
$$

or equivalently

$$
\frac{\partial^2\Phi}{\partial t^2} + C_t\frac{\partial\Phi}{\partial t} + C_{r_*r_*}\frac{\partial^2\Phi}{\partial r_*^2} + C_{r_*}\frac{\partial\Phi}{\partial r_*} + C_{\theta\theta}\frac{\partial^2\Phi}{\partial\theta^2} + C_\theta\frac{\partial\Phi}{\partial\theta} + C_{\mathrm{SO}}\,\Phi \;=\; 0, \tag{4.12}
$$

where the coefficients C's depend on (r, θ), the spin weight, the rotation parameter, and the azimuthal index (m). Their explicit expressions are given by [55, 56]

$$
C_t = 2s\frac{M(a^2-r^2) + r\Delta_{BL}}{\Sigma_{BL}^2} + 2ia\frac{2mMr + s\Delta\cos(\theta)}{\Sigma_{BL}^2}, \tag{4.13a}
$$

$$
C_{r_*r_*} = -\frac{(r^2+a^2)^2}{\Sigma_{BL}^2}, \tag{4.13b}
$$

$$
C_{r_*} = \frac{2}{r\Sigma_{BL}^2}\Big[rs(M-r)(r^2+a^2) - (3a^2+4r^2)\Delta_{BL}\Big] - \frac{2iam(r^2+a^2)}{\Sigma_{BL}^2}, \tag{4.13c}
$$

$$
C_{\theta\theta} = -\frac{\Delta_{BL}}{\Sigma_{BL}^2}, \tag{4.13d}
$$

$$
C_\theta = -\frac{\Delta_{BL}}{\Sigma_{BL}^2}\cot(\theta), \tag{4.13e}
$$

$$
C_{\mathrm{SO}} = 2iam\frac{2rs(M-r) - 3\Delta_{BL}}{r\Sigma_{BL}^2} + \frac{\Delta_{BL}\Big[6Mr(s+1) - r^2(7s+6) - 6\Delta_{BL} + r^2\big(s\cot(\theta) + m\csc(\theta)\big)^2\Big]}{r^2\Sigma_{BL}^2}. \tag{4.13f}
$$

4.1.2 From second to first-order differential equations

When dealing with second–order differential equations, a common numerical strategy is to rewrite them as systems of first–order equations. This reformulation is advantageous because many stable and accurate integration methods are specifically designed for first–order form. As a simple example, consider the one–dimensional wave equation,

$$\frac{\partial^2 u}{\partial t^2} = v_p^2 \frac{\partial^2 u}{\partial x^2}, \tag{4.14}$$

where $u(t, x)$ denotes the wave field and v_p is the propagation velocity.

To eliminate the second derivatives, we introduce an auxiliary variable $v(t, x)$ and define the system in such a way that only first–order derivatives appear. One convenient choice is

$$\frac{\partial u}{\partial t} = v_p \frac{\partial v}{\partial x}, \tag{4.15a}$$

$$\frac{\partial v}{\partial t} = v_p \frac{\partial u}{\partial x}, \tag{4.15b}$$

which is equivalent to the original wave equation. The above pair of equations can be expressed in matrix form as

$$\frac{\partial}{\partial t}\begin{bmatrix} u \\ v \end{bmatrix} = \begin{bmatrix} 0 & v_p \\ v_p & 0 \end{bmatrix} \frac{\partial}{\partial x}\begin{bmatrix} u \\ v \end{bmatrix}. \tag{4.16}$$

Thus, the wave equation is recast as a system of advection–type equations for the vector

$$\mathbf{u}(t, x) \equiv \begin{bmatrix} u \\ v \end{bmatrix}, \qquad \frac{\partial \mathbf{u}}{\partial t} = \mathbf{V}_p \frac{\partial \mathbf{u}}{\partial x}. \tag{4.17}$$

For the Teukolsky equation the situation is more involved due to the presence of cross derivatives. Starting from Eq. (4.12), normalized so that the coefficient of $\partial_{tt}\Phi$ is unity, we seek an equivalent system of the form [55]

$$\frac{\partial}{\partial t}\begin{bmatrix} \Phi \\ \Pi \end{bmatrix} + \begin{bmatrix} \beta_{11} & \beta_{12} \\ \beta_{21} & \beta_{22} \end{bmatrix} \frac{\partial}{\partial r_*}\begin{bmatrix} \Phi \\ \Pi \end{bmatrix} + \begin{bmatrix} \gamma_{11} & \gamma_{12} \\ \gamma_{21} & \gamma_{22} \end{bmatrix} \begin{bmatrix} \Phi \\ \Pi \end{bmatrix} = 0. \tag{4.18}$$

with coefficients depending on (r, θ) but not on t. This expression is equivalent to

$$\frac{\partial \Phi}{\partial t} + \beta_{11} \frac{\partial \Phi}{\partial r_*} + \beta_{12} \frac{\partial \Pi}{\partial r_*} + \gamma_{11}\, \Phi + \gamma_{12}\, \Pi = 0, \tag{4.19a}$$

$$\frac{\partial \Pi}{\partial t} + \beta_{21} \frac{\partial \Phi}{\partial r_*} + \beta_{22} \frac{\partial \Pi}{\partial r_*} + \gamma_{21}\, \Phi + \gamma_{22}\, \Pi = 0. \tag{4.19b}$$

To simplify the structure we impose

$$\beta_{12} = 0, \qquad \gamma_{11} = 0, \qquad \gamma_{12} = -1, \tag{4.20}$$

and introduce the auxiliary field

$$\Pi := \frac{\partial \Phi}{\partial t} + \beta_{11} \frac{\partial \Phi}{\partial r_*}. \tag{4.21}$$

This definition eliminates second time derivatives in favour of first–order radial and temporal derivatives. Differentiating Eq. (4.21) yields

$$\frac{\partial \Pi}{\partial t} = \frac{\partial^2 \Phi}{\partial t^2} + \beta_{11}\,\frac{\partial^2 \Phi}{\partial t\,\partial r_*}, \tag{4.22a}$$

$$\frac{\partial \Pi}{\partial r_*} = \frac{\partial^2 \Phi}{\partial r_*\,\partial t} + \left(\frac{\partial \beta_{11}}{\partial r_*}\right)\frac{\partial \Phi}{\partial r_*} + \beta_{11}\,\frac{\partial^2 \Phi}{\partial r_*^2}. \tag{4.22b}$$

Substituting (4.21)–(4.22b) into Eq. (4.18) yields to

$$\frac{\partial^2 \Phi}{\partial t^2} - \gamma_{22}\,\frac{\partial \Phi}{\partial t} - (\beta_{11}+\beta_{22})\frac{\partial^2 \Phi}{\partial t\,\partial r_*} + \beta_{22}\beta_{11}\,\frac{\partial^2 \Phi}{\partial r_*^2} - \left(\beta_{21} - \beta_{22}\frac{\partial \beta_{11}}{\partial r_*} - \gamma_{22}\beta_{11}\right)\frac{\partial \Phi}{\partial r_*} - \gamma_{21}\,\Phi \;=\; 0. \tag{4.23}$$

If we compare term by term with Eq. (4.12) fixes the remaining coefficients. From the mixed term we obtain

$$\beta_{22} = -\beta_{11}, \qquad \beta_{11} = \sqrt{-C_{r_*r_*}} = \frac{r^2+a^2}{\Sigma_{BL}} \equiv b. \tag{4.24}$$

The final first–order system reads

$$\frac{\partial \Phi}{\partial t} = \Pi - b\,\frac{\partial \Phi}{\partial r_*}, \tag{4.25a}$$

$$\frac{\partial \Pi}{\partial t} = -\,b\,\frac{\partial \Pi}{\partial r_*} + \beta_{21}\,\frac{\partial \Phi}{\partial r_*} + \gamma_{21}\,\Phi + \gamma_{22}\,\Pi, \tag{4.25b}$$

with

$$\gamma_{22} = C_t, \qquad \beta_{21} = C_{r_*} + b\,\frac{\partial b}{\partial r_*} - C_t\,b, \qquad \gamma_{21} = C_{\rm so} + \underbrace{C_{\theta\theta}\,\frac{\partial^2}{\partial \theta^2} + C_\theta\,\frac{\partial}{\partial \theta}}_{l_{31}}. \tag{4.26}$$

The angular operator (l_{31}) is naturally absorbed into the source term $(\gamma_{21}\Phi)$ such that the Teukolsky equation has been recast as a first–order hyperbolic system for (Φ, Π) with clear characteristic structure.

4.1.3 Decomposition into real and imaginary parts

Since the coefficients of the Teukolsky equation are in general complex, a purely real formulation is preferable for numerical purposes. To achieve this, we separate the dynamical fields into their real and imaginary components,

$$\Phi = \Phi_R + i\,\Phi_I, \tag{4.27a}$$

$$\Pi = \Pi_R + i\,\Pi_I. \tag{4.27b}$$

Substituting these definitions into the first–order system (4.25) and collecting the independent real and imaginary parts, we obtain the coupled set [55]

$$\frac{\partial \Phi_R}{\partial t} + b\,\frac{\partial \Phi_R}{\partial r_*} - \Pi_R = 0, \tag{4.28a}$$

$$\frac{\partial \Phi_I}{\partial t} + b\,\frac{\partial \Phi_I}{\partial r_*} - \Pi_I = 0, \tag{4.28b}$$

$$\frac{\partial \Pi_R}{\partial t} + \beta^R_{21}\frac{\partial \Phi_R}{\partial r_*} - \beta^I_{21}\frac{\partial \Phi_I}{\partial r_*} - b\,\frac{\partial \Pi_R}{\partial r_*} + \gamma^R_{21}\Phi_R - \gamma^I_{21}\Phi_I + C^R_t\Pi_R - C^I_t\Pi_I = 0, \tag{4.28c}$$

$$\frac{\partial \Pi_I}{\partial t} + \beta^I_{21}\frac{\partial \Phi_R}{\partial r_*} + \beta^R_{21}\frac{\partial \Phi_I}{\partial r_*} - b\,\frac{\partial \Pi_I}{\partial r_*} + \gamma^I_{21}\Phi_R + \gamma^R_{21}\Phi_I + C^I_t\Pi_R + C^R_t\Pi_I = 0. \tag{4.28d}$$

This real system can be written more compactly in block–matrix notation as

$$\begin{bmatrix}\Phi_R\\ \Phi_I\\ \Pi_R\\ \Pi_I\end{bmatrix}_t + \underbrace{\begin{bmatrix} b & 0 & 0 & 0\\ 0 & b & 0 & 0\\ \beta^R_{21} & -\beta^I_{21} & -b & 0\\ \beta^I_{21} & \beta^R_{21} & 0 & -b\end{bmatrix}}_{\text{radial advection}}\begin{bmatrix}\Phi_R\\ \Phi_I\\ \Pi_R\\ \Pi_I\end{bmatrix}_{r_*} + \underbrace{\begin{bmatrix} 0 & 0 & -1 & 0\\ 0 & 0 & 0 & -1\\ \gamma^R_{21} & -\gamma^I_{21} & C^R_t & -C^I_t\\ \gamma^I_{21} & \gamma^R_{21} & C^I_t & C^R_t\end{bmatrix}}_{\text{source terms}}\begin{bmatrix}\Phi_R\\ \Phi_I\\ \Pi_R\\ \Pi_I\end{bmatrix} = \mathbf{0}. \tag{4.29}$$

Thus, the original complex Teukolsky system is recast into a fully real, first–order hyperbolic system for four coupled variables, which is directly amenable to finite–difference and spectral time evolutions. To make the system explicit, we now write down the coefficients that appear in the first–order formulation [55, 56]

$$\beta^R_{21} = \frac{2rs(M-r)(r^2+a^2) - (3a^2+4r^2)\Delta_{BL}}{r\Sigma^2_{BL}} - \frac{2bs\,M(a^2-r^2) + r\Delta_{BL}}{\Sigma^2_{BL}} + b\,\frac{\partial b}{\partial r_*}, \tag{4.30a}$$

$$\beta^I_{21} = -\frac{2am(r^2+a^2)}{\Sigma^2_{BL}} - \frac{2ba}{\Sigma^2_{BL}}\Big(2mMr + s\Delta_{BL}\cos(\theta)\Big), \tag{4.30b}$$

$$\gamma^R_{21} = \frac{\Delta_{BL}}{r^2\Sigma^2_{BL}}\left(6Mr(s+1) - r^2(7s+6) - 6\Delta_{BL} + r^2\Big(s\cot(\theta) + m\csc(\theta)\Big)^2\right) - \frac{\Delta_{BL}}{\Sigma^2_{BL}}\frac{\partial^2}{\partial\theta^2} \tag{4.30c}$$

$$- \frac{\Delta_{BL}}{\Sigma^2_{BL}}\cot(\theta)\,\frac{\partial}{\partial\theta}, \tag{4.30d}$$

$$\gamma^I_{21} = \frac{2am}{r\Sigma^2_{BL}}\Big(2rs(M-r) - 3\Delta\Big), \tag{4.30e}$$

$$C^R_t = \frac{2sM(a^2-r^2) + r\Delta_{BL}}{\Sigma^2_{BL}}, \tag{4.30f}$$

$$C^I_t = \frac{2a}{\Sigma^2_{BL}}\Big(2mMr + s\Delta_{BL}\cos(\theta)\Big). \tag{4.30g}$$

4.2 Derivation of the 4th order algorithm

To integrate the first–order system we employ a finite–difference scheme that is fourth order both in space and in time. The construction follows a Taylor expansion in time, where higher–order time

derivatives are eliminated in favor of spatial derivatives by repeatedly using the evolution equation. As a guide, consider the linear advection problem with constant speed v,

$$\frac{\partial u}{\partial t} \;=\; v\,\frac{\partial u}{\partial x}, \tag{4.31}$$

and expand the solution at fixed x

$$u(t+\delta t,x) \;=\; u \;+\; \frac{\partial u}{\partial t}\,\delta t \;+\; \frac{1}{2}\,\frac{\partial^2 u}{\partial t^2}\,\delta t^2 \;+\; \frac{1}{6}\,\frac{\partial^3 u}{\partial t^3}\,\delta t^3 \;+\; \frac{1}{24}\,\frac{\partial^4 u}{\partial t^4}\,\delta t^4 \;+\; \cdots . \tag{4.32}$$

Using (4.31) to substitute time derivatives by spatial ones (e.g. $\partial_t^2 u = v^2\,\partial_x^2 u$, $\partial_t^3 u = v^3\,\partial_x^3 u$, etc.), we obtain

$$u(t+\delta t,x) \;=\; u \;+\; v\,\frac{\partial u}{\partial x}\,\delta t \;+\; \frac{1}{2}\,v^2\,\frac{\partial^2 u}{\partial x^2}\,\delta t^2 \;+\; \frac{1}{6}\,v^3\,\frac{\partial^3 u}{\partial x^3}\,\delta t^3 \;+\; \frac{1}{24}\,v^4\,\frac{\partial^4 u}{\partial x^4}\,\delta t^4 \;+\; \cdots . \tag{4.33}$$

Truncating the Taylor expansion at $\mathcal{O}(\delta t^2)$ yields the classical Lax–Wendroff scheme, which is second order accurate in both space and time. By instead retaining all contributions up to $\mathcal{O}(\delta t^4)$ and discretising the spatial derivatives with fourth–order finite differences, we obtain a fully fourth–order accurate update formula.

Let $U_j^n \approx u(t_n, x_j)$ with $x_j = j\delta x$ and introducing the Courant parameter

$$\alpha = \frac{v\,\delta t}{\delta x}, \tag{4.34}$$

the resulting scheme takes the form [55]

$$\begin{aligned} U_j^{n+1} = U_j^n &+ \frac{\alpha}{12}\left(U_{j-2}^n - 8U_{j-1}^n + 8U_{j+1}^n - U_{j+2}^n\right) - \frac{\alpha^2}{24}\left(U_{j-2}^n - 16U_{j-1}^n + 30U_j^n - 16U_{j+1}^n + U_{j+2}^n\right) \\ &+ \frac{\alpha^3}{48}\left(U_{j-3}^n - 8U_{j-2}^n + 13U_{j-1}^n - 13U_{j+1}^n + 8U_{j+2}^n - U_{j+3}^n\right) - \frac{\alpha^4}{144}\Big(U_{j-3}^n - 12U_{j-2}^n + 39U_{j-1}^n \\ &- 56U_j^n + 39U_{j+1}^n - 12U_{j+2}^n + U_{j+3}^n\Big). \end{aligned} \tag{4.35}$$

All spatial derivatives appearing in the scheme are discretized by means of fourth–order accurate finite difference operators; the explicit stencils are provided in Appendix E.

This explicit construction highlights the fourth–order character of the method: the update involves a symmetric stencil covering seven grid points. In practice, the same strategy carries over to the Teukolsky system (4.29), where each component of $\mathbf{u} = (\Phi_R, \Phi_I, \Pi_R, \Pi_I)^T$ is advanced according to (4.35), with the corresponding characteristic speeds.

4.3 Stability analysis

The stability of the finite–difference scheme can be investigated through a von Neumann analysis. In this approach one considers constant coefficients and assumes that any solution can be decomposed into Fourier modes. The key idea is to track how each mode is amplified (or damped) after one timestep.

Let the discrete solution at grid point j and time level n be expressed as

$$U_j^n = \xi^n e^{ikj\delta x}, \tag{4.36}$$

where k is the wavenumber and $\xi(k)$ denotes the amplification factor. Stability is guaranteed if $|\xi(k)| \leq 1$ for all k.

By substituting the ansatz (4.36) into the fourth–order update formula (4.35), one obtains a closed algebraic expression for $\xi(k)$. This expression can be separated into real and imaginary parts, and after some algebra the squared modulus of the amplification factor takes the form [55]

$$
\begin{aligned}
|\xi(k)|^2 = 1 &+ \frac{8}{9}\alpha^2\Big(\cos(k\delta x) - 5\Big)\sin^6\left(\frac{k\delta x}{2}\right) - \frac{4}{9}\alpha^4\Big(4\cos(k\delta x) - 17\Big)\sin^8\left(\frac{k\delta x}{2}\right) \\
&+ \frac{1}{54}\alpha^6\Big(133\cos(k\delta x) - 34\cos(2k\delta x) + 3\cos(3k\delta x) - 150\Big)\sin^6\left(\frac{k\delta x}{2}\right) \\
&+ \frac{4}{81}\alpha^8\Big(\cos(k\delta x) - 4\Big)^2\sin^8\left(\frac{k\delta x}{2}\right).
\end{aligned}
\tag{4.37}
$$

This periodic function of $k\delta x$ satisfies $|\xi| \leq 1$ provided the Courant parameter obeys $\alpha \lesssim 1.5$. Hence the Courant stability condition for the fourth–order scheme is

$$
v\delta t \leq 1.5\,\delta x, \tag{4.38}
$$

which is less restrictive than for second–order methods such as Lax–Wendroff. An expansion of (4.37) for small $k\Delta x$ gives

$$
|\xi(k)|^2 = 1 - \left(\frac{\alpha^2}{18} + \frac{\alpha^6}{72}\right)(k\delta x)^6 + \mathcal{O}\left((k\delta x)^8\right). \tag{4.39}
$$

Thus numerical damping enters only at sixth order in $k\delta x$, indicating excellent accuracy for long–wavelength modes compared with second–order schemes, whose damping appears already at quadratic or quartic order.

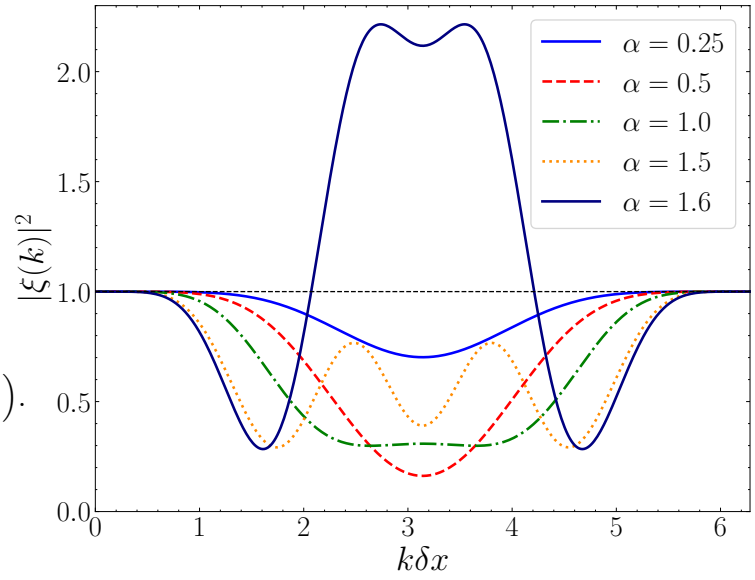


Figure 4.1: **Amplification factor versus CFL number**, reproduced using the code in [55].

4.4 Boundary conditions

4.4.1 Radial boundaries

In our evolutions we adopt Sommerfeld–type boundary conditions both at the horizon and at large radius. Within tortoise coordinates r_*, the horizon formally lies at $r_* \to -\infty$, but in practice the computational grid can be truncated at a sufficiently negative value (e.g. $r_* \approx -50M$), which provides an accurate approximation while keeping the domain finite. At these boundaries the field is required to behave as a pure ingoing wave at the inner edge and as a pure outgoing wave at the outer edge, which can be summarized as

$$
\frac{\partial\Phi}{\partial t}(t, r_*, \theta) = \begin{cases} \dfrac{\partial\Phi}{\partial r_*}(t, r_*, \theta), & r_* = r_{\min} \ \text{(ingoing)}, \\ -\dfrac{\partial\Phi}{\partial r_*}(t, r_*, \theta), & r_* = r_{\max} \ \text{(outgoing)}. \end{cases} \tag{4.40}
$$

These first–order relations are directly consistent with the continuum problem. In practice, however, when using a fourth–order finite difference stencil one must compute higher derivatives of Eq. (4.40) in order to match the Taylor expansion used in the scheme. Table 4.1 summarizes the resulting expressions for the first few orders.

Inner boundary ($r_* = r_{\min}$)	Outer boundary ($r_* = r_{\max}$)
$\dfrac{\partial\Phi}{\partial t} = \dfrac{\partial\Phi}{\partial r_*}$	$\dfrac{\partial\Phi}{\partial t} = -\dfrac{\partial\Phi}{\partial r_*}$
$\dfrac{\partial^2\Phi}{\partial t^2} = \dfrac{\partial^2\Phi}{\partial r_*^2}$	$\dfrac{\partial^2\Phi}{\partial t^2} = \dfrac{\partial^2\Phi}{\partial r_*^2}$
$\dfrac{\partial^3\Phi}{\partial t^3} = \dfrac{\partial^3\Phi}{\partial r_*^3}$	$\dfrac{\partial^3\Phi}{\partial t^3} = -\dfrac{\partial^3\Phi}{\partial r_*^3}$
$\dfrac{\partial^4\Phi}{\partial t^4} = \dfrac{\partial^4\Phi}{\partial r_*^4}$	$\dfrac{\partial^4\Phi}{\partial t^4} = \dfrac{\partial^4\Phi}{\partial r_*^4}$

Table 4.1: **Radial boundary conditions** derived from Eq. (4.40) [55].

Since the numerical grid is finite, centered difference operators cannot be directly applied at the extreme points of the domain. In these regions one must instead employ the off–centered stencils listed in Appendix E. Table 4.2 summarizes the grid indices in the r_* direction where such operators are required.

Derivative	Evaluated at
$\dfrac{\partial}{\partial r_*}$, $\dfrac{\partial^2}{\partial r_*^2}$	$j = 1$ and $j = N_r - 1$
$\dfrac{\partial^3}{\partial r_*^3}$, $\dfrac{\partial^4}{\partial r_*^4}$	$j = 2$ and $j = N_r - 2$

Table 4.2: **Off-centered derivative operators.** Grid points where these operators are applied. The grid has $N_r + 1$ points labeled $0, \ldots, N_r$ [55].

For the auxiliary field (Eq. (4.6)), the boundary conditions follow directly from the Sommerfeld prescription (4.40), namely

$$\Pi = \begin{cases} (1+b)\,\dfrac{\partial\Phi}{\partial r_*}, & r_* = r_{\min} \ \text{(ingoing)}, \\ (b-1)\,\dfrac{\partial\Phi}{\partial r_*}, & r_* = r_{\max} \ \text{(outgoing)}. \end{cases} \tag{4.41}$$

4.4.2 Angular boundary conditions

The angular part of the computational grid requires special treatment near the symmetry axis, at $\theta = 0$ and $\theta = \pi$. The correct boundary condition depends on the azimuthal number m and reflects the parity of the solution across the axis. Specifically, one finds

$$\Phi(t, r_*, \theta) = 0, \qquad m = \pm 1, \pm 3, \pm 5, \ldots, \tag{4.42a}$$

$$\frac{\partial\Phi}{\partial\theta}(t, r_*, \theta) = 0, \qquad m = 0, \pm 2, \pm 4, \ldots. \tag{4.42b}$$

These conditions arise from the parity of the solution under reflections about $\theta = 0$ and $\theta = \pi$. For even m, the field is symmetric,

$$\begin{cases} \Phi(t, r_*, \theta) = \quad \Phi(t, r_*, -\theta), \\ \Phi(t, r_*, \pi + \theta) = \quad \Phi(t, r_*, \pi - \theta), \end{cases} \qquad m = 0, \pm 2, \ldots, \tag{4.43}$$

whereas for odd m it is antisymmetric,

$$\begin{cases} \Phi(t, r_*, \theta) = -\Phi(t, r_*, -\theta), \\ \Phi(t, r_*, \pi + \theta) = -\Phi(t, r_*, \pi - \theta). \end{cases} \qquad m = \pm 1, \pm 3, \ldots. \tag{4.44}$$

In order to impose these properties consistently, we employ a staggered grid in the θ direction. The coordinate values $\theta = 0$ and $\theta = \pi$ are not included explicitly, but instead lie halfway between the first two and last two grid points. This arrangement avoids the singular behaviour of terms such as $\cot\theta$ in the Teukolsky equation. As a consequence, a number of additional ghost zones are introduced at the boundaries: two before $\theta = 0$ and two after $\theta = \pi$. The total grid thus contains $N_\theta + 3$ points, with the ghost cells updated at each time step using the symmetry relations (4.43)–(4.44).

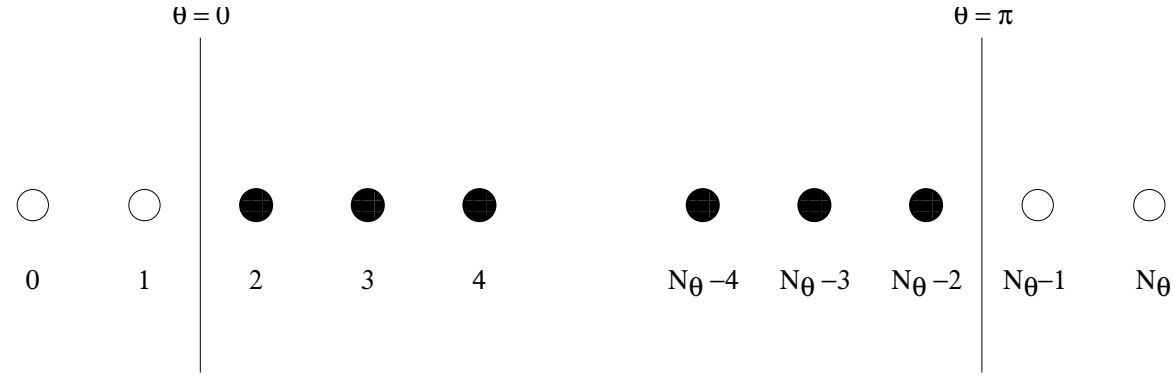


Figure 4.2: **Staggered angular grid with ghost zones.** Black circles represent physical grid points, while white circles denote ghost zones. The poles ($\theta = 0$ and $\theta = \pi$) are always located halfway between the first two and last two grid points, ensuring that the boundary conditions are implemented via the symmetry relations [55].

4.5 Implementation

For practical purposes, the evolution system (4.29) can be expressed in compact form as

$$\frac{\partial \mathbf{u}}{\partial t} \;=\; -\,\mathbf{M}\,\frac{\partial \mathbf{u}}{\partial r_*} - \,(\mathbf{L} + \mathbf{A})\,\mathbf{u}. \tag{4.45}$$

It is convenient to define $\mathbf{B} := -\mathbf{M}$ and $\mathbf{S} := -(\mathbf{L} + \mathbf{A})$, so that the evolution equation takes the form

$$\frac{\partial \mathbf{u}}{\partial t} \;=\; \mathbf{B}\,\frac{\partial \mathbf{u}}{\partial r_*} + \mathbf{S}\,\mathbf{u}. \tag{4.46}$$

This rewriting is useful because in the Taylor expansion of the update scheme, higher–order time derivatives are systematically replaced by combinations of spatial derivatives using Eq. (4.46). Explicitly,

one finds [55]

$$\frac{\partial \mathbf{u}}{\partial t} = \mathbf{B}\,\frac{\partial \mathbf{u}}{\partial r_*} + \mathbf{S}\,\mathbf{u}, \tag{4.47a}$$

$$\frac{\partial^2 \mathbf{u}}{\partial t^2} = \mathbf{B}\left(\frac{\partial \mathbf{B}}{\partial r_*}\,\frac{\partial \mathbf{u}}{\partial r_*} + \frac{\partial}{\partial r_*}(\mathbf{S}\,\mathbf{u}) + \mathbf{B}\,\frac{\partial^2 \mathbf{u}}{\partial r_*^2}\right) + \mathbf{S}\,\frac{\partial \mathbf{u}}{\partial t}, \tag{4.47b}$$

$$\begin{aligned}\frac{\partial^3 \mathbf{u}}{\partial t^3} = \mathbf{B}\Bigg\{&\frac{\partial}{\partial r_*}\left(\mathbf{S}\,\frac{\partial \mathbf{u}}{\partial t}\right) + \mathbf{B}^2\,\frac{\partial \mathbf{u}}{\partial r_*} + \frac{\partial \mathbf{B}}{\partial r_*}\left[\frac{\partial}{\partial r_*}(\mathbf{S}\,\mathbf{u}) + 3\,\mathbf{B}\,\frac{\partial^2 \mathbf{u}}{\partial r_*^2}\right] + \mathbf{B}\left(\frac{\partial \mathbf{u}}{\partial r_*}\,\frac{\partial \mathbf{B}}{\partial r_*} + \frac{\partial^2}{\partial r_*^2}(\mathbf{S}\,\mathbf{u}) + \mathbf{B}\,\frac{\partial^3 \mathbf{u}}{\partial r_*^3}\right)\Bigg\} \\ &+ \mathbf{S}\,\frac{\partial^2 \mathbf{u}}{\partial t^2},\end{aligned} \tag{4.47c}$$

$$\begin{aligned}\frac{\partial^4 \mathbf{u}}{\partial t^4} = \mathbf{B}\Bigg\{&\frac{\partial}{\partial r_*}\left(\mathbf{S}\,\frac{\partial^2 \mathbf{u}}{\partial t^2}\right) + \mathbf{B}^3\,\frac{\partial \mathbf{u}}{\partial r_*} + \mathbf{B}^2\left[\frac{\partial}{\partial r_*}(\mathbf{S}\,\mathbf{u}) + 7\,\mathbf{B}\,\frac{\partial^2 \mathbf{u}}{\partial r_*^2}\right] + \frac{\partial \mathbf{B}}{\partial r_*}\left[\frac{\partial}{\partial r_*}\left(\mathbf{S}\,\frac{\partial \mathbf{u}}{\partial t}\right) + \mathbf{B}\left(4\,\frac{\partial \mathbf{u}}{\partial r_*}\,\frac{\partial^2 \mathbf{B}}{\partial r_*^2}\right.\right. \\ &\left. + 3\,\frac{\partial^2}{\partial r_*^2}(\mathbf{S}\,\mathbf{u}) + 6\,\mathbf{B}\,\frac{\partial^3 \mathbf{u}}{\partial r_*^3}\right)\Bigg] + \mathbf{B}\Bigg[\frac{\partial^2}{\partial r_*^2}(\mathbf{S}\,\mathbf{u})\,\frac{\partial \mathbf{B}}{\partial r_*} + \frac{\partial^2}{\partial r_*^2}\left(\mathbf{S}\,\frac{\partial \mathbf{u}}{\partial t}\right) + \mathbf{B}\Big(4\,\frac{\partial^2 \mathbf{B}}{\partial r_*^2}\,\frac{\partial^2 \mathbf{u}}{\partial r_*^2} + \frac{\partial \mathbf{u}}{\partial r_*}\,\frac{\partial^3 \mathbf{B}}{\partial r_*^3} \\ &+ \frac{\partial^3}{\partial r_*^3}(\mathbf{S}\,\mathbf{u}) + \mathbf{B}\,\frac{\partial^4 \mathbf{u}}{\partial r_*^4}\Big)\Bigg]\Bigg\} + \mathbf{S}\,\frac{\partial^3 \mathbf{u}}{\partial t^3}.\end{aligned} \tag{4.47d}$$

The important point is that all higher time derivatives are *algebraically* replaced by combinations of $\mathbf{u}$ and its spatial derivatives. This prevents the numerical accumulation of error that would result from applying the first–derivative stencil repeatedly. Instead, each order of the Taylor expansion is computed directly from the coefficients $\mathbf{B}$ and $\mathbf{S}$, which depend only on r_* and θ but not on t.

This strategy guarantees that the scheme maintains the intended fourth–order accuracy, while at the same time avoiding instabilities near the boundaries. Moreover, products such as $\mathbf{S}\,\mathbf{u}$ or $\mathbf{S}\,\partial_t\mathbf{u}$ are treated consistently by storing $\partial_t\mathbf{u}$ at each timestep and reusing it when required, rather than expanding it further. In this sense, the substitution is performed "numerically" rather than symbolically, which turns out to be both more stable and more efficient.

4.6 Initial data

In our simulations, the initial data are specified as a Gaussian pulse in the radial tortoise coordinate, centered around $r_* = 75M$. Explicitly, at $t = 0$ we set

$$\Phi(0, r_*, \theta) \;=\; \exp\left[-\frac{(r_* - 75)^2}{100}\right]\,{}_{-2}Y_\ell^0(\theta), \tag{4.48}$$

where the angular dependence is provided by the spin-weighted spherical harmonics with spin weight $s = -2$. For the lowest multipoles, the explicit angular dependence (up to normalization) is given by [55]

$$\ell = 2: \quad {}_{-2}Y_2^0(\theta) \;\propto\; \sin^2(\theta), \tag{4.49a}$$

$$\ell = 3: \quad {}_{-2}Y_3^0(\theta) \;\propto\; \cos(\theta)\,\sin^2(\theta), \tag{4.49b}$$

$$\ell = 4: \quad {}_{-2}Y_4^0(\theta) \;\propto\; \Big(5 + 7\cos(2\theta)\Big)\,\sin^2(\theta). \tag{4.49c}$$

4.7 Convergence tests

To assess the accuracy of the numerical scheme we performed a systematic convergence test, both in the radial (r_*) and angular (θ) directions. The procedure consists in evolving the same initial configuration with three different grid spacings, hereafter denoted as *coarse*, *medium*, and *fine*. The mesh sizes are chosen such that their ratios remain constant,

$$\frac{\delta r_*^{\text{coarse}}}{\delta r_*^{\text{medium}}} = \frac{\delta r_*^{\text{medium}}}{\delta r_*^{\text{fine}}} = \rho_{r_*}, \tag{4.50}$$

with $\rho_{r_*} > 1$ a fixed refinement factor. For a fourth–order scheme, the numerical error in each resolution scales as $(\delta r_*)^4$, so the discrete solutions can be written as

$$\Psi_{\text{coarse}} = \Psi_{\text{true}} + k\,(\delta r_*)^4, \tag{4.51a}$$

$$\Psi_{\text{medium}} = \Psi_{\text{true}} + k\left(\frac{\delta r_*}{\rho_{r_*}}\right)^4, \tag{4.51b}$$

$$\Psi_{\text{fine}} = \Psi_{\text{true}} + k\left(\frac{\delta r_*}{\rho_{r_*}^2}\right)^4, \tag{4.51c}$$

where k is an r_*–independent constant. Eliminating Ψ_{true}, one obtains the convergence relation

$$\rho_{r_*}^4\,(\Psi_{\text{fine}} - \Psi_{\text{medium}}) = \Psi_{\text{medium}} - \Psi_{\text{coarse}}. \tag{4.52}$$

When the curves on both sides of this equation overlap, fourth–order convergence is confirmed.

The convergence tests have been carried out with a fixed BH mass $M = 1$ and Courant factor $C = 0.5$. The computational domain in tortoise coordinates spans $-50M \leq r_* \leq 950M$, discretized with $N_{r_*} \times N_\theta = 1000 \times 8$ grid points. The radial resolution was varied as $\delta r_* = \{1.0, 0.5, 0.25\}M$, while the angular spacing was set to $\delta\theta = \pi/8$. We restrict to the case $a = 0$, $\ell = 2$, $m = 0$, $s = -2$, and adopt as initial data an ingoing Gaussian pulse centered at $r_* = 75M$.

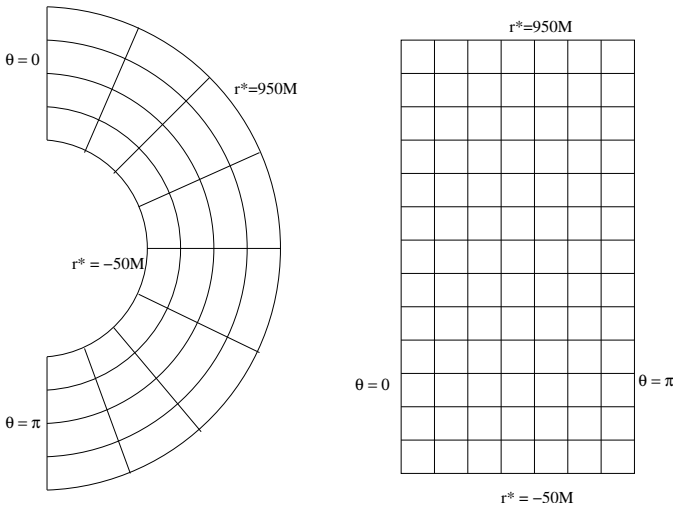


Figure 4.3: **Two–dimensional computational grid.** Structure of the mesh in the (r_*, θ) plane, showing both the physical points and the ghost zones used to impose boundary conditions [55].

Figure 4.4 displays the convergence test along the radial direction. At $t = 200M$ the discrepancies between resolutions are hardly noticeable, showing excellent agreement among the different grids. At later times, such as $t = 1000M$, the accumulated numerical error becomes more visible, but the expected fourth–order convergence relation is still satisfied within numerical precision, in agreement with the behavior reported in the original code paper [55].

The time evolution of this convergence pattern is illustrated in Figure 4.5. Here the test is shown for a sequence of snapshots from $t = 100M$ up to $t = 1000M$. The results clearly demonstrate that

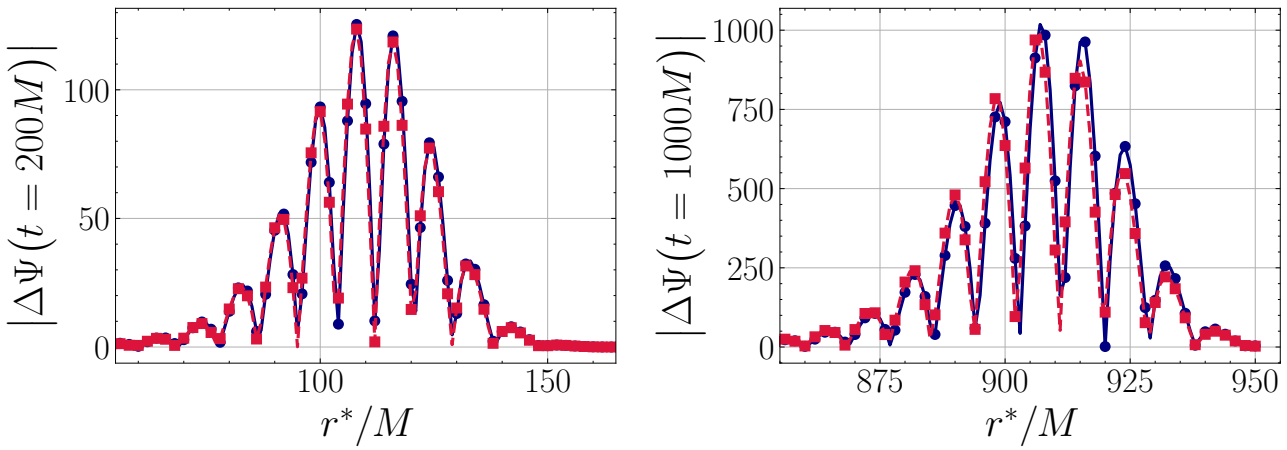


Figure 4.4: **Fourth–order convergence in the radial direction.** The convergence test defined by Eq. (4.52) is shown at the equatorial plane $\theta = \pi/2$. The solid blue line with circles corresponds to $2^4(\Psi_{\rm fine} - \Psi_{\rm med})$, while the dashed red line with squares shows $\Psi_{\rm med} - \Psi_{\rm coarse}$. **Left:** $t = 200M$, when the Gaussian pulse has just scattered off the potential barrier. **Right:** $t = 1000M$, where the accumulated numerical error slightly increases the deviation. Reproduced using the code in [55].

the method retains its fourth–order convergence properties throughout the entire simulation, with the discrepancies between resolutions increasing gradually over time but remaining well controlled.

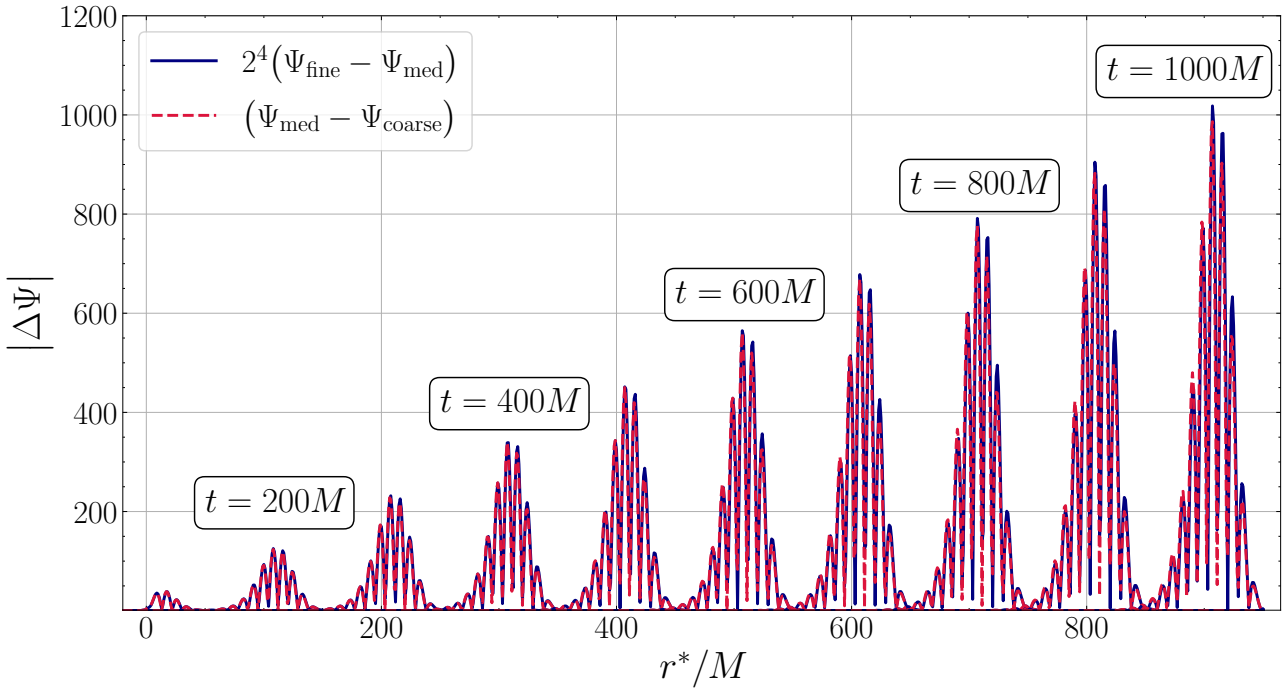


Figure 4.5: **Fourth–order convergence in the radial direction.** The convergence test defined by Eq. (4.52) is shown at the equatorial plane $\theta = \pi/2$. The solid navy line with circles corresponds to $2^4(\Psi_{\rm fine} - \Psi_{\rm med})$, while the dashed crimson line with squares shows $\Psi_{\rm med} - \Psi_{\rm coarse}$. Labels indicate different times from $t = 100M$ up to $t = 1000M$ in steps of $100M$. Reproduced using the code in [55].

A similar convergence test was carried out for the angular grid. In this case, the staggered structure of the θ discretization requires an interpolation procedure, since the fine and medium grids do not share the same collocation points, as illustrated in Fig. 4.6.

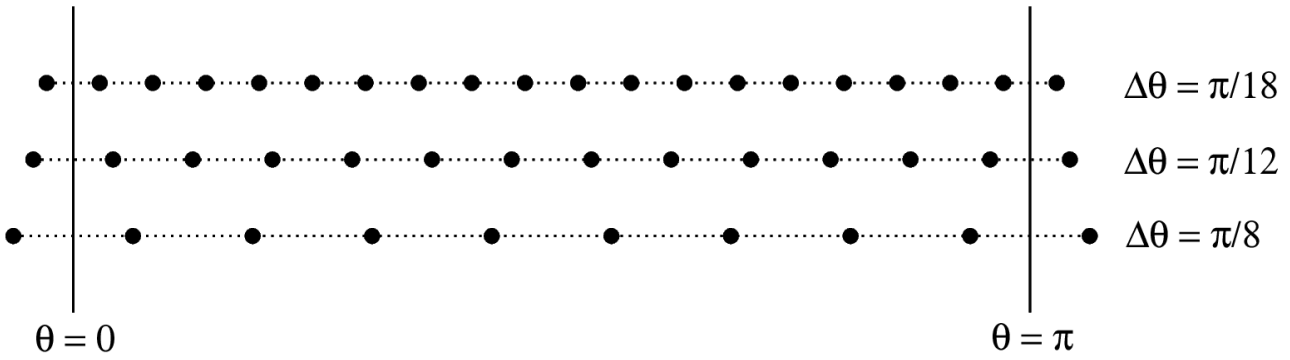


Figure 4.6: **Staggered angular grid points.** Illustration of the θ discretization showing that the fine and medium grids do not share the same collocation points, which makes interpolation necessary for the convergence test [55].

We used a sixth–order Lagrange polynomial to re–express the medium and fine solutions at the positions of the coarse grid before computing differences. As illustrated in Fig. 4.7, the expected fourth–order behaviour is observed until round–off errors dominate at late times.

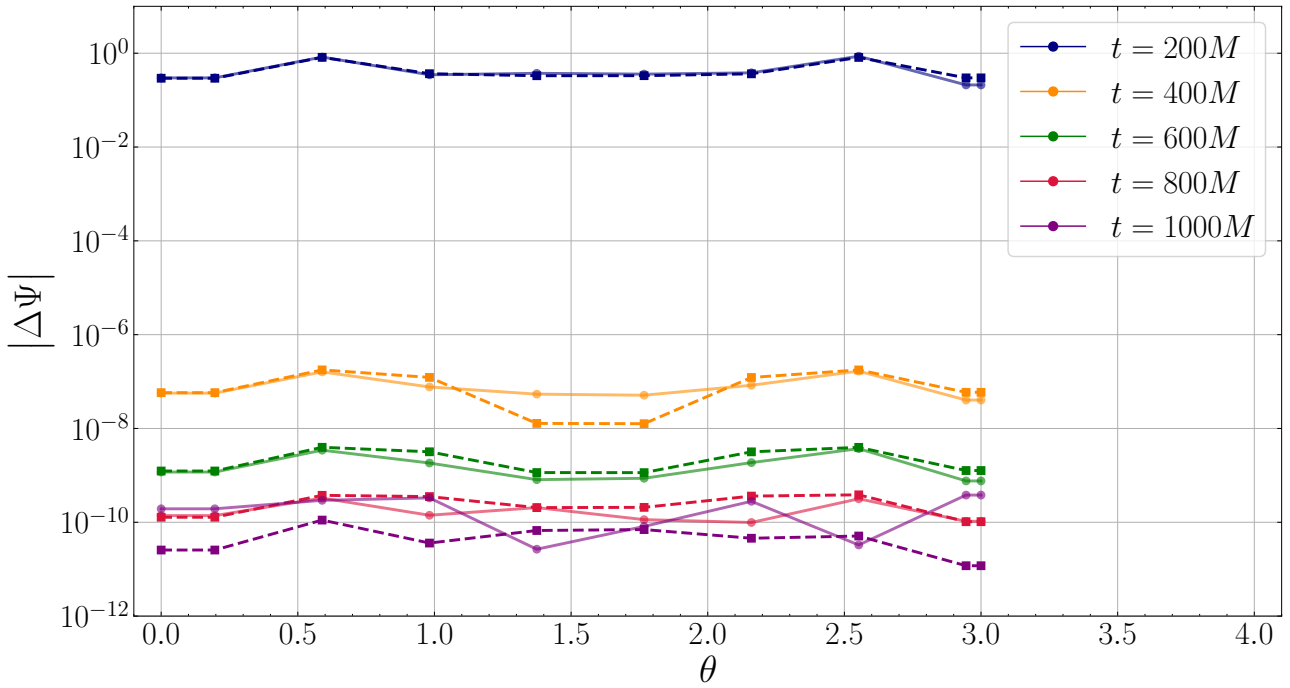
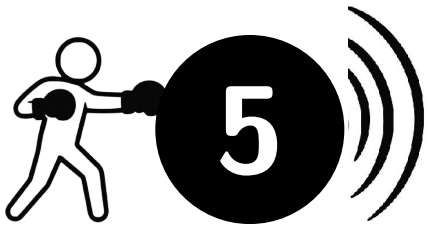


Figure 4.7: **Fourth–order convergence in the angular direction.**The test is carried out by interpolating the fine and medium solutions onto the coarse angular grid. Reproduced using the code in [55].

Part III

Results

CHAPTER



Numerical results in Schwarzschild spacetime

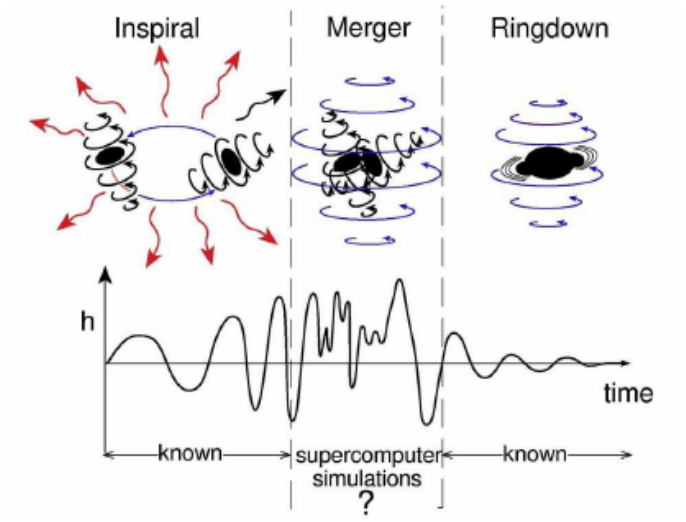
Contents

5.1 Motivation **73**
5.2 Setup **75**
5.3 Tests for varying the Gaussian width **76**
5.4 Tests for changing the frequency **91**

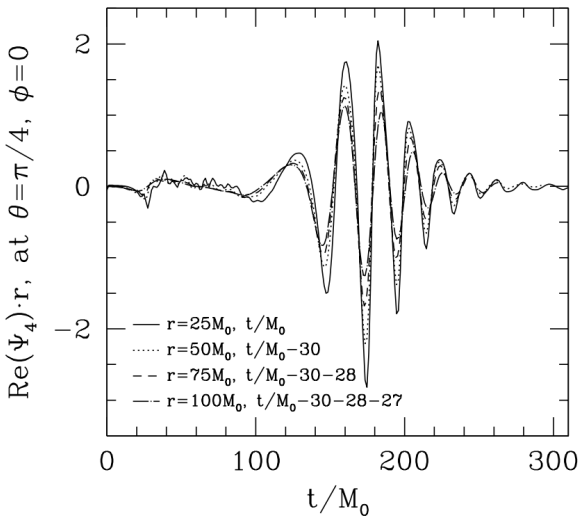
5.1 Motivation

NR has played a central role in GW astrophysics by enabling detailed simulations of the full dynamics of compact binary mergers. One of its most important outcomes is the excellent agreement with Linear Perturbation Theory (LPT). From the earliest simulations to more recent works, waveform comparisons have shown a very precise matching of QNMs for different values of ℓ and m [48]. This agreement holds not only at first order, but also when extending LPT calculations to second order, where a similarly good correspondence with NR has been demonstrated [42, 45]. This establishes LPT as a reliable theoretical framework, while also raising questions about its limitations and about which aspects of the signal remain elusive in NR.

LPT predicts that the full GW signal can be decomposed into three stages: the prompt response, the ringdown dominated by QNMs, and the late-time tails. While the ringdown is well established in both NR and observations, the late-time tails remain problematic: up to 2025 [59], they had not been clearly identified in NR simulations, and in standard BSSN formulations they are still absent. This raises several questions: are the tails too weak to be resolved numerically? Are they buried in numerical noise or gauge effects? Do they depend on the choice of initial perturbation? Understanding these issues is essential, since tails are a robust prediction of GR and emerge unavoidably in analytic treatments. A central question that motivates this thesis is therefore: *can we learn from LPT how to excite tails in NR?*



(a) Qualitative sketch by Kip Thorne of the expected gravitational-wave signal from a binary BH merger. The inspiral and ringdown appear regular and predictable, while the merger is depicted as a nonlinear and chaotic stage [57].



(b) Result from the first NR simulation of a binary BH merger. The waveform, extracted from the NP scalar Ψ_4 at different radii, shows the inspiral, merger, and ringdown phases with quantitative accuracy [58].

Figure 5.1: **Early expectations versus numerical results for binary BH waveforms. (a)** Thorne's conceptual picture of the waveform. **(b)** The first successful NR simulation of a binary BH merger.

From a theoretical standpoint, tails arise from the low-frequency branch cut of the Green's function [60]. Unlike QNMs, which are discrete complex resonances, tails correspond to the continuous backscattering of waves off the spacetime curvature at large radii, where the effective potential decays as $1/r^2$. Therefore, tails are a low-frequency phenomenon. This has important consequences: sharply localized perturbations predominantly excite high-frequency components and leave almost no tail, whereas extended perturbations enhance low-frequency content and thus produce clearer tails.

From an astrophysical perspective, however, tails are essentially undetectable. Their relative amplitude with respect to the fundamental mode can be as small as $A_{\rm tail}/A_0 \sim 10^{-7}$. For typical signal-to-noise ratios (SNR ~ 10), the tail contribution is entirely hidden by noise. Even in the case of future space-based detectors such as LISA, with SNR $\sim 10^3$, the effective signal-to-noise ratio for tails would be

$$\mathrm{SNR}_{\rm tail} \sim \mathrm{SNR} \times \frac{A_{\rm tail}}{A_0} \sim 10^3 \times 10^{-7} \sim 10^{-4},$$

orders of magnitude below detectability. Thus, late-time tails should be regarded as a theoretically fundamental but observationally inaccessible feature. Their study is therefore motivated not by prospects of direct detection, but by the need to understand the mathematical structure of wave propagation in curved spacetime and to bridge analytic and numerical approaches.

The prompt response is also of interest. While often ignored in practice by fitting the ringdown from the first peak, its physical definition is unclear. Astrophysically, the prompt phase may encode information about the nonlinear-to-linear transition, and questions arise: where exactly does the prompt start? How do initial conditions control its amplitude? Are there resonances that influence the prompt–ringdown transition?

To investigate these open problems we employ Numerical Linear Perturbation Theory (NLPT), which offers a controlled environment to study waveform phases and the role of initial data. We introduce two toy models to systematically vary the perturbations:

1. Head-on type model:
$$\Psi(t=0,r_*) = A\exp\left[-\frac{\left(r_*-r_*^0\right)^2}{2\sigma^2}\right], \tag{5.1}$$
where the parameter σ controls the width of the initial perturbation. This model idealizes a head-on collision of BHs. Narrow perturbations (σ small) excite high frequencies and suppress tails, whereas wide perturbations (σ large) enhance low frequencies and produce clearer tails.

2. Quasi-circular type model:
$$\Psi(t=0,r_*) = A\exp\left[-\frac{\left(r_*-r_*^0\right)^2}{2\sigma^2}\right]\cos\Big[\omega_0\big(r_*-r_*^0\big)\Big], \tag{5.2}$$
where the frequency ω_0 mimics orbital motion. This simplified representation of quasi-circular inspirals is astrophysically relevant, since most detectable mergers are inspiraling binaries. Varying ω_0 allows us to search for resonances and to quantify how orbital dynamics condition the excitation of QNMs and tails.

We apply both models in Schwarzschild and Kerr spacetimes. In all cases, we extract two main observables:

- the amplitude ratios $A^R_{\ell mn} = (A_{\ell mn}/A_{\ell m0})$ which measure the relative excitation of overtones,
- the tail starting time, i.e. the instant when the signal transitions from being dominated by QNMs to a power-law tail.

The motivation of this work lies in clarifying the structure of BHPT beyond the ringdown, focusing on tails and prompt response. While astrophysically inaccessible, tails are a key theoretical feature of GR. By combining NLPT with simple but well-motivated toy models, we aim to disentangle how initial data and BH geometry control the excitation of different signal phases, thereby strengthening the bridge between perturbation theory and NR.

5.2 Setup

We study the time-domain evolution of gravitational perturbations in BHs within the framework of BHPT. For the Schwarzschild case we use the RW equation for axial perturbations,
$$\left(-\frac{\partial^2}{\partial t^2}+\frac{\partial^2}{\partial r_*^2}-V_{\rm RW}(r)\right)\Psi(t,r_*)=0, \tag{5.3}$$
with potential
$$V_{\rm RW}(r) = \left(1-\frac{2M}{r}\right)\left[\frac{\ell(\ell+1)}{r^2}-\frac{6M}{r^3}\right]. \tag{5.4}$$

As initial data we employ the two families of toy models introduced previously, representing head-on and quasi-circular configurations. Their free parameters (σ in the head-on model and ω_0 in the quasi-circular model) are varied systematically to explore their impact on the excitation of different signal phases. Both setups are evolved in Schwarzschild spacetime, and waveforms are extracted at fixed locations in the wave zone.

5.3 Tests for varying the Gaussian width

5.3.1 Fundamental mode extraction

The quantitative extraction of the QNM parameters from the numerical waveforms is performed with the goal of determining, for each initial Gaussian width, the oscillation frequency and damping time of the dominant ($\ell = 2$) Schwarzschild QNM, and comparing them with theoretical predictions. A systematic fitting procedure is adopted and applied consistently across all simulations.

We begin our analysis with the waveform obtained for $\sigma = 1$, displayed in Figure 5.2. The plot shows the complete signal extracted at $r^*_{\rm obs} = 50$, together with an inset that magnifies the intermediate regime. After a brief transient, the waveform settles into a well-defined oscillatory phase, clearly dominated by the fundamental QNM, before gradually transitioning to the characteristic power–law tail. The inset emphasizes the region where the damped sinusoidal behaviour is most pronounced, which will be used as the fitting window in the subsequent analysis.

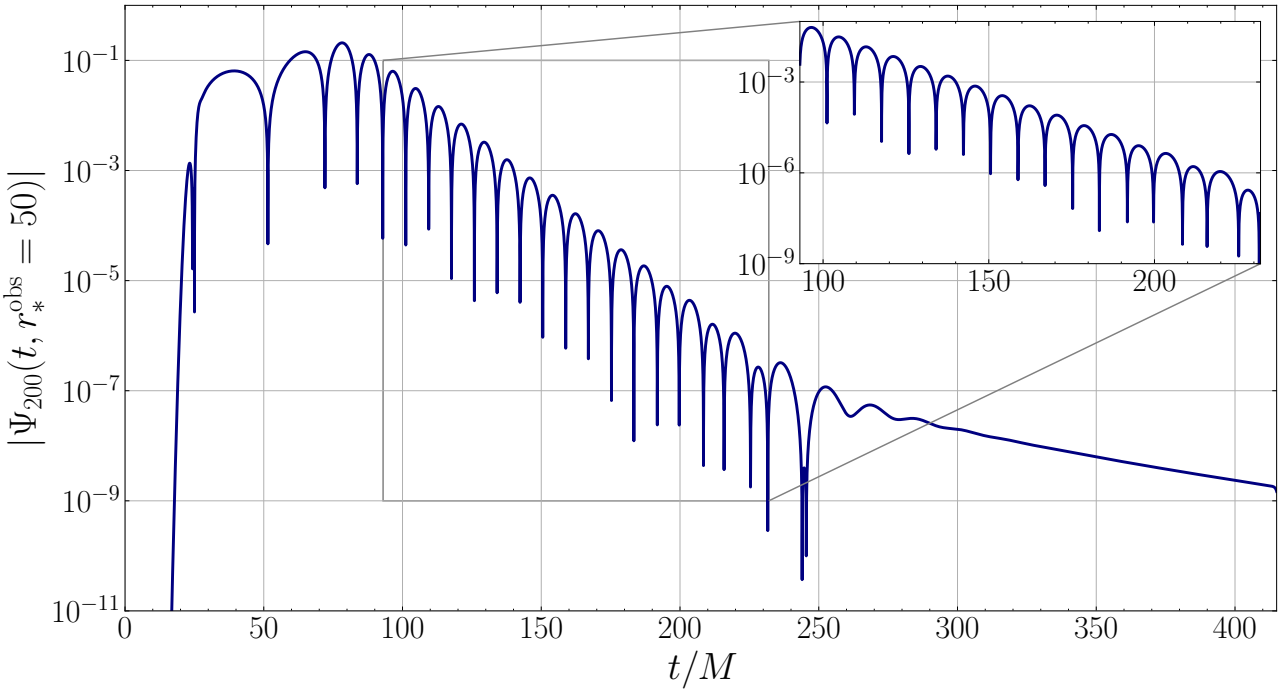


Figure 5.2: **Time-domain waveform for $\sigma = \sigma_1$, extracted at $r^*_{\rm obs} = 50$.** The main panel shows $|\Psi_{200}(t, r^*_{\rm obs} = 50)|$ in logarithmic scale across the full simulation time, from the initial prompt response to the late-time tail. The inset highlights the intermediate regime dominated by QNM oscillations.

To isolate the ringdown regime, we restrict our analysis to the interval $t \in [93, 175]\, M$, where the QNM contribution is dominant while both the initial prompt and the late–time tail remain subleading.

For convenience, we shift the time coordinate so that the fitting window begins at $t = 0$. This reparametrization does not alter the physical content of the signal, but it simplifies the fitting procedure in two important ways:

- First, it removes the need for an additional reference time parameter in the fit, which would otherwise be strongly correlated with the phase.
- Second, it improves the numerical stability of the nonlinear least–squares optimization, since all fitted parameters are referred to a common time origin.

The shifted waveform is displayed in Fig. 5.3, where the exponential decay and oscillatory pattern of the fundamental mode are clearly visible.

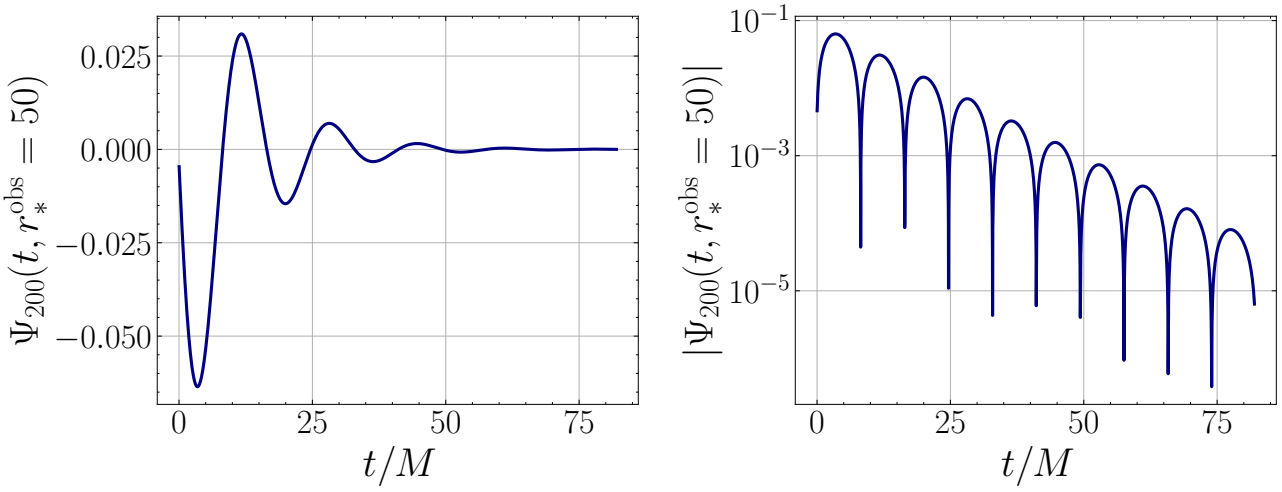


Figure 5.3: **Shifted waveform for $\sigma = 1$ in the fitting window** $t \in [93, 175]\, M$. The time axis has been redefined so that the fitting window begins at $t = 0$. The left panel shows the waveform on a linear scale, while the right panel displays the same data on a logarithmic scale.

We next fit the shifted waveform to a pure QNM template,

$$\Psi^{\rm fit}_{\rm QNM}(t) = A\, e^{-t/\tau} \cos(\omega t + \phi), \qquad (5.5)$$

where the four parameters (A, ω, τ, ϕ) are determined by nonlinear least–squares minimization. This procedure allows us to extract direct estimates of the fundamental QNM frequency (ω) and damping time (τ) from the numerical data, without the need to include additional contributions. The quality of the fit is assessed through the coefficient of determination (R^2), which for $\sigma = 1$ attains values above 0.9999, confirming the clear dominance of the QNM signal within the chosen window. Figure 5.4 displays the

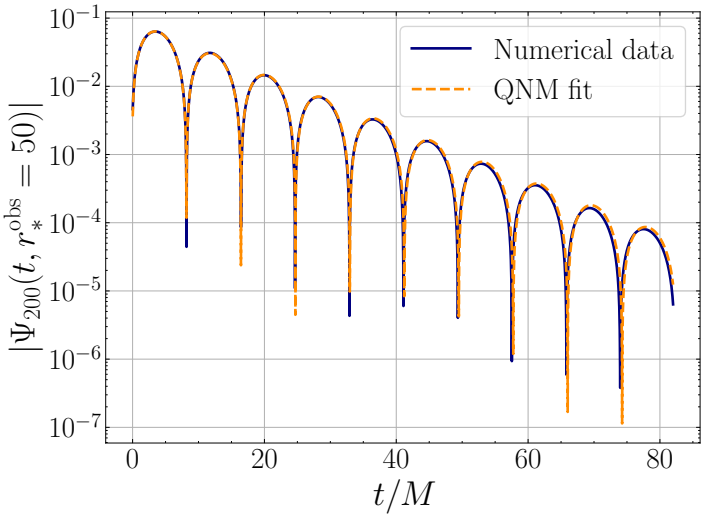


Figure 5.4: **QNM fit of the waveform with $\sigma = 1$ in the shifted window** $t \in [0, 82]\, M$.

numerical waveform together with the best–fit QNM template, showing excellent agreement throughout the fitting interval, with residuals at the level of machine precision.

From the fit we obtain an oscillation frequency of $\omega_{\rm fit} = 0.380$ and a damping time of $\tau_{\rm fit} = 11.263$, which are in excellent agreement with the theoretical Schwarzschild values $\omega_{\rm th} = 0.373$ and $\tau_{\rm th} = 11.240$. The relative deviations are only 1.8% for the frequency and 0.2% for the damping time, while the quality of the fit remains exceptionally high with $R^2 \simeq 0.999$. These results confirm that, for narrow initial data, the waveform is cleanly dominated by the fundamental QNM, and that a pure damped sinusoid provides an accurate description of the signal within the chosen window.

We next extend the fit to incorporate the late–time tail contribution, using the augmented template

$$\Psi^{\rm fit}_{\rm QNM+tail}(t) = A\, e^{-t/\tau} \cos(\omega t + \phi) + B\, t^{-p}. \tag{5.6}$$

This form enables us to test whether a residual power–law component is already present within the fitting window and to quantify its influence on the extracted QNM parameters. For $\sigma = 1$, no parameter is fixed a priori: all quantities $(A, \omega, \tau, \phi, B, p)$ are determined simultaneously by nonlinear least–squares minimization. The fitted frequency and damping time remain essentially unchanged compared to the pure QNM fit,

$$\omega_{\rm fit} = 0.380, \qquad \tau_{\rm fit} = 11.262, \tag{5.7}$$

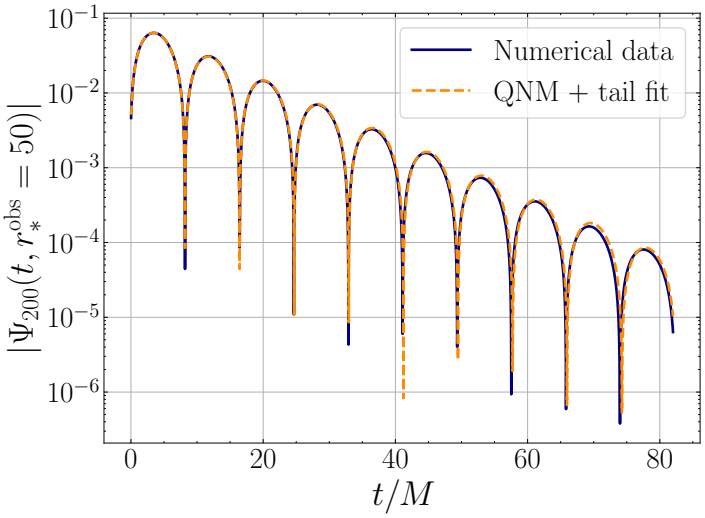


Figure 5.5: **Fit including both QNM and tail contributions for $\sigma = 1$.**

while the tail amplitude and exponent take small values, $B \simeq -6.6 \times 10^{-5}$ and $p \simeq 0.87$. The results of this extended fit, together with those from the pure QNM analysis, are summarized in Table 5.1. This side–by–side comparison shows that, for $\sigma = 1$, both models yield essentially identical estimates of the oscillation frequency and damping time, with $R^2 \approx 0.999$. The additional tail contribution is numerically negligible, and its exponent lies far from the theoretical expectation ($p = 7$), confirming that the chosen time window is fully dominated by the fundamental QNM.

Model	A_{200}	ω_{200}	τ_{200}	ϕ_{200}	B	p	R^2	$(\omega_{\rm fit}/\omega_{\rm th},\ \tau_{\rm fit}/\tau_{\rm th})$
QNM only	0.088	0.380	11.263	1.604	–	–	0.999	(1.017, 1.002)
QNM+tail	0.088	0.380	11.262	1.603	-6.58×10^{-5}	0.869	0.999	(1.018, 1.002)

Table 5.1: **Comparison of fit results for $\sigma = 1$**, using a pure QNM template and a combined QNM+tail model. Theoretical values are $\omega_{\rm th} = 0.373$, $\tau_{\rm th} = 11.240$.

Having established the fitting procedure with the representative case $\sigma = 1$, we now turn to the complete set of simulations. The results of the pure QNM fits and the combined QNM+tail fits are collected in Tables 5.2 and 5.3, respectively.

A global inspection shows clear systematic trends: for narrow to moderately broad pulses ($\sigma \leq 6$), both the pure QNM and the combined QNM+tail fits yield frequencies and damping times in excellent

σ	A_{200}	ω_{200}	τ_{200}	ϕ_{200}	R^2	$\omega_{\rm fit}/\omega_{\rm th}$	$\tau_{\rm fit}/\tau_{\rm th}$
1	0.089	0.380	11.263	1.605	0.999	1.018	1.002
2	0.148	0.379	11.247	1.514	0.999	1.015	1.001
3	0.163	0.378	11.204	1.360	0.999	1.013	0.997
4	0.142	0.379	11.077	1.126	0.999	1.014	0.985
5	-0.076	0.380	11.154	-1.178	0.999	1.017	0.992
6	-0.033	0.377	11.539	-0.343	0.997	1.009	1.027
7	0.013	0.358	11.295	0.519	0.968	0.959	1.005
8	-0.013	0.292	11.091	0.650	0.796	0.780	0.987
9	-0.188	0.123	4.444	1.336	0.891	0.330	0.395
10	0.536	0.150	11.289	1.829	0.999	0.401	1.004

Table 5.2: **Fitted QNM parameters from the numerical waveforms for different Gaussian pulse widths**. Theoretical values correspond to the fundamental $\ell = 2$ Schwarzschild QNM, with $\omega_{\rm th} = 0.373$ and $\tau_{\rm th} = 11.240$.

σ	A_{200}	ω_{200}	τ_{200}	ϕ_{200}	B	p	R^2	$\omega_{\rm fit}/\omega_{\rm th}$	$\tau_{\rm fit}/\tau_{\rm th}$
1	0.089	0.380	11.262	1.603	-0.000	0.869	0.999	1.018	1.002
2	0.148	0.380	11.246	1.511	-0.000	0.795	0.999	1.016	1.001
3	0.163	0.379	11.199	1.358	-0.000	0.786	0.999	1.013	0.996
4	0.143	0.379	11.058	1.130	-0.000	0.354	0.999	1.014	0.984
5	-0.077	0.380	11.007	-1.179	0.001	0.406	0.999	1.016	0.979
6	-0.034	0.378	11.160	-0.363	0.001	0.428	0.999	1.012	0.988
7	-0.013	0.358	11.264	0.519	0.000	4.969	0.968	0.959	1.002
8	-0.001	0.358	12.412	0.920	0.003	0.292	0.965	0.957	1.104
9	0.144	0.163	4.496	-1.921	0.004	0.353	0.994	0.435	0.399
10	0.306	0.150	16.982	1.787	-0.080	0.009	1.000	0.519	1.511

Table 5.3: **Fitted parameters including both QNM and tail contributions, for Gaussian initial data with different widths**. The theoretical reference values are $\omega_{\rm th} = 0.373$ and $\tau_{\rm th} = 11.240$.

agreement with the theoretical predictions. The coefficients of determination remain extremely high ($R^2 \gtrsim 0.999$), indicating that the waveform in this regime is almost entirely dominated by the fundamental QNM.

In contrast, for broader pulses ($\sigma \geq 7$) the tail contribution becomes significant already within the fitting window. This is reflected in the deterioration of the QNM-only fits, with noticeably lower R^2 values and systematic biases in both, the frequency and damping time. The augmented model including the tail partially stabilizes the fits, but the extracted parameters still exhibit increasing deviations as the waveform transitions more rapidly into the late–time power–law decay. In the extreme cases $\sigma = 9, 10$, the fitted frequency is underestimated by more than 50%, while the damping time is either strongly suppressed or inflated, indicating that the signal is no longer dominated by quasinormal ringing.

These systematic behaviours are summarized in Fig. 5.6, which displays the normalized frequency ($\omega_{\rm fit}/\omega_{\rm th}$) and damping time ($\tau_{\rm fit}/\tau_{\rm th}$), as functions of the Gaussian width. For small σ, both ratios remain tightly clustered around unity, whereas for larger σ they drift away, reflecting the increasing

contamination from the tail.

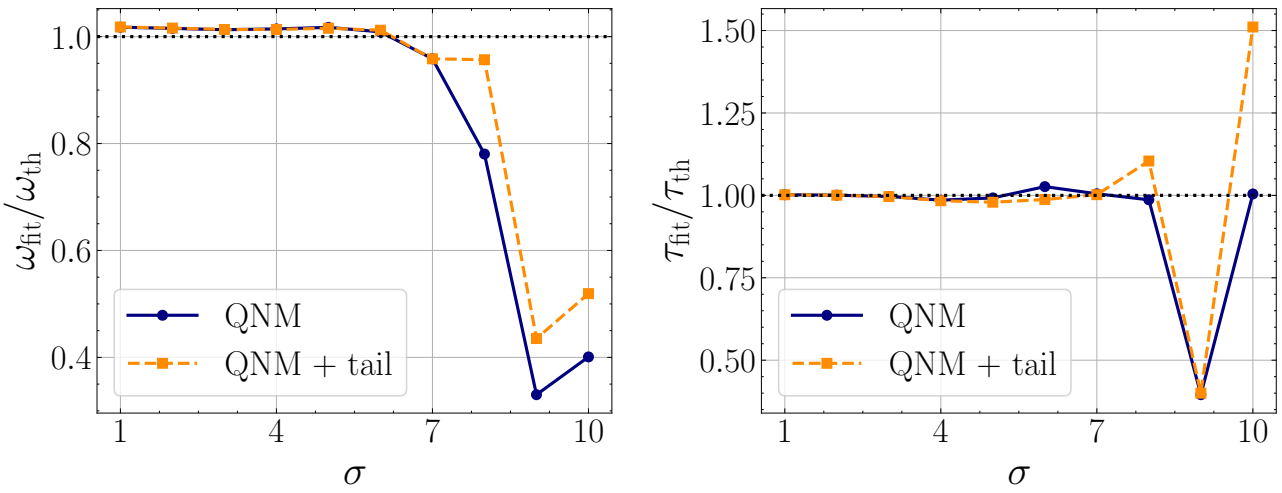


Figure 5.6: **Normalized QNM frequency and damping time as functions of the Gaussian width.** Blue markers correspond to pure QNM fits, while orange markers include both QNM and tail contributions. For $\sigma \leq 6$, the two approaches agree and are consistent with the theoretical predictions (dashed line). For $\sigma \geq 7$, the presence of the tail biases the extraction and leads to increasing deviations.

Finally, to complement the quantitative fits, Fig. 5.7 shows how the waveform morphology extracted at $r^*_{\rm obs} = 50$ evolves with the Gaussian width, displaying representative cases with $\sigma = 1, 5, 9$.

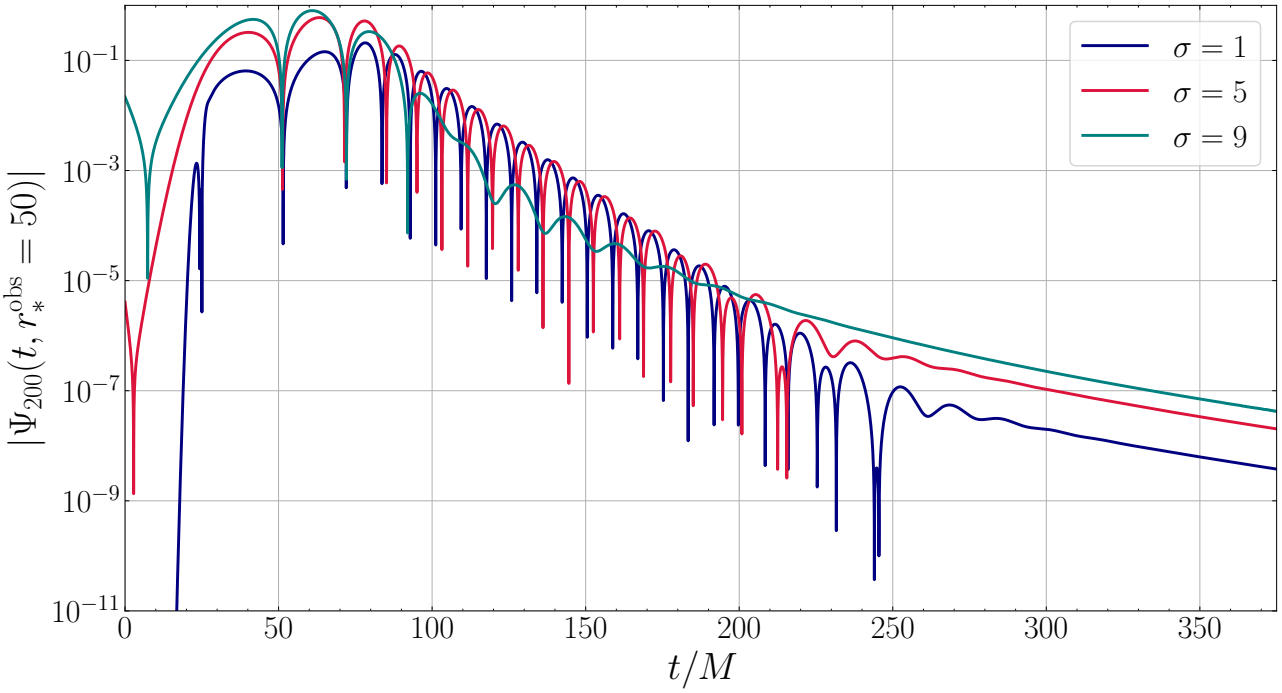


Figure 5.7: **Waveforms extracted at $r^*_{\rm obs} = 50$ for three representative values of the Gaussian width.** The cases $\sigma = 1, 5, 9$ illustrate the transition from a clean QNM-dominated ringdown ($\sigma = 1$) to a tail-dominated decay ($\sigma = 9$).

For the narrow pulse ($\sigma = 1$), the waveform exhibits a clean ringdown phase with well–defined

damped oscillations, fully dominated by the fundamental QNM before the transition to the late–time tail. For the intermediate case ($\sigma = 5$), the QNM ringing is still clearly visible, but the onset of the tail occurs earlier and reduces the effective fitting window. Finally, for the broad case ($\sigma = 9$), the power–law decay dominates almost immediately after the initial burst, and the QNM oscillations are strongly suppressed. This progressive change illustrates how the spectral content of the initial perturbation controls the relative importance of the QNM and tail regimes.

5.3.2 Asymptotic regime: late-time tails

The analysis of QNM frequencies in Sec. 5.3.1 is complemented here by a study of the asymptotic decay of the waveform at very late times. In this regime the signal is no longer governed by damped oscillations but by power-law tails. For massless fields in Schwarzschild spacetime, the late-time behaviour is expected to follow

$$\Psi(t) \sim B\, t^{-p}, \qquad t \gg M, \tag{5.8}$$

where the exponent p depends on the multipole index ℓ of the perturbation. For tensorial perturbations the theoretical prediction is $p = 2\ell + 3$. In the specific case $\ell = 2$, one obtains $p_{\rm th} = 7$.

To extract this exponent from the numerical data, a late-time window $t \in [350, 400]\, M$ is selected in the waveform for $\sigma = 1$, where the signal is clearly tail dominated. A linear fit on logarithmic axes is then performed,

$$\log|\Psi(t)| = \log B - p \log t, \tag{5.9}$$

which corresponds to fitting a straight line to the log–log plot of the signal amplitude. For $\sigma = 1$ the fit yields $p = 7.3334 \pm 0.0003$, consistent with the expected power-law decay.

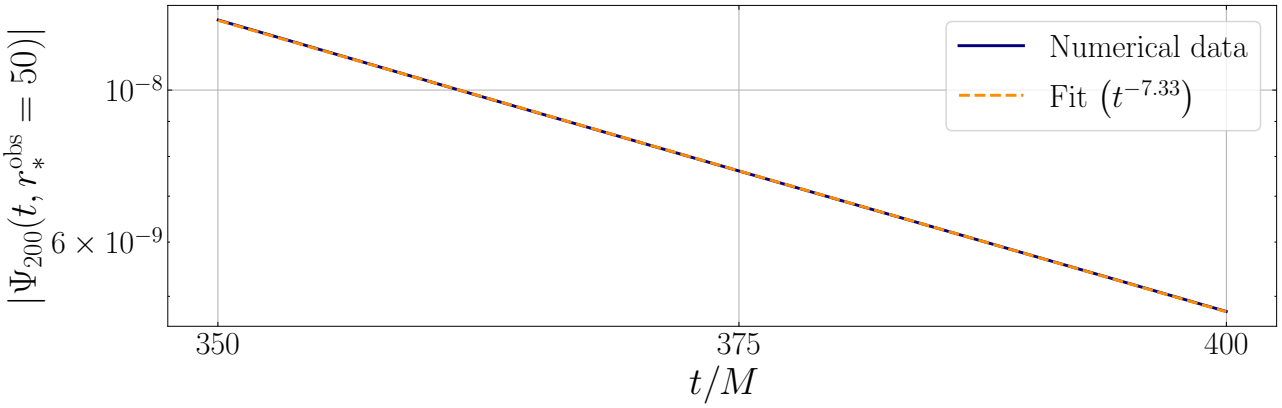


Figure 5.8: **Late-time power-law decay for $\sigma = 1$ on a logarithmic scale.** The numerical data (blue) is well fitted by the expected tail template (orange dashed line).

The results for the full set of simulations are presented in Table 5.4, reporting the fitted amplitude, its uncertainty, the power-law exponent with error estimates, and the ratio $(p/p_{\rm th})$.

The fitted exponents lie systematically above the theoretical prediction, with deviations that increase as σ grows. For narrow pulses the agreement is good, with $p/p_{\rm th} \approx 1.048$ and uncertainties at the 10^{-4} level. For broader pulses ($\sigma \gtrsim 8$), the quality of the fits deteriorates, leading to larger uncertainties in both p and the amplitude. In particular, for $\sigma = 10$ the fit yields $p = 7.4762 \pm 0.0230$, corresponding to a 6.8% deviation from the t^{-7} decay law. These results confirm the emergence of the expected

σ	B	B_{error}	p	p_{error}	p/p_{th}
1	7.811×10^{12}	1.440×10^{10}	7.333	0.0003	1.048
2	5.820×10^{10}	9.933×10^{7}	7.336	0.0003	1.048
3	9.089×10^{10}	1.404×10^{8}	7.340	0.0003	1.049
4	1.285×10^{11}	1.755×10^{8}	7.347	0.0002	1.050
5	1.770×10^{11}	2.170×10^{8}	7.359	0.0002	1.051
6	2.444×10^{11}	5.719×10^{8}	7.377	0.0004	1.054
7	3.159×10^{11}	1.689×10^{9}	7.388	0.0009	1.056
8	4.402×10^{11}	6.417×10^{9}	7.415	0.0025	1.059
9	5.447×10^{11}	3.582×10^{10}	7.424	0.0112	1.061
10	8.626×10^{11}	1.166×10^{11}	7.476	0.0230	1.068

Table 5.4: **Late-time tail fits in Schwarzschild.** Fitted amplitudes and power-law exponents for different Gaussian widths σ. The theoretical exponent is $p_{\text{th}} = 7$. Amplitudes are affected by systematic late-time biases and should not be taken as physical; the reliable observables are the σ-dependence and the stability of the exponent.

power-law tail, while indicating that broader initial data enhances contamination effects (finite-time windowing, residual QNMs, and numerical noise) that bias the exponent.

The extremely large tail amplitudes reported in Table 5.4 are an artifact of the fitting procedure: linear regression on a finite log–log window introduces an arbitrary vertical offset that is absorbed into the amplitude, yielding unphysical magnitudes. This does not compromise the extraction of the exponent, which is robust against such offsets. Later we recover the correct amplitudes through a consistent normalisation procedure. For the present discussion, the relevant information is the systematic variation of the fitted amplitudes with σ, rather than their absolute values.

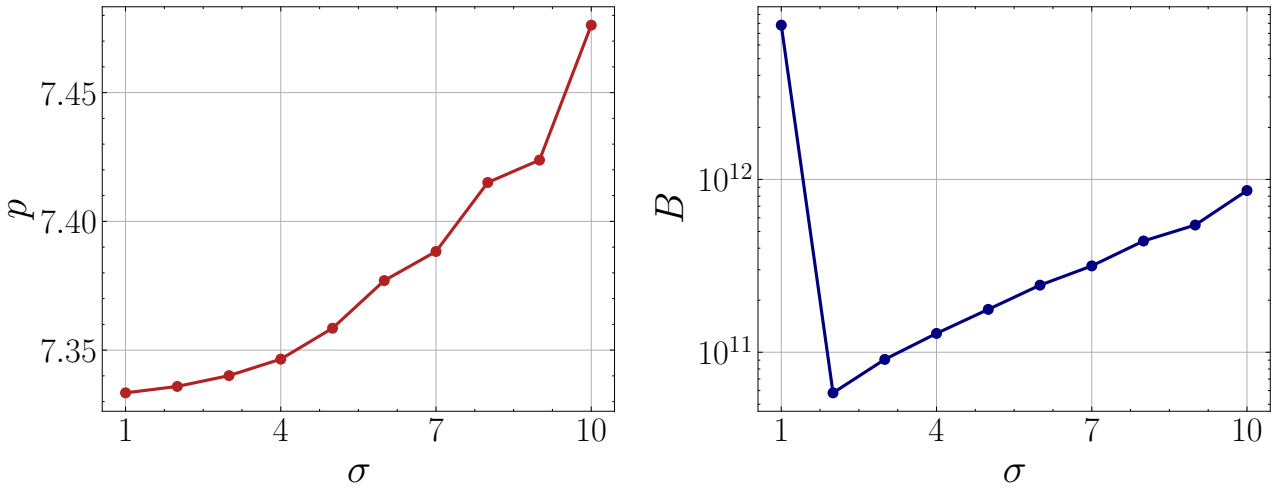


Figure 5.9: **Tail fits as a function of the Gaussian width.** Left: fitted power-law exponent p normalised by the theoretical value $p_{\text{th}} = 7$ as a function of σ. For $\sigma \lesssim 6$ the agreement is excellent, whereas broader pulses yield systematically larger exponents and growing uncertainties. Right: fitted tail amplitude as a function of σ, with markers showing the values obtained from the late-time power-law fits for each simulation.

5.3.3 Overtones analysis

So far, our analysis has focused exclusively on the fundamental mode ($n = 0$), either with or without the inclusion of a power–law tail. While this approach captures the dominant dynamics of the intermediate ringdown, it neglects potential contributions from higher overtones ($n \geq 1$). These modes, although more strongly damped, are generically excited by the initial perturbation and can leave a noticeable imprint on the early ringdown signal. To investigate their role, we now extend the fitting model to incorporate a finite number of overtones and analyze their relative importance as a function of the Gaussian width.

As in the previous section, we time–shift the waveform so that the fitting interval begins at $t = 0$. For the present analysis we restrict attention to the early ringdown window $t \in [90, 140]\, M$, where the contribution of overtones is expected to be most significant. The extended model represents the waveform as a superposition of damped sinusoids,

$$\Psi^{\rm fit}_{\rm QNM}(t) = \sum_{\ell mn} A_{\ell mn}\, e^{-t/\tau_{\ell mn}} \cos(\omega_{\ell mn} t + \phi_{\ell mn}). \tag{5.10}$$

where $\omega_{\ell mn}$ and $\tau_{\ell mn}$ denote the theoretical frequency and damping time of the n-th overtone, obtained from Leaver's continued–fraction method [61]. The amplitudes ($A_{\ell mn}$) and phases ($\phi_{\ell mn}$), in contrast, are determined through nonlinear fitting. In what follows we restrict to $n = 3$, i.e. the fundamental mode together with the first three overtones. The values ($\omega_{\ell mn}, \tau_{\ell mn}$) are fixed to their theoretical predictions, so that the fit directly probes the relative excitation amplitudes and phases.

To account for possible residual contamination from the asymptotic regime, we also consider an augmented template that supplements the overtone expansion with a power–law tail,

$$\Psi^{\rm fit}_{\rm QNM+tail}(t) = \sum_{\ell mn} A_{\ell mn}\, e^{-t/\tau_{\ell mn}} \cos(\omega_{\ell mn} t + \phi_{\ell mn}) + B\, t^{-p}, \tag{5.11}$$

so that any deviations from a purely quasinormal description can be absorbed by the additional tail parameters (B, p). Both templates are applied consistently to all simulations within the chosen time window. To illustrate the construction of the overtone models, let us consider explicitly the case with a single overtone ($n = 1$). The corresponding fitting template reads

$$\begin{aligned}\Psi^{\rm fit}_{201}(t) &= A_{200}\, e^{-t/\tau_{200}} \cos(\omega_{200}\, t + \phi_{200}) + A_{201}\, e^{-t/\tau_{201}} \cos(\omega_{201}\, t + \phi_{201}) \\ &= A_{200}\, e^{-0.0889623\, t} \cos(0.373672\, t + \phi_{200}) + A_{201}\, e^{-0.273915\, t} \cos(0.346711\, t + \phi_{201}).\end{aligned} \tag{5.12}$$

where the frequencies and damping times of both modes are also fixed to their theoretical values, while the amplitudes (A_{200}, A_{201}) and phases (ϕ_{200}, ϕ_{201}) are determined by nonlinear least–squares fitting too. This procedure is then extended by successively including higher overtones up to $n = 3$, applied consistently to both the pure QNM model and the augmented QNM+tail model.

The quality of these fits is illustrated in Fig. 5.10. The upper panel shows the numerical waveform together with the best–fit models including up to three overtones. The curves overlap almost perfectly, indicating that the fundamental mode already captures the dominant dynamics, while higher overtones provide only minor corrections. The lower panel quantifies these corrections by displaying the differences between successive models and the absolute contributions of the first two overtones. At the beginning of the fitting interval the overtones contribute at the level of 10^{-2}–10^{-3}, but their effect decays rapidly due to their stronger damping. The differences between consecutive models remain very small, confirming that additional overtones improve the fit only marginally once the fundamental mode is included.

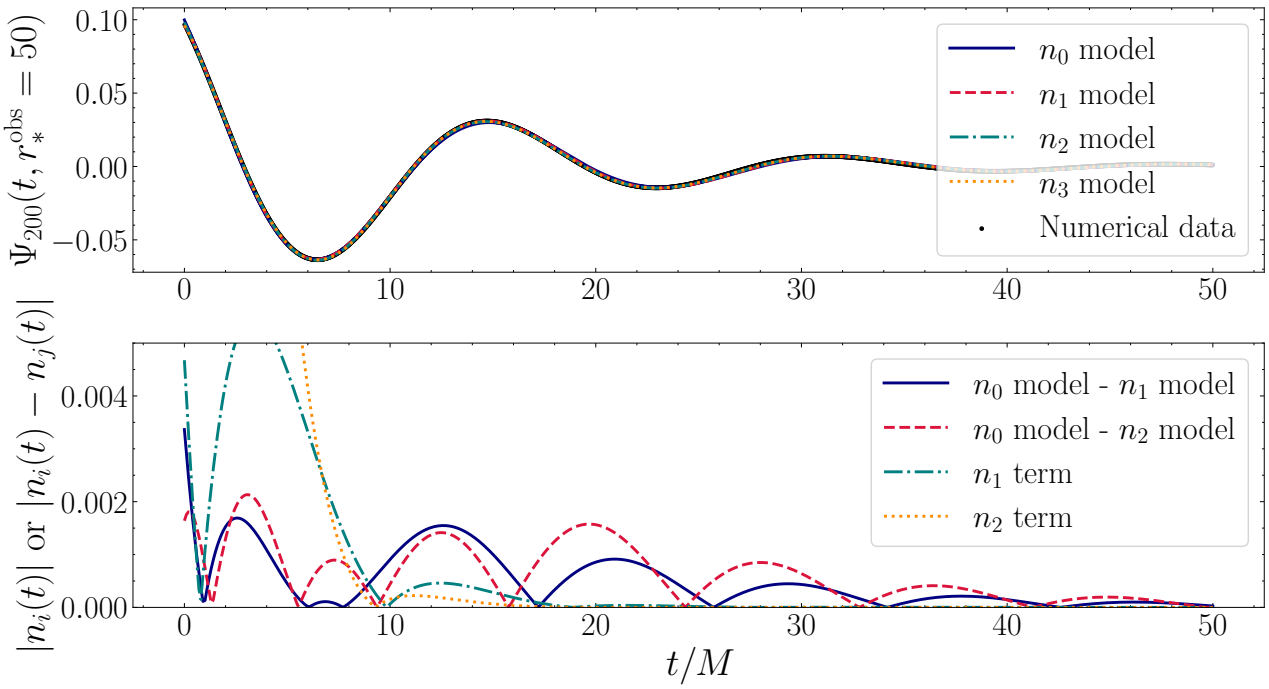


Figure 5.10: **Comparison of overtone QNM fits.** Top: numerical data versus models including up to $n = 3$. Bottom: differences between successive models and absolute contributions of the first two overtones.

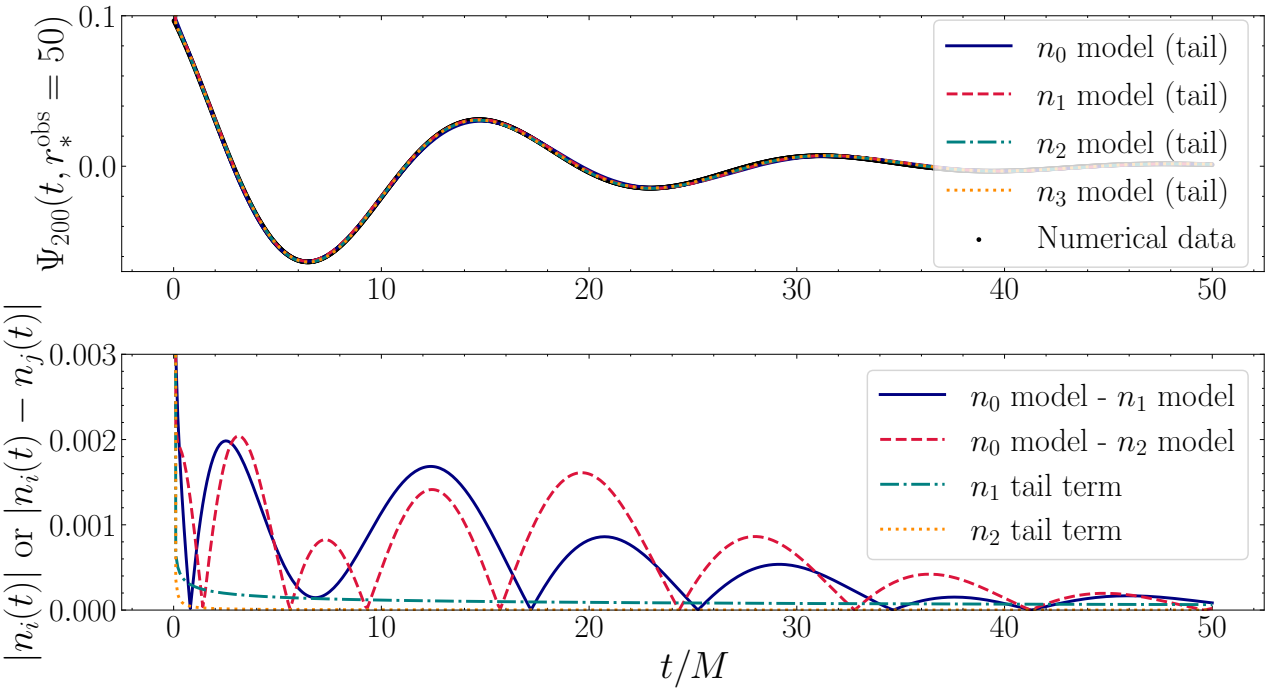


Figure 5.11: **Comparison of overtone QNM + tail fits.** Top panel compares numerical data with QNM models including up to $n = 3$ with power-law tails, while the bottom panel shows the differences between successive models together with the absolute contributions of the first two tail terms.

The same analysis can be repeated with the extended models that include a power–law tail in addition to the overtone expansion. Figure 5.11 shows the corresponding fits. The upper panel confirms that the inclusion of the tail does not significantly alter the reconstruction within the interval $t \in [90, 140]\, M$: the waveform is again very well captured by the fundamental mode, with overtones providing only minor corrections. The lower panel shows that the residual differences between successive models remain of the same order as in the pure QNM case, while the tail contribution is numerically negligible in this regime. This demonstrates that, within the chosen window, the extracted dynamics are insensitive to the addition of a power–law term, and that higher overtones dominate over the tail.

The plot in Fig. 5.12 displays the amplitude ratios $A^R_{20n} = A_{20n}/A_{200}$ for the first ($n = 1$) and second ($n = 2$) overtones as functions of the Gaussian width σ. Solid lines correspond to pure QNM fits, while dashed lines include an explicit tail contribution in the fitting model. For narrow pulses ($\sigma \lesssim 6$), all ratios remain close to zero, showing that the waveform is dominated by the fundamental mode, with only a small excitation of the first overtone. Once the Gaussian width reaches $\sigma \approx 7$, however, the ratios increase sharply as the tail contribution enters the fitting window.

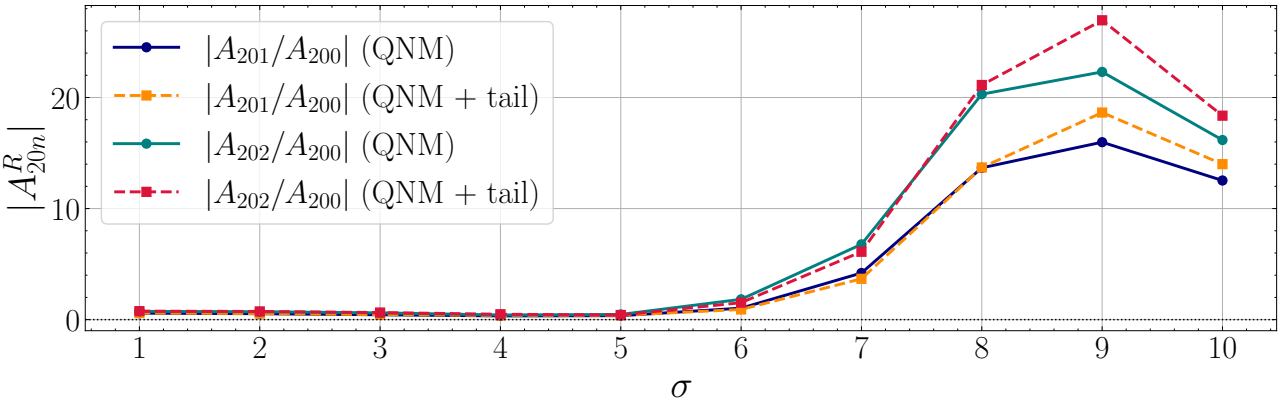


Figure 5.12: **Amplitude ratios for $n = 1$ and $n = 2$.** Extracted from numerical ringdown fits as a function of the Gaussian width σ. Solid lines show fits including only QNMs, while dashed lines also include the late–time tail. Blue and orange correspond to $|A_{201}/A_{200}|$, and green and red to $|A_{202}/A_{200}|$.

From this point on, the second overtone ratio (A^R_{202}) already exceeds unity, implying—if taken literally—that the overtone dominates over the fundamental mode. This interpretation is unphysical: what actually occurs is that the fitting model, unable to fully capture the tail, assigns part of its contribution to the second overtone. Including the tail in the fit (dashed curves) mitigates this artificial enhancement but does not remove it completely. The key conclusion is that overtone amplitudes can only be extracted reliably for $\sigma \lesssim 6$, where the tail is negligible. For broader pulses, the fitted ratios are contaminated by the tail and therefore lose their physical meaning.

Figure 5.13 extends the analysis to the third overtone. While the first overtone remains moderate even for large σ, both the second and especially the third overtone show a dramatic growth once $\sigma \gtrsim 7$. The extracted ratios reach values well above one hundred, far beyond any physically meaningful excitation of subdominant modes. This behaviour highlights the intrinsic limitation of the fitting procedure: when the tail is not properly isolated, its contribution is redistributed among the higher overtones, and the effect becomes more pronounced as the overtone index increases. Including the tail in the template (dashed curves) may alleviate the problem but cannot prevent the artificial enhancement.

Therefore, the third overtone provides a clear diagnostic of the breakdown of the fitting model: its unphysical growth serves as a quantitative signal that the extraction of overtone amplitudes has ceased to be reliable.

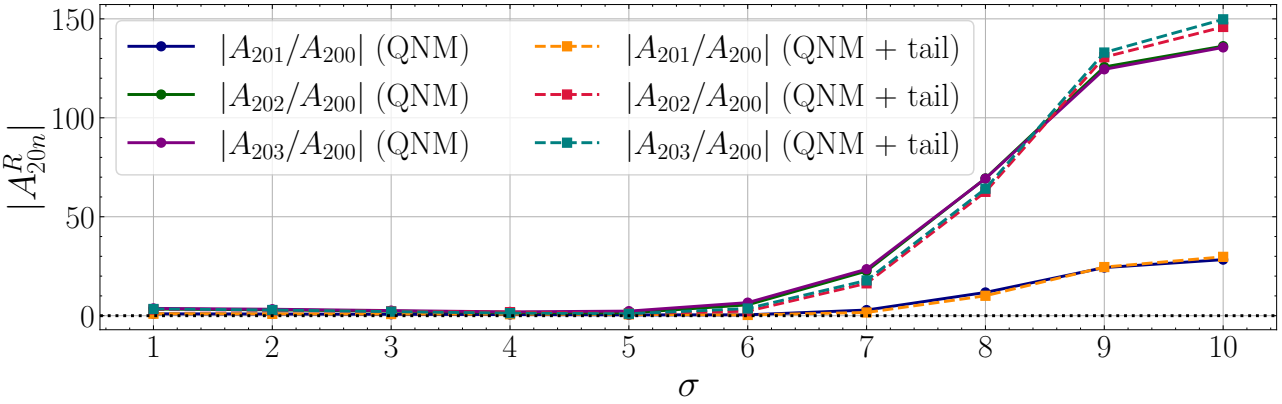


Figure 5.13: **Amplitude ratios up to $|A_3/A_0|$.** Amplitude ratios up to $|A_3/A_0|$ for the third overtone as a function of the Gaussian width.

5.3.4 Tail starting time

The transition from quasinormal ringing to the late–time tail is gradual: the exponentially damped QNMs are progressively overtaken by the power–law decay. To quantify this transition in each simulation, we define the *tail starting time* as the instant when the signal ceases to be dominated by exponentially decaying oscillations and enters a monotonic power–law regime. To determine this time in a robust way, we restrict the analysis to the interval $t \in [100, 400]\, M$, which excludes the prompt response and contains only the ringdown and the tail. Within this window the signal is rescaled by an exponential factor,

$$\Psi_{\text{transf}}(t) = \Psi_{200}(t)\, e^{t/\tau_{200}}, \tag{5.13}$$

where τ_{200} denotes the damping time of the fundamental mode. This transformation removes the leading exponential decay, leaving the residual evolution to highlight deviations from pure QNM behaviour. Figure 5.14 illustrates this procedure: the left panel shows the original waveform within the restricted window, while the right panel displays the rescaled signal, where the onset of the tail appears as a clear departure from the late–time plateau.

To suppress the rapid oscillations associated with the quasinormal ringing and uncover the slower underlying trend, we apply a moving average to the absolute value of the transformed signal,

$$\Psi_{\text{smooth}}(t_k) = \frac{1}{r}\sum_{j=0}^{r-1} \left|\Psi_{\text{transf}}(t_{k-j})\right|, \qquad k = r, \ldots, m, \tag{5.14}$$

where r is the averaging window.[1] This operation acts as a low–pass filter: the fast oscillatory content of the QNM and possible overtones is averaged out, leaving a slowly varying envelope. Physically, this envelope captures the long–timescale behaviour of the waveform, where the transition from exponential decay to the power–law tail becomes apparent. Figure 5.15 illustrates the procedure. The

[1] This corresponds to the implementation of `MovingAverage[list, r]` in Mathematica, which computes the arithmetic mean of each window of r consecutive elements.

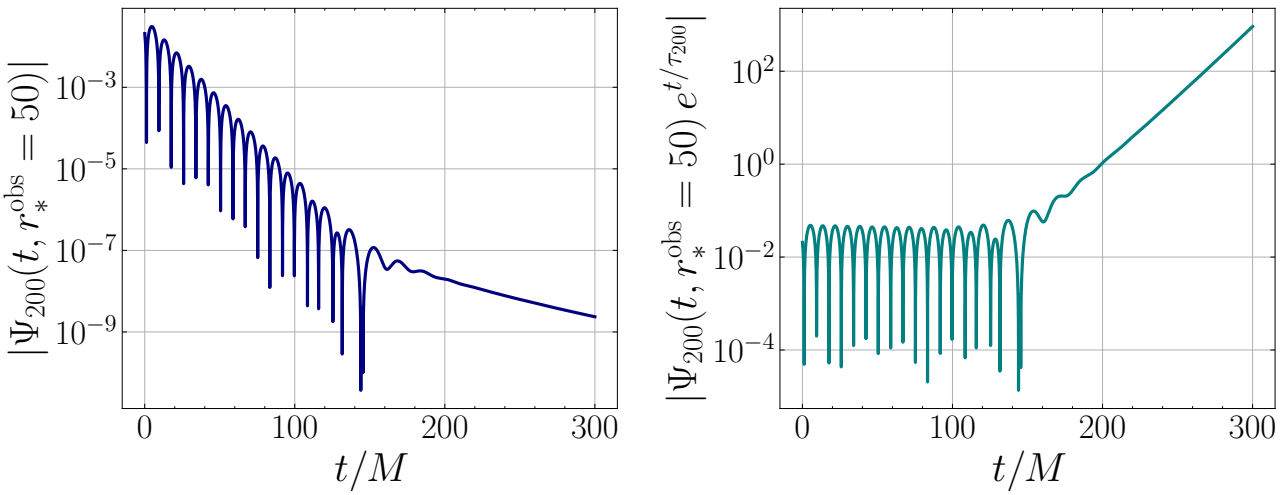


Figure 5.14: **Procedure to reveal the onset of the tail.** Left: raw waveform restricted to the fitting window. Right: rescaled signal $(\Psi_{200}(t, r_*^{\rm obs} = 50)\, e^{t/\tau_{200}})$, where the onset of the power-law tail manifests as a departure from flat behaviour.

raw transformed signal (teal) exhibits strong oscillations, while the moving–averaged curve (dashed red) smooths out these fluctuations and highlights the underlying trend. At early times the smoothed signal remains nearly constant, consistent with the QNM–dominated regime, and later it shows a clear monotonic growth, marking the onset of the tail.

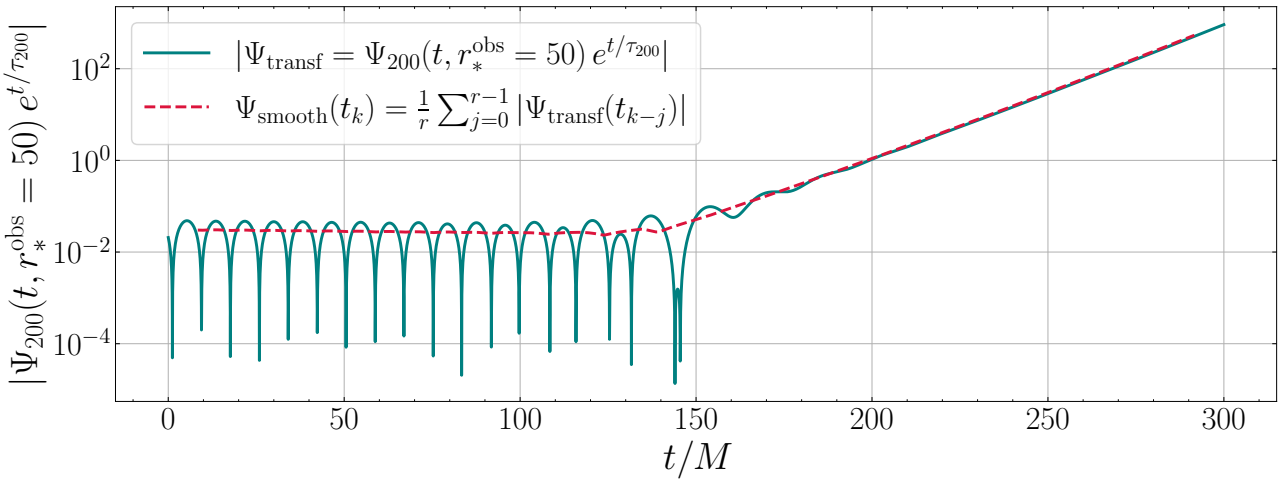


Figure 5.15: **Determination of the tail starting time.** The raw transformed signal (teal) shows fast oscillations, while the moving–averaged curve (dashed red) reveals the slow trend. The onset of the tail is visible as the transition from flat behaviour to monotonic growth.

To determine the onset of the tail quantitatively, we identify the last local minimum of $\Psi_{\rm smooth}$ before it begins its monotonic growth.

Local minima are detected by comparing neighbouring points,

$$\Psi_{\text{smooth}}(t_i) < \Psi_{\text{smooth}}(t_{i-1}), \tag{5.15a}$$

$$\Psi_{\text{smooth}}(t_i) < \Psi_{\text{smooth}}(t_{i+1}), \tag{5.15b}$$

for a sequence of discrete times $\{t_i\}$. The index of the last such minimum is denoted i_*, and the corresponding time is taken as the tail starting time,

$$t_{\text{tail}} = t_{i_*}, \quad \Psi_{\text{smooth}}(t_{\text{tail}}) = \Psi_{\text{smooth}}(t_{i_*}). \tag{5.16}$$

Figure 5.16 shows the procedure for $\sigma = 1$, with the full smoothed signal on the left and a zoom into the late–time minimum on the right. The resulting tail starting times t_{tail} are summarised in Figure 5.17: for narrow pulses the transition occurs relatively late, while for broader ones it shifts progressively earlier, with the tail dominating soon after the prompt burst.

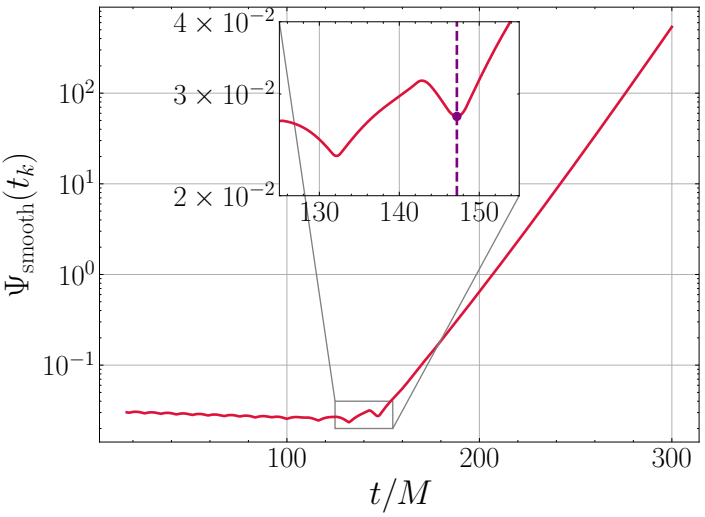


Figure 5.16: **Smoothed waveform $\Psi(t, r_*^{\text{obs}} = 50)\, e^{t/\tau_{200}}$ with a zoomed-in region around the local minimum at $t \approx 147\,M$.** The inset highlights the deviation that signals the onset of the tail.

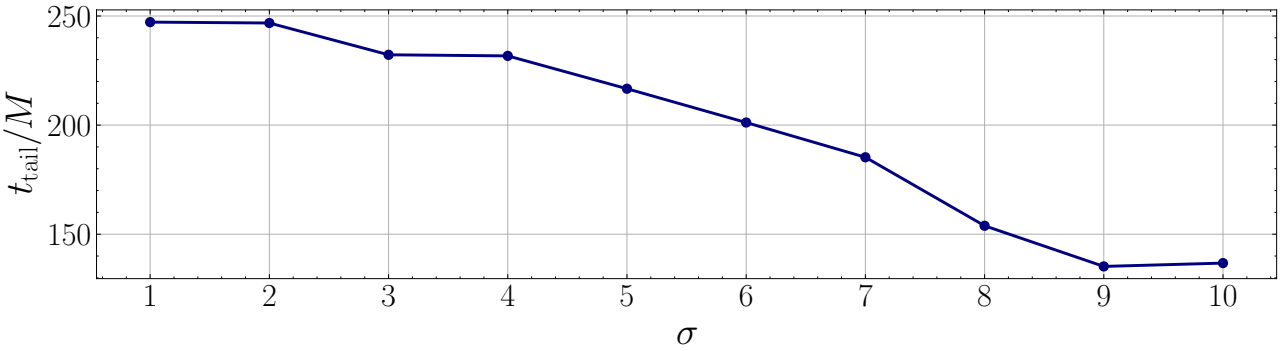


Figure 5.17: **Tail onset vs. Gaussian width.** Starting time of the late–time decay as a function of σ. Larger widths lead to an earlier onset, reflecting a faster transition from the quasinormal ringing to the tail.

5.3.5 Recovery of the tail amplitude

In the previous section we determined the onset time of the late–time tail. We now turn to a direct measurement of its amplitude and exponent. The starting point is, again, the numerical waveform in the asymptotic regime, modeled as a superposition of the fundamental QNM and the power–law tail,

$$\Psi_{200}(t) \;\approx\; A_{200}\, e^{-t/\tau_{200}} \cos(\omega_{200} t + \phi_{200}) \;+\; B\, t^{-p}. \tag{5.17}$$

Taking the absolute value and applying a moving average suppresses the oscillations of the cosine, leaving a smoothed signal of the form

$$\Psi_{\text{smooth}}(t) \;\approx\; A_{200}\, e^{-t/\tau_{200}} \;+\; B\, t^{-p}. \tag{5.18}$$

This makes explicit the two slowly varying components: an exponential decay and a power–law term. To isolate the latter, we multiply by an exponential factor that cancels the leading QNM decay,

$$\Psi_{\rm transf}(t) \;=\; \Psi_{\rm smooth}(t)\, e^{t/\tau_{200}} \;\approx\; A \;+\; B\, t^{-p} e^{t/\tau_{200}}. \tag{5.19}$$

After this transformation the QNM contribution reduces to a constant A, while the tail appears as a growing correction. It is convenient to define the auxiliary variable

$$T(t) \;=\; t^{-p}\, e^{t/\tau_{200}}, \tag{5.20}$$

so that the transformed signal acquires the linear form

$$\Psi_{\rm transf}(t) \;\approx\; A \;+\; B\, T(t). \tag{5.21}$$

In this representation, tail extraction reduces to a linear regression: fixing $p_{\rm th} = 7$, the transformed signal $\Psi_{\rm transf}$ is fitted as a straight line in T, with intercept A (residual fundamental QNM) and slope B (tail amplitude). Using a time window (e.g. $t \in [100, 350], M$), applying the moving average and transformation (5.19), and fitting the data with (5.21), we directly obtain

$$\Psi_{\rm fit}(t) \approx 1104.53 + 4.13417 \times 10^{9}\; t, \tag{5.22}$$

from which the amplitude at $t = 247.2$ is

$$B = 4.13417 \times 10^{9} \cdot 247.2^{-7} = 7.33 \times 10^{-8}. \tag{5.23}$$

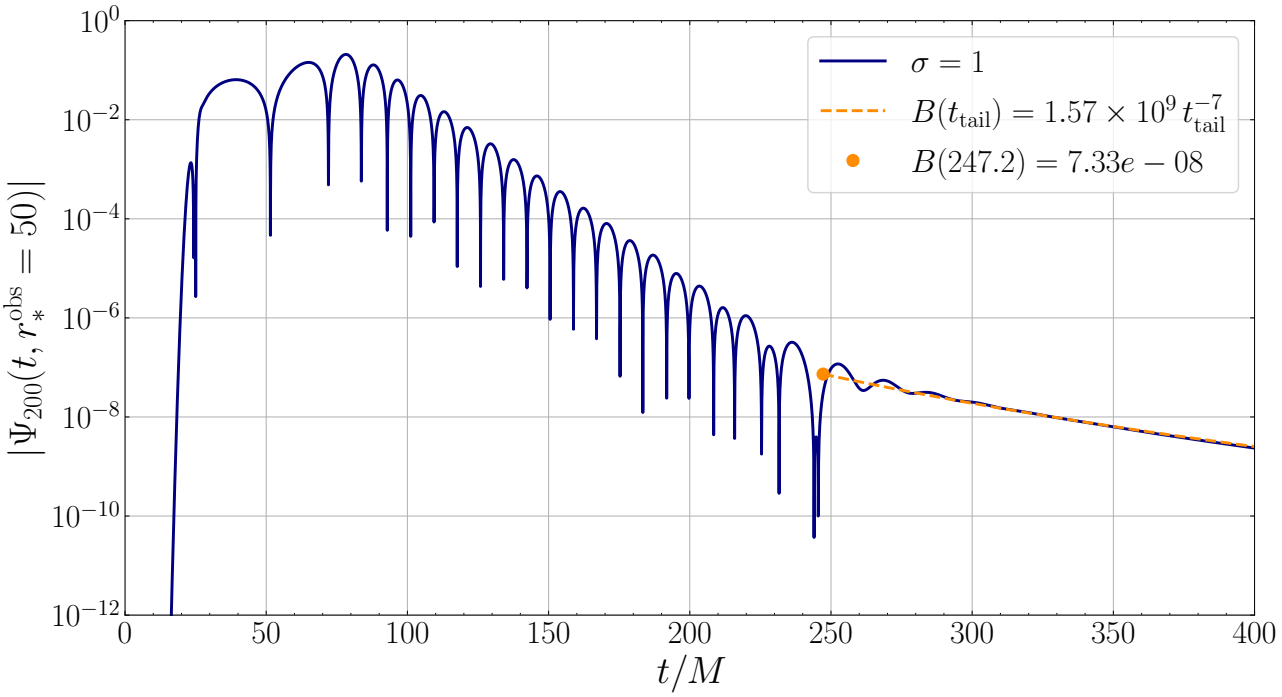


Figure 5.18: **Recovered tail amplitude for $\sigma = 1$.** The dashed line shows the extrapolated tail from the starting time, while the orange marker indicates the amplitude recovered at $t = 247.2\, M$.

5.3.6 Prompt response

The prompt response is highly sensitive to the width of the initial perturbation. Figure 5.19 compares the time evolution of the field for $\sigma \in \{1, \ldots, 10\}$: narrow pulses ($\sigma \lesssim 4$) yield weaker signals starting later, while broader ones ($\sigma \gtrsim 5$) produce an earlier and stronger excitation.

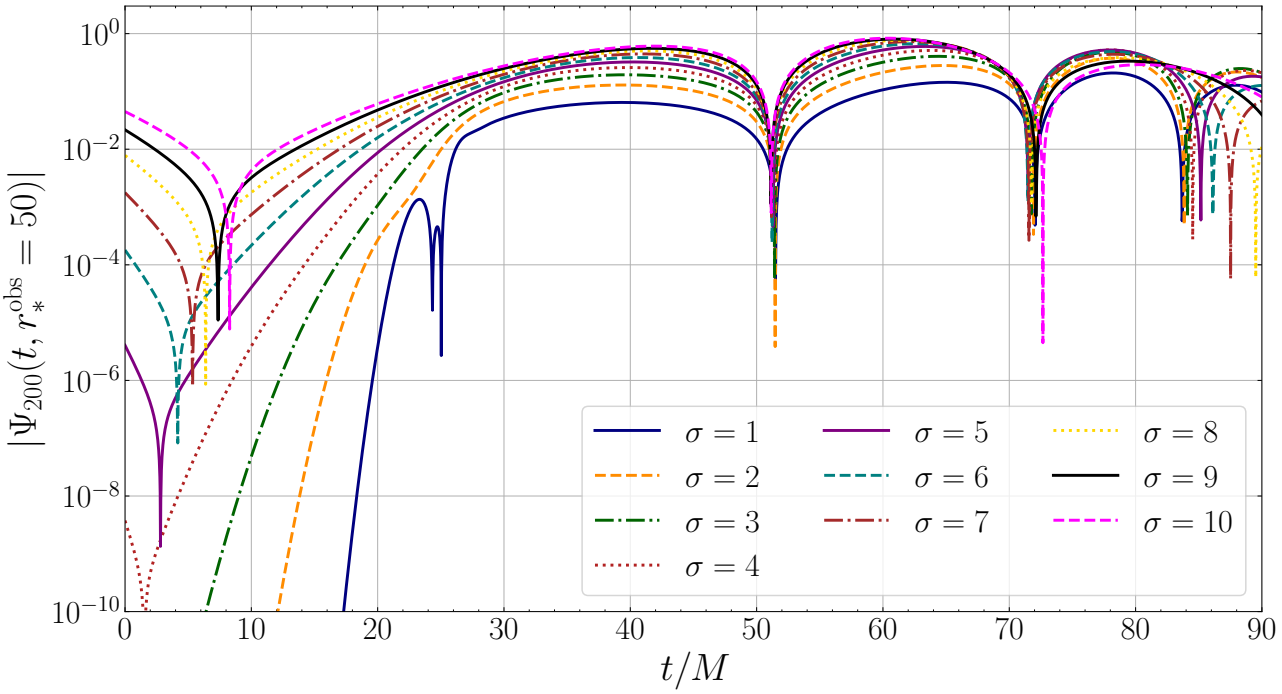


Figure 5.19: **Time evolution of the perturbed field** $|\Psi(t, r_{\rm obs} = 50)|$ for $\sigma \in \{1, \ldots, 10\}$ with $a = 0.0$, $l = 2$. Narrow pulses yield a delayed, weaker signal, while broad ones lead to an earlier and stronger response.

To quantify this, we measure the prompt duration $t^{\rm end}_{\rm prompt}$ and the maximum amplitude $A_{\rm max}$ as functions of σ. As shown in Fig. 5.20, $t^{\rm end}_{\rm prompt}$ remains nearly constant up to $\sigma \simeq 4$ ($t \sim 78M$),

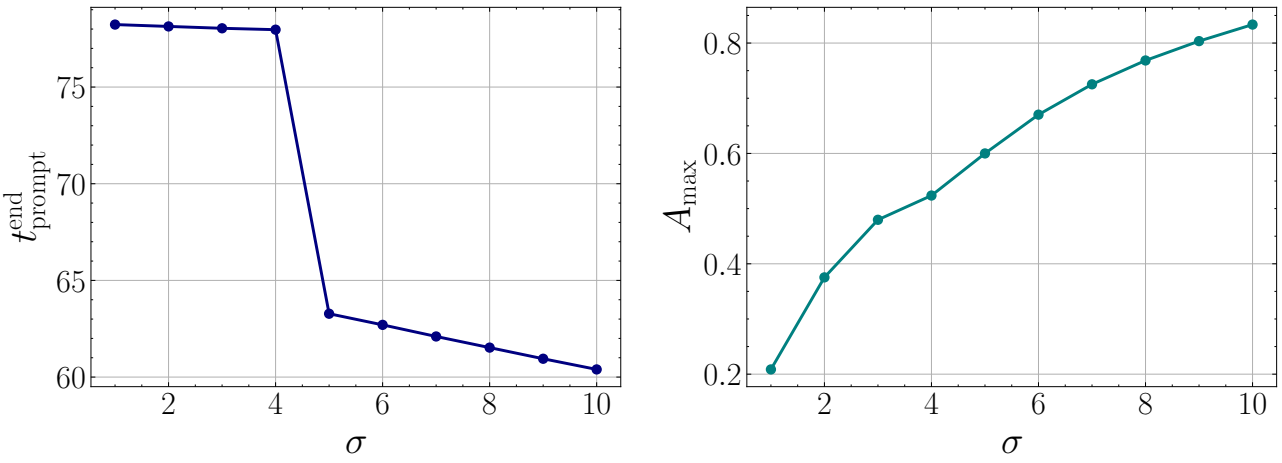


Figure 5.20: **Dependence of the prompt response on σ.** Left: end time $t^{\rm end}_{\rm prompt}$. Right: maximum amplitude $A_{\rm max}$. Narrow pulses last longer and are weaker, while broad ones are shorter and stronger.

then drops abruptly to $t \sim 60M$, while $A_{\max}$ increases monotonically with σ, confirming that broader pulses excite the BH more efficiently.

Having determined the prompt duration and the tail onset, we can clearly separate each waveform into three stages: prompt response, quasinormal ringing, and late–time tail. Figure 5.21 illustrates this classification for $\sigma = 1, 5, 9$.

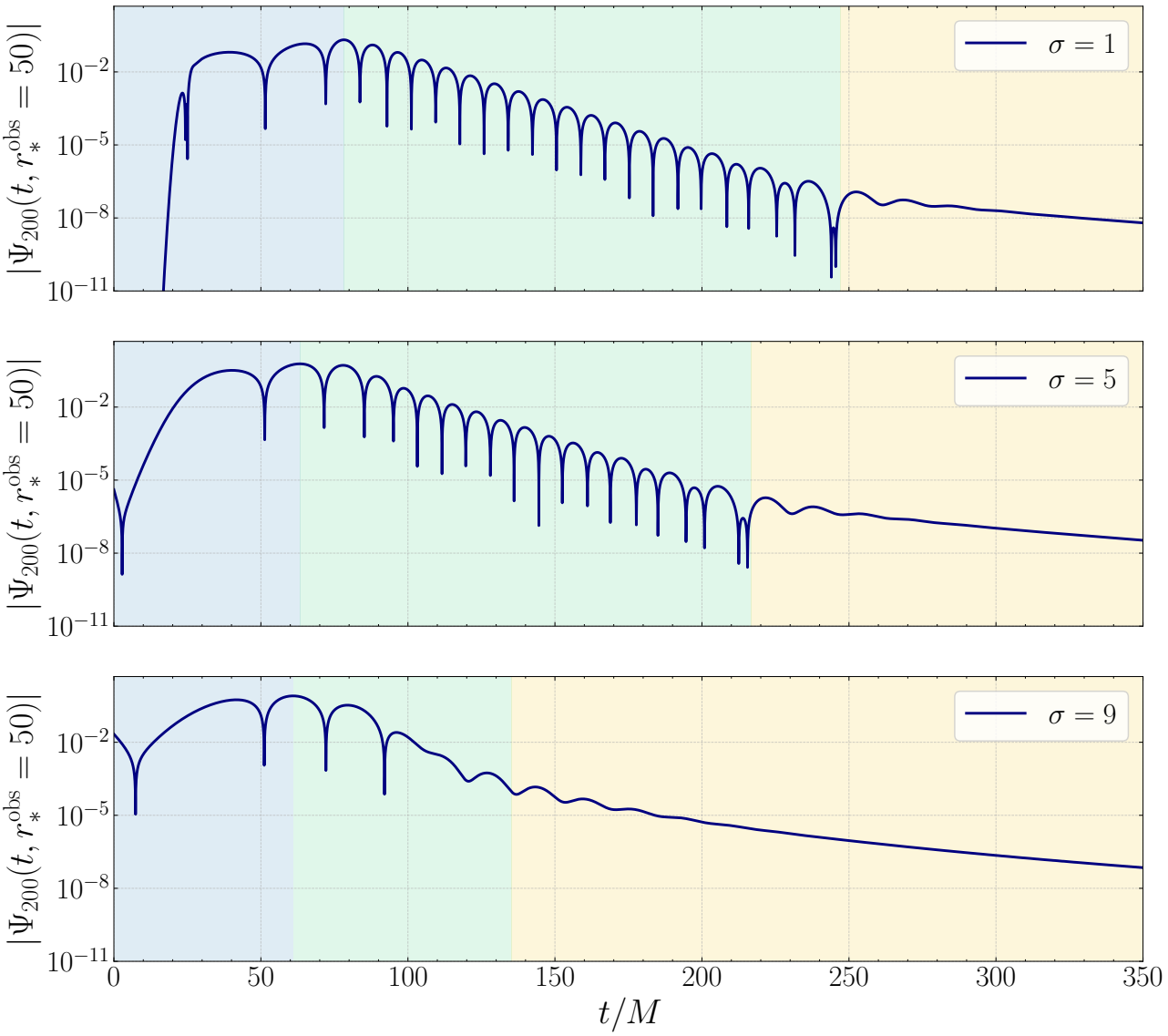


Figure 5.21: **Three dynamical phases for $\sigma = 1, 5, 9$.** The shaded regions indicate the different regimes: blue for the prompt response, green for the QNM ringing, and yellow for the late–time tail. Vertical lines mark the onset of the QNM phase and the tail starting time.

5.4 Tests for changing the frequency

To complement the study of how the Gaussian width shapes the ringdown dynamics, we now investigate the role of the carrier frequency (ω_0) of the initial perturbation. Varying ω_0 provides direct control over the spectral overlap between the injected pulse and the quasinormal spectrum of the BH. In

particular, values of ω_0 close to the fundamental frequency are expected to maximize the excitation of the dominant QNM, while strongly off–resonant choices should suppress it and enhance the relative importance of subdominant features such as overtones and late–time tails.

The injection frequency is sampled over the range

$$\omega_0 \in \{0.185,\ 0.247,\ 0.308,\ 0.370,\ 0.432,\ 0.493,\ 0.555,\ 0.617,\ 0.678,\ 0.740\}, \tag{5.24}$$

and the analysis follows the same steps as in the σ–variation: the waveforms are extracted at $r_*^{\rm obs} = 50$, shifted to a common fitting window, and analyzed with both the pure QNM template and the extended QNM+tail model.

5.4.1 QNM extraction

The results of the fitting analysis for different values of ω_0 are summarized in Fig. 5.22, which compares the extracted frequency and damping time from pure QNM fits and from extended QNM+tail fits. Both models reproduce the theoretical predictions with excellent accuracy when ω_0 is tuned close to the fundamental frequency ($\omega_{200} \simeq 0.374$). In this resonant regime, the fitted frequency and damping time ratios are essentially unity, and the extracted amplitude (Fig. 5.23) reaches its maximum, confirming efficient excitation of the fundamental mode.

Away from resonance, systematic deviations emerge. For both low and high frequencies, the fitted frequency develops a slight upward bias, while the damping time tends to be overestimated. These discrepancies grow with detuning, reaching about 6–7% at the edges of the frequency range. The origin of this behaviour is clear in the waveforms (Fig. 5.24): off-resonant pulses excite the fundamental QNM only weakly, so the late-time tail becomes dominant almost immediately, contaminating the ringdown fit.

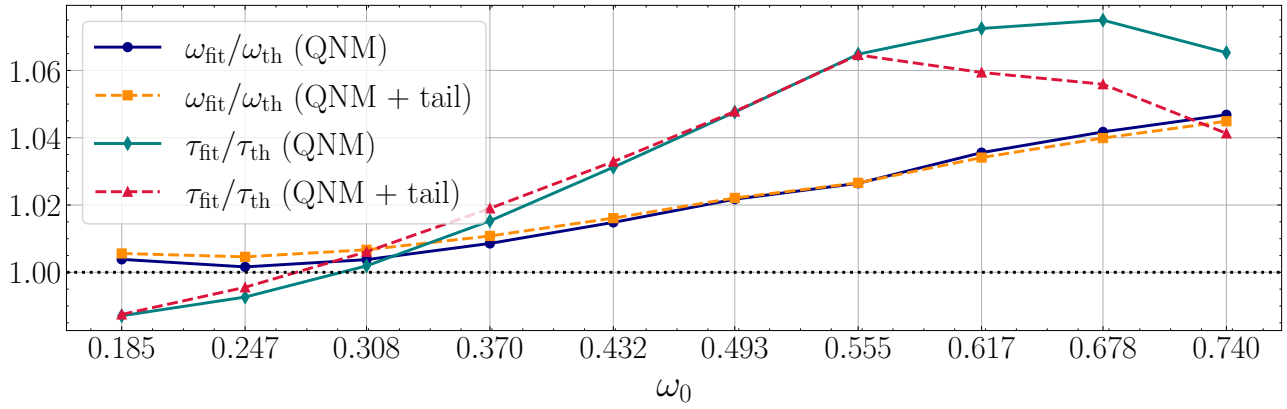


Figure 5.22: **Normalised frequency and damping time as a function of the driving frequency ω_0.** Solid lines: pure QNM fits. Dashed lines: QNM+tail fits. Both models agree well with theory near resonance, while deviations appear away from it; the inclusion of the tail reduces these deviations slightly, especially in the damping time.

The inclusion of an explicit tail contribution partly mitigates this issue. As seen in Fig. 5.22, the QNM+tail fits (orange/red curves) show slightly more stable behaviour away from resonance, especially for the damping time, where the pure QNM model tends to drift upwards more strongly. However, the improvement is modest: the fitted amplitudes remain virtually unchanged (Fig. 5.23), and significant

deviations persist at large detuning. This indicates that the limitation is not the fitting model itself but the weak excitation of the mode when ω_0 lies far from resonance.

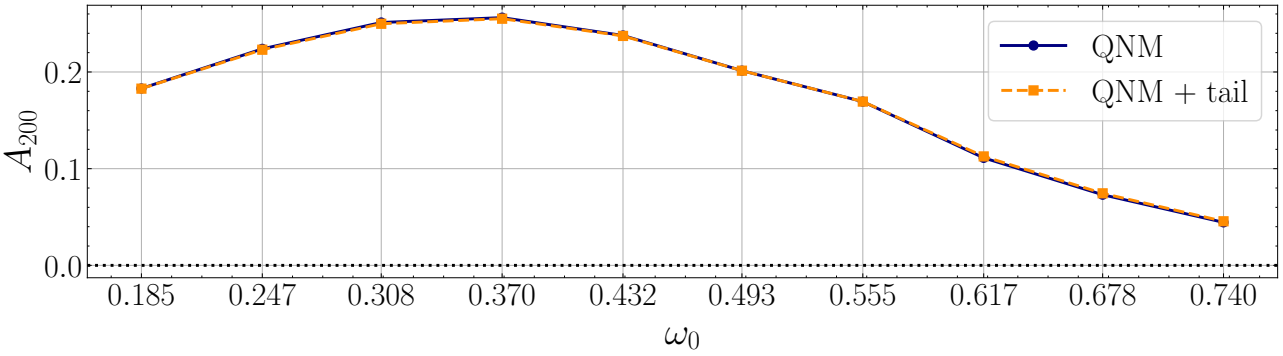


Figure 5.23: **Fitted amplitude versus ω_0.** The excitation peaks near resonance and decreases away from it. QNM and QNM+tail fits give nearly identical amplitudes, indicating that the extended model mainly improves damping time stability.

Altogether, these results establish a consistent picture: reliable extraction of quasinormal parameters requires initial data tuned to excite the fundamental mode efficiently. This occurs only within a narrow frequency window around $\omega_0 \simeq \omega_{\rm th}$, while outside this regime the tail contribution dominates and the quasinormal ringing is quickly suppressed.

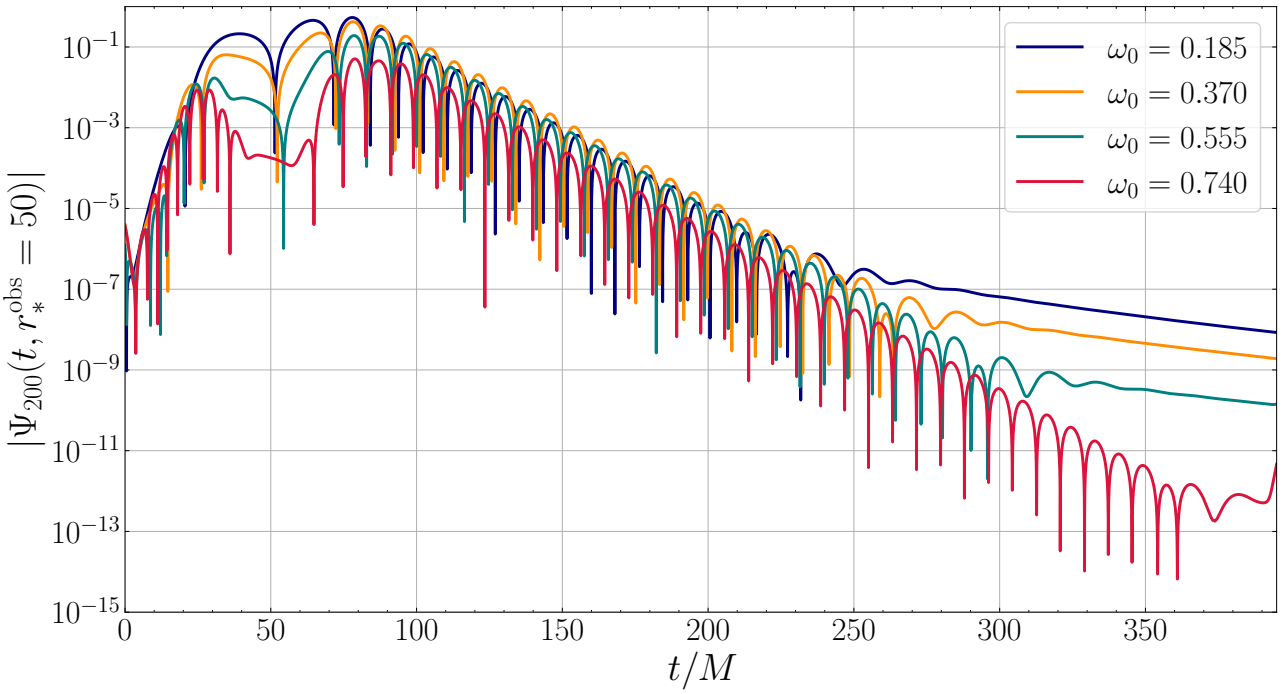


Figure 5.24: **Waveforms for $\omega_0 = 0.185, 0.370, 0.555, 0.740$.** Off-resonance cases (blue and red) are tail-dominated almost immediately after the burst, suppressing quasinormal ringing, whereas near resonance ($\omega_0 = 0.370$) the signal develops a long-lived quasinormal stage that enables accurate parameter extraction.

5.4.2 Late–time tails

Figure 5.25 summarizes the tail fits as a function of the driving frequency ω_0. The amplitude (right panel) decreases almost monotonically by several orders of magnitude as ω_0 grows, showing that broader spectral content (low ω_0) excites the tail more efficiently, while sharply tuned perturbations yield only a weak late–time signal. The absolute values are not physical, but the scaling with ω_0 is robust.

The exponent (left panel) lies slightly above the theoretical $p_{\rm th} = 7$ at low frequencies and converges towards it for larger ω_0, although numerical noise dominates for $\omega_0 \gtrsim 0.6$. Thus, low–frequency perturbations produce strong but mildly biased tails, whereas high–frequency ones leave only a faint signal after the QNM ringing. Both the σ– and ω_0–scans confirm that the tail excitation is dictated by the spectral width of the initial data.

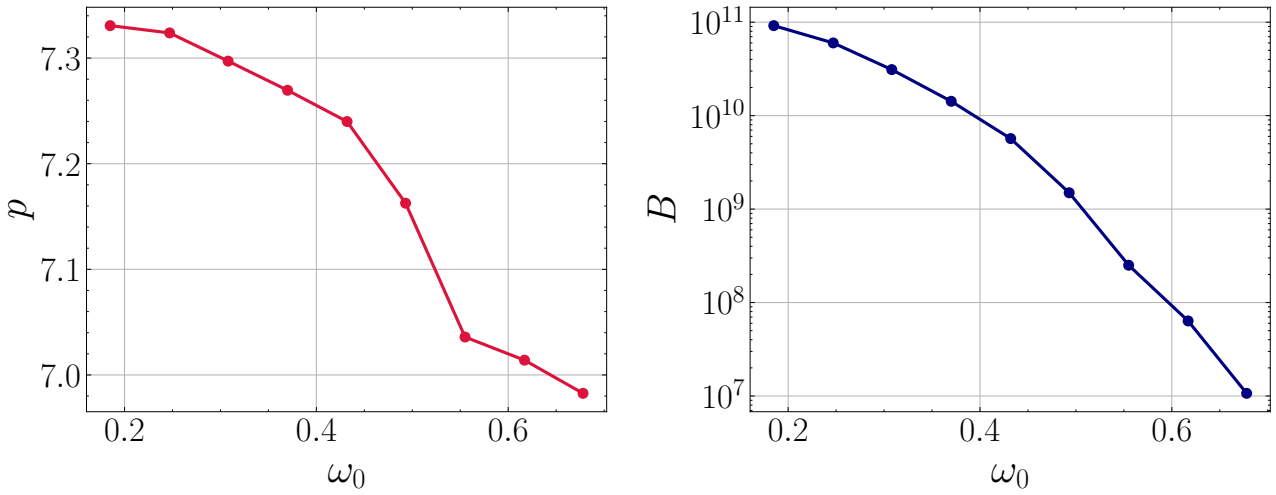


Figure 5.25: **Tail exponent and amplitude versus ω_0.** Left: the fitted exponent p lies above the theoretical value ($p_{\rm th} = 7$) at low frequencies and approaches it as ω_0 increases, but becomes unreliable for $\omega_0 \gtrsim 0.6$ due to numerical errors. Right: the tail amplitude decreases nearly monotonically over several orders of magnitude; its absolute value is not physical, but the relative scaling with ω_0 is robust.

5.4.3 Overtones

Figure 5.26 summarizes the dependence of the first and second overtones on the carrier frequency ω_0 of the initial Gaussian, showing the amplitude ratios A^R_{201} and A^R_{202} for both pure QNM and extended QNM+tail fits; at low ω_0 the waveform is almost entirely dominated by the fundamental, while increasing ω_0 leads to steadily larger ratios, with the first overtone approaching the strength of the fundamental and the second becoming non–negligible, although this apparent growth reflects the reduced excitation of the fundamental away from resonance rather than a genuine dominance of the overtones, and the inclusion of a tail contribution only produces minor quantitative shifts without altering the overall trend.

To clarify the relative role of each mode, Fig. 5.27 displays the ratios of the cosine–projected amplitudes with respect to the fundamental. This representation highlights the in–phase contributions, avoiding spurious amplification from phase shifts, and shows clearly that while the first overtone can

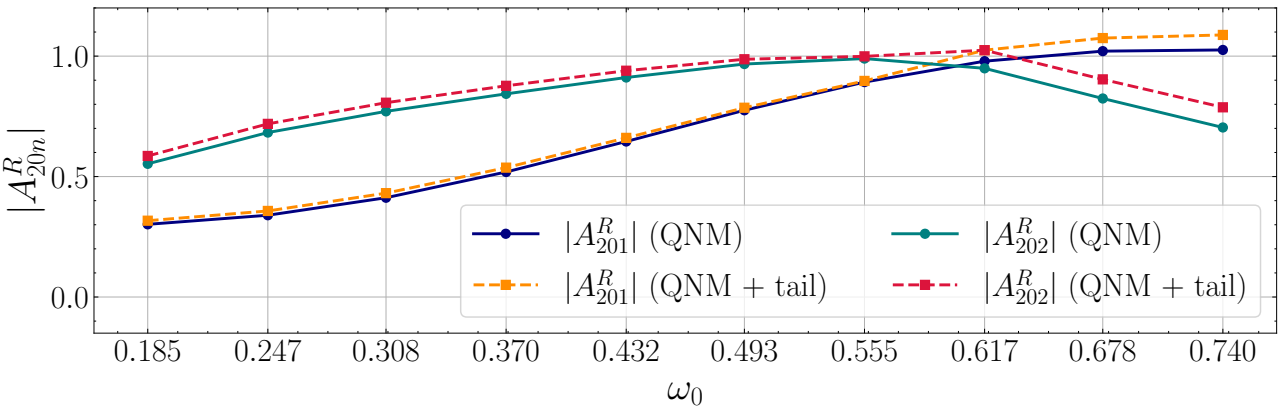


Figure 5.26: **Amplitude ratios $|A^R_{201}|$ (blue/orange) and $|A^R_{202}|$ (green/red) as a function of the Gaussian frequency ω_0.** Solid lines: pure QNM fits. Dashed lines: QNM + tail fits.

approach the fundamental near resonance, the second overtone remains subdominant at all frequencies, with its apparent growth at $\omega_0 \gtrsim 0.6$ reflecting only the reduced excitation of the fundamental mode.

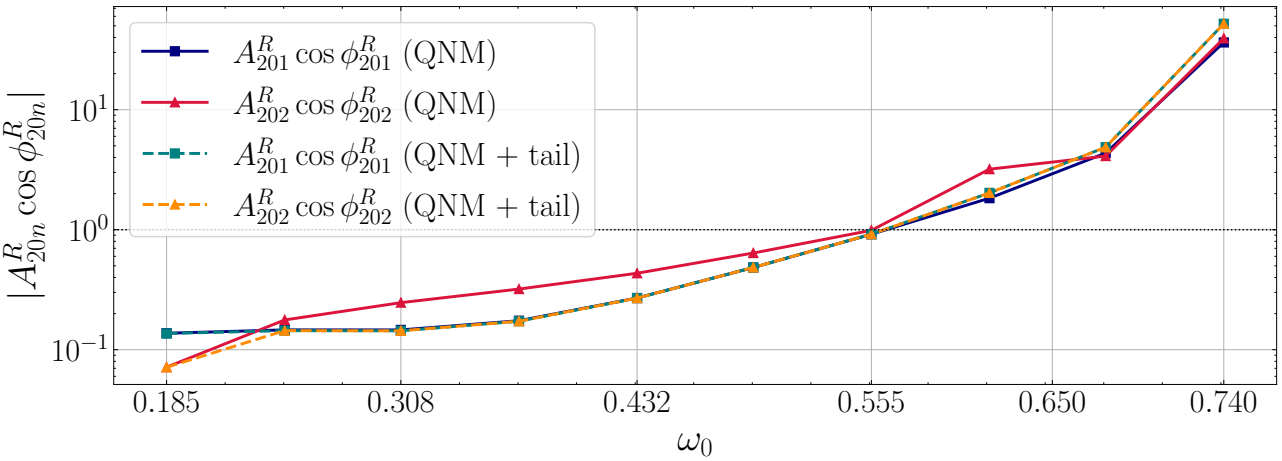


Figure 5.27: **Cosine–projected ratios $|A_{20n}\cos\phi_{20n}|/|A_{200}\cos\phi_{200}|$ for $n = 1, 2$.** The first overtone approaches the strength of the fundamental near resonance, while the second overtone remains consistently weaker; the apparent rise at high ω_0 simply reflects the weaker excitation of the fundamental.

The excitation of the third overtone ($n = 3$) exhibits a markedly different behaviour from that of the lower modes. As shown in Fig. 5.28, the ratios $|A_{201}/A_{200}|$, $|A_{202}/A_{200}|$, and $|A_{203}/A_{200}|$ all grow with ω_0. While the first overtone increases smoothly and reaches values of order unity for $\omega_0 \sim 0.7$, the second and third overtones display a much stronger growth. Already for $\omega_0 \gtrsim 0.5$, the extracted $n = 2$ and $n = 3$ amplitudes appear to rival or even surpass the fundamental, peaking at $|A_{202}/A_{200}| \sim |A_{203}/A_{200}| \approx 6$. This is clearly unphysical, since higher overtones cannot dominate over the fundamental. The most natural interpretation is that residual late–time contamination is being absorbed into oscillatory components, which the fitting procedure misattributes to $n = 2$ and $n = 3$.

The normalized ratios of the cosine–projected amplitudes, shown in Fig. 5.29, illustrate how the apparent importance of higher overtones increases as the carrier frequency ω_0 moves away from resonance. While the fundamental mode dominates for $\omega_0 \lesssim 0.4$, the ratios grow rapidly at larger

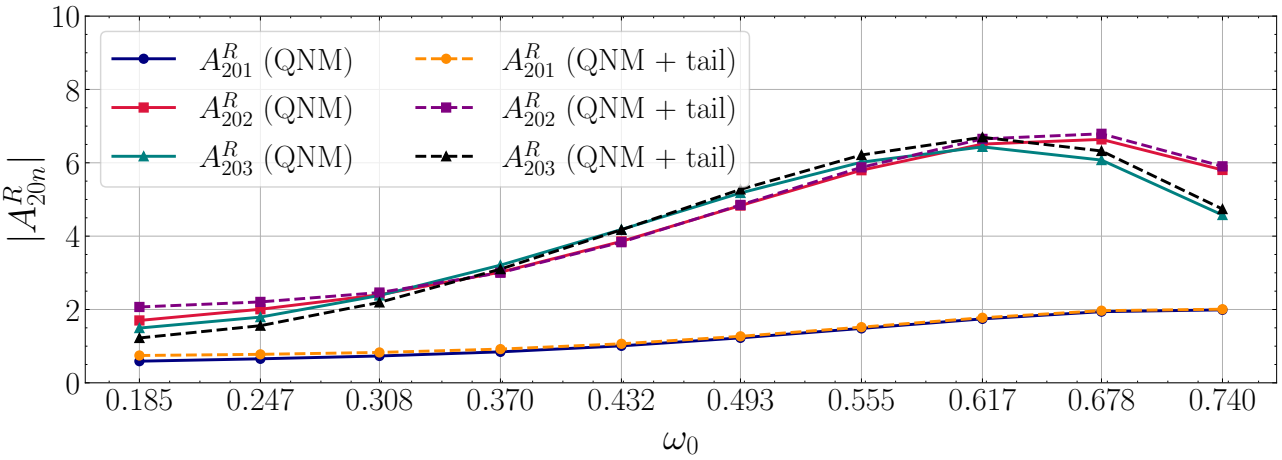


Figure 5.28: **Amplitude ratios A^R_{20n} as a function of the Gaussian frequency ω_0.** Blue: pure QNM fits. Red: QNM+tail fits. The second and third overtones become artificially large for $\omega_0 \gtrsim 0.5$, signalling contamination from the late–time signal rather than genuine excitation.

frequencies, with $n = 2$ and $n = 3$ reaching values well above unity. This does not reflect a genuine enhancement of the overtones, but rather the weakening of the fundamental excitation: once the dominant ringing is suppressed, the regression tends to absorb the residual tail signal into higher oscillatory components, artificially inflating their relative amplitudes.

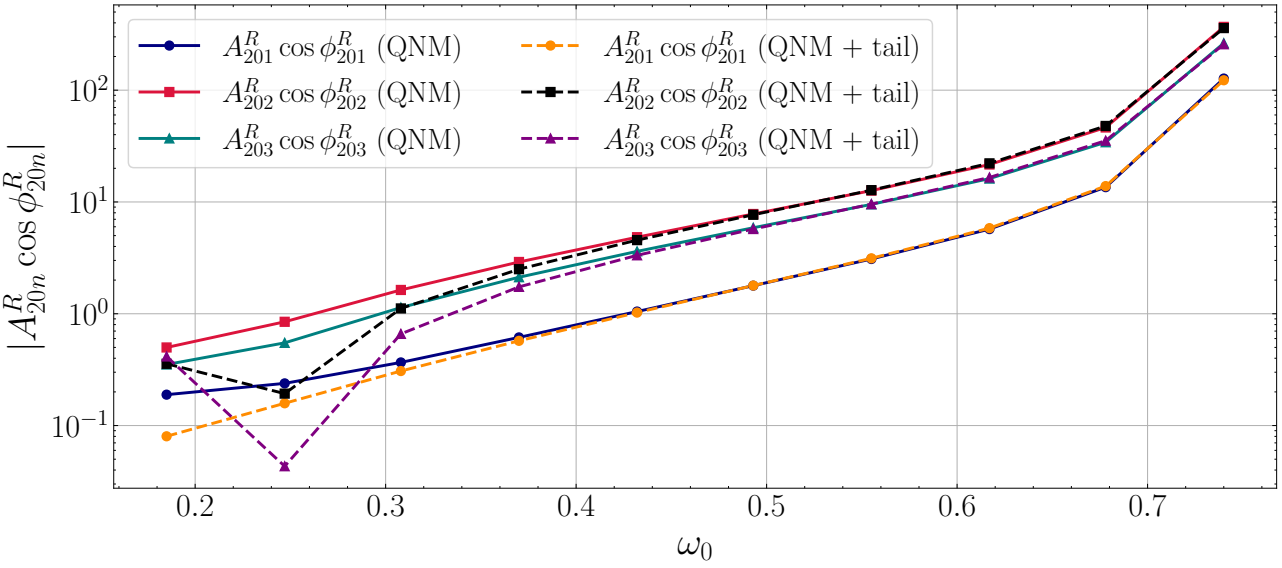


Figure 5.29: **Normalized overtone ratios.** Ratios of the cosine–projected amplitudes $|A^R_{20n}\cos\phi^R_{20n}|$ relative to the fundamental, extracted from both pure QNM fits (solid) and extended QNM+tail fits (dashed).

5.4.4 Tail starting time

We now examine how the onset of the power–law tail depends on the injection frequency ω_0. Applying the same procedure as before, we extract the tail starting time for each simulation. The results are listed in Table 5.5 and displayed in Fig. 5.30.

ω_0	0.185	0.247	0.308	0.370	0.432	0.493	0.555	0.617	0.678	0.740
$t_{\rm tail}/M$	232.61	248.09	263.17	264.44	279.99	295.36	310.33	312.42	341.90	375.34

Table 5.5: **Tail onset as a function of the injection frequency.** Tail starting time $t_{\rm tail}$ extracted for each value of the initial frequency ω_0.

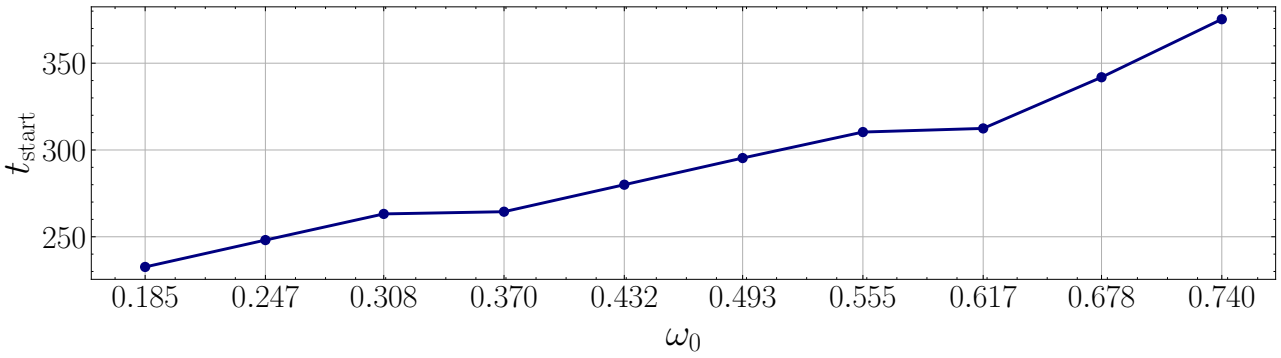


Figure 5.30: **Tail starting time as a function of the injection frequency** ω_0. The onset shifts systematically to later times as ω_0 increases.

The dependence on ω_0 is monotonic: the larger the injection frequency, the later the tail becomes dominant. At the lowest values, $\omega_0 = 0.185$–0.247, the tail sets in already around $t/M \simeq 230$–250, leaving a relatively short-lived quasinormal ringing. Near resonance, $t_{\rm tail}$ shifts to 260–270 M, while for the highest frequencies the transition is postponed far beyond $300\,M$, reaching almost $400\,M$ at $\omega_0 = 0.740$.

This behaviour contrasts with the σ–scan, where broader pulses drove an earlier onset of the tail. The comparison shows that the two parameters control different aspects of the dynamics: the Gaussian width σ regulates the balance between the prompt burst and the onset of ringing, whereas the carrier frequency ω_0 governs how long the QNM phase persists before giving way to the late–time decay. In other words, σ modulates *how quickly* the system enters the ringdown, while ω_0 determines *how long* the ringdown survives before the tail inevitably takes over.

5.4.5 Recovery of the tail amplitude

As in the analysis performed for the σ–scan, we now recover the absolute amplitude of the late–time tail. The procedure is illustrated in the case $\omega_0 = 0.185$. The fitted signal can be written as

$$\Psi_{\rm fit}(t) \;\approx\; 2.05 \times 10^{3} \;+\; 1.37 \times 10^{10}\, t, \tag{5.25}$$

from which the tail coefficient B is extracted at the reference time $t = 232.607$, yielding

$$B \;=\; 1.21 \times 10^{9} \cdot 232.607^{-7} \;=\; 3.71 \times 10^{-7}. \tag{5.26}$$

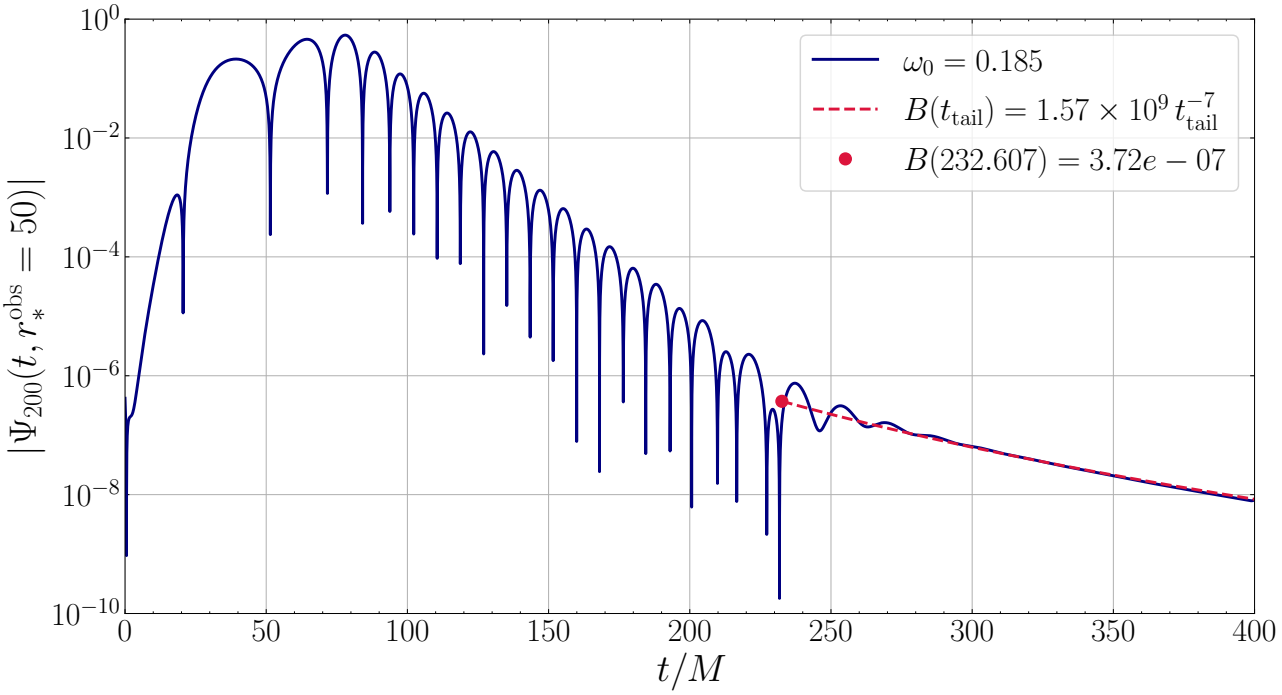


Figure 5.31: **Recovery of the tail amplitude for** $\omega_0 = 0.185$, obtained from the fitted late–time behaviour.

5.4.6 Prompts

In terms of the prompt, we now turn to the effect of varying the central frequency ω_0 of the initial perturbation. Figure 5.32 summarizes how the prompt response changes with ω_0, showing both the prompt end time $t^{\rm end}_{\rm prompt}$ and the maximum amplitude $A_{\rm max}$.

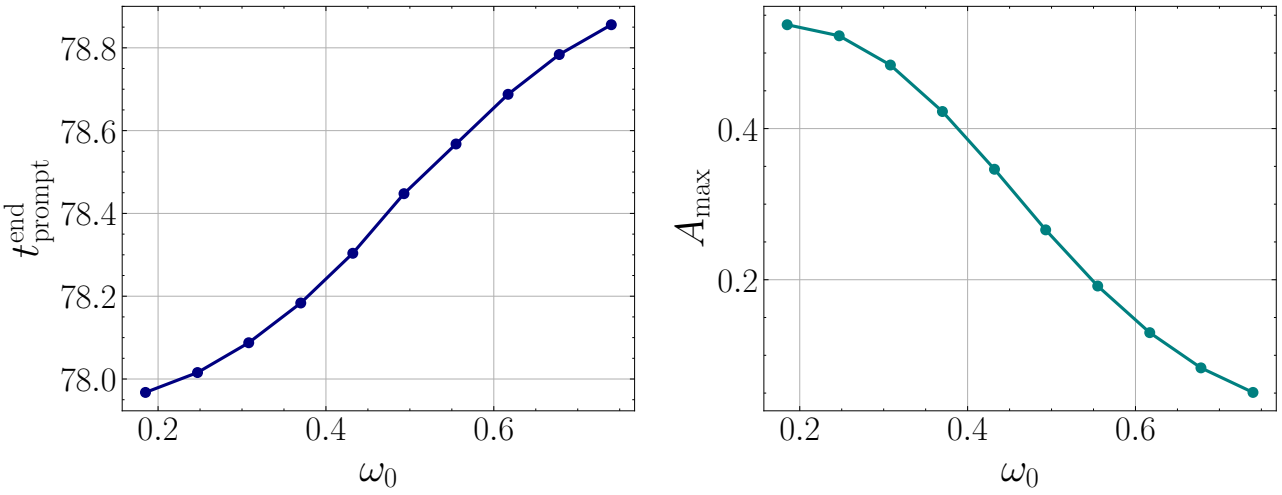


Figure 5.32: **Dependence of the prompt response on the central frequency** ω_0**.** Left: prompt end time $t^{\rm end}_{\rm prompt}$, growing monotonically with ω_0. Right: maximum amplitude $A_{\rm max}$, decreasing rapidly with ω_0.

As seen in Fig. 5.32, increasing ω_0 leads to a longer prompt stage, with $t^{\rm end}_{\rm prompt}$ shifting from about

$78.0M$ at low frequencies ($\omega_0 \sim 0.2$) to nearly $78.9M$ at high frequencies ($\omega_0 \sim 0.7$). At the same time, the maximum amplitude decreases significantly: while low–frequency pulses ($\omega_0 \lesssim 0.25$) excite a strong prompt with $x_n^{\max} \gtrsim 0.5$, higher–frequency perturbations ($\omega_0 \gtrsim 0.6$) yield much weaker responses, with amplitudes below 0.1. This behavior indicates that low–frequency initial data couples more efficiently to the black hole, whereas high–frequency data produces a delayed but fainter prompt.

The impact of this trend is clearly visible in the time evolution of the field. Figure 5.33 shows the waveforms at $r_{\rm obs} = 50$ for $\omega_0 \in \{0.185, \ldots, 0.740\}$. At low frequencies, the prompt dominates with an intense early burst, while at higher frequencies the signal builds up more slowly and the quasinormal ringing emerges comparatively stronger.

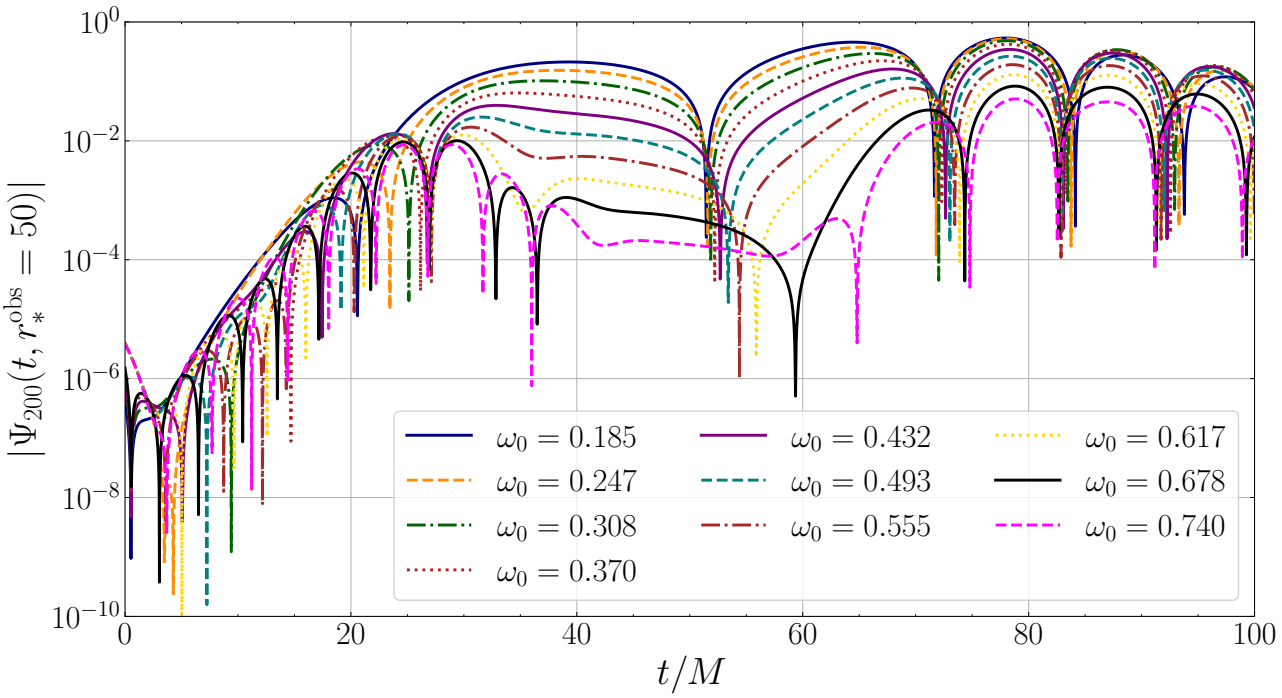
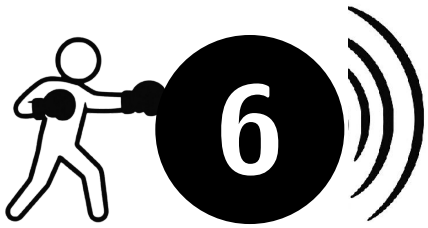


Figure 5.33: **Time evolution of the perturbed field** $|\Psi_{200}(t, r_{\rm obs} = 50)|$ for $\omega_0 \in \{0.185, \ldots, 0.740\}$ with $a = 0.0$, $\ell = 2$. Low–frequency pulses yield a strong, early prompt response, while high–frequency pulses excite a weaker but longer prompt.

CHAPTER



Numerical results in Kerr spacetime

Contents

6.1 Motivation and Setup **101**
6.2 Head–on case varying the spin **102**
6.3 Quasi-circular case varying ω_0 . . . . . **108**

6.1 Motivation and Setup

After having analyzed the late–time tails arising from the numerical solution of the RW equation, we now turn to the analogous problem for the Teukolsky equation, in order to study gravitational perturbations in rotating BHs. The master equation to be solved numerically reads

$$\left\{\left[\frac{r^2+a^2}{\Delta_{BL}}-a^2\sin^2\theta\right]\frac{\partial^2}{\partial t^2}+\frac{4Mar}{\Delta_{BL}}\frac{\partial^2}{\partial t\partial\phi}-4\left[r+ia\cos\theta-\frac{M(r^2+a^2)}{\Delta_{BL}}\right]\frac{\partial}{\partial t}-\Delta_{BL}^2\frac{\partial}{\partial r}\left(\Delta_{BL}^{-1}\frac{\partial}{\partial r}\right)\right.$$
$$\left.-\frac{1}{\sin\theta}\frac{\partial}{\partial\theta}\left(\sin\theta\frac{\partial}{\partial\theta}\right)-\left(\frac{1}{\sin^2\theta}-\frac{a^2}{\Delta_{BL}}\right)\frac{\partial^2}{\partial\phi^2}+4\left[\frac{a(r-M)}{\Delta}+\frac{i\cos\theta}{\sin^2\theta}\right]\frac{\partial}{\partial\phi}+(4\cot^2\theta+2)\right\}\Psi_{-2}=0. \tag{6.1}$$

We solve this equation numerically using the fourth–order scheme described in Chapter 4. The procedure closely follows the strategy adopted for the RW case: two types of initial data are considered, namely head–on and quasi–circular profiles. In both cases, the Gaussian width is fixed to $\sigma = 7.07$, the initial pulse is centered at $r_*^0 = 75$, and the main extraction point is chosen at $r_*^0 = 20$[1]. For the quasi–circular case, we vary the frequency parameter (ω_0) from zero up to 0.5, always including the specific resonant value associated with each spin parameter.

[1]We adopt these values because they are consistent with those used in the original implementation of this code [55], which ensures a reliable comparison.

6.2 Head–on case varying the spin

In this set of tests we employ the following Gaussian initial data profile

$$\Psi(0, r_*, \theta) = \exp\left[-\frac{(r_* - 75)^2}{100}\right] \sin^2(\theta)\,. \tag{6.2}$$

We evolve this perturbation for BHs with spin parameters ranging from $a = 0.0$ to $a = 0.9$ in steps of 0.1, and we also include the extremal astrophysical limit proposed by Thorne at $a = 0.998$. The resulting waveforms clearly illustrate how the spin affects both the amplitude and decay of the signal. In particular, the inset zoom in Fig. 6.1 highlights that the quasinormal ringing regime is different for each run, with the oscillation frequency and damping rate varying with the black hole spin. Nevertheless, the late–time power–law tail always decays towards the same asymptotic slope, independent of a, confirming the universality of the tail behavior. The complete set of runs is shown in Figure 6.1.

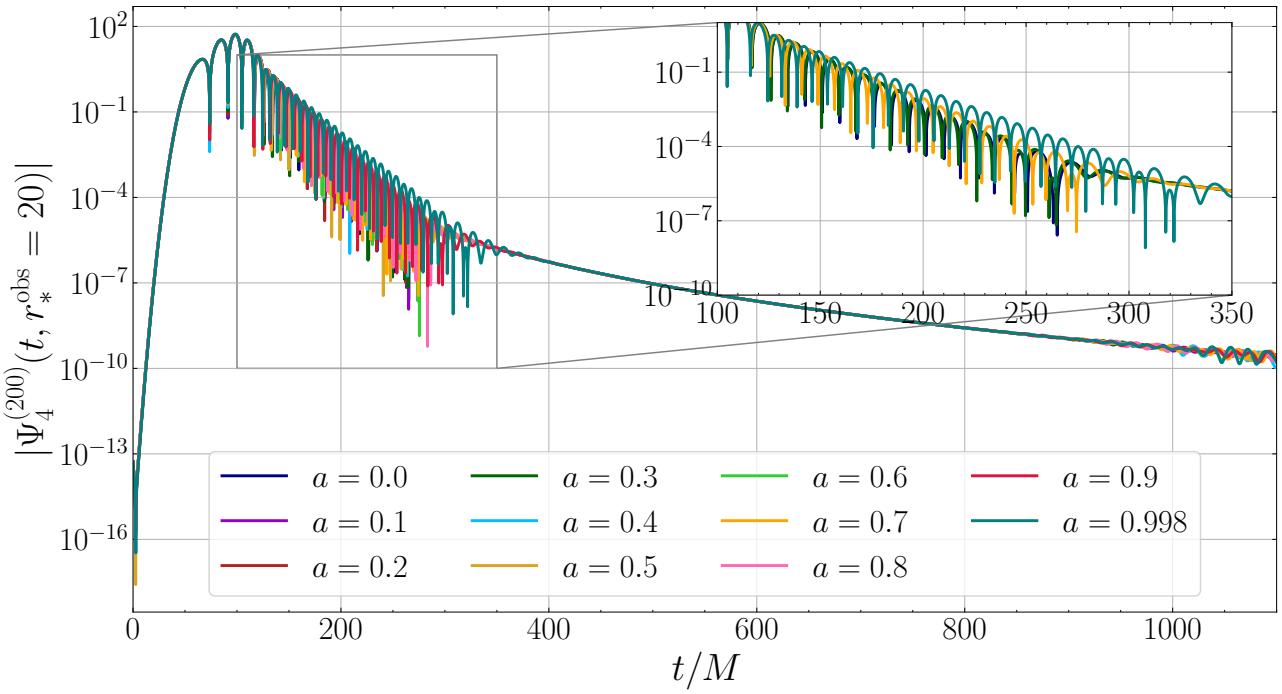


Figure 6.1: **Numerical waveforms for different values of the spin parameter,** obtained with Gaussian head–on initial data. The inset highlights how the quasinormal ringing regime changes with spin, while the late–time tail exhibits the same universal decay across all cases.

6.2.1 Local power index

A useful diagnostic to characterize the late–time decay of perturbationsis the local power index (which is the same as the exponent we always look for), introduced in [62]. Given a waveform extracted at a fixed observer position,the instantaneous decay rate is defined as

$$p(t) \;=\; -\frac{t}{\Psi_4^{(200)}(t)}\,\frac{\mathrm{d}\Psi_4^{(200)}(t)}{\mathrm{d}t}. \tag{6.3}$$

In practice, the time derivative is evaluated with a high–order finite difference stencil. For instance, using the five–point formula one has

$$\left.\frac{\mathrm{d}\Psi_4^{(200)}}{\mathrm{d}t}\right|_{t_i} \simeq \frac{\Psi_{4,i-2}^{(200)} - 8\Psi_{4,i-1}^{(200)} + 8\Psi_{4,i+1}^{(200)} - \Psi_{4,i+2}^{(200)}}{12\,\Delta t}\,, \tag{6.4}$$

which yields fourth–order accuracy in time. Substituting (6.4) into (6.3) provides the numerical evaluation of $p(t)$ along the evolution. At sufficiently late times the local power index approaches the theoretical decay exponent of the tail, and its average value over a suitable time window gives a robust numerical estimate.

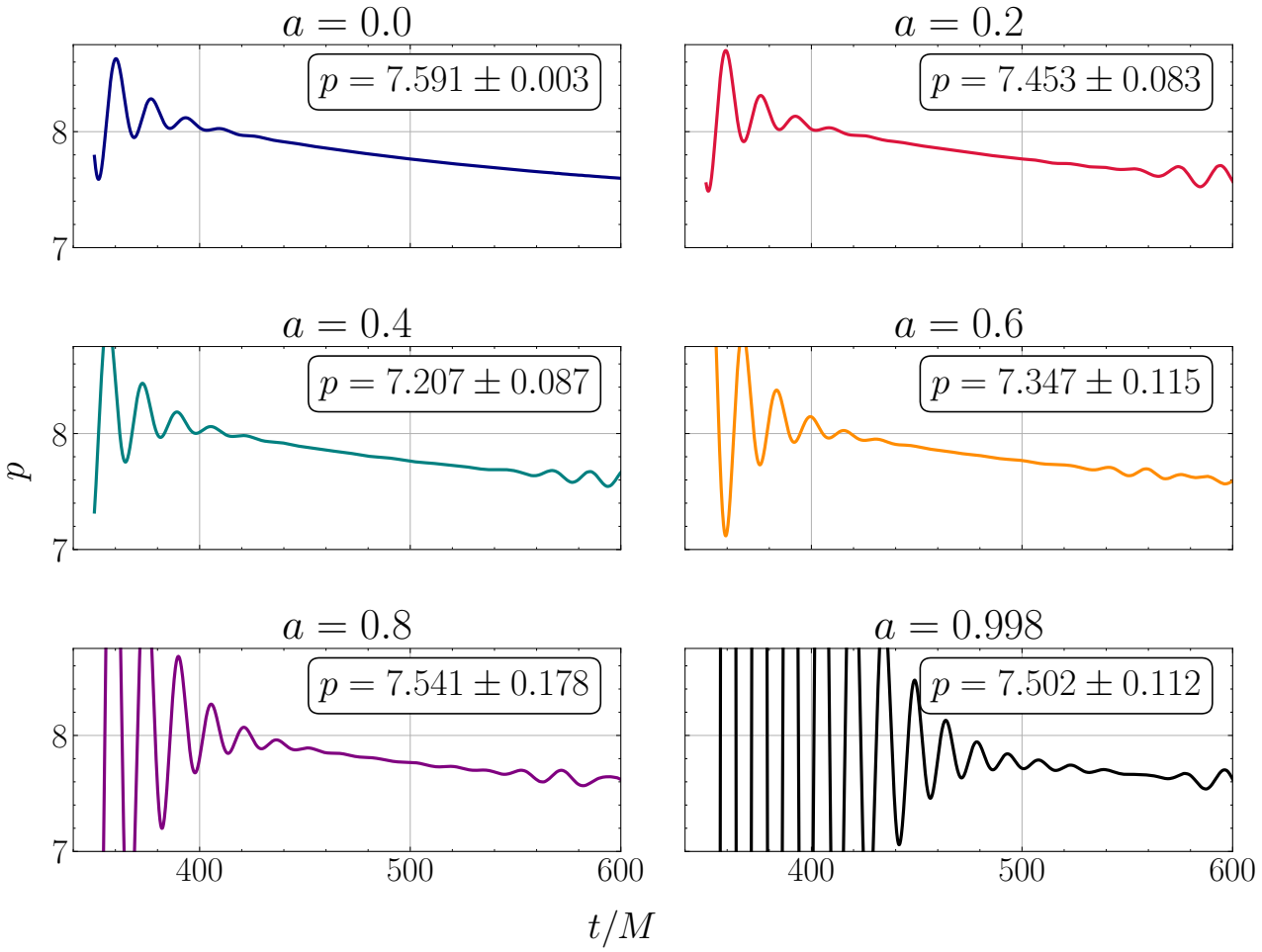


Figure 6.2: **Local power index for $\ell = 2$, $m = 0$ perturbations.** Each panel corresponds to a different spin parameter of the background BH. The shaded curves represent the local power index computed from the numerical waveform, while the insets report the mean value μ and its statistical error over the interval $t \in [350, 600]\,M$.

6.2.2 Amplitude ratios

Figure 6.3 displays the evolution of the amplitude ratio $|A^R_{201}|$ for several overtones $n = 1, 2, 3, 4$ as a function of the BH spin parameter. The behavior of the first two overtones ($n = 1, 2$) is rather regular: their relative amplitudes remain small ($\lesssim 0.2$) and only mildly dependent on the spin. This indicates

that the lowest overtones provide a robust and stable contribution to the ringdown signal, and can be reliably extracted independently of the specific fitting strategy.

By contrast, the higher overtones ($n = 3, 4$) exhibit a much stronger dependence on the spin. For moderate values of a their relative amplitudes decrease, but in the near-extremal regime they rise sharply, reaching values that become comparable to or even larger than the fundamental mode. This suggests that for rapidly rotating BHs, higher overtones might temporarily dominate the early ringdown dynamics.

Another important feature is the systematic difference between the "pure QNM model" (solid lines) and the "QNM + tail model" (dashed lines). While for $n = 1, 2$ both descriptions are nearly indistinguishable, for $n = 3, 4$ the inclusion of the late-time tail strongly modifies the inferred amplitude ratios. This highlights the intrinsic degeneracy between higher overtones and the onset of the power-law tail: depending on the choice of the fitting window, part of the signal can be absorbed either into a subdominant overtone or into the tail contribution.

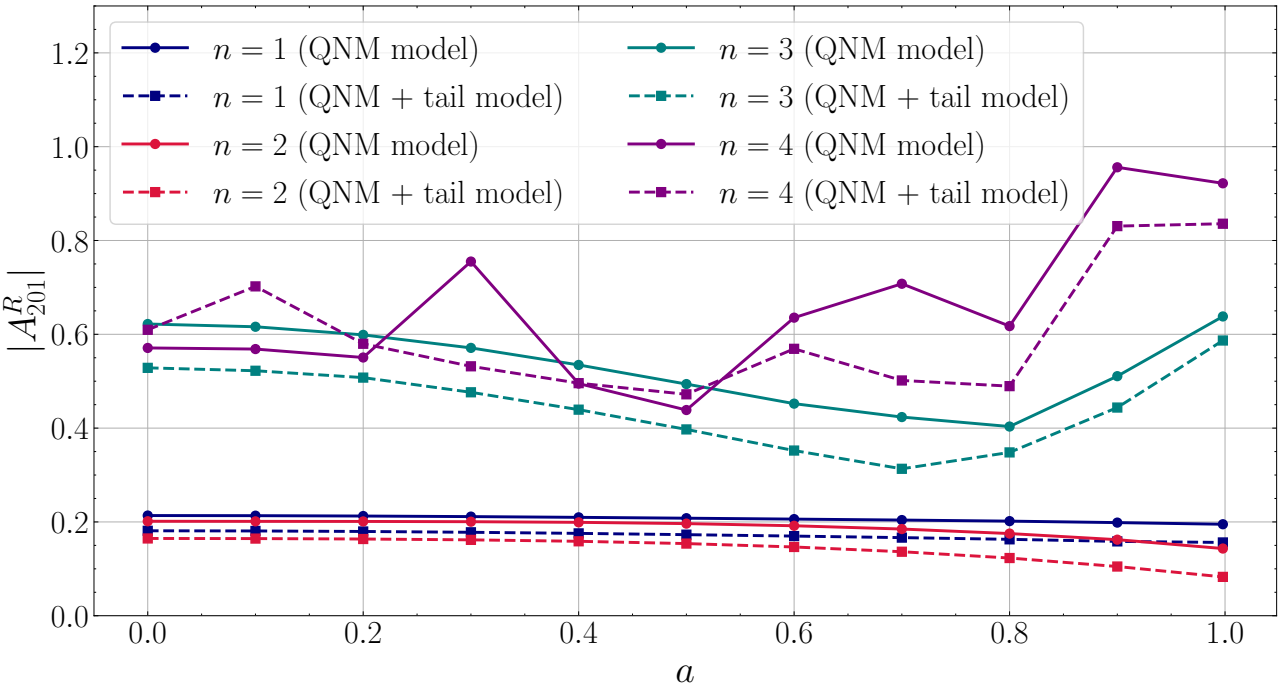


Figure 6.3: **Amplitude ratios of overtones across spins.** The first overtones ($n = 1, 2$) remain small and nearly spin-independent, while higher overtones ($n = 3, 4$) grow strongly with spin and are significantly affected by the tail contribution.

Overall, these results support the interpretation that the first few overtones ($n = 1, 2$) provide a physically meaningful and reliable extension of the fundamental mode, while the inclusion of higher-n modes should be handled with care. Their apparent growth at high spin and their sensitivity to the treatment of the tail suggest that they may reflect a mixing of different physical mechanisms rather than a clear signature of a single QNM. In particular, the sharp increase of $n = 3, 4$ near extremality should not be interpreted as genuine excitation, but rather as an artifact of the fitting procedure absorbing late–time contributions into higher overtones.

6.2.3 Tail starting time

In addition to the amplitude ratios, we also investigate the onset of the late–time tail as a function of the BH spin. The tail starting time is estimated by fitting the numerical signal to a power–law decay (t^{-7}) and determining the earliest time from which the fit remains stable.

Figure 6.4 displays the measured values of the tail starting time for spins in the range $a = 0.0$ to $a = 0.998$. The results show that the tail starting time increases monotonically with the spin, meaning that the transition from quasinormal ringing to the late–time tail is progressively delayed for rapidly rotating BHs. This behavior reflects the longer persistence of quasinormal oscillations in the near–extremal regime, where the damping times of the fundamental modes become significantly larger.

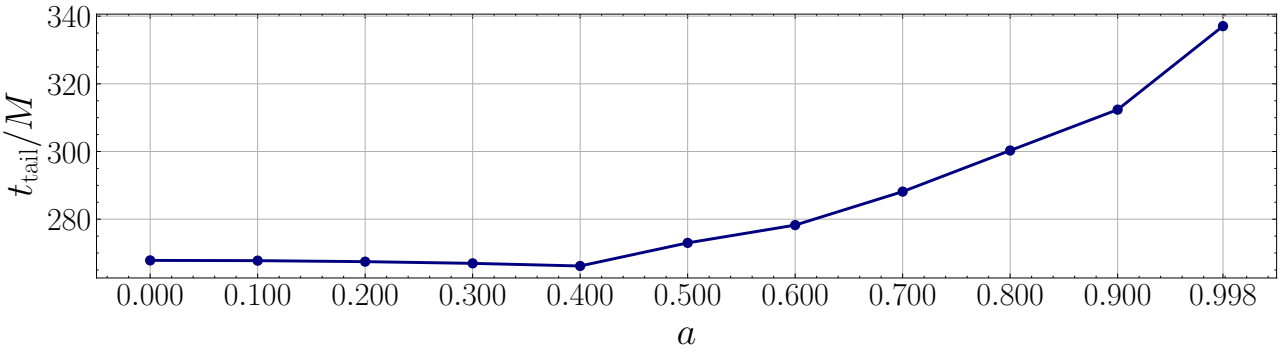


Figure 6.4: **Tail onset versus spin.** Tail starting time as a function of the spin parameter. The onset of the late–time tail shifts to later times as the spin increases, reflecting the slower damping of quasinormal oscillations in the near–extremal regime.

To better connect this trend with the BH geometry, we also re–express the horizontal axis in terms of the horizon size (see Eq. (1.26)) which reduces to $r_+ = 2M$ in the Schwarzschild case and approaches $r_+ = M$ in the extremal Kerr limit. Figure 6.5 shows the same data plotted as a function of r_+. The monotonic decrease of r_+ with increasing spin provides a complementary perspective: as the horizon shrinks, the onset of the tail is pushed to later times, highlighting the interplay between BH rotation, horizon geometry, and the persistence of quasinormal ringing.

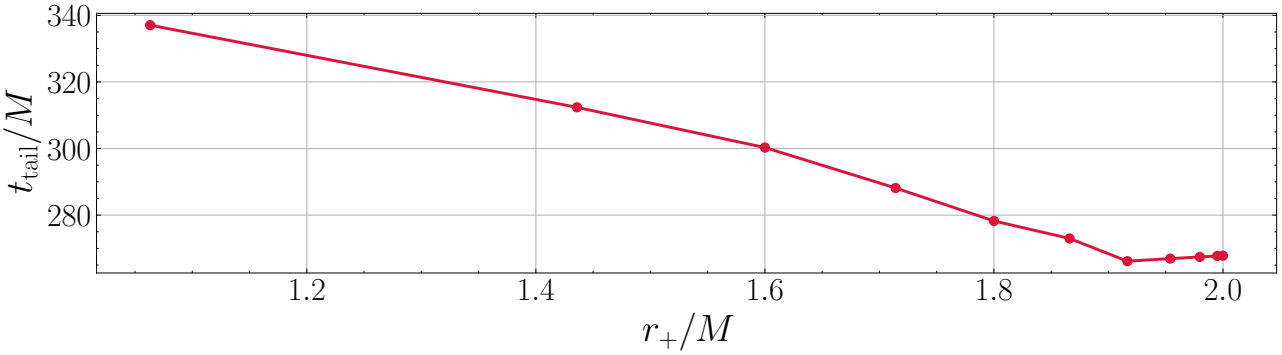


Figure 6.5: **Tail onset versus horizon radius.** Tail starting time as a function of the horizon radius r_+. As the horizon shrinks with increasing spin, the onset of the tail is delayed, showing the close connection between horizon geometry and the persistence of quasinormal ringing.

6.2.4 Amplitude and tail exponent recovery

An essential step in the characterization of late–time behavior is the reconstruction of the amplitude of the power–law tail at the precise instant when the ringdown transitions into the polynomial regime. Following the same procedure outlined in the previous chapter, we recover the amplitudes at the tail starting time and compare them directly with the numerical signal. The agreement turns out to be excellent: the reconstructed curve overlaps with the waveform almost exactly, confirming that our method is capable of isolating the tail contribution in a consistent and reproducible way.

Figure 6.6 illustrates this result for the near–extremal case ($a = 0.998$). The orange dashed curve, corresponding to the predicted late–time tail $B(t) \propto t^{-7}$, follows the numerical signal without visible deviations once the tail starting time is reached. This demonstrates that the amplitude recovery procedure does not only provide the correct scaling law, but also the right normalization to describe the physical signal.

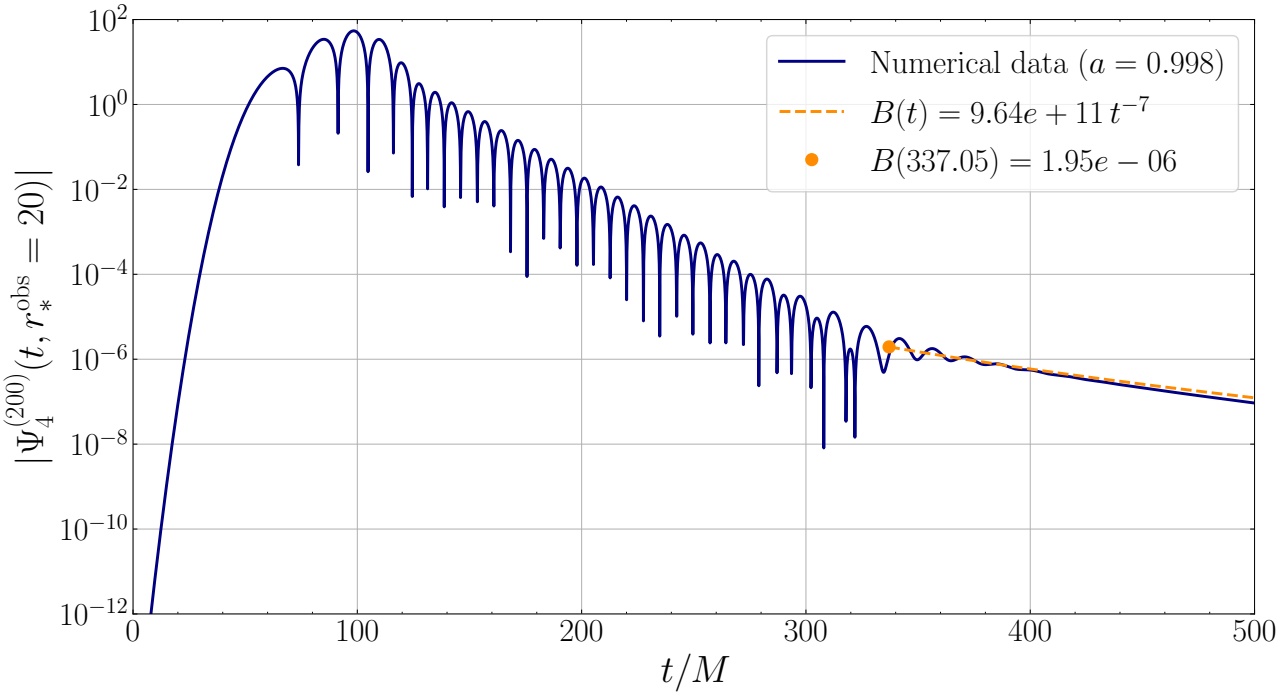


Figure 6.6: **Numerical waveform and reconstructed tail for $a = 0.998$.** The numerical waveform is compared with the recovered late–time tail $B(t) \propto t^{-7}$. The reconstructed tail reproduces both the slope and the amplitude of the data, validating the recovery method.

In addition to the amplitudes, we also assess the accuracy of the recovered tail exponent by means of the statistical coefficient of determination (R^2). As shown in Figure 6.7, the best fits are consistently obtained when the exponent lies in the interval $p \in [7, 8]$, which matches the theoretical prediction for scalar perturbations on Kerr backgrounds. The fact that R^2 peaks precisely in this region provides strong evidence that the simulations faithfully capture the asymptotic decay regime, and that our fitting strategy is robust against numerical noise and finite–time effects.

Taken together, these two results show that both the amplitude and the decay exponent of the late–time tail can be reliably extracted from the numerical evolution. This not only provides an independent verification of the predicted power–law decay in Kerr spacetimes, but also highlights the

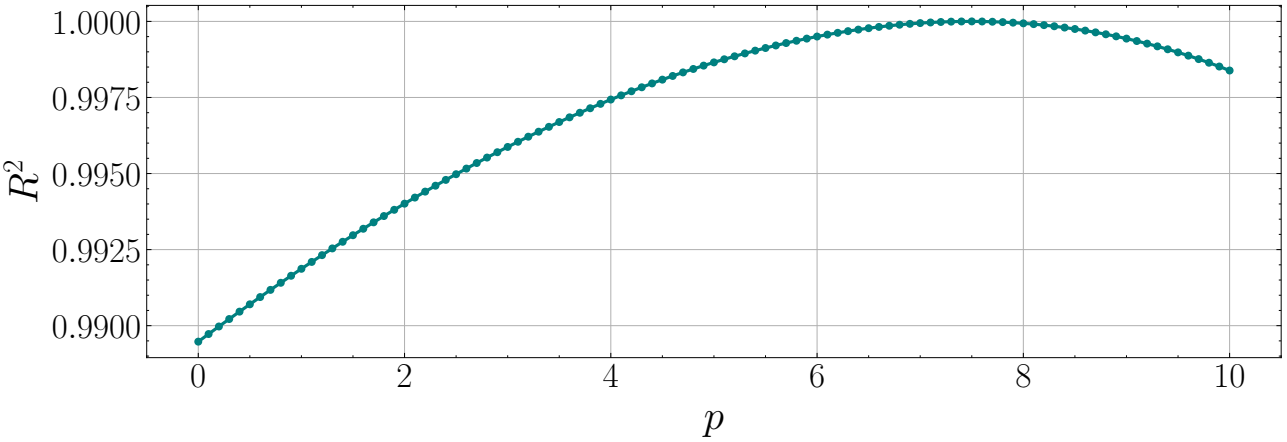


Figure 6.7: **Coefficient of determination versus tail exponent for $a = 0.998$.** The coefficient R^2 is shown as a function of the fitted tail exponent p. The maximum correlation is obtained for p between 7 and 8, in excellent agreement with the theoretical expectation.

precision of the numerical scheme in capturing extremely small amplitudes at late times. Therefore, the tail analysis reinforces the robustness of our simulations and offers a powerful tool for probing the subtle interplay between quasinormal ringdown and polynomial decay.

6.2.5 Prompt response

Figure 6.8 displays the prompt response for a set of BHs with spin parameters ranging from $a = 0.0$ to $a = 0.998$.

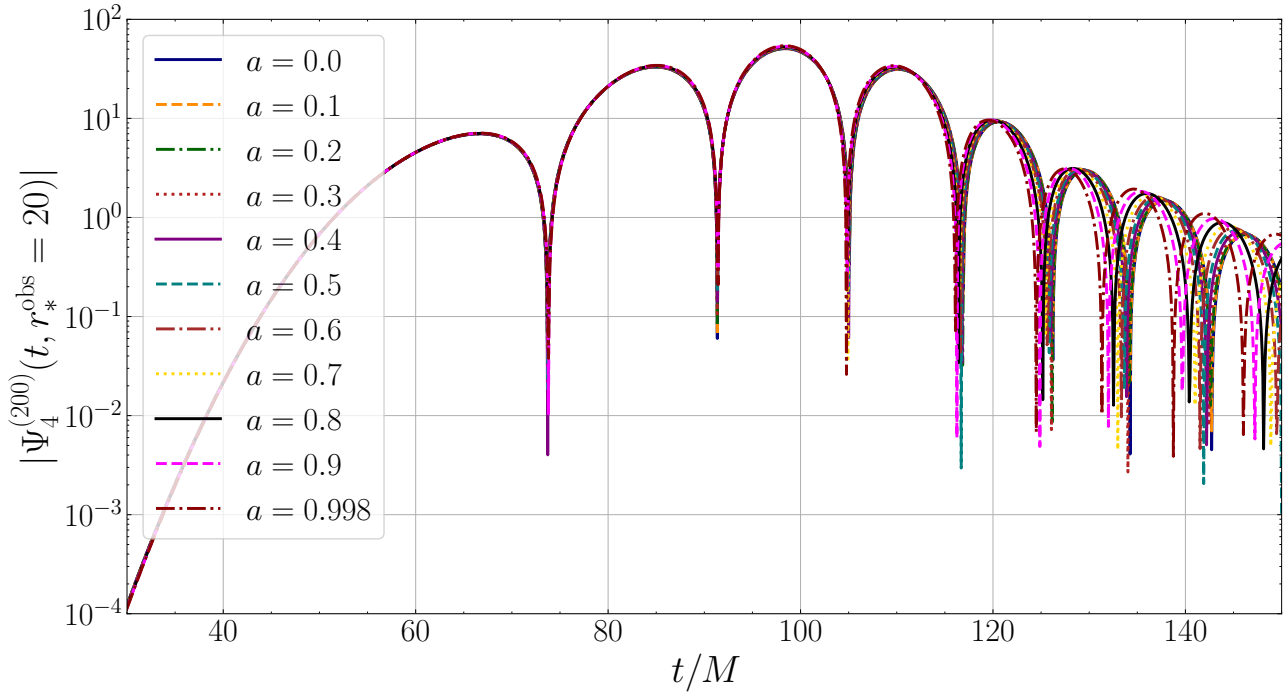


Figure 6.8: **Prompt response for different spins.** Prompt responses obtained for BHs with spin values between $a = 0.0$ and $a = 0.998$.

The temporal profile of the burst is essentially the same for all cases, showing that the prompt duration and onset are almost insensitive to the rotation. The main difference is the amplitude: the prompt grows systematically with a, becoming significantly stronger close to the extremal limit. This indicates that the BH spin enhances the scattering efficiency of the initial perturbation, amplifying the burst without altering its timescale.

This behaviour is quantified in Fig. 6.9, which shows the time and amplitude of the maximum of the prompt as functions of a. The left panel confirms that the peak occurs at essentially the same time for all spins, with only a negligible shift in the near–extremal case. In contrast, the right panel reveals a clear monotonic increase of the maximum amplitude with spin, consistent with the trend observed in Fig. 6.8.

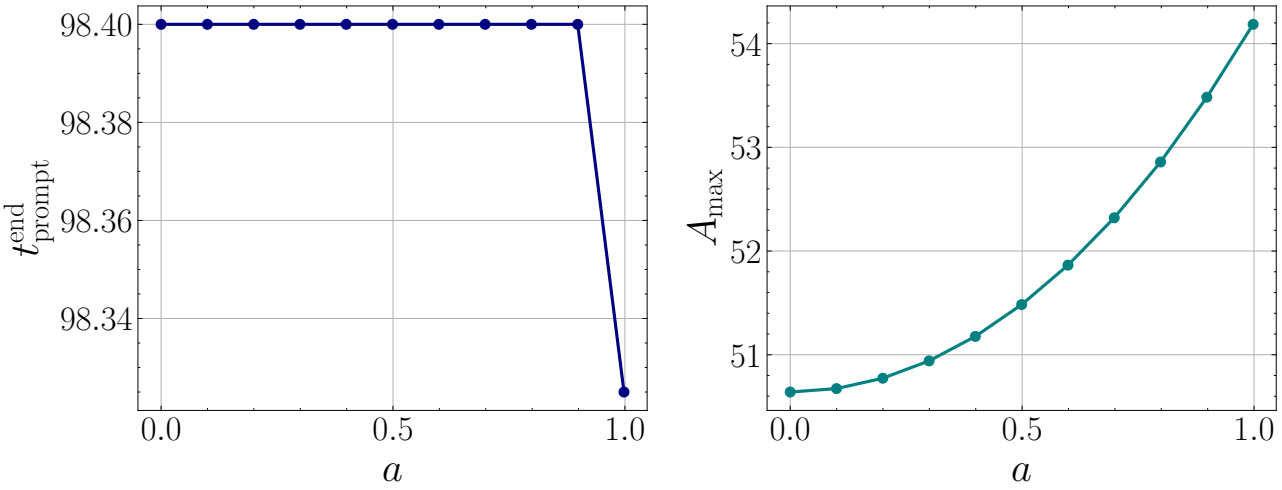


Figure 6.9: **Prompt peak timing and amplitude versus spin.** Time of occurrence (left) and maximum amplitude (right) of the prompt as functions of the spin parameter. The peak time is nearly independent of a, while the amplitude grows steadily with rotation.

Then, the prompt is largely universal in shape and duration, but its amplitude is strongly modulated by the BH spin. Rapidly rotating backgrounds produce significantly more intense bursts, while the onset of the subsequent QNM ringing remains essentially unchanged.

6.3 Quasi-circular case varying ω_0

In this section we investigate the effect of varying the frequency parameter (ω_0) in the initial data. We employ the Gaussian-modulated pulse

$$\Psi(t=0,r_*) = \exp\left[-\frac{(r_*-75)^2}{100}\right]\cos\Big[\omega_0(r_*-75)\Big]\sin^2(\theta), \tag{6.5}$$

where ω_0 is varied between 0.0 and 0.5. The study has been performed for three different spin values, namely $a=0.0$, $a=0.3$, and $a=0.7$. The motivation for this setup is to test how different quasi-circular initial configurations project onto the BH QNMs, and how close one can get to resonance by tuning ω_0. In particular, we expect that for values of ω_0 close to the real part of the fundamental QNM frequency, the excitation of the ringdown signal will be enhanced.

The resulting signals are shown in Fig. 6.10, where we display the time evolution of $|\Psi_4^{(200)}(t, r_*^{\rm obs} = 20)|$ for the three spins. Each panel corresponds to a different spin value and contains the signals obtained for all values of ω_0. The comparison clearly illustrates the interplay between the initial frequency content of the perturbation and the spin of the BH in shaping the observed ringdown waveform.

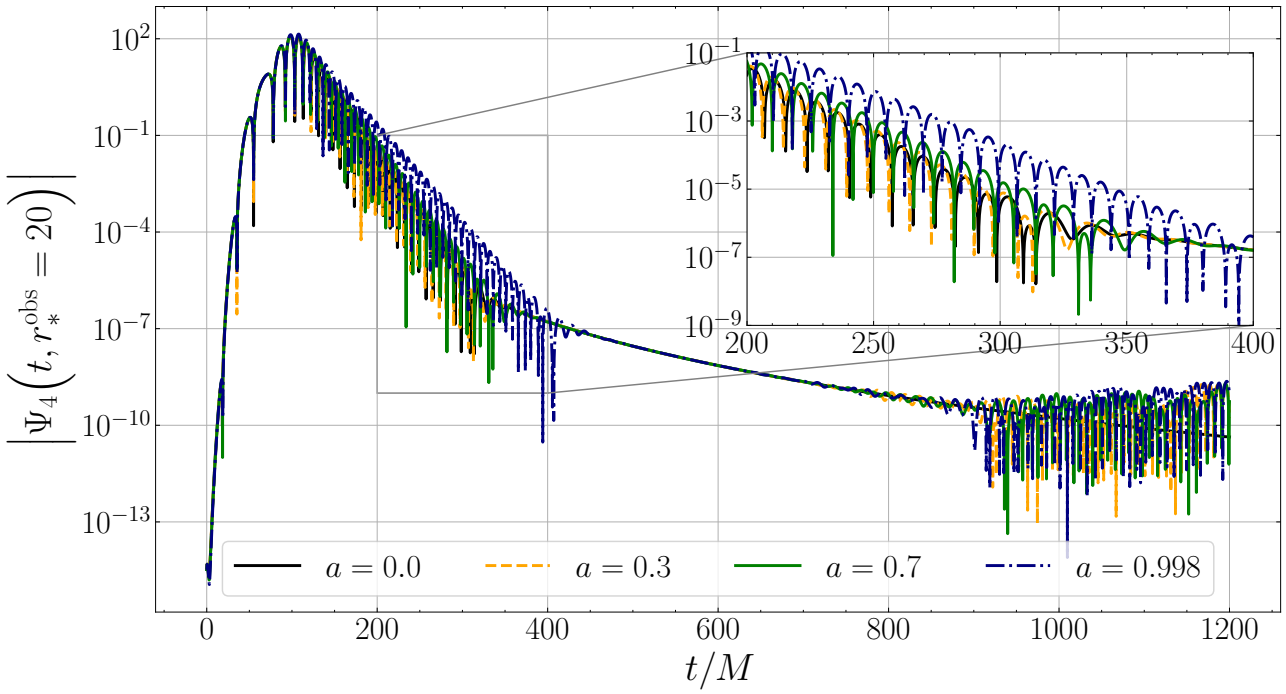


Figure 6.10: **Ringdown waveforms for different spins.** Waveforms extracted at $r_*^{\rm obs} = 20$ for quasi–circular initial data with $\omega_0 = 0.2$, comparing BH spins $a = 0.0, 0.3, 0.7$, and 0.998. The inset highlights the QNM ringing phase, where the dependence of the oscillation frequency and damping on the spin becomes evident, while the late–time tails display a universal decay.

6.3.1 Amplitude ratios

In order to quantify the relative excitation of the different overtones, we compute the amplitude ratios $|A^R_{20n}|$, which measure the strength of the $n \geq 1$ QNMs compared to the fundamental mode.

Figure 6.11 shows the dependence of these ratios on the initial frequency parameter ω_0 for several values of the spin. In the Schwarzschild case ($a = 0$), the excitation of overtones is strongest for broad initial pulses (small ω_0), with ratios exceeding unity in some cases, indicating that the first few overtones can dominate the early ringdown. As ω_0 increases, the projection onto higher modes is quickly suppressed and the ratios become negligible. This behaviour is progressively reduced for rotating BHs: in the near–extremal case ($a = 0.998$), the overtone amplitudes remain small and nearly independent of ω_0, confirming that rotation stabilizes the dominance of the fundamental mode.

A complementary view is provided in Figure 6.12, which compares the ratios for $\ell = 2$ and $\ell = 3$. The overall behaviour is consistent across multipoles, with overtone excitation concentrated at small ω_0 and rapidly decaying at higher values. The inclusion of the higher multipole does not alter the qualitative picture, reinforcing the robustness of the observed trend.

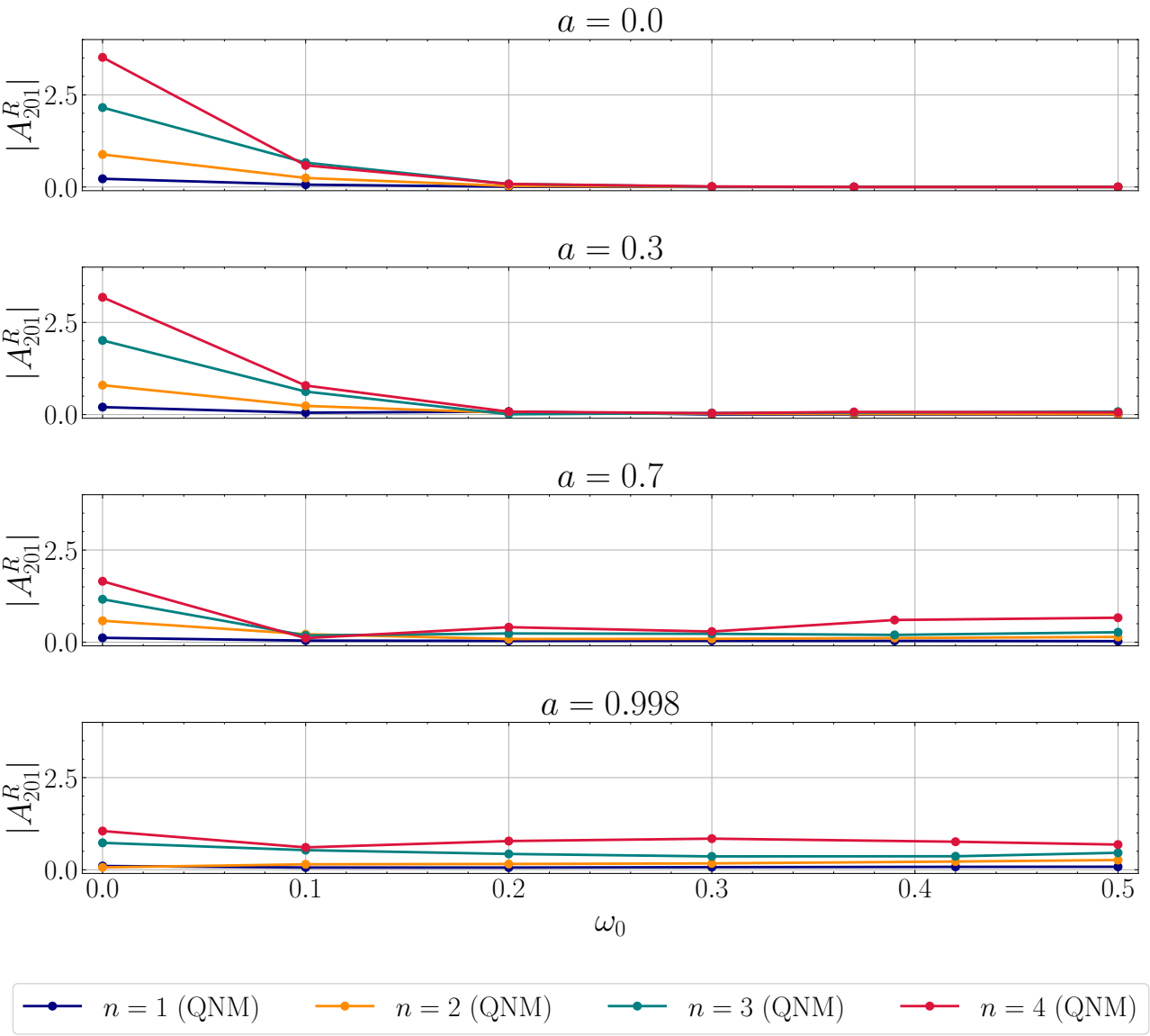


Figure 6.11: **Amplitude ratios $|A^R_{201}|$ as a function of ω_0.** Results are shown for spins $a = 0.0, 0.3, 0.7$, and 0.998. Different colors correspond to the first four overtones $n = 1, 2, 3, 4$. Broad perturbations ($\omega_0 \lesssim 0.1$) excite higher overtones efficiently, while sharply tuned pulses leave the fundamental mode dominant.

The spin dependence is further illustrated in Figure 6.13, where the ratios are plotted as a function of a for the first four overtones. While the fundamental mode clearly dominates in Schwarzschild, the contribution of the overtones increases steadily with rotation. In particular, the $n = 3$ and $n = 4$ modes show a nearly monotonic growth, reaching ratios comparable to the fundamental close to the astrophysical extremal limit ($a = 0.998$). The comparison between pure QNM fits and QNM+tail fits (dashed lines) indicates that late–time tails do not qualitatively change the modal hierarchy, though they can slightly enhance the overtone contribution for high spin.

Altogether, the results reveal a dual behaviour: overtone excitation is favored by broad, low–frequency initial pulses (small ω_0) and by rapidly rotating BHs. In the near–extremal regime, higher

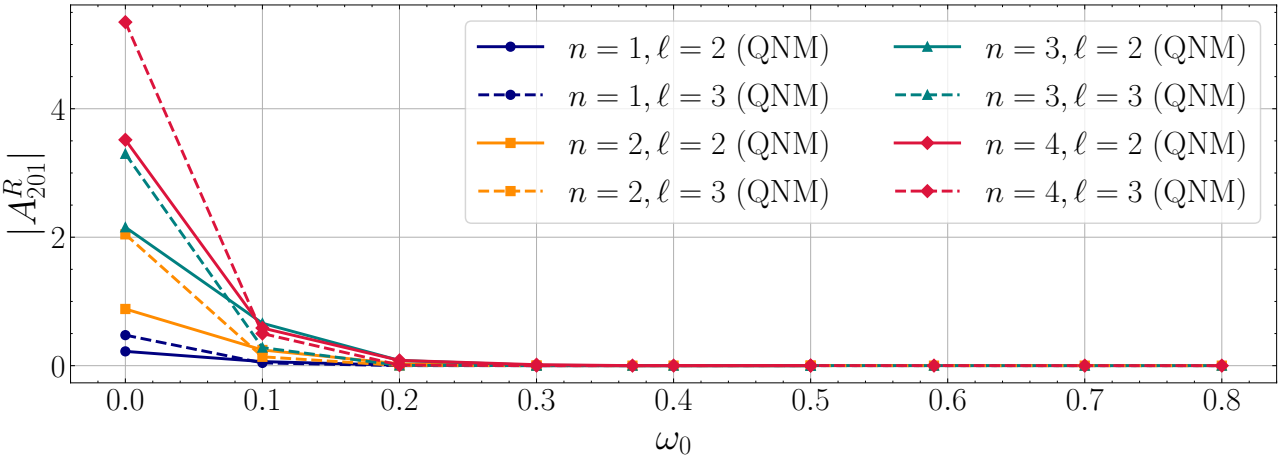


Figure 6.12: **Comparison of amplitude ratios for $\ell = 2$ and $\ell = 3$.** Amplitude ratios $|A^R_{20n}|$ as a function of ω_0 for the first four overtones. Solid lines correspond to pure QNM fits, while dashed lines include the contribution of the late–time tail. Results are consistent across multipoles, confirming that the excitation pattern is mainly controlled by the spectral content of the initial perturbation.

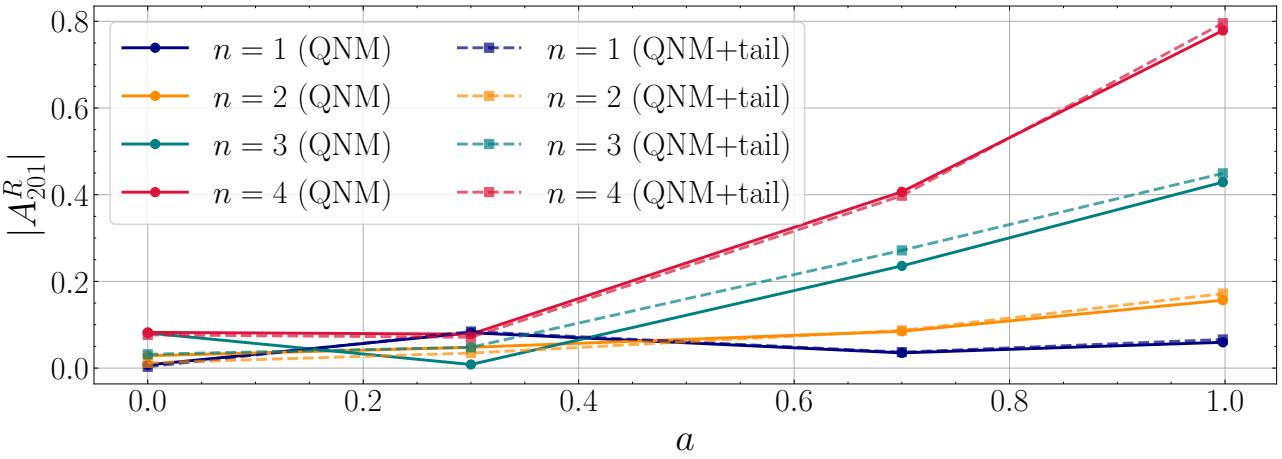


Figure 6.13: **Amplitude ratios $|A^R_{20n}|$ across spins.** Dependence of the ratios on the spin parameter a for the first four overtones. Solid lines correspond to pure QNM fits, while dashed lines include the contribution of the late–time tail. Higher overtones ($n = 3, 4$) grow steadily with spin, approaching the strength of the fundamental near the extremal limit.

overtones can approach the fundamental in strength, suggesting that they might play a significant role in the early ringdown dynamics.

6.3.2 Tail starting time analysis

In Fig. 6.14 we present the tail starting times $t_{\rm tail}$ extracted from quasi–circular initial data for different values of the injection frequency ω_0, considering both $\ell = 2$ and $\ell = 3$ multipoles and several spin parameters. The general trend is clear: $t_{\rm tail}$ increases monotonically with ω_0 for all cases. This behaviour is physically intuitive: broad, low–frequency pulses ($\omega_0 \lesssim 0.1$) excite a wide spectral content, leading to a relatively fast onset of the power–law tail, whereas sharply tuned perturbations close to resonance delay the transition, as the quasinormal ringing persists for longer.

The role of the spin is also evident. For fixed ω_0, higher rotation tends to shift $t_{\rm tail}$ to later times, reflecting the slower damping of the dominant quasinormal mode in Kerr. This trend is particularly pronounced for $a = 0.7$, where the growth of $t_{\rm tail}$ with ω_0 is significantly steeper than in the Schwarzschild case ($a = 0.0$). The intermediate case $a = 0.3$ lies between these two extremes, confirming a smooth dependence on a.

Finally, comparing the multipoles, we find that $\ell = 3$ systematically yields larger $t_{\rm tail}$ than $\ell = 2$, especially in the near–extremal regime. This indicates that higher multipoles couple less efficiently to the late–time tail, leaving the quasinormal ringing to dominate for longer durations before the power–law decay emerges.

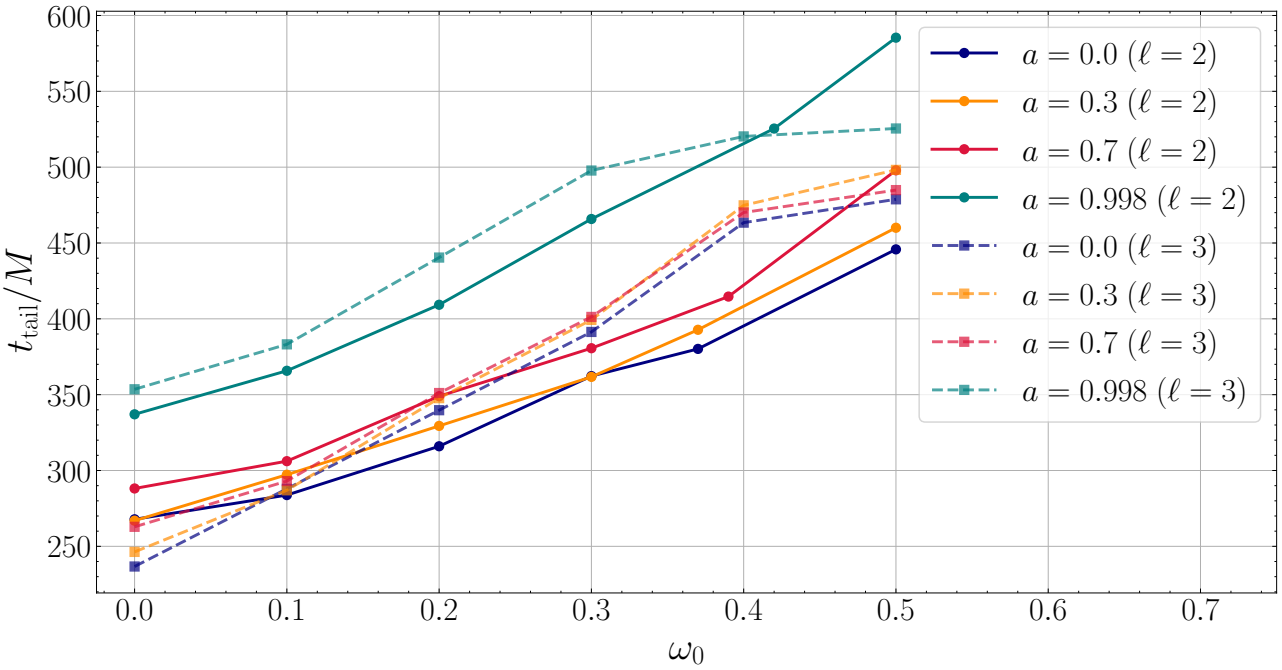


Figure 6.14: **Tail starting times across spins and multipoles.** Dependence of $t_{\rm tail}$ on the injection frequency ω_0 for spins $a = 0.0$, 0.3, 0.7, and 0.998, comparing $\ell = 2$ (solid) and $\ell = 3$ (dashed). The onset of the tail is systematically delayed both by higher rotation and by higher multipoles, reflecting the longer persistence of the quasinormal ringing.

6.3.3 Resonance amplitudes

In order to identify resonant excitations, we fitted the ringdown waveforms with a damped sinusoid model for the QNMs. The extracted amplitudes A_{200} as a function of the initial frequency ω_0 are shown in Figure 6.15 for spins $a = 0.0, 0.3, 0.7$, and 0.998. For small ω_0, the amplitudes are modest and similar across spins, but clear peaks appear as ω_0 approaches the real part of the fundamental QNM frequency (vertical dashed lines). The resonance is most pronounced for $a = 0.998$, where the amplitude exceeds the Schwarzschild value by more than a factor of four, confirming that the excitation is maximized when the initial perturbation is tuned to the natural ringing frequency of the BH.

To highlight the resonant behavior more clearly, in Figure 6.16 we isolate the resonance peaks for each spin and connect them with a guiding curve. This representation emphasizes how the maximum excitation amplitude grows steadily with the spin, reaching its largest value in the near–extremal case.

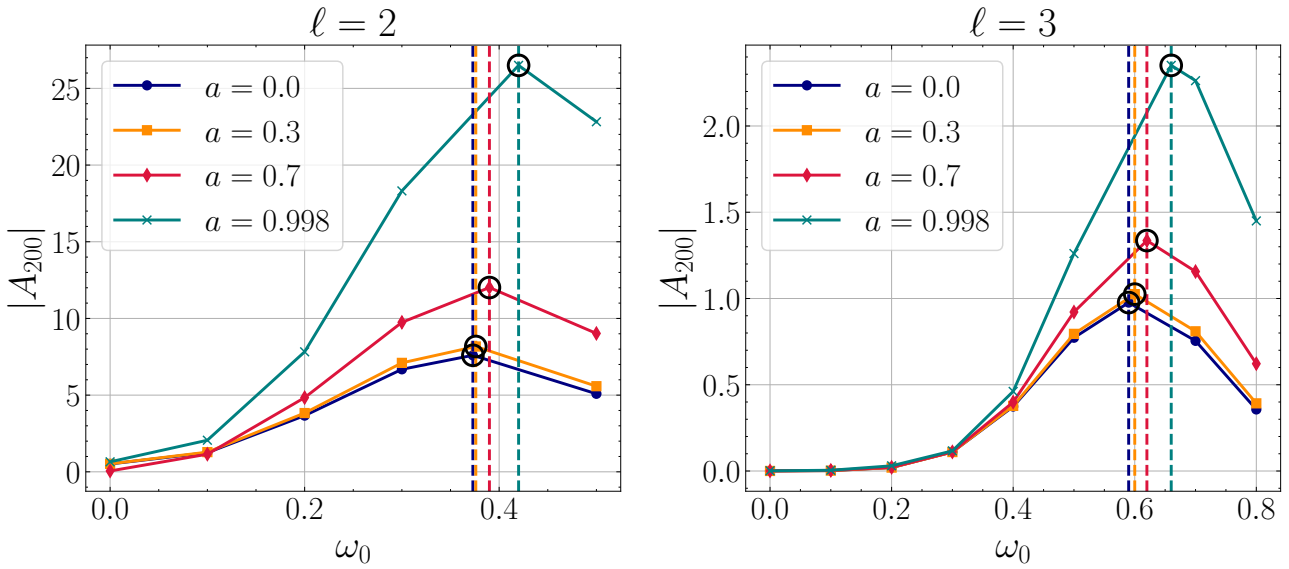


Figure 6.15: **Fitted amplitudes of the ringdown signal.** Obtained from a simple damped sinusoid model, shown as a function of the initial frequency parameter ω_0 for spins $a = 0.0, 0.3, 0.7$, and 0.998. The vertical dashed lines indicate the fundamental QNM frequencies for each spin.

Moreover, the alignment of these resonant points with the corresponding QNM frequencies confirms the physical interpretation of the peaks as resonance phenomena, rather than numerical artifacts. Finally, the comparison between $\ell = 2$ and $\ell = 3$ shows that both multipoles exhibit a clear resonant peak aligned with the fundamental QNM frequency and growing with spin. However, the quadrupolar case ($\ell = 2$) consistently dominates in magnitude, producing resonance amplitudes more than an order of magnitude larger than in the $\ell = 3$ case.

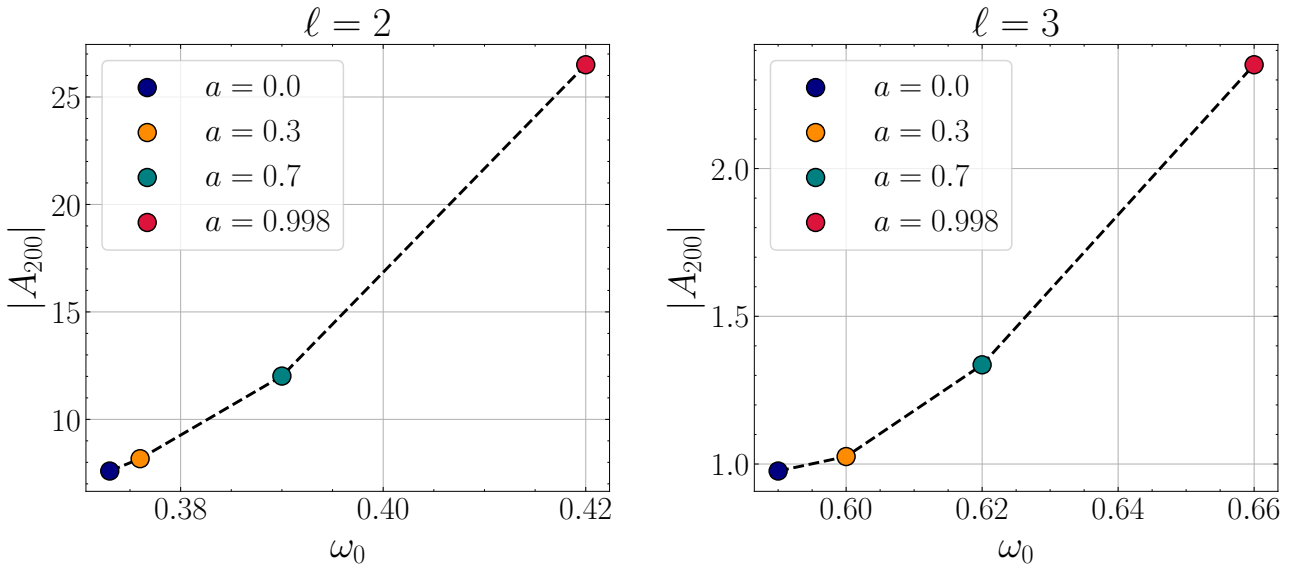


Figure 6.16: **Resonant amplitudes across spins.** Extracted from Figure 6.15, shown as isolated points for each spin and connected by a guiding curve.

6.3.4 Amplitude and tail exponent recovery

In order to validate our procedure, we illustrate in Figure 6.17 a representative example corresponding to $a = 0.3$ and $\omega_0 = 0.2$. The upper panel shows the numerical signal together with the power–law fit $B(t) = 3.69 \times 10^{11} t^{-7}$ evaluated at the tail starting time $t_0 = 329.4$, where the agreement is excellent. This confirms that our method allows us to reliably recover the late–time amplitudes directly from the numerical data. The lower panel presents the R^2 coefficient as a function of the power–law exponent p. The maximum is reached in the range $p \in [7, 8]$, consistent with the theoretical prediction of a $1/t^7$ decay for this type of perturbations. Although here we only display a single case for clarity, similar results are obtained for all spins and initial data, supporting the robustness of both the amplitude recovery and the exponent estimation.

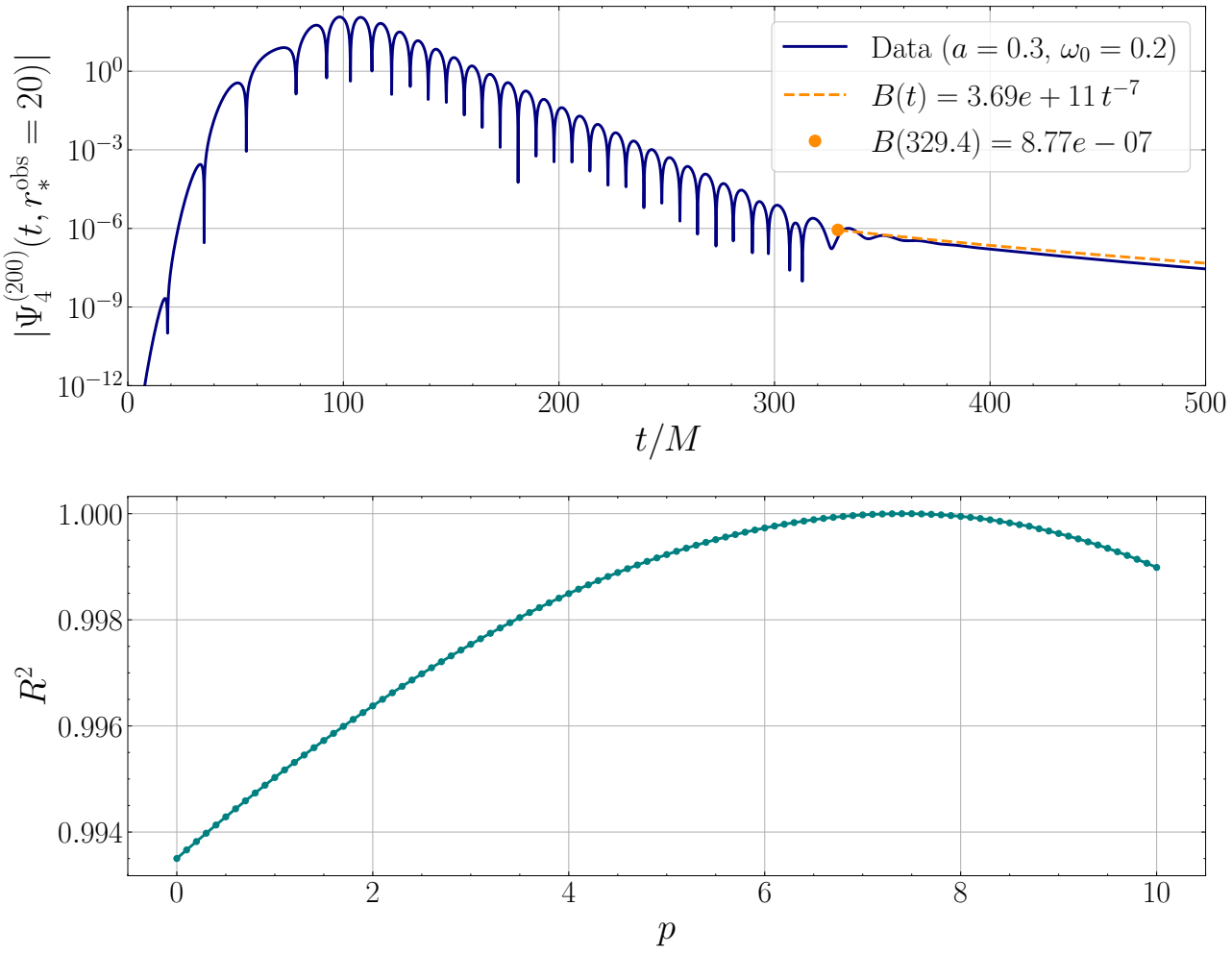


Figure 6.17: **Amplitude recovery and R^2 for $a = 0.3$, $\omega_0 = 0.2$.** Upper panel: recovered tail amplitude at $t_{\rm tail}$. Lower panel: coefficient of determination R^2 as a function of the fitted exponent p.

6.3.5 Prompts

The early–time prompt response can be characterized by tracking the time and amplitude of its global maximum as a function of the initial frequency parameter ω_0. The results are shown in Figure 6.18 for

$\ell = 2$ and in Figure 6.19 for $\ell = 3$, across different spins.

For $\ell = 2$ (Fig. 6.18), the prompt peaks occur at $\sim 98M$ for small ω_0, independently of spin. As ω_0 increases, the peak is delayed for rapidly rotating BHs, reaching $\sim 108M$ for $a = 0.998$. The maximum amplitudes grow with ω_0 up to a resonant peak at $\omega_0 \simeq 0.4$, more than twice as large in the near–extremal case than in Schwarzschild.

For $\ell = 3$ (Fig. 6.19), the same pattern is observed, with the resonance shifted to $\omega_0 \sim 0.6$. In both cases, spin enhances the delay and amplification of the prompt, confirming that the initial frequency content and the BH spin jointly determine the efficiency of its excitation.

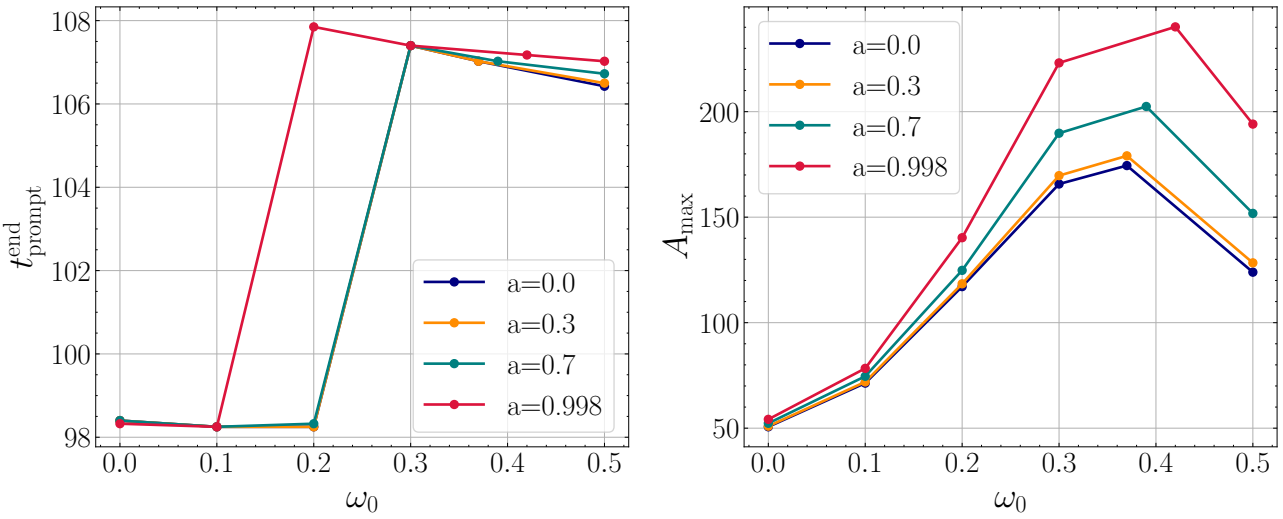


Figure 6.18: **Prompt peak timing and amplitude for $\ell = 2$.** Time (left) and amplitude (right) of the maximum prompt signal as a function of the initial frequency parameter ω_0, for spins $a = 0.0, 0.3, 0.7$, and 0.998.

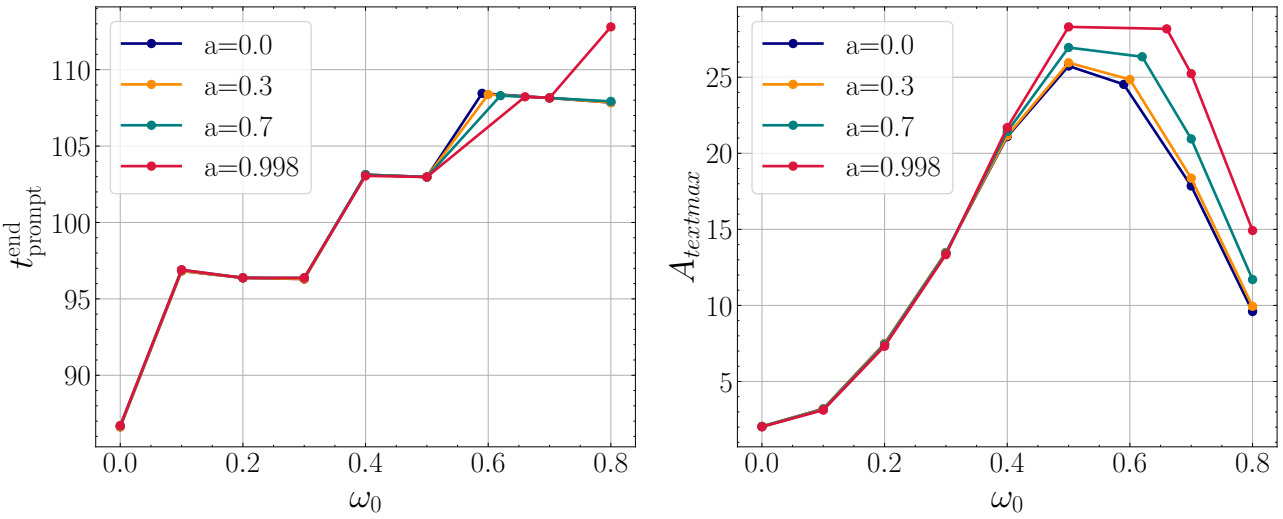
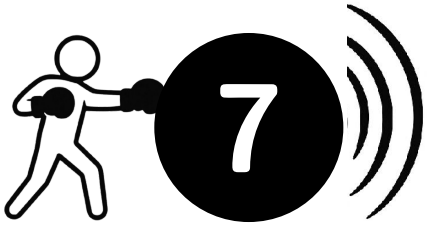


Figure 6.19: **Prompt peak timing and amplitude for $\ell = 3$.** Time (left) and amplitude (right) of the maximum prompt signal as a function of the initial frequency parameter ω_0, for spins $a = 0.0, 0.3, 0.7$, and 0.998.

CHAPTER



Discussion and conclusions

In this thesis we have carried out a detailed study of the time–domain evolution of BH perturbations in both Schwarzschild and Kerr spacetimes, employing NLPT as our main tool. The analysis was based on the evolution of the RW equation in the Schwarzschild case and the Teukolsky equation in the Kerr case, and it was designed to disentangle the contributions of the three canonical stages of the waveform (the prompt response, the QNM ringing, and the late–time tail) and to understand how they are shaped by the interplay of initial data and the background geometry. To this end, we systematically varied the width σ and the carrier frequency ω_0 of the perturbation, as well as the spin a of the BH. In this way, we were able to map out how the spectral content of the perturbation and the rotational properties of the spacetime determine the observable features of the signal.

The main quantitative results can be summarized as follows:

- The **prompt response** is highly sensitive to the characteristics of the initial perturbation. Broad pulses and low values of ω_0 generate an earlier and stronger prompt, which in turn shortens the duration of the subsequent QNM window. This effect becomes even more pronounced in rapidly rotating Kerr BHs (the near–extremal regime amplifies the prompt and delays its maximum).

- The **QNM ringing** appears most clearly for narrow perturbations ($\sigma \lesssim 6$) and for carrier frequencies tuned close to the fundamental Schwarzschild resonance ($\omega_0 \simeq 0.374$). In this regime the waveform is cleanly dominated by the fundamental mode, and the extracted frequencies and damping times agree with theoretical predictions to within $< 2\%$. As the spin is increased, the QNM spectrum shifts in line with Kerr theory, and the relative importance of higher overtones becomes more significant.

- The analysis of **amplitude ratios** (A^R_{20n}) provides a useful diagnostic for the reliability of overtone extraction. When the waveform is relatively free of tail contamination, the ratios behave consistently (peaking near resonant ω_0 and decreasing away from resonance). However, for broad pulses or strongly off–resonant initial data, the fitting procedure incorrectly attributes part of the

tail contribution to higher modes, producing spurious ratios. In this sense, amplitude ratios serve not only to characterize modal excitation but also to identify the limitations of overtone analysis.

- The **late–time tail** is a robust feature of the signal, always emerging with a power–law decay $\Psi(t) \sim t^{-p}$ and with an exponent $p \simeq 7$ for $\ell = 2$, consistent with the Price law prediction. Its onset time ($t_{\rm tail}$) is not fixed but depends on the initial perturbation (broader pulses lead to an earlier onset, confirming the interpretation of tails as a low–frequency phenomenon). The inclusion of spin does not alter the decay index but does affect the relative amplitude (which becomes more prominent as the BH approaches extremality).

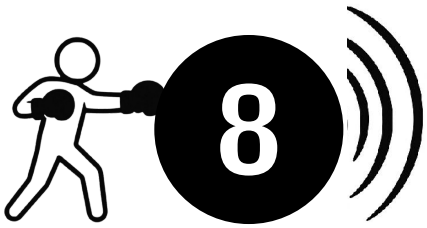
Beyond these quantitative statements, several broader insights arise from the analysis. Perhaps the most important is the dual nature of the BH ringdown. On the one hand, the QNM spectrum (the set of complex frequencies) is universal, depending only on the mass and spin of the BH. On the other hand, the amplitudes of the modes (and therefore the detailed shape of the observed signal) are strongly influenced by the properties of the initial perturbation. This duality explains why the QNM spectrum is robust and well suited for GW spectroscopy, while at the same time tails remain so elusive in both NR simulations and observations. In astrophysically realistic scenarios (such as binary BH mergers) the perturbations resemble narrow, high–frequency pulses that maximize QNM visibility but naturally suppress the tail.

From the point of view of GW astronomy, our results reinforce two complementary messages. First, tails are theoretically robust but astrophysically irrelevant (their amplitude is suppressed by at least seven orders of magnitude relative to the fundamental mode, far below the sensitivity of current and planned detectors such as LISA). Second, overtones remain an essential component of the observable ringdown. Their robust excitation under resonant conditions, and their systematic growth with spin, suggest that highly spinning BHs may produce particularly rich spectra (offering promising opportunities for precision tests of GR). The fact that reliable overtone extraction requires a waveform uncontaminated by tails is consistent with current analyses (only the fundamental mode and, in a few cases, the first overtone have been measured with confidence).

This study is not without limitations. We have restricted our analysis to the linear regime (thus neglecting nonlinear mode coupling and second–order effects). Our procedure for measuring tail amplitudes is subject to systematic bias from finite–time windows and residual QNM contamination, and the initial data employed (Gaussian and frequency–modulated pulses) are idealizations that cannot fully capture the complexity of astrophysical merger dynamics. Nevertheless, these simplified setups allow a controlled exploration of the underlying physics and provide a bridge between analytic predictions and NR simulations.

In conclusion, the BH ringdown is not a monolithic decay but a structured signal composed of prompt, QNM, and tail phases (whose relative visibility depends on the interplay between geometry and initial data). Quasinormal frequencies encypher the universal properties of the BH, while amplitudes retain memory of the perturbation that excited them. This duality is a defining feature of BHPT, and it explains both the robustness of QNM detection in GW astronomy and the theoretical subtlety of late–time tails in curved spacetimes.

Chapter



Future perspectives

The most natural step following this work is to move beyond NLPT and perform full NR simulations that explicitly incorporate the lessons learned here about the interplay of QNM ringing and late–time tails. Our study has shown that the visibility and relative strength of tails depend sensitively on the spectral content of the initial perturbation, which helps to clarify why they remain elusive in merger simulations. By transferring this understanding to the nonlinear regime, one can design numerical experiments that probe tails under controlled conditions and test whether the suppression observed in astrophysical scenarios is indeed as robust as predicted. Several concrete directions naturally emerge:

- **Guided NR experiments.** The parameter dependence mapped out with Gaussian and frequency–modulated perturbations in NLPT can be used to set up initial data in NR tailored to maximize tail excitation. This could provide the first clear numerical evidence of tails in fully nonlinear spacetimes.
- **Second–order perturbations.** Extending the analysis beyond the linear regime would allow us to quantify mode–coupling and self–interaction effects, which are expected to become relevant for highly spinning or highly dynamical BHs. This would bridge the gap between analytic predictions and the rich phenomenology observed in NR.
- **Hyperboloidal slicing.** Adopting hyperboloidal foliations in future simulations would provide direct access to null infinity, enabling a cleaner extraction of late–time behaviour and reducing the systematic bias from finite–time windows encountered in this work.
- **Astrophysical realism.** Replacing toy initial data with inspiral- or plunge–motivated perturbations would clarify how merger dynamics shape overtone excitation and tail suppression. This would link perturbative insights more closely to gravitational–wave observations.

Bibliography

[1] A. Einstein. Die Feldgleichungen der Gravitation. *Sitzungsberichte der Königlich Preussischen Akademie der Wissenschaften*, pages 844–847, January 1915. URL: https://ui.adsabs.harvard.edu/abs/1915SPAW.....844E.

[2] A. Einstein. Näherungsweise integration der feldgleichungen der gravitation. *Sitzungsberichte der Königlich Preußischen Akademie der Wissenschaften (Berlin)*, pages 688–696, January 1916. URL: https://ui.adsabs.harvard.edu/abs/1916SPAW.....688E.

[3] C. W. Misner, K. S. Thorne, and J. A. Wheeler. *Gravitation*. W. H. Freeman, San Francisco, 1973.

[4] R. M. Wald. *General Relativity*. The University of Chicago Press, 1984.

[5] S. M. Carroll. *Spacetime and Geometry: An Introduction to General Relativity*. Cambridge University Press, 2019.

[6] Tomás Ortín. *Gravity and Strings*. Cambridge Monographs on Mathematical Physics. Cambridge University Press, 2004.

[7] J. L. Ripley. Notes on the newman–penrose formalism, July 2023. URL: https://jlripley314.github.io/physics/newman_penrose_formalism.pdf.

[8] V. P. Frolov and I. D. Novikov. *Black hole physics : basic concepts and new developments*. 1998. URL: https://ui.adsabs.harvard.edu/abs/1998bhp..book.....F.

[9] K. Schwarzschild. Über das Gravitationsfeld eines Massenpunktes nach der Einsteinschen Theorie. *Sitzungsberichte der Königlich Preussischen Akademie der Wissenschaften*, pages 189–196, January 1916. URL: https://ui.adsabs.harvard.edu/abs/1916SPAW.....189S.

[10] D. Baumann. *General Relativity Lecture Notes*. University of Amsterdam, 2019. URL: http://cosmology.amsterdam/wp-content/uploads/2021/10/GR-Oct19.pdf.

[11] D. Tong. *Lectures on General Relativity*. University of Cambridge, 2022. URL: http://www.damtp.cam.ac.uk/user/tong/gr/gr.pdf.

[12] B. F. Schutz and C. M. Will. Black hole normal modes - A semianalytic approach. , 291:L33–L36, April 1985. doi:10.1103/PhysRevD.35.3621.

[13] R. P. Kerr. Gravitational Field of a Spinning Mass as an Example of Algebraically Special Metrics. *Phys. Rev. Lett.*, 11:237–238, Sep 1963. doi:10.1103/PhysRevLett.11.237.

[14] R. H. Boyer and R. W. Lindquist. Maximal Analytic Extension of the Kerr Metric. *Journal of Mathematical Physics*, 8(2):265–281, February 1967. doi:10.1063/1.1705193.

[15] R. Penrose and R. M. Floyd. Extraction of rotational energy from a black hole. *Nature*, 229:177–179, 1971. doi:10.1038/physci229177a0.

[16] R. Brito, V. Cardoso, and P. Pani. *Superradiance: New Frontiers in Black Hole Physics*. Springer International Publishing, 2020. arXiv:1501.06570[gr-qc], doi:10.1007/978-3-030-46622-0.

[17] J. M. Bardeen, W. H. Press, and S. A. Teukolsky. Rotating Black Holes: Locally Nonrotating Frames, Energy Extraction, and Scalar Synchrotron Radiation. *The Astrophysical Journal*, 178:347–370, December 1972. doi:10.1086/151796.

[18] M. Maggiore. *Gravitational Waves: Volume 1, Theory and Experiments*. Oxford University Press, 2008.

[19] B. F. Schutz. *A First Course in General Relativity*. Cambridge University Press, 2nd edition, 2009.

[20] A. Einstein. Über gravitationswellen. *Sitzungsberichte der Königlich Preußischen Akademie der Wissenschaften (Berlin)*, pages 154–167, January 1918. URL: https://ui.adsabs.harvard.edu/abs/1918SPAW.....154E.

[21] R. A. Hulse and J. H. Taylor. Discovery of a pulsar in a binary system. *The Astrophysical Journal Letters*, 195:L51–L53, January 1975. URL: https://ui.adsabs.harvard.edu/abs/1975ApJ...195L..51H, doi:10.1086/181708.

[22] B. P. Abbott et al. (LIGO Scientific Collaboration and Virgo Collaboration). Observation of Gravitational Waves from a Binary Black Hole Merger. *Physical Review Letters*, 116(6):061102, February 2016. arXiv:1602.03837[gr-qc], doi:10.1103/physrevlett.116.061102.

[23] B. Bonga. *Foundations of gravitational waves and black hole perturbation theory*. 2025. URL: https://hef.ru.nl/~bbonga/documents/foundations-gw/foundationsGW.pdf.

[24] M. Isi. Parametrizing gravitational-wave polarizations. *Classical and Quantum Gravity*, 40(20):203001, September 2023. arXiv:2208.03372[gr-qc], doi:10.1088/1361-6382/acf28c.

[25] R. A. Isaacson. Gravitational Radiation in the Limit of High Frequency. I. The Linear Approximation and Geometrical Optics. *Phys. Rev.*, 166(5):1263–1271, February 1968. doi:10.1103/PhysRev.166.1263.

[26] R. A. Isaacson. Gravitational Radiation in the Limit of High Frequency. II. Nonlinear Terms and the Effective Stress Tensor. *Phys. Rev.*, 166:1272–1280, Feb 1968. doi:10.1103/PhysRev.166.1272.

[27] X. Jiménez Forteza, S. Bhagwat, P. Pani, and V. Ferrari. Spectroscopy of binary black hole ringdown using overtones and angular modes. *Physical Review D*, 102(4), August 2020. arXiv:2005.03260[gr-qc], doi:10.1103/physrevd.102.044053.

[28] M. Bailes et al. Gravitational-wave physics and astronomy in the 2020s and 2030s. *Nature Reviews Physics*, 3(5):344–366, January 2021. doi:10.1038/s42254-021-00303-8.

[29] E. Berti. *Black Hole Perturbation Theory*. Lectures at the ICTS Summer School on Gravitational-Wave Astronomy, Bangalore, India, July 2016. URL: https://www.icts.res.in/event/page/3071.

[30] Event Horizon Telescope Collaboration. First sagittarius a* event horizon telescope results. iv. variability, morphology, and black hole mass. *The Astrophysical Journal Letters*, 930(2):L15, May 2022. arXiv:2311.08697[astro-ph], doi:10.3847/2041-8213/ac6736.

[31] Ruth A Daly, Megan Donahue, Christopher P O'Dea, Biny Sebastian, Daryl Haggard, and Anan Lu. New black hole spin values for sagittarius a* obtained with the outflow method. *Monthly Notices of the Royal Astronomical Society*, 527(1):428–436, 10 2023. arXiv:https://academic.oup.com/mnras/article-pdf/527/1/428/52716172/stad3228.pdf, doi:10.1093/mnras/stad3228.

[32] T. Regge and J. A. Wheeler. Stability of a Schwarzschild Singularity. *Phys. Rev.*, 108:1063–1069, Nov 1957. doi:10.1103/PhysRev.108.1063.

[33] F. J. Zerilli. Effective Potential for Even-Parity Regge-Wheeler Gravitational Perturbation Equations. *Phys. Rev. Lett.*, 24:737–738, Mar 1970. doi:10.1103/PhysRevLett.24.737.

[34] S. A. Teukolsky. Perturbations of a Rotating Black Hole. I. Fundamental Equations for Gravitational, Electromagnetic, and Neutrino-Field Perturbations. *The Astrophysical Journal*, 185:635–648, oct 1973. doi:10.1086/152444.

[35] H. Okawa, H. Witek, and V. Cardoso. Black holes and fundamental fields in numerical relativity: Initial data construction and evolution of bound states. *Physical Review D*, 89(10), May 2014. arXiv:1401.1548[gr-qc], doi:10.1103/physrevd.89.104032.

[36] Karl Martel. *Particles and black holes: time-domain integration of the equations of black-hole perturbation theory*. PhD thesis, University of Guelph, 2003. URL: https://hdl.handle.net/10214/19461.

[37] Jordin Janssen, Béatrice Bonga, and Badri Krishnan. Isospectrality of quasi-normal mode frequencies in four- and five-dimensional black holes: Perturbation theory on schwarzschild and black string spacetimes, February 2025. URL: https://hef.ru.nl/~bbonga/documents/Thesis-2025%20-IsospectralityofQNMFrequenciesSchwarzschildandBSspacetimes_JordinJanssen.pdf.

[38] Vincent Moncrief. Odd-parity stability of a Reissner-Nordström black hole. *Phys. Rev. D*, 9:2707–2709, May 1974. doi:10.1103/PhysRevD.9.2707.

[39] K. Glampedakis, A. D. Johnson, and D. Kennefick. Darboux transformation in black hole perturbation theory. *Phys. Rev. D*, 96:024036, Jul 2017. arXiv:1702.06459[gr-qc], doi:10.1103/PhysRevD.96.024036.

[40] Alessandro Nagar and Luciano Rezzolla. Gauge-invariant non-spherical metric perturbations of Schwarzschild black-hole spacetimes. *Class. Quant. Grav.*, 22:R167, 2005. [Erratum: Class.Quant.Grav. 23, 4297 (2006)]. arXiv:gr-qc/0502064, doi:10.1088/0264-9381/22/16/R01.

[41] E. Newman and R. Penrose. An Approach to Gravitational Radiation by a Method of Spin Coefficients. *Journal of Mathematical Physics*, 3(3):566–578, May 1962. doi:10.1063/1.1724257.

[42] N. Loutrel, J. L. Ripley, E. Giorgi, and F. Pretorius. Second-order perturbations of Kerr black holes: Formalism and reconstruction of the first-order metric. *Phys. Rev. D*, 103:104017, May 2021. arXiv:2008.11770[gr-qc], doi:10.1103/PhysRevD.103.104017.

[43] Manuela Campanelli and Carlos O. Lousto. Second order gauge invariant gravitational perturbations of a Kerr black hole. *Physical Review D*, 59(12), May 1999. arXiv:9811019[gr-qc], doi:10.1103/physrevd.59.124022.

[44] João Paulo Cavalcante. Isomonodromy Method and Black Holes Quasinormal Modes: numerical results and extremal limit analysis, 2023. arXiv:2307.16209.

[45] Justin L. Ripley, Nicholas Loutrel, Elena Giorgi, and Frans Pretorius. Numerical computation of second-order vacuum perturbations of Kerr black holes. *Physical Review D*, 103(10), May 2021. arXiv:2010.00162[gr-qc], doi:10.1103/physrevd.103.104018.

[46] L. Santoni. *Black Hole Perturbation Theory*. Lectures on Aspects of Black Hole Perturbation Theory course, Institut de Physique Théorique (IPhT), Saclay, 2024. URL: https://courses.ipht.fr/sites/default/files/local-media-files--2024-07-12%2019%3A15/BHPT.pdf.

[47] V. Baibhav et al. Agnostic black hole spectroscopy: Quasinormal mode content of numerical relativity waveforms and limits of validity of linear perturbation theory. *Physical Review D*, 108(10), November 2023. doi:10.1103/physrevd.108.104020.

[48] E. Berti, V. Cardoso, and A. O. Starinets. Quasinormal modes of black holes and black branes. *Classical and Quantum Gravity*, 26(16):163001, July 2009. doi:10.1088/0264-9381/26/16/163001.

[49] R. A. Konoplya and Alexander Zhidenko. Quasinormal modes of black holes: From astrophysics to string theory. *Reviews of Modern Physics*, 83(3):793–836, July 2011. arXiv:1102.4014[gr-qc], doi:10.1103/revmodphys.83.793.

[50] R. F. Rosato and P. Pani. On the universality of late-time ringdown tail. *Phys. Rev. D*, 112:024080, Jul 2025. arXiv:2505.08877[gr-qc], doi:10.1103/4yvq-57x6.

[51] R. H. Price. Nonspherical Perturbations of Relativistic Gravitational Collapse. I. Scalar and Gravitational Perturbations. *Physical Review D*, 5(10):2419–2438, May 1972. doi:10.1103/PhysRevD.5.2419.

[52] M. Giesler, M. Isi, M. A. Scheel, and S. A. Teukolsky. Black Hole Ringdown: The Importance of Overtones. *Physical Review X*, 9(4), December 2019. arXiv:1903.08284[gr-qc], doi:10.1103/physrevx.9.041060.

[53] X. Jiménez Forteza and P. Mourier. High-overtone fits to numerical relativity ringdowns: Beyond the dismissed n=8 special tone. *Physical Review D*, 104(12), December 2021. arXiv:2107.11829[gr-qc], doi:10.1103/physrevd.104.124072.

[54] Richard P. Brent. *Algorithms for Minimization without Derivatives*. Prentice-Hall Series in Automatic Computation. Prentice-Hall, Englewood Cliffs, NJ, 1973. Edited by George Forsythe. Errata: Math. Comp. 29 (1975), 1166. MR 51#7283.

[55] E. Pazos-Ávalos and C. O. Lousto. Numerical integration of the Teukolsky equation in the time domain. *Physical Review D*, 72(8), October 2005. arXiv:0409065[gr-qc], doi:10.1103/physrevd.72.084022.

[56] W. Krivan, P. Laguna, P. Papadopoulos, and N. Andersson. Dynamics of perturbations of rotating black holes. *Physical Review D*, 56(6):3395–3404, September 1997. arXiv:9702048[gr-qc], doi:10.1103/physrevd.56.3395.

[57] B.F. Schutz. *The Art and Science of Black Hole Mergers*, page 321–332. Springer-Verlag. arXiv:0410121v1[gr-qc], doi:10.1007/11403913_63.

[58] Frans Pretorius. Evolution of binary black-hole spacetimes. *Physical Review Letters*, 95(12), September 2005. arXiv:0507014[gr-qc], doi:10.1103/physrevlett.95.121101.

[59] Rüter Hannes R. Carullo Gregorio. Amicis, Marina De. Late-time tails in nonlinear evolutions of merging black holes. *Phys. Rev. Lett.*, pages –, Sep 2025. arXiv:2412.06887, doi:10.1103/2brx-xnyr.

[60] Nils Andersson. Evolving test fields in a black-hole geometry. *Physical Review D*, 55(2):468–479, January 1997. arXiv:9607064[gr-qc], doi:10.1103/physrevd.55.468.

[61] Leo C. Stein. qnm: A Python package for calculating Kerr quasinormal modes, separation constants, and spherical-spheroidal mixing coefficients. *J. Open Source Softw.*, 4(42):1683, 2019. arXiv:1908.10377, doi:10.21105/joss.01683.

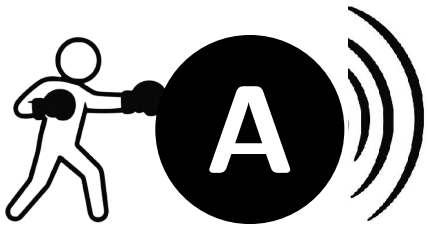
[62] Lior M. Burko and Amos Ori. Late-time evolution of nonlinear gravitational collapse. *Phys. Rev. D*, 56:7820–7832, Dec 1997. URL: https://link.aps.org/doi/10.1103/PhysRevD.56.7820, doi:10.1103/PhysRevD.56.7820.

[63] Alan L. Myers. Natural system of units in general relativity. 2016. URL: https://www.seas.upenn.edu/~amyers/NaturalUnits.pdf.

[64] A. Svyatkovskyy Kholyavka and R. Alves Batista. Multimessenger signatures of particle acceleration by black holes. Master's thesis, Autonomous University of Madrid, September 2024.

[65] Wikipedia. Geometrized unit system, July 2024. URL: https://en.wikipedia.org/wiki/Geometrized_unit_system.

Appendix



Geometrized unit system

In this appendix, we summarize the system of geometrized units, following [63] and [64].

A system of geometrized units is one in which the speed of light (c) and the gravitational constant (G) are set equal to one

$$c = G = 1. \tag{A.1}$$

Numerically, their values in SI units are

$$c = 2.9979 \times 10^{8}\ \mathrm{m\,s^{-1}}, \qquad G = 6.67430 \times 10^{-11}\ \mathrm{m^{3}\,kg^{-1}\,s^{-2}}. \tag{A.2}$$

Since in this unit system the speed of light is set to unity, time and length become directly equivalent: the time it takes light to travel a given distance equals that distance, so time is measured in units of length. Moreover, momentum and energy are components of the four-momentum, whose norm is given by the mass. Consequently, in geometrized units, energy, momentum, and mass all share the same dimension, namely length [65].

In the context of the international system, a quantity with dimensions

$$\left[kg^{\alpha}\, m^{\beta}\, s^{\gamma}\right], \tag{A.3}$$

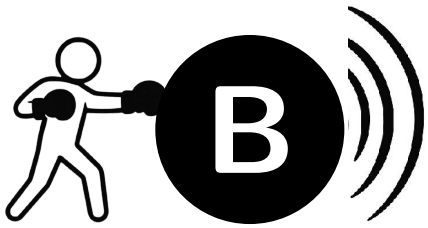
is expressed in geometrized units simply as a power of length,

$$\left[m^{\alpha+\beta+\gamma}\right]. \tag{A.4}$$

To convert from geometrized units back to international system units, one multiplies by the factor

$$G^{-\alpha}\, c^{2\alpha-\gamma}. \tag{A.5}$$

Appendix



Spherical Harmonics

When dealing with perturbations around a spherically symmetric background, the angular dependence can always be separated using functions that live on the unit two–sphere $\mathcal{S}^2$. These are the spherical harmonics, which appear in three different guises: scalars, vectors and tensors. Each type provides a complete orthogonal basis on $\mathcal{S}^2$, allowing us to expand any field with angular indices into a discrete set of modes. In what follows we will briefly review these constructions, following the references [7, 36, 37].

What makes this decomposition especially powerful in BH perturbation theory is the fact that spherical harmonics can be classified according to their parity. Under the transformation

$$(\theta, \phi) \;\longmapsto\; (\pi - \theta, \pi + \phi), \tag{B.1}$$

the harmonics are either *even* (they pick up a factor $(-1)^\ell$) or *odd* (they pick up $(-1)^{\ell+1}$). This simple property ensures that even and odd sectors decouple, giving rise to two independent sets of equations: the RW sector (odd) and the ZM sector (even).

B.1 Scalar harmonics

The scalar spherical harmonics $Y^{\ell m}(\theta, \phi)$ are the familiar functions from quantum mechanics. They are eigenfunctions of the Laplacian on $\mathcal{S}^2$

$$D^A D_A Y^{\ell m} = -\ell(\ell+1)\, Y^{\ell m}. \tag{B.2}$$

Any scalar function defined on the sphere can be decomposed as

$$S(\theta, \phi) = \sum_{\ell, m} s_{\ell m}\, Y^{\ell m}(\theta, \phi). \tag{B.3}$$

The orthogonality relation is

$$\int_{\mathcal{S}^2} Y^{\ell m}\, Y^{\ell' m' *}\, d\Omega = \delta_{\ell \ell'}\, \delta_{m m'}. \tag{B.4}$$

B.2 Vector harmonics

Vectors on the sphere can be expanded in terms of two independent bases, one even and one odd:

$$Y_A^{\ell m} := D_A Y^{\ell m}, \tag{B.5}$$

$$X_A^{\ell m} := -\epsilon_A{}^B D_B Y^{\ell m}, \qquad \epsilon_{\theta\phi} = \sin\theta. \tag{B.6}$$

A generic vector field V_A on the sphere decomposes as

$$V_A = \sum_{\ell,m} \left(v_{\ell m}\, Y_A^{\ell m} + w_{\ell m}\, X_A^{\ell m}\right). \tag{B.7}$$

The orthogonality relations read

$$\int_{\mathcal{S}^2} Y_A^{\ell m}\, Y^{A\,\ell' m'*}\, d\Omega = \ell(\ell+1)\,\delta_{\ell\ell'}\delta_{mm'}, \tag{B.8}$$

$$\int_{\mathcal{S}^2} X_A^{\ell m}\, X^{A\,\ell' m'*}\, d\Omega = \ell(\ell+1)\,\delta_{\ell\ell'}\delta_{mm'}, \tag{B.9}$$

$$\int_{\mathcal{S}^2} Y_A^{\ell m}\, X^{A\,\ell' m'*}\, d\Omega = 0. \tag{B.10}$$

B.3 Tensor harmonics

For metric perturbations we need symmetric rank–2 tensors on $\mathcal{S}^2$, which again split into even and odd parity:

$$Y_{AB}^{\ell m} := \Big(D_A D_B + \tfrac{1}{2}\ell(\ell+1)\,\Omega_{AB}\Big) Y^{\ell m}, \tag{B.11}$$

$$X_{AB}^{\ell m} := -\tfrac{1}{2}\Big(\epsilon_A{}^C D_B + \epsilon_B{}^C D_A\Big) D_C Y^{\ell m}. \tag{B.12}$$

A general symmetric tensor can then be expanded as

$$T_{AB} = \sum_{\ell,m} \Big(v_{\ell m}\,\Omega_{AB} Y^{\ell m} + w_{\ell m}\, Y_{AB}^{\ell m} + u_{\ell m}\, X_{AB}^{\ell m}\Big). \tag{B.13}$$

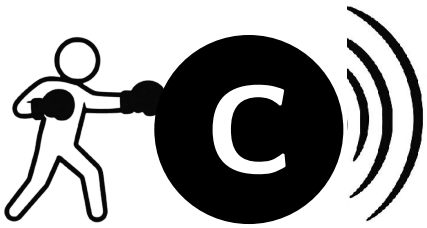
The orthogonality relations are

$$\int_{\mathcal{S}^2} Y_{AB}^{\ell m}\, Y^{AB\,\ell' m'*}\, d\Omega \propto \delta_{\ell\ell'}\delta_{mm'}, \tag{B.14}$$

$$\int_{\mathcal{S}^2} X_{AB}^{\ell m}\, X^{AB\,\ell' m'*}\, d\Omega \propto \delta_{\ell\ell'}\delta_{mm'}, \tag{B.15}$$

$$\int_{\mathcal{S}^2} Y_{AB}^{\ell m}\, X^{AB\,\ell' m'*}\, d\Omega = 0. \tag{B.16}$$

Appendix



Perturbation on Schwarzschild spacetime

In this appendix we collect the linearized geometric relations on a Schwarzschild background that will be used in subsection 2.1.2. We perturb the metric as $g^p_{\mu\nu} \to g_{\mu\nu} + \gamma_{\mu\nu}$ and work consistently to first order in $\gamma_{\mu\nu}$. We first list the perturbed Christoffel symbols, and from them obtain the perturbations of the Riemann, Ricci, Ricci scalar and Einstein tensors; the latter simplifies because the background is Ricci–flat (${}^{(4)}R = 0$). For later use we also give the explicit $(t, r) \oplus (\theta, \phi)$ components and the odd/even (axial/polar) projections built from spherical harmonics. Here, we will follow [7, 37].

C.1 Perturbations of the Christoffel symbols

The Christoffel symbols of the perturbed metric can be decomposed as

$$ {}^{p}\Gamma^{\lambda}_{\mu\nu} = {}^{(4)}\Gamma^{\lambda}_{\mu\nu} + \delta\Gamma^{\lambda}_{\mu\nu}, \qquad \text{with} \qquad \delta\Gamma^{\lambda}_{\mu\nu} = \frac{1}{2} g^{\lambda\alpha} \left(\nabla_\mu \gamma_{\alpha\nu} + \nabla_\nu \gamma_{\alpha\mu} - \nabla_\alpha \gamma_{\mu\nu} \right), \tag{C.1} $$

where $\gamma_{\mu\nu}$ denotes the metric perturbation, ${}^{(4)}\Gamma^{\lambda}_{\mu\nu}$ are the background Schwarzschild Christoffel symbols and $\delta\Gamma^{\lambda}_{\mu\nu}$ their perturbations. The non–vanishing perturbed Christoffel symbols then read [37]

$$ \delta\Gamma^{a}_{bc} = C^{a}_{bc}, \tag{C.2a} $$

$$ \delta\Gamma^{a}_{bC} = \frac{1}{2} g^{ac} \left(\mathcal{D}_b \gamma_{cC} + D_C \gamma_{cb} - \mathcal{D}_c \gamma_{bC} \right) - \frac{1}{r} r_b \gamma^{a}{}_{C}, \tag{C.2b} $$

$$ \delta\Gamma^{a}_{BC} = \frac{1}{2} \left(D_B \gamma^{a}{}_{C} + D_C \gamma^{a}{}_{B} - \mathcal{D}^{a} \gamma_{BC} \right) - r\, r_b\, \Omega_{BC}\, \gamma^{ab}, \tag{C.2c} $$

$$ \delta\Gamma^{A}_{bc} = \frac{1}{2r^2} \left(\mathcal{D}_b \gamma^{A}_{c} + \mathcal{D}_c \gamma^{A}_{b} - D^{A} \gamma_{bc} \right), \tag{C.2d} $$

$$ \delta\Gamma^{A}_{bC} = \frac{1}{2r^2} \left(\mathcal{D}_b \gamma^{A}_{C} + D_C \gamma^{A}_{b} - D^{A} \gamma_{bC} \right) - \frac{1}{r^3} r_b \gamma^{A}_{C}, \tag{C.2e} $$

$$ \delta\Gamma^{A}_{BC} = \frac{1}{r^2} C^{A}_{BC} + \frac{1}{r} r_a \Omega_{BC} \gamma^{Aa}, \tag{C.2f} $$

where the auxiliary quantities C^a_{bc} and C^A_{BC} are defined as

$$C^a_{bc} := \frac{1}{2}\left(\mathcal{D}_c\gamma^a{}_b + \mathcal{D}_b\gamma^a{}_c - \mathcal{D}^a\gamma_{bc}\right), \tag{C.3a}$$

$$C^A_{BC} := \frac{1}{2}\left(D_C\gamma^A{}_B + D_B\gamma^A{}_C - D^A\gamma_{BC}\right). \tag{C.3b}$$

C.2 Perturbations of the Riemann tensor

The Riemann tensor of the perturbed spacetime splits as

$${}^pR^\lambda{}_{\mu\nu\rho} = {}^{(4)}R^\lambda{}_{\mu\nu\rho} + \delta R^\lambda{}_{\mu\nu\rho}, \qquad \text{with} \qquad \delta R^\lambda{}_{\mu\nu\rho} = -2\nabla_{[\mu}\left(\delta\Gamma^\lambda_{\nu]\rho}\right). \tag{C.4}$$

Equivalently, one can write the perturbation as

$$\delta R_{\mu\nu\rho}{}^\lambda = -\nabla_{[\mu}\nabla_{\nu]}\gamma^\lambda{}_\rho - \nabla_{[\mu|\rho|}\gamma^\lambda{}_{\nu]} + \nabla_{[\mu}\nabla^\lambda\gamma_{\nu]\rho}. \tag{C.5}$$

C.3 Perturbations of the Ricci tensor

By contraction, the Ricci tensor becomes

$${}^pR_{\mu\nu} = {}^{(4)}R_{\mu\nu} + \delta R_{\mu\nu}, \qquad \text{with} \qquad \delta R_{\mu\nu} = -2\nabla_{[\nu}\left(\delta\Gamma^\lambda_{\mu]\lambda}\right). \tag{C.6}$$

Expanding explicitly the perturbation yields to

$$\delta R_{\mu\nu} = -\frac{1}{2}\,{}^{(4)}\Box\,\gamma_{\mu\nu} - \frac{1}{2}\nabla_\mu\nabla_\nu\gamma^\lambda{}_\lambda + \nabla_\lambda\nabla_{(\mu}\gamma_{\nu)}{}^\lambda, \tag{C.7}$$

where ${}^{(4)}\Box := \nabla^\mu\nabla_\mu$. The explicit components in the (t,r) and (θ,ϕ) sectors are provided above [37]

$$\begin{aligned}\delta R_{ab} = {}& \mathcal{D}_m C^m_{ab} + \frac{2}{r}r_m C^m_{ab} - \frac{1}{2}\mathcal{D}_a\mathcal{D}_b\gamma^m_m - \frac{1}{2r^2}D^M D_M\gamma_{ab} + \frac{1}{2r^2}D_M(\mathcal{D}_a\gamma^M_b + \mathcal{D}_b\gamma^M_a) - \frac{1}{2r^2}\mathcal{D}_a\mathcal{D}_b\gamma^M_M \\ & + \frac{1}{2r^3}(r_a\mathcal{D}_b\gamma^M_M + r_b\mathcal{D}_a\gamma^M_M) - \frac{1}{r^4}(r_a r_b - r\mathcal{D}_a r_b)\gamma^M_M,\end{aligned} \tag{C.8a}$$

$$\begin{aligned}\delta R_{aB} = {}& \frac{1}{2}D_B\Big(\mathcal{D}_m\gamma^m_a - \mathcal{D}_a\gamma^m_m + \frac{1}{r}r_a\gamma^m_m\Big) - \frac{1}{2}\Big(\Box\gamma_{aB} - \mathcal{D}_m\mathcal{D}_a\gamma^m_B\Big) - \frac{1}{r}(r_a\mathcal{D}_m\gamma^m_B - r_m\mathcal{D}_a\gamma^m_B) \\ & - \frac{1}{r^2}(r_a r^m + r\mathcal{D}_a r^m)\gamma^m_B + \frac{1}{2r^2}D^M(D_B\gamma_{aM} - D_M\gamma_{aB}) - \frac{1}{2r^2}\mathcal{D}_a(D_M\gamma^M_B - D_B\gamma^M_M) \\ & - \frac{1}{r^3}r_a(D_M\gamma^M_B - D_B\gamma^M_M),\end{aligned} \tag{C.8b}$$

$$\begin{aligned}\delta R_{AB} = {}& \Omega_{AB}\Big[r r_a\mathcal{D}_b\Big(\gamma^{ab} - \frac{1}{2}g^{ab}\gamma^m_m\Big) + (r_a r_b + r\mathcal{D}_a r_b)\gamma^{ab}\Big] - \frac{1}{2}D_A D_B\gamma^a_a + \frac{1}{2}\mathcal{D}_a(D_A\gamma^a_B + D_B\gamma^a_A) \\ & + \frac{1}{r}r_a\Omega_{AB}D_M\gamma^{aM} - \frac{1}{2}\Box\gamma_{AB} + \frac{1}{r^2}D_M C^M_{AB} - \frac{1}{2r^2}D_A D_B\gamma^M_M + \frac{1}{r}r^a\mathcal{D}_a\Big(\gamma_{AB} - \frac{1}{2}\Omega_{AB}\gamma^M_M\Big) \\ & - \frac{2}{r^2}r^a r_a\Big(\gamma_{AB} - \frac{1}{2}\Omega_{AB}\gamma^M_M\Big).\end{aligned} \tag{C.8c}$$

C.4 Perturbations of the Ricci scalar

The Ricci scalar splits as

$${}^pR = {}^{(4)}R + \delta R, \qquad \text{with} \qquad \delta(g^{\mu\nu}R_{\mu\nu}) = g^{\mu\nu}\delta R_{\mu\nu} = \delta R = -{}^{(4)}\Box\,\gamma^\mu{}_\mu + \nabla_\mu\nabla_\nu\gamma^{\mu\nu}. \tag{C.9}$$

C.5 Perturbations of the Einstein tensor

Finally, the Einstein tensor takes the form

$$ {}^{p}G_{\mu\nu} = {}^{(4)}G_{\mu\nu} + \delta G_{\mu\nu}, \qquad \text{with} \qquad \delta G_{\mu\nu} = \delta R_{\mu\nu} - \frac{1}{2}\, g_{\mu\nu}\, \delta R - \frac{1}{2}\, \gamma_{\mu\nu}\, {}^{(4)}R. \tag{C.10} $$

This relation mirrors the structure of the full Einstein tensor, with the perturbation $\delta G_{\mu\nu}$ expressed in terms of the perturbed Ricci tensor, Ricci scalar, and the trace of $\gamma_{\mu\nu}$. It provides the basic starting point for linearized Einstein equations, where matter perturbations would appear on the right-hand side. Since the Schwarzschild background is Ricci–flat (${}^{(4)}R = 0$) this reduces to [36]

$$ \begin{aligned} \delta G_{\mu\nu} &= \delta R_{\mu\nu} - \frac{1}{2}\, g_{\mu\nu}\, \delta R \\ &= -\frac{1}{2}\, {}^{(4)}\Box\, \gamma_{\mu\nu} + \nabla_\lambda \nabla_{(\mu} \gamma_{\nu)}{}^{\lambda} - \frac{1}{2}\nabla_\nu \nabla_\mu \gamma^\lambda{}_\lambda - \frac{1}{2} g_{\mu\nu} \left(\nabla^\rho \nabla^\lambda \gamma_{\lambda\rho} - {}^{(4)}\Box\, \gamma^\lambda{}_\lambda \right). \end{aligned} \tag{C.11} $$

The corresponding component expressions in the (t, r) and (θ, ϕ) decomposition are listed above [37]

$$ \begin{aligned} \delta G_{ab} = {}& \frac{1}{2} g_{ab} \Box \gamma^c_c - \frac{1}{2} \mathcal{D}_a \mathcal{D}_b \gamma^c_c + \frac{2}{r} r^c \mathcal{D}_{(a} \gamma_{b)c} + \frac{1}{r} r^c \left(g_{ab} \mathcal{D}^d \gamma_{cd} - \mathcal{D}_c \gamma_{ab} \right) + \mathcal{D}_c \mathcal{D}_{(a} \gamma^c_{b)} - \frac{1}{2} \Box \gamma_{ab} \\ & - g_{ab} \Big(\frac{1}{r} (\mathcal{D}_c r) \gamma^{cd} + \frac{2}{r} \mathcal{D}^c r\, \gamma_{cd} + \frac{1}{r^2} r^c r^d \gamma_{cd} - \frac{1}{2} \mathcal{D}^d \mathcal{D}_c \gamma^c_d \Big) + \frac{1}{2r^2} D_A D^A (g_{ab} \gamma^c_c - \gamma_{ab}) \\ & + \frac{1}{r^3} \Big(2 r_{(a} D_A \gamma^A_{b)} - g_{ab} r^c D_A \gamma^A_c \Big) + D_A \mathcal{D}_{(a} \gamma^A_{b)} + \frac{1}{2r^2} g_{ab} D^C \mathcal{D}_C \gamma^c_c \\ & + \frac{1}{2} g_{ab} \Big(\Box \gamma^A_A - \frac{1}{r^4} D_B D_A \gamma^{AM} + \frac{1}{r^2} D^B D^A \gamma_{AB} \Big) + \frac{r^2 - 1}{r^4} r_a r_b \gamma^A_A \\ & + \frac{1}{2r^3} g_{ab} \Big((\Box r - r^c r_c) \gamma^A_A + \frac{2r^2 + 1}{2r^3} g_{ab} r^c \mathcal{D}_c \gamma^A_A - \frac{1}{r} r_{(a} \mathcal{D}_{b)} \gamma^A_A - \frac{1}{2} \mathcal{D}_a \mathcal{D}_b \gamma^A_A \Big), \end{aligned} \tag{C.12a} $$

$$ \begin{aligned} \delta G_{aB} = {}& \frac{1}{2r} r_a D_B \gamma^b_b - D_B \mathcal{D}_a \gamma^b_b + \frac{1 - r^2}{r^2} r^b r_{(a} \gamma_{b)B} + \frac{r^2 + 1}{2r} r^b \mathcal{D}_a \gamma_{bB} - \frac{1}{2} (\Box \gamma_{aB} - \mathcal{D}_b \gamma^b_B) \\ & - \frac{1}{r} r_a \mathcal{D}_b \gamma^b_B + \frac{1}{2} \mathcal{D}_b \mathcal{D}_a \gamma^b_B - \frac{1 - r}{2r} (\Box r) \gamma_{aB} - \frac{1}{2} \Box \gamma_{aB} + \frac{1}{2} D_A D_B \gamma^A_a - \frac{1}{2r^2} D^A D_A \gamma_{aB} \\ & + \frac{1 - r^2}{r^3} D^A \gamma_{aB} + \mathcal{D}_a D_{[A} \gamma^A_{B]}, \end{aligned} \tag{C.12b} $$

$$ \begin{aligned} \delta G_{AB} = {}& r r^a \mathcal{D}_a \left(\frac{1}{2} \mathcal{D}_a \gamma^b_b - \mathcal{D}_b \gamma^{ab} \right) + \frac{1}{2} r^2 \Omega_{AB} \mathcal{D}_a \mathcal{D}_b \gamma^{ab} + \frac{1}{2} \Omega_{AB} \left(r^2 \Box \gamma^a_a + D^M D_M \gamma^a_a \right) - \frac{1}{2} D_B D_A \gamma^a_a \\ & + \mathcal{D}_a D_{(A} \gamma^a_{B)} - \Omega_{AB} D_M \mathcal{D}_a \gamma^{aM} - 2 r^a r_a \gamma_{AB} + \frac{1}{2r^2} r^a r_a \Omega_{AB} \gamma^M_M \\ & + \frac{1 - r^2}{r} \left(\Box \gamma_{AB} - \frac{1}{2} r (\Box) \Omega_{AB} \gamma^M_M \right) + \frac{r^2 + 1}{2r} \Omega_{AB} r^a \mathcal{D}_a \gamma^M_M - \frac{1}{2} \Box \gamma_{AB} + \frac{1}{r^2} D_M D^M \gamma_{AB} \\ & - \frac{1}{2r^2} \left(D^M D_M \gamma_{AB} + \Omega_{AB} D_M D_N \gamma^{MN} \right) + \frac{1}{2} \Omega_{AB} D^M D^N \gamma_{MN}. \end{aligned} \tag{C.12c} $$

C.6 Explicit calculations (2.41) and (2.49)

In the previous sections we have obtained the general expressions for the perturbations of the Christoffel symbols, Riemann, Ricci and Einstein tensors on a Schwarzschild background. We now turn to the explicit evaluation of the Ricci tensor components when the metric perturbations are expanded in spherical harmonics. In this framework, the perturbations naturally split into odd (axial) and even (polar) sectors, which decouple due to the spherical symmetry of the background. For clarity, we list the explicit form of the Ricci tensor perturbations ($\delta R_{\mu\nu}$) in each sector, starting with the odd–parity part [37]

$$\begin{aligned}
\delta R^{(\mathrm{odd})}_{ab} &= \mathcal{D}_m C^m_{ab} + \frac{2}{r} r_m C^m_{ab} - \frac{1}{2}\mathcal{D}_a\mathcal{D}_b\gamma^M_M - \frac{1}{2r^2}D^M D_M\gamma_{ab} + \frac{1}{2r^2}D_M(\mathcal{D}_a\gamma^M_b + \mathcal{D}_b\gamma^M_a) \\
&\quad - \frac{1}{2r^2}\mathcal{D}_a\mathcal{D}_b\gamma^M_M + \frac{1}{2r^3}(r_a\mathcal{D}_b\gamma^M_M + r_b\mathcal{D}_a\gamma^M_M) - \frac{1}{r^4}(r_a r_b - r\mathcal{D}_a r_b)\gamma^M_M \\
&= \frac{1}{2r^2}D^M(\mathcal{D}_a h_b + \mathcal{D}_b h_a)X_M \\
&= \frac{1}{2r^2}(\mathcal{D}_a h_b + \mathcal{D}_b h_a)D^M X_M \\
&= 0, \qquad \text{(C.13a)}
\end{aligned}$$

$$\begin{aligned}
\delta R^{(\mathrm{odd})}_{aB} &= \frac{1}{2}D_B\left(\mathcal{D}_m\gamma^m_a - \mathcal{D}_a\gamma^m_m + \frac{1}{r}r_a\gamma^m_m\right) - \frac{1}{2}(\Box\gamma_{aB} - \mathcal{D}_m\mathcal{D}_a\gamma^m_B) - \frac{1}{r}(r_a\mathcal{D}_m\gamma^m_B - r_m\mathcal{D}_a\gamma^m_B) \\
&\quad - \frac{1}{r^2}(r_a r^m + r\mathcal{D}_a r^m)\gamma^m_B\frac{1}{2r^2}D^M(D_B\gamma_{aM} - D_M\gamma_{aB}) - \frac{1}{2r^2}\mathcal{D}_a(D_M\gamma^M_B - D_B\gamma^M_M) \\
&\quad - \frac{1}{r^3}r_a(D_M\gamma^M_B - D_B\gamma^M_M) \\
&= \left[-\frac{1}{2}\Box h_a + \frac{1}{2}\mathcal{D}^b\mathcal{D}_a h_b + \frac{1}{r}r^b\mathcal{D}_a h_b - \frac{1}{r}r_a\mathcal{D}^b h_b - \frac{1}{r^2}r^b r_b h_a - \frac{1}{r}h_b\mathcal{D}_a\mathcal{D}^b r\right]X_B, \qquad \text{(C.13b)}
\end{aligned}$$

$$\begin{aligned}
\delta R^{(\mathrm{odd})}_{AB} &= \Omega_{AB}\Big[r r_a\mathcal{D}_b(\gamma^{ab} - \frac{1}{2}g^{ab}\gamma^m_m) + (r_a r_b + r\mathcal{D}_a r_b)\gamma^{ab}\Big] - \frac{1}{2}D_A D_B\gamma^a_a + \frac{1}{2}\mathcal{D}_a(D_A\gamma^a_B + D_B\gamma^a_A) \\
&\quad + \frac{1}{r}r_a\Omega_{AB}D_M\gamma^{aM} - \frac{1}{2}\Box\gamma_{AB} + \frac{1}{r^2}D_M C^M_{AB} - \frac{1}{2r^2}D_A D_B\gamma^M_M + \frac{1}{r}r^a\mathcal{D}_a(\gamma_{AB} - \frac{1}{2}\Omega_{AB}\gamma^M_M) \\
&\quad - \frac{2}{r^2}r^a r_a(\gamma_{AB} - \frac{1}{2}\Omega_{AB}\gamma^M_M) \\
&= -\frac{1}{2}\mathcal{D}^a h_a\left(D_A X_B + D_B X_A\right) + \frac{1}{r}\Omega_{AB}\mathcal{D}_a h^a X^M \\
&= \frac{1}{2}\mathcal{D}^a h_a(D_A X_B + D_B X_A) + \frac{1}{r}\Omega_{AB}h_a D^M X_M \\
&= -\frac{1}{2}\mathcal{D}^a h_a(D_A X_B + D_B X_A) := [\mathcal{D}^a h_a]X_{AB}. \qquad \text{(C.13c)}
\end{aligned}$$

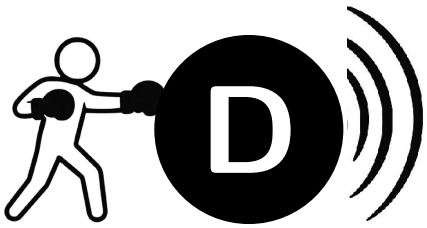
Proceeding in the same way for the even–parity sector, one obtains [37]

$$\begin{aligned}
\delta R^{(\text{even})}_{ab} &= \mathcal{D}_m C^m_{ab} + \frac{2}{r} r_m C^m_{ab} - \frac{1}{2}\mathcal{D}_a\mathcal{D}_b\gamma^m_m - \frac{1}{2r^2}D^M D_M\gamma_{ab} + \frac{1}{2r^2}D_M(\mathcal{D}_a\gamma^M_b + \mathcal{D}_b\gamma^M_a) - \frac{1}{2r^2}\mathcal{D}_a\mathcal{D}_b\gamma^M_M \\
&\quad + \frac{1}{2r^3}(r_a\mathcal{D}_b\gamma^M_M + r_b\mathcal{D}_a\gamma^M_M) - \frac{1}{r^4}(r_a r_b - r\mathcal{D}_a r_b)\gamma^M_M \\
&= \Bigg[\frac{1}{2}\mathcal{D}_m(\mathcal{D}_b f^m_a + \mathcal{D}_a f^m_b - \mathcal{D}^m f_{ab}) + \frac{1}{r}r_m(\mathcal{D}_b f^m_a + \mathcal{D}_a f^m_b - \mathcal{D}^m f_{ab}) - \frac{1}{2}\mathcal{D}_a\mathcal{D}_b f^m_m + \frac{\ell(\ell+1)}{2r^2}f_{ab} \\
&\quad - \frac{1}{r^2}\mathcal{D}_a\mathcal{D}_b(r^2K) + \frac{1}{r^3}\big(r_a\mathcal{D}_b(r^2K) + r_b\mathcal{D}_a(r^2K)\big) - \frac{2}{r^2}(r_a r_b - r\mathcal{D}_a r_b)K\Bigg]Y \\
&= \frac{1}{2}\mathcal{D}_b\mathcal{D}_m f^m_a + \frac{8M}{r^3 d(d-1)}(df_{ba} - g_{ba}f^m_m) + \mathcal{D}_a\mathcal{D}_m f^m_b - \Box f_{ab} + \frac{2}{r}r_m(\mathcal{D}_b f^m_a + \mathcal{D}_a f^m_b - \mathcal{D}^m f_{ab}) \\
&\quad - \mathcal{D}_a\mathcal{D}_b f^m_m + \frac{\ell(\ell+1)}{r^2}f_{ab} - \frac{2}{r}(r_b\mathcal{D}_a K - r_a\mathcal{D}_b K) - 2\mathcal{D}_a\mathcal{D}_b K\Bigg]Y, \qquad \text{(C.14a)}
\end{aligned}$$

$$\begin{aligned}
\delta R^{(\text{even})}_{aB} &= \frac{1}{2}D_B\Big(\mathcal{D}_b\gamma^b_a - \mathcal{D}_a\gamma^b_b + \frac{1}{r}r_a\gamma^b_b\Big) - \frac{1}{2}(\overset{\wedge}{\Box}\gamma_{aB} - \mathcal{D}_b\mathcal{D}_a\gamma^b_B) - \frac{1}{r}(r_a\mathcal{D}_b\gamma^b_B - r_b\mathcal{D}_a\gamma^b_B) - \frac{1}{r^2}(r_a r_b + r\mathcal{D}_a r_b)\,\gamma^b_B \\
&\quad + \frac{1}{2r^2}D^M(D_B\gamma_{aM} - D_M\gamma_{aB}) - \frac{1}{2r^2}\mathcal{D}_a(D_M\gamma^M_B - D_B\gamma^M_M) - \frac{1}{r^3}r_a(D_M\gamma^M_B - D_B\gamma^M_M) \\
&= \frac{1}{2}D_B\Big(\mathcal{D}_b f^b_a - \mathcal{D}_a f^b_b + \frac{1}{r}r_a f^b_b\Big)D_B Y - \frac{1}{2r^2}\mathcal{D}_a(r^2K)D_B Y + \frac{1}{r}r_a K D_B Y \\
&= \frac{1}{2}\Big[\mathcal{D}_b f^b_a - \mathcal{D}_a f^b_b + \frac{1}{r}r_a f^b_b - \mathcal{D}_a K\Big]Y_B, \qquad \text{(C.14b)}
\end{aligned}$$

$$\begin{aligned}
\delta R^{(\text{even})}_{AB} &= \Omega_{AB}\Bigg[r r_a\mathcal{D}_b\left(f^{ab} - \frac{1}{2}g^{ab}f^m_m\right) + (r_a r_b + r\mathcal{D}_a r_b)f^{ab}\Bigg] - \frac{1}{2}D_A D_B\gamma^a_a + \frac{1}{2}\mathcal{D}_a\left(D_A\gamma^a_B + D_B\gamma^a_A\right) \\
&\quad + \frac{1}{r}r_a\Omega_{AB}D_M\gamma^{aM} - \frac{1}{2}\Box\,\gamma_{AB} + \frac{1}{r^2}D_M C^M_{AB} - \frac{1}{2r^2}D_A D_B\gamma^M_M + \frac{1}{r}r^a\mathcal{D}_a\left(\gamma_{AB} - \frac{1}{2}\Omega_{AB}\gamma^M_M\right) \\
&\quad - \frac{2}{r^2}r^a r_a\left(\gamma_{AB} - \frac{1}{2}\Omega_{AB}\gamma^M_M\right) \\
&= \Omega_{AB}\Bigg[r r_a\mathcal{D}_b\left(f^{ab} - \frac{1}{2}g^{ab}f^m_m\right) + (r_a r_b + r\mathcal{D}_a r_b)f^{ab}\Bigg] - \frac{1}{2}f^a_a D_A D_B Y - \frac{1}{2}(r^2K)\Box Y \\
&\quad + \frac{1}{2}\Big[K(D_A D_B Y + D_B D_A Y - \Omega_{AB}D^M D_M Y) - K D_A D_B Y\Big] \\
&= \Bigg[r r_a\mathcal{D}_b f^{ab} - \frac{1}{2}r r^b\mathcal{D}_b f^m_m + r_a r_b f^{ab} + r\mathcal{D}_a r_b f^{ab} - \frac{1}{2}\Box(r^2K) + \frac{1}{2}\ell(\ell+1)K\Bigg]\Omega_{AB}Y \\
&\quad + \frac{1}{4}\ell(\ell+1)f^a_a\,\Omega_{AB}Y - \frac{1}{2}f^a_a Y_{AB}. \qquad \text{(C.14c)}
\end{aligned}$$

Appendix



Newman–Penrose formalism

In this appendix we follow the treatments of [7, 42, 45] to introduce the NP formalism, a special case of the tetrad approach in which the internal metric takes the form

$$\eta_{(a)(b)} = \begin{pmatrix} 0 & 1 & 0 & 0 \\ 1 & 0 & 0 & 0 \\ 0 & 0 & 0 & -1 \\ 0 & 0 & -1 & 0 \end{pmatrix}. \tag{D.1}$$

This choice reflects the fact that instead of an orthonormal frame, we work with a *null tetrad*, built out of two real null vectors and a pair of complex conjugate null vectors. The four basis vectors are denoted as

$$l^i \equiv e^i_{(1)}, \qquad n^i \equiv e^i_{(2)}, \qquad m^i \equiv e^i_{(3)}, \qquad \bar{m}^i \equiv e^i_{(4)}, \tag{D.2a}$$

$$e^i_{(1)} = n^i, \qquad e^i_{(2)} = l^i, \qquad e^i_{(3)} = -\bar{m}^i, \qquad e^i_{(4)} = -m^i. \tag{D.2b}$$

With this basis, the spacetime metric can be written in the compact form

$$g_{ij} = 2l_{(i}n_{j)} - 2m_{(i}\bar{m}_{j)}, \qquad g^{ij} = 2l^{(i}n^{j)} - 2m^{(i}\bar{m}^{j)} \tag{D.3}$$

The construction ensures that l^i and n^i are real null vectors, while m^i and $\bar{m}^i$ are complex null vectors that are conjugate to each other. The normalization conditions follow directly from the internal metric (D.1)

$$l_i m^i = l_i \bar{m}^i = n_i m^i = n_i \bar{m}^i = l_i l^i = n_i n^i = m_i m^i = \bar{m}_i \bar{m}^i = 0, \qquad l_i n^i = -m_i \bar{m}^i = 1. \tag{D.4}$$

D.1 Directional derivatives and Ricci rotation coefficients

We can introduce a compact notation for the directional derivatives along the null tetrad. Each of the four basis vectors defines a preferred derivative operator

$$D \equiv l^i \nabla_i, \qquad \Delta \equiv n^i \nabla_i, \qquad \delta \equiv m^i \nabla_i, \qquad \bar{\delta} \equiv \bar{m}^i \nabla_i, \tag{D.5}$$

where D and Δ represent derivatives along the real null directions, while δ and $\bar{\delta}$ act along the complex conjugate ones.

In addition, the full set of Ricci rotation coefficients can be encoded into twelve complex scalars, traditionally referred to as the NP spin coefficients. These are defined as specific contractions of the Ricci coefficients

$$\kappa \equiv \gamma_{(3)(1)(1)} = -m^i l^j \nabla_j l_i, \qquad \sigma \equiv \gamma_{(3)(1)(3)} = -m^i m^j \nabla_j l_i, \tag{D.6a}$$

$$\lambda \equiv \gamma_{(2)(4)(4)} = \bar{m}^i \bar{m}^j \nabla_j n_i, \qquad \nu \equiv \gamma_{(2)(4)(2)} = \bar{m}^i n^j \nabla_j n_i, \tag{D.6b}$$

$$\rho \equiv \gamma_{(3)(1)(4)} = -m^i \bar{m}^j \nabla_j l_i, \qquad \mu \equiv \gamma_{(2)(4)(3)} = \bar{m}^i m^j \nabla_j n_i, \tag{D.6c}$$

$$\tau \equiv \gamma_{(3)(1)(2)} = -m^i n^j \nabla_j l_i, \qquad \pi \equiv \gamma_{(2)(4)(1)} = \bar{m}^i l^j \nabla_j n_i. \tag{D.6d}$$

and the combinations

$$\epsilon \equiv \tfrac{1}{2}\left(\gamma_{(2)(1)(1)} + \gamma_{(3)(4)(1)}\right) = -\tfrac{1}{2}\left(n^i l^j \nabla_j l_i - \bar{m}^i l^j \nabla_j m_i\right), \tag{D.7a}$$

$$\gamma \equiv \tfrac{1}{2}\left(\gamma_{(2)(1)(2)} + \gamma_{(3)(4)(2)}\right) = -\tfrac{1}{2}\left(n^i n^j \nabla_j l_i - \bar{m}^i n^j \nabla_j m_i\right), \tag{D.7b}$$

$$\alpha \equiv \tfrac{1}{2}\left(\gamma_{(2)(1)(4)} + \gamma_{(3)(4)(4)}\right) = -\tfrac{1}{2}\left(n^i \bar{m}^j \nabla_j l_i - \bar{m}^i \bar{m}^j \nabla_j m_i\right), \tag{D.7c}$$

$$\beta \equiv \tfrac{1}{2}\left(\gamma_{(2)(1)(3)} + \gamma_{(3)(4)(3)}\right) = -\tfrac{1}{2}\left(n^i m^j \nabla_j l_i - \bar{m}^i m^j \nabla_j m_i\right). \tag{D.7d}$$

The twelve coefficients $\kappa, \sigma, \lambda, \nu, \rho, \mu, \tau, \pi, \epsilon, \gamma, \alpha, \beta$ contain the full information of the connection in the NP basis. By antisymmetry of the Ricci rotation coefficients, only half are independent. Since indices (3) and (4) correspond to complex conjugate null vectors, it is enough to specify those with (3), the others following by conjugation. In this way, the twenty-four Ricci coefficients reduce to twelve complex quantities.

D.2 Components of Weyl and Ricci tensors

The Riemann tensor can be decomposed into the traceless Weyl tensor and the Ricci tensor, and the independent tetrad projections of these tensors are summarized by a small set of scalars.

D.2.1 Weyl scalars

In four dimensions the Weyl tensor has ten independent components, which are encoded in the five complex Weyl scalars

$$\Psi_0 \equiv -C_{1313} = -C_{pqrs}\, l^p m^q l^r m^s, \tag{D.8a}$$

$$\Psi_1 \equiv -C_{1213} = -C_{pqrs}\, l^p n^q l^r m^s, \tag{D.8b}$$

$$\Psi_2 \equiv -C_{1342} = -C_{pqrs}\, l^p m^q \bar{m}^r n^s, \tag{D.8c}$$

$$\Psi_3 \equiv -C_{1242} = -C_{pqrs}\, l^p n^q \bar{m}^r n^s, \tag{D.8d}$$

$$\Psi_4 \equiv -C_{2424} = -C_{pqrs}\, n^p \bar{m}^q n^r \bar{m}^s. \tag{D.8e}$$

These quantities capture the independent degrees of freedom of the free gravitational field in the NP formalism.

D.2.2 Ricci scalars

Similarly, the Ricci tensor can be expressed in terms of four real and three complex scalars. The Ricci scalars are defined as

$$\Phi_{00} \equiv \tfrac{1}{2} R_{pq}\, l^p l^q, \qquad \Phi_{22} \equiv \tfrac{1}{2} R_{pq}\, n^p n^q, \tag{D.9a}$$

$$\Phi_{02} \equiv \tfrac{1}{2} R_{pq}\, m^p m^q, \qquad \Phi_{20} \equiv \tfrac{1}{2} R_{pq}\, \bar{m}^p \bar{m}^q, \tag{D.9b}$$

$$\Phi_{11} \equiv \tfrac{1}{4} R_{pq}\, (l^p n^q + m^p \bar{m}^q), \qquad \Phi_{01} \equiv \tfrac{1}{2} R_{pq}\, l^p m^q, \tag{D.9c}$$

$$\Phi_{10} \equiv \tfrac{1}{2} R_{pq}\, l^p \bar{m}^q, \qquad \Phi_{12} \equiv \tfrac{1}{2} R_{pq}\, n^p m^q, \tag{D.9d}$$

$$\Phi_{21} \equiv \tfrac{1}{2} R_{pq}\, n^p \bar{m}^q, \qquad \Lambda \equiv -\tfrac{1}{24} R. \tag{D.9e}$$

Because the Ricci tensor is symmetric, these definitions are sufficient to reconstruct all its tetrad components in terms of the NP scalars.

D.3 Commutation relations between directional derivatives

The four NP operators D, Δ, δ and $\bar{\delta}$ do not commute in general. Their commutators can be expressed in terms of the spin coefficients. Formally, one writes

$$[e^i_{(a)} \nabla_i, e^j_{(b)} \nabla_j] = C^{(c)}_{(a)(b)} e^k_{(c)} \nabla_k = \big(\gamma_{(c)(b)(a)} - \gamma_{(c)(a)(b)}\big) e^k_{(c)} \nabla_k, \tag{D.10}$$

where $C^{(c)}_{(a)(b)}$ are the structure constants associated with the tetrad basis. Working out these commutators explicitly yields the following relations

$$[D, \Delta] = -(\gamma + \bar{\gamma}) D - (\epsilon + \bar{\epsilon}) \Delta + (\pi + \bar{\tau}) \delta + (\bar{\pi} + \tau) \bar{\delta}, \tag{D.11a}$$

$$[D, \delta] = (\bar{\pi} - \beta - \bar{\alpha}) D - \kappa \Delta + (\epsilon - \bar{\epsilon} + \bar{\pi}) \delta + \sigma \bar{\delta}, \tag{D.11b}$$

$$[\Delta, \delta] = \bar{\nu} D + (-\tau + \bar{\alpha} + \beta) \Delta + (\gamma - \bar{\gamma} - \mu) \delta - \bar{\lambda} \bar{\delta}, \tag{D.11c}$$

$$[\delta, \bar{\delta}] = (\mu - \bar{\mu}) D + (\rho - \bar{\rho}) \Delta + (-\alpha + \bar{\beta}) \delta + (\bar{\alpha} - \beta) \bar{\delta}. \tag{D.11d}$$

D.4 Ricci identities

By combining the Ricci rotation coefficients with tetrad projections of the Riemann tensor, one arrives at the *Ricci identities* of the NP formalism. These relations express derivatives of the spin coefficients in terms of quadratic combinations of themselves and curvature scalars, replacing the complexity of the Riemann tensor with a set of complex variables. Once a tetrad is fixed, they serve as transport equations along the null directions $l^i, n^i, m^i, \bar{m}^i$, determining the evolution of curvature.

$$D\rho - \bar{\delta}\kappa = (\rho^2 + \sigma\bar{\sigma}) + \rho(\epsilon + \bar{\epsilon}) - \bar{\kappa}\,\tau - \kappa(3\alpha + \bar{\beta} - \pi) + \Phi_{00}, \tag{D.12a}$$

$$D\sigma - \delta\kappa = \sigma(\rho + \bar{\rho} + 3\epsilon - \bar{\epsilon}) - \kappa(\tau - \bar{\pi} + \alpha + 3\beta) + \Psi_0, \tag{D.12b}$$

$$D\tau - \Delta\kappa = \rho(\tau + \bar{\pi}) + \sigma(\bar{\tau} + \pi) + \tau(\epsilon - \bar{\epsilon}) - \kappa(3\gamma + \bar{\gamma}) + \Psi_1 + \Phi_{01}, \tag{D.12c}$$

$$\delta\alpha - \delta\epsilon = \alpha(\rho + \bar{\epsilon} - 2\epsilon) + \beta\sigma - \bar{\beta}\bar{\sigma} - \kappa\lambda - \bar{\kappa}\gamma + \pi(\epsilon + \rho) + \Phi_{10}, \tag{D.12d}$$

$$D\beta - \delta\epsilon = \sigma(\alpha + \pi) + \beta(\bar{\rho} - \epsilon) - \kappa(\mu + \gamma) - \epsilon(\bar{\alpha} - \bar{\pi}) + \Psi_1, \tag{D.12e}$$

$$D\gamma - \Delta\epsilon = \alpha(\tau + \bar{\pi}) + \beta(\bar{\tau} + \pi) - \gamma(\epsilon + \bar{\epsilon}) - \epsilon(\gamma + \bar{\gamma}) + \pi\tau - \nu\kappa + \Psi_2 + \Phi_{11} - \Lambda, \tag{D.12f}$$

$$D\lambda - \bar{\delta}\pi = (\rho\lambda + \bar{\sigma}\mu) + \pi(\pi + \alpha - \bar{\beta}) - \nu\bar{\kappa} - \lambda(3\epsilon - \bar{\epsilon}) + \Phi_{20}, \tag{D.12g}$$

$$D\mu - \delta\pi = (\bar{\rho}\mu + \sigma\lambda) + \pi(\bar{\pi} - \alpha + \bar{\beta}) - \mu(\epsilon + \bar{\epsilon}) - \nu\kappa + \Psi_2 + 2\Lambda, \tag{D.12h}$$

$$D\nu - \Delta\pi = \mu(\pi + \bar{\pi}) + \lambda(\bar{\tau} + \pi) + \pi(\gamma - \bar{\gamma}) - \nu(3\epsilon + \bar{\epsilon}) + \Psi_3 + \Phi_{21}, \tag{D.12i}$$

$$\Delta\lambda - \bar{\delta}\nu = -\lambda(\mu + \bar{\mu} + 3\gamma - \bar{\gamma}) + \nu(3\alpha + \bar{\beta} + \pi - \bar{\tau}) - \Psi_4, \tag{D.12j}$$

$$\delta\rho - \bar{\delta}\sigma = \rho(\bar{\alpha} + \beta) - \sigma(3\alpha - \bar{\beta}) + \tau(\rho - \bar{\rho}) + \kappa(\mu - \bar{\mu}) - \Psi_1 + \Phi_{01}, \tag{D.12k}$$

$$\delta\alpha - \bar{\delta}\beta = \mu\rho - \lambda\sigma + \alpha\bar{\alpha} + \beta\bar{\beta} - 2\alpha\beta + \gamma(\rho - \bar{\rho}) + \epsilon(\mu - \bar{\mu}) - \Psi_2 + \Phi_{11} + \Lambda, \tag{D.12l}$$

$$\delta\lambda - \bar{\delta}\mu = \nu(\rho - \bar{\rho}) + \pi(\mu - \bar{\mu}) + \mu(\alpha + \bar{\beta}) + \lambda(\bar{\alpha} - 3\beta) - \Psi_3 + \Phi_{21}, \tag{D.12m}$$

$$\Delta\nu - \bar{\delta}\mu = (\mu^2 + \lambda\bar{\lambda}) + \mu(\gamma + \bar{\gamma}) - \nu\pi + \nu(\tau - 3\beta - \bar{\alpha}) + \Phi_{22}, \tag{D.12n}$$

$$\delta\gamma - \bar{\delta}\beta = \gamma(\tau - \bar{\alpha} - \beta) + \mu\tau - \sigma\nu - \epsilon\bar{\nu} - \beta(\gamma - \bar{\gamma} - \mu) + \alpha\bar{\lambda} + \Phi_{12}, \tag{D.12o}$$

$$\Delta\tau - \delta\gamma = (\mu\sigma + \lambda\bar{\rho}) + \tau(\tau + \beta - \bar{\alpha}) - \sigma(3\gamma - \bar{\gamma}) - \kappa\nu + \Phi_{02}, \tag{D.12p}$$

$$\Delta\rho - \bar{\delta}\tau = -\bar{\rho}\mu + \sigma\lambda + \tau(\bar{\beta} - \alpha - \bar{\pi}) + \rho(\gamma + \bar{\gamma}) + \nu\kappa - \Psi_2 - 2\Lambda, \tag{D.12q}$$

$$\Delta\alpha - \delta\gamma = \nu(\rho + \epsilon) - \lambda(\tau + \beta) + \alpha(\bar{\gamma} - \mu) + \gamma(\bar{\beta} - \bar{\tau}) - \Psi_3. \tag{D.12r}$$

D.5 Weyl scalars in terms of Ricci rotation coefficients

The relations obtained in the previous subsection can be rearranged to express the Weyl scalars Ψ_i directly as combinations of the spin coefficients and their derivatives. In this sense, the Ψ_i act as a compact encoding of the curvature content of the spacetime, written entirely in terms of the NP formalism. Explicitly, one finds

$$\Psi_0 = \bar{\alpha}\kappa + 3\beta\kappa - \kappa\pi - 3\epsilon\sigma + \bar{\epsilon}\sigma - \rho\sigma - \bar{\rho}\sigma + \kappa\tau + D(\sigma) - \delta(\kappa), \tag{D.13a}$$

$$\Psi_1 = \bar{\alpha}\epsilon + \bar{\beta}\epsilon + \gamma\kappa + \kappa\mu - \bar{\epsilon}\pi - \beta\rho - \alpha\sigma - \pi\sigma + D(\beta) - \delta(\epsilon), \tag{D.13b}$$

$$\Psi_2 = -2\Lambda + \epsilon\mu + \bar{\epsilon}\mu + \kappa\nu + \bar{\alpha}\pi - \beta\pi - \pi\bar{\pi} - \mu\bar{\mu} - \lambda\sigma + D(\mu) - \delta(\pi), \tag{D.13c}$$

$$\Psi_3 = \bar{\beta}\gamma + \bar{\alpha}\gamma - \beta\lambda - \alpha\bar{\mu} + \epsilon\nu + \nu\rho - \lambda\tau - \bar{\gamma}\tau - \Delta(\alpha) + \bar{\delta}(\gamma), \tag{D.13d}$$

$$\Psi_4 = -3\gamma\lambda + \bar{\gamma}\lambda - \lambda\mu - \lambda\bar{\mu} + 3\alpha\nu + \bar{\beta}\nu + \nu\pi - \nu\bar{\tau} - \Delta(\lambda) + \bar{\delta}(\nu). \tag{D.13e}$$

D.6 Components of the Bianchi identities

From the definition of the Bianchi identity in terms of Ricci Rotation coefficien together with the definitions of the NP scalars and the Ricci rotationcoefficients, one obtains the Bianchi identities expressed as first–order differential relations for the Weyl scalars. Explicitly, these can be written as

$$-\bar{\delta}\Psi_0 + D\Psi_1 + (4\alpha - \pi)\Psi_0 - 2(2\rho + \epsilon)\Psi_1 + 3\kappa\Psi_2 + \mathcal{R}_a = 0, \tag{D.14}$$

$$\delta\Psi_1 - \Delta\Psi_2 - \lambda\Psi_0 + 2(\pi - \alpha)\Psi_1 + 3\rho\Psi_2 - 2\kappa\Psi_3 + \mathcal{R}_b = 0, \tag{D.15}$$

$$-\bar{\delta}\Psi_2 + D\Psi_3 + 2\lambda\Psi_1 - 3\pi\Psi_2 + 2(\epsilon - \rho)\Psi_3 + \kappa\Psi_4 + \mathcal{R}_c = 0, \tag{D.16}$$

$$\bar{\delta}\Psi_3 - \Delta\Psi_4 - 3\lambda\Psi_2 + 2(2\pi + \alpha)\Psi_3 - (4\epsilon - \rho)\Psi_4 + \mathcal{R}_d = 0, \tag{D.17}$$

$$-\Delta\Psi_0 + \delta\Psi_1 + (4\gamma - \mu)\Psi_0 - 2(2\tau + \beta)\Psi_1 + 3\sigma\Psi_2 + \mathcal{R}_e = 0, \tag{D.18}$$

$$-\Delta\Psi_1 + \delta\Psi_2 + \nu\Psi_0 + 2(\gamma - \mu)\Psi_1 - 3\tau\Psi_2 + 2\sigma\Psi_3 + \mathcal{R}_f = 0, \tag{D.19}$$

$$-\Delta\Psi_2 + \delta\Psi_3 + 2\nu\Psi_1 - 3\mu\Psi_2 + 2(\beta - \tau)\Psi_3 + \sigma\Psi_4 + \mathcal{R}_g = 0, \tag{D.20}$$

$$-\Delta\Psi_3 + \delta\Psi_4 + 3\nu\Psi_2 - 2(\gamma + 2\mu)\Psi_3 - (\tau - 4\beta)\Psi_4 + \mathcal{R}_h = 0. \tag{D.21}$$

The terms $\mathcal{R}_a, \ldots, \mathcal{R}_h$ encode the contributions from the Ricci scalars,

$$\mathcal{R}_a = -D\Phi_{01} + \delta\Phi_{00} + 2(\epsilon + \bar{\rho})\Phi_{01} + 2\sigma\Phi_{10} - 2\kappa\Phi_{11} - \bar{\kappa}\Phi_{02} + (\bar{\pi} - 2\bar{\alpha} - 2\beta)\Phi_{00}, \tag{D.22}$$

$$\mathcal{R}_b = \bar{\delta}\Phi_{01} - \Delta\Phi_{00} - 2(\alpha + \bar{\tau})\Phi_{01} + 2\rho\Phi_{11} + \bar{\sigma}\Phi_{02} - (\mu - 2\gamma - 2\bar{\gamma})\Phi_{00} - 2\tau\Phi_{10} - 2D\Lambda, \tag{D.23}$$

$$\mathcal{R}_c = -D\Phi_{21} + \delta\Phi_{20} + 2(\bar{\rho} - \epsilon)\Phi_{21} - 2\mu\Phi_{10} + 2\pi\Phi_{11} - \kappa\Phi_{22} - (2\bar{\alpha} - 2\beta - \bar{\pi})\Phi_{20} - 2\bar{\delta}\Lambda, \tag{D.24}$$

$$\mathcal{R}_d = -\Delta\Phi_{20} + \bar{\delta}\Phi_{21} + (2\alpha - \bar{\tau})\Phi_{21} + 2\nu\Phi_{10} + \bar{\sigma}\Phi_{22} - 2\lambda\Phi_{11} - (\bar{\mu} + 2\gamma - 2\bar{\gamma})\Phi_{20}, \tag{D.25}$$

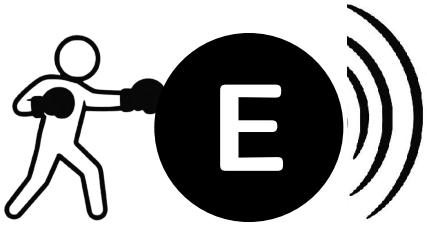
$$\mathcal{R}_e = -D\Phi_{02} + \delta\Phi_{01} + 2(\bar{\pi} - \beta)\Phi_{01} - 2\kappa\Phi_{12} - \bar{\lambda}\Phi_{00} + 2\sigma\Phi_{11} + (\bar{\rho} + 2\epsilon - 2\bar{\epsilon})\Phi_{02}, \tag{D.26}$$

$$\mathcal{R}_f = \Delta\Phi_{01} - \bar{\delta}\Phi_{02} + 2(\mu - \gamma)\Phi_{01} - 2\rho\Phi_{12} - \bar{\nu}\Phi_{00} + 2\tau\Phi_{11} + (\bar{\tau} - 2\bar{\beta} + 2\alpha)\Phi_{02} + 2\delta\Lambda, \tag{D.27}$$

$$\mathcal{R}_g = -D\Phi_{22} + \delta\Phi_{21} + 2(\pi + \beta)\Phi_{21} - 2\mu\Phi_{11} - \bar{\lambda}\Phi_{20} + 2\pi\Phi_{12} + (\bar{\mu} - 2\epsilon - 2\bar{\epsilon})\Phi_{22} - 2\Delta\Lambda, \tag{D.28}$$

$$\mathcal{R}_h = \Delta\Phi_{21} - \bar{\delta}\Phi_{22} + 2(\bar{\mu} + \gamma)\Phi_{21} - \bar{\nu}\Phi_{20} + 2\lambda\Phi_{12} + (\bar{\tau} - 2\alpha - 2\bar{\beta})\Phi_{22}. \tag{D.29}$$

Appendix



Fourth–order finite difference formulas

In this appendix we reproduce the explicit fourth–order finite difference formulas presented in [55], which are employed throughout this work to approximate spatial derivatives. We denote by $u_j \equiv u(x_j)$ the value of the function on a uniform grid $x_j = jh$, with spacing h. The truncation error involves higher–order derivatives of u evaluated at some intermediate point $\xi \in [x_j - h,\, x_j + h]$.

E.1 First derivative

The following expressions provide fourth–order accurate approximations for the first derivative. Equation (E.1a) corresponds to the *centered* stencil. Equations (E.1b) and (E.1c) are *off–centered* formulas, shifted by one and two grid points, respectively.

$$u'(x_j) = \frac{-u_{j-2} + 8u_{j-1} - 8u_{j+1} + u_{j+2}}{12h} - \frac{1}{30}h^4 u^{(5)}(\xi), \tag{E.1a}$$

$$u'(x_j) = \frac{-3u_{j-1} - 10u_j + 18u_{j+1} - 6u_{j+2} + u_{j+3}}{12h} + \frac{1}{20}h^4 u^{(5)}(\xi), \tag{E.1b}$$

$$u'(x_j) = \frac{-25u_j + 48u_{j+1} - 36u_{j+2} + 16u_{j+3} - 3u_{j+4}}{12h} - \frac{1}{5}h^4 u^{(5)}(\xi). \tag{E.1c}$$

E.2 Second derivative

For the second derivative, Eq. (E.2a) is the *centered* stencil, while (E.2b) and (E.2c) are *off–centered*, displaced by one and two points, respectively.

$$u''(x_j) = \frac{-u_{j-2} + 16u_{j-1} - 30u_j + 16u_{j+1} - u_{j+2}}{12h^2} - \frac{1}{90}h^4 u^{(6)}(\xi), \tag{E.2a}$$

$$u''(x_j) = \frac{10u_{j-1} - 15u_j - 4u_{j+1} + 14u_{j+2} - 6u_{j+3} + u_{j+4}}{12h^2} - \frac{13}{180}h^4 u^{(6)}(\xi), \tag{E.2b}$$

$$u''(x_j) = \frac{45u_j - 154u_{j+1} + 214u_{j+2} - 156u_{j+3} + 61u_{j+4} - 10u_{j+5}}{12h^2} - \frac{137}{180}h^4 u^{(6)}(\xi). \tag{E.2c}$$

E.3 Third derivative

Equation (E.3a) is the *centered* stencil. Equations (E.3b), (E.3c), and (E.3d) are *off–centered*, shifted by one, two, and three grid points, respectively.

$$u^{(3)}(x_j) = \frac{u_{j-3} - 8u_{j-2} + 13u_{j-1} - 13u_{j+1} + 8u_{j+2} - u_{j+3}}{8h^3} - \frac{7}{120}h^4 u^{(7)}(\xi), \tag{E.3a}$$

$$u^{(3)}(x_j) = \frac{-u_{j-2} + 8u_{j-1} - 35u_j + 48u_{j+1} - 29u_{j+2} + 8u_{j+3} - u_{j+4}}{8h^3} + \frac{1}{15}h^4 u^{(7)}(\xi), \tag{E.3b}$$

$$u^{(3)}(x_j) = \frac{-15u_{j-1} + 56u_j - 83u_{j+1} + 64u_{j+2} - 29u_{j+3} + 8u_{j+4} - u_{j+5}}{8h^3} - \frac{7}{120}h^4 u^{(7)}(\xi), \tag{E.3c}$$

$$u^{(3)}(x_j) = \frac{-49u_{j-1} + 232u_j - 461u_{j+1} + 496u_{j+2} - 307u_{j+3} + 104u_{j+4} - 15u_{j+5}}{8h^3} - \frac{15}{8h^3}u_{j+6} + \frac{29}{15}h^4 u^{(7)}(\xi). \tag{E.3d}$$

E.4 Fourth derivative

Equation (E.4a) is the *centered* formula. Equations (E.4b), (E.4c), and (E.4d) are the *off–centered* variants, shifted by one, two, and three points, respectively.

$$u^{(4)}(x_j) = \frac{-u_{j-3} + 12u_{j-2} - 39u_{j-1} + 56u_j - 39u_{j+1} + 12u_{j+2} - u_{j+3}}{6h^4} - \frac{7}{240}h^4 u^{(8)}(\xi), \tag{E.4a}$$

$$u^{(4)}(x_j) = \frac{4u_{j-2} - 11u_{j-1} + 31u_j - 44u_{j+1} + 27u_{j+2} - 8u_{j+3} + u_{j+4}}{6h^4} + \frac{11}{80}h^4 u^{(8)}(\xi), \tag{E.4b}$$

$$u^{(4)}(x_j) = \frac{21u_{j-2} - 112u_{j-1} + 255u_j - 324u_{j+1} + 251u_{j+2} - 120u_{j+3} + 33u_{j+4} - 4u_{j+5}}{6h^4} + \frac{127}{240}h^4 u^{(8)}(\xi), \tag{E.4c}$$

$$u^{(4)}(x_j) = \frac{56u_{j-3} - 333u_{j-2} + 852u_{j-1} - 1219u_j + 1056u_{j+1} - 555u_{j+2} + 164u_{j+3} - 21u_{j+4}}{6h^4} + \frac{967}{240}h^4 u^{(8)}(\xi). \tag{E.4d}$$